



HAL
open science

Tuning the redox properties of cobalt particles supported on oxides by an In-between graphene layer

Wen Luo

► **To cite this version:**

Wen Luo. Tuning the redox properties of cobalt particles supported on oxides by an In-between graphene layer. Theoretical and/or physical chemistry. Université de Strasbourg, 2016. English. NNT : 2016STRAF007 . tel-01389467

HAL Id: tel-01389467

<https://theses.hal.science/tel-01389467>

Submitted on 28 Oct 2016

HAL is a multi-disciplinary open access archive for the deposit and dissemination of scientific research documents, whether they are published or not. The documents may come from teaching and research institutions in France or abroad, or from public or private research centers.

L'archive ouverte pluridisciplinaire **HAL**, est destinée au dépôt et à la diffusion de documents scientifiques de niveau recherche, publiés ou non, émanant des établissements d'enseignement et de recherche français ou étrangers, des laboratoires publics ou privés.

ÉCOLE DOCTORALE DES SCIENCES CHIMIQUES

ICPEES, UMR 7515

Institut de chimie et procédés pour l'énergie, l'environnement et la santé

THÈSE

présentée par :

Wen LUO

soutenue le : **24 Mars 2016**

pour obtenir le grade de : **Docteur de l'université de Strasbourg**

Discipline/ Spécialité : Chimie/ Chimie Physique

**Tuning the Redox Properties of Cobalt Particles Supported on Oxides
by an In-between Graphene Layer**

**Modification des Propriétés Redox de Particules de Cobalt Supportées Sur des
Oxydes par Insertion d'une Couche de Graphène**

THÈSE dirigée par:

M. ZAFEIRATOS Spiros

Chargé de recherche, Université de Strasbourg, Strasbourg

RAPPORTEURS:

M. PICCOLO Laurent

Chargé de recherche, IRCELYON, Lyon

M. NEOPHYTIDES Stelios

Research Director, FORTH/ICE-HT, Patras

AUTRES MEMBRES DU JURY:

M. PHAM-HUU Cuong

Directeur de recherche, Université de Strasbourg, Strasbourg

M. LE NORMAND François

Directeur de recherche, Université de Strasbourg, Strasbourg

M. TESCHNER Detre

Max Plank Society Research Fellow, Fritz-Haber-Institut, Berlin

Acknowledgements

I would like to express my gratitude to all the people who have supported me during my study for the PhD degree of Université de Strasbourg in ICPEES (Institut de chimie et procédés pour l'énergie, l'environnement et la santé). The China Scholarship Council (CSC) is greatly acknowledged for the financial supporting of my PhD study.

I will be always grateful to my supervisor, Dr. Spiros Zafeiratos, for his scientific guidance, fruitful discussions and constant support during my PhD study. He is always readily available to help me to solve the problems and to provide me the instructions on my research. He is so kind and patient which provides a great atmosphere in the lab for conducting research. I really enjoy the time of staying in the lab.

I would like to thank my colleagues in our group, Dr. Vasiliki Papaefthimiou, Dr. Won-hui Doh, Dr. Yeuk Ting Law and Sylwia Turczyniak. They are so generous to share their experience and knowledge with me and offer enormous help to me on both technical and scientific issues. I cannot remember how many problems that I met were solved by Doh. I am truly thankful also for Vasiliki in helping me on the French abstract and the proof-reading of the whole thesis.

I would like to thank Prof. Andrzej Machocki and the group members in his lab in the chemical technology department in Lublin for their warm welcome and assistance during my stay in Lublin.

I would also like to thank the staff of the technical and administrative department in ICPEES. Dr. Thierry Dintzer helped me with the SEM experiments and Christophe Melart helped me with Raman measurements. Thanks to Alain Rach, Sécou Sall, Véronique Verkruysse, Francine Jacky... for their support all along.

I would also like to thank the members of the jury, Dr. Laurent Piccolo, Dr. Stelios Neophytides, Dr. Cuong Pham-Huu, Dr. François Le Normand and Dr. Detre Teschner, for reading the manuscript and providing helpful comments.

Special thanks of all my Chinese friends in Strasbourg (Qian, Wei, Yuefeng, Jingjie, Nan, Yige, Qinqin, Xuemei, Yunjie, Quan, Zhenxin...) for their company and help in my daily life and PhD study. Special thanks to Qing for her understanding and supporting. I would also like to thank the colleagues in ICPEES (Viktorias, Sébastien...) for their help in the lab.

Above all, I would like to thank my parents and my brother for their enduring support throughout my study.

Table of Content

Acknowledgements	i
Table of Content.....	iii
R ésum é.....	1
Chapter 1 Introduction.....	16
1.1 Metal-Support interaction in catalysis.....	16
1.1.1 Fundamental aspects of metal-support interaction.....	16
1.1.2 Interactions of cobalt with support.....	17
1.2 Modification of Co-support interaction.....	29
1.2.1 Modification of Co-ZnO interactions in steam reforming of ethanol ..	30
1.2.2 Modification of Co-SiO ₂ interactions in Fischer-Tropsch synthesis....	32
1.2.3 Modification of Co-Carbon interactions in Fischer-Tropsch synthesis	34
1.3 Graphene	38
1.3.1 General introduction of graphene.....	38
1.3.2 Synthesis of Graphene.....	40
1.4 Motivation and outline of the dissertation	46
1.5 References	48
Chapter 2 Experimental techniques.....	66
2.1 Materials preparation.....	66
2.1.1 Preparation of substrates	66
2.1.2 Metal deposition.....	68
2.2 Characterization Methods	69
2.2.1 X-ray Photoemission Spectroscopy (XPS)	69
2.2.2 Raman spectroscopy.....	77
2.2.3 Low energy ion scattering (LEIS).....	80
2.2.4 High resolution electron energy loss spectroscopy (HREELS)	81
2.2.5 Atomic force microscopy (AFM).....	81

2.2.6	Scanning Electron microscopy (SEM)	84
2.3	UHV experimental apparatuses	84
2.4	References	87
Chapter 3 Investigation of Co interaction with bare, and graphene-covered, ZnO substrates in UHV conditions		90
3.1	Introduction	90
3.2	Experimental methods	91
3.3	Results and discussion	92
3.3.1	Characterization of ZnO and Graphene-ZnO substrates	92
3.3.2	Graphene's effect to the Co-ZnO interactions	94
3.3.3	The stability of graphene	98
3.4	Conclusions	102
3.5	References	103
Chapter 4 Influence of graphene interlayer on the redox properties of oxides supported Co particles.....		112
4.1	Introduction	112
4.2	Experimental Methods	113
4.2.1	Materials	113
4.2.2	Characterization	114
4.3	Results and discussion. Part I: low pressure redox behavior	116
4.3.1	Characterization of the <i>as-prepared</i> samples	116
4.3.2	Oxidation and reduction at 5×10^{-7} mbar	117
4.3.3	Comparison of normal and grazing angle XPS	120
4.3.4	Stability of the graphene layer under redox treatments	123
4.3.5	Discussion	124
4.4	Results and discussion. Part II: medium pressure redox	126
4.4.1	The as-prepared samples	126
4.4.2	Annealing in O ₂ ambient	128
4.4.3	Annealing in H ₂ ambient	130
4.4.4	Stability of the graphene layer under redox treatments	133

4.5	Conclusions	138
4.6	References	139
Chapter 5 Interaction of bimetallic PtCo layers with bare and graphene-covered ZnO (0001) supports.....		148
5.1	Introduction	148
5.2	Experimental part	149
5.3	Results and discussion.....	150
5.3.1	UHV annealing.....	150
5.3.2	Low pressure redox	155
5.3.3	Medium pressure conditions	158
5.3.4	Morphology of supported bimetallic Co-Pt	163
5.3.5	Quality of Graphene	164
5.4	Conclusions	166
5.5	References	167
Chapter 6 Summary, general conclusion and perspectives		172
6.1	General conclusion.....	172
6.2	Perspective	175
6.3	References	177
Appendix.....		179
Symbols and Abbreviation		185

Résumé

a) Introduction Générale

Partout dans le monde, plus de 85% de tous les produits chimiques sont fabriqués à l'aide de catalyseurs.¹ Les catalyseurs sont divisés en des catalyseurs homogènes, qui sont solubles dans le milieu réactionnel, et les catalyseurs hétérogènes, qui restent à l'état solide. Un catalyseur métallique hétérogène est typiquement constitué de l'élément actif métallique, des promoteurs, et d'un matériau de support. Pendant de nombreuses années, les supports ont été présumés d'être catalytiquement inertes, et il était considéré que leur rôle principal est de faciliter la formation de petites particules et d'assurer leur stabilité thermique. Cependant, depuis les années 80, des preuves ont surgi que le support peut avoir une influence marquée sur les propriétés des particules attachées sur lui. Cet effet, habituellement cité comme «interaction métal-support (MSI)», est reconnu jouer un rôle clé non seulement dans la catalyse, mais aussi dans d'autres applications importants comme la microélectronique, des dispositifs photovoltaïques, des capteurs de gaz, etc.² En catalyse hétérogène, un certain nombre de modèles ont été proposés pour expliquer l'influence des effets MSI. Les deux aspects qui sont prédominants proposent que l'effet soit dû à une perturbation de la fonction de métal électronique ou structurelle (par exemple un effet de transport de charge) ou dû à un transport de masse de l'appui sur le métal (par exemple l'encapsulation).² Il est donc envisagé qu'on pourrait traiter des propriétés catalytiques, par bien accorder l'interaction entre le métal et le support.

Le cobalt est un des métaux de transition importants utilisés comme catalyseurs dans plusieurs réactions chimiques.³⁻⁵ Il joue un rôle majeur dans le processus industriel de production d'hydrocarbures liquides à partir du charbon, appelé la synthèse Fischer - Tropsch.⁶ Au cours des dernières années, Cobalt est considéré comme un matériau potentiel pour le reformage d'hydrocarbures pour la production de carburants renouvelables. Le rôle de

l'interaction de cobalt avec des supports dans les réactions catalytiques reste une question en suspens. Il a été donc proposé que la taille des particules de cobalt, ainsi que sa réductibilité et stabilité sont fortement affectés par le support. Par exemple, dans la synthèse Fischer - Tropsch, Al_2O_3 est considéré comme fortement interagissant avec Co, provoquant la formation de petites particules de cobalt. Cependant, un effet négatif de cette interaction est une diminution de la réductibilité du cobalt et la formation d'espèces inactives du cobalt, tels que l'aluminate de cobalt.⁷ SiO_2 a été décrit à avoir une interaction relativement faible avec Co, qui est considéré comme préférable pour la réductibilité du cobalt et la formation de particules larges, mais dans certains cas, la formation de l'inactif silicate de cobalt a été rapporté.⁸ D'autre part, ZnO est un support habituellement utilisé pour des catalyseurs du reformage d'éthanol, mais il a été signalé à fortement interagir et oxyder cobalt, par une réaction à l'état solide à température élevée.^{9,10} Des matériaux à base de carbone, tels que les nanotubes de carbone et des fibres de carbone, pourraient potentiellement surmonter ces difficultés, car ils ont une interaction limitée avec le métal.^{11,12} Cependant, il est difficile de préparer des matériaux de carbone en pellets avec une haute stabilité mécanique, et le coût plus élevé des nanotubes de carbone (NTC) est également un problème majeur. Les études mentionnées ci-dessus désignent la nécessité d'une nouvelle approche pour développer des catalyseurs de Co supportés avec des interactions appropriées.

Le graphène est considéré comme un matériau de support attractif pour les clusters métalliques, en raison de ses caractéristiques électroniques, structurales et chimiques uniques.¹³ En outre, le graphène a été étudié comme un couvercle de protection ultra-mince de métaux tels que Cu, Cu/Ni, Ag, Fe, etc., contre la corrosion par l'air, l' H_2O_2 et les environnements électrochimiques.¹⁴⁻¹⁷ Cependant, l'effet du graphène à l'interaction métal - support, et en particulier en utilisant comme support un oxyde, n'a pas été étudié jusqu'à présent. Dans ce travail, l'interaction de cobalt avec des substrats différents (SiO_2 , ZnO, graphite pyrolytique hautement orienté (HOPG)) a été étudiée par des méthodes spectroscopiques et analytiques microscopiques. Pour la première fois, une mono-couche de graphène a été

utilisé comme une couche tampon pour ajuster l'interaction Co-support. Les propriétés redox de catalyseurs de Co supportés ont été étudiées sous pression basse (5×10^{-7} mbar) et moyenne (7mbar) d'oxygène et d'hydrogène (O_2/H_2). En outre, l'effet du graphène à l'interaction d'un catalyseur bimétallique (platine/cobalt) avec des supports a été également étudié

La thèse est divisée en 6 chapitres. Le premier chapitre contient une introduction et une revue de la littérature reliée au sujet de cette thèse. Le deuxième chapitre explique les principes théoriques et les détails techniques des méthodes de préparation des échantillons, et les techniques expérimentales utilisées dans cette thèse. Les substrats graphène-oxyde ont été préparés par transfert de monocouches de graphène préparés par dépôt chimique en phase vapeur(CVD) sur des cristaux d'oxyde planaires. Pour la caractérisation des échantillons, la spectroscopie de photoélectrons (XPS) a été principalement utilisée mais également la spectroscopie Raman (Raman), la microscopie à force atomique (AFM) et la spectroscopie haute résolution des électrons de perte d'énergie (HREELS).

b) Résultats et interprétation

i. Enquête de Co interaction avec ZnO et graphène-couverte ZnO dans des conditions UHV

Le troisième chapitre décrit l'étude de nanoparticules de cobalt supporté sur ZnO (0001) (Co/ZnO) et sur graphène-ZnO (0001) (Co/G-ZnO). L'interaction entre Co et ZnO a été étudiée in situ par recuit des échantillons sous ultravide (UHV) et en effectuant une analyse quantitative et chimique de leur surface en utilisant l'XPS.

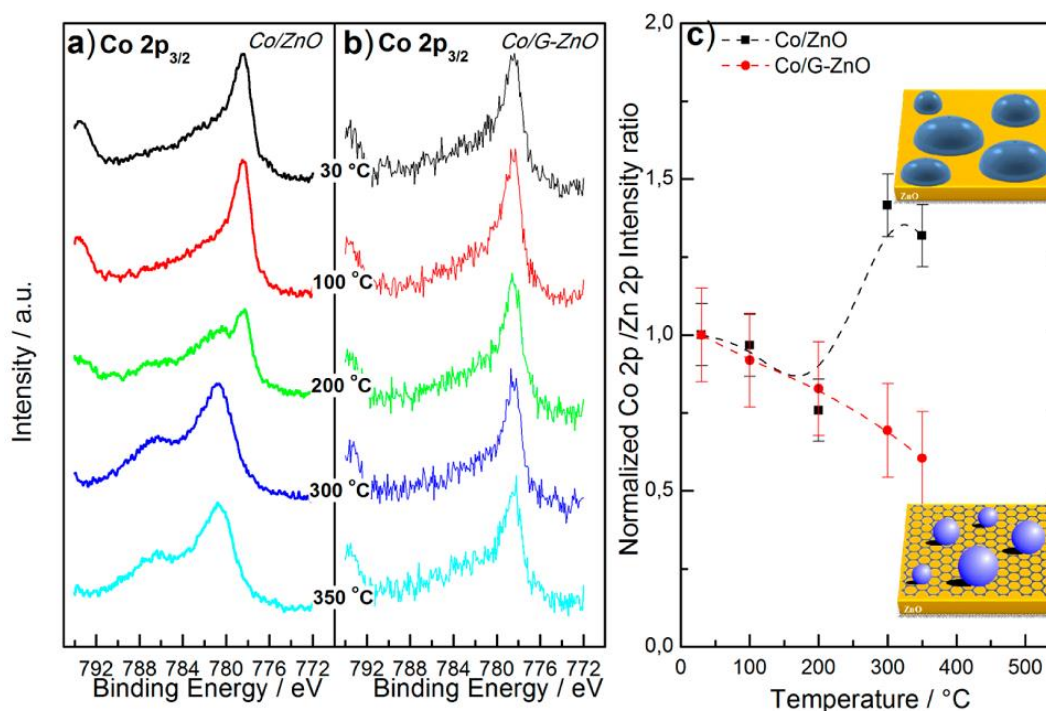


Figure 1 Les spectres XPS de (a) Co/ZnO et (b) Co/G-ZnO après calcination à des températures différentes. (c) Variation des rapports d'intensité XPS Co 2p/Zn 2p des échantillons Co/ZnO et Co/G-ZnO avec la température. Pour faciliter la comparaison, les rapports d'intensité Co 2p/Zn 2p sont normalisés au rapport initial à 30 °C. Les barres d'erreur représentent la diffusion de données en tant que l'écart entre la valeur moyenne obtenue dans trois expériences répétées. Une représentation graphique de la morphologie des particules de cobalt après calcination à la température plus élevée est comprise.

Les résultats ont montré que cobalt est progressivement oxydé par ZnO lors du recuit sous UHV, par une réaction à l'état solide entre Co et ZnO. Dans la Figure 1a, à 300 °C, Co est complètement oxydé en CoO. En revanche, le recuit de l'échantillon Co/G-ZnO ne provoque aucun effet évident à la forme du pic XPS Co 2p, Co restant à l'état métallique même après un recuit à 350 °C (Figure 1b). On suppose alors que la monocouche de graphène agit comme une barrière physique qui empêche la diffusion de Co et qui est aussi imperméable de l'oxygène du support. Les images AFM en combinaison avec les résultats XPS ont montré que, après le recuit, les particules du CoO supportés en ZnO, sont devenues plus plates tandis que le cobalt métallique supporté en G-ZnO était en forme de nanoparticules, agglomérés en particules plus grosses (Figure 2). Les résultats Raman ont montré que la monocouche de graphène était de bons états après le transfert sur la surface de ZnO, après le dépôt de Co et après le recuit. Un

transfert de charge entre Co et graphène a été aussi observé. Globalement, il est montré que la monocouche de graphène pourrait effectivement empêcher l'oxydation de Co par le support (ZnO) et qu'elle a également un effet sur la morphologie des particules de Co.

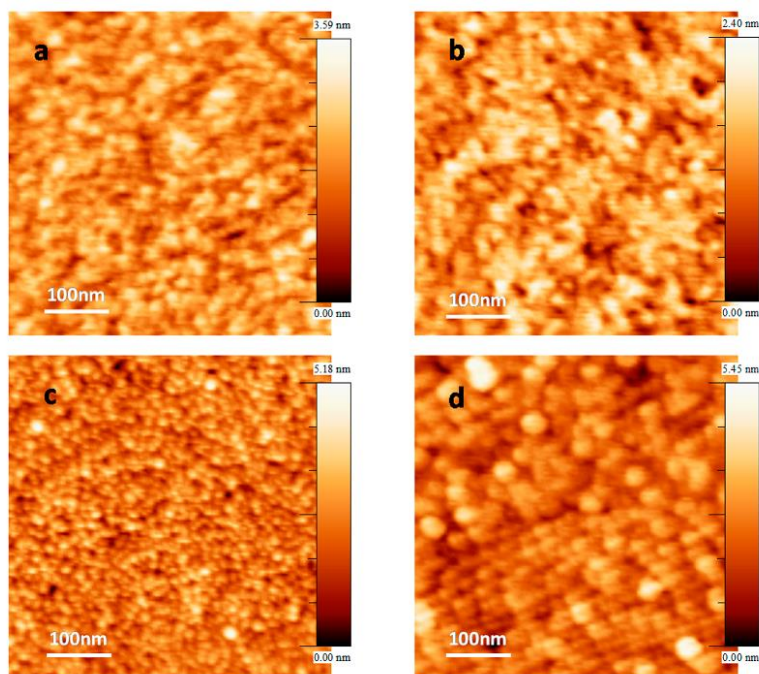


Figure 2 Les images AFM ($500 \times 500 \text{ nm}^2$) de (a) Frais Co/ZnO, (b) Co/ZnO après calcination à $350 \text{ }^\circ\text{C}$, (c) Frais Co/G-ZnO, et (d) Co/G-ZnO après calcination à $350 \text{ }^\circ\text{C}$

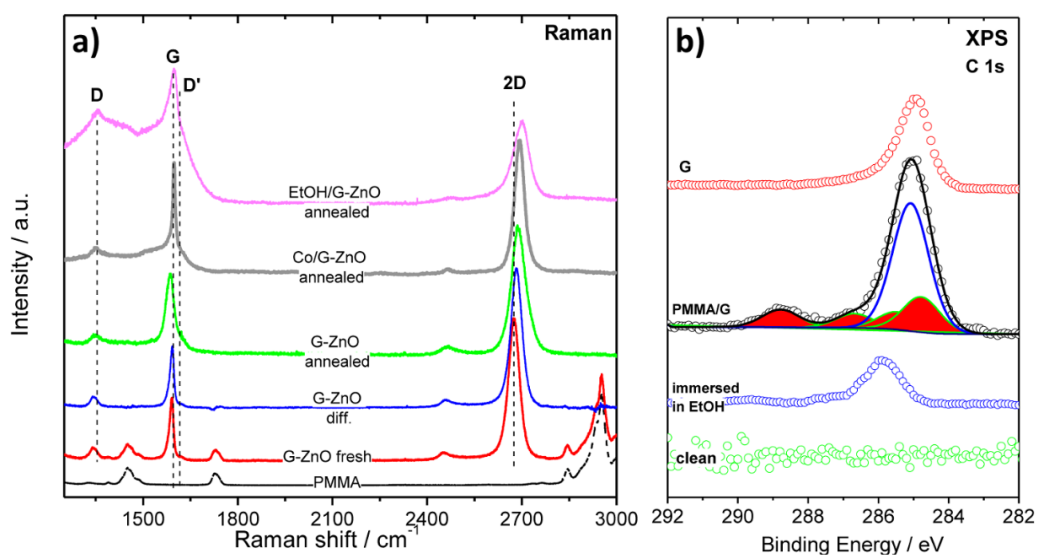


Figure 1 (a) Spectres Raman du PMMA et du G-ZnO avant et après recuit ainsi qu'après cycles de dépôt de cobalt et de l'exposition à l'éthanol. (b) Spectres de C1s des échantillons

ii. Modification des propriétés d'oxydo-réduction de cobalt par le graphène

Dans le quatrième chapitre, cinq échantillons ont été préparés et étudiés: CoZnO, CoGZnO, CoSiO₂, CoGSiO₂ et CoHOPG. Les propriétés d'oxydation / réduction de tous les échantillons sous O₂/H₂ à des pressions de 5×10^{-7} mbar (pression basse) et 7 mbar (pression moyenne) ont été étudiées.

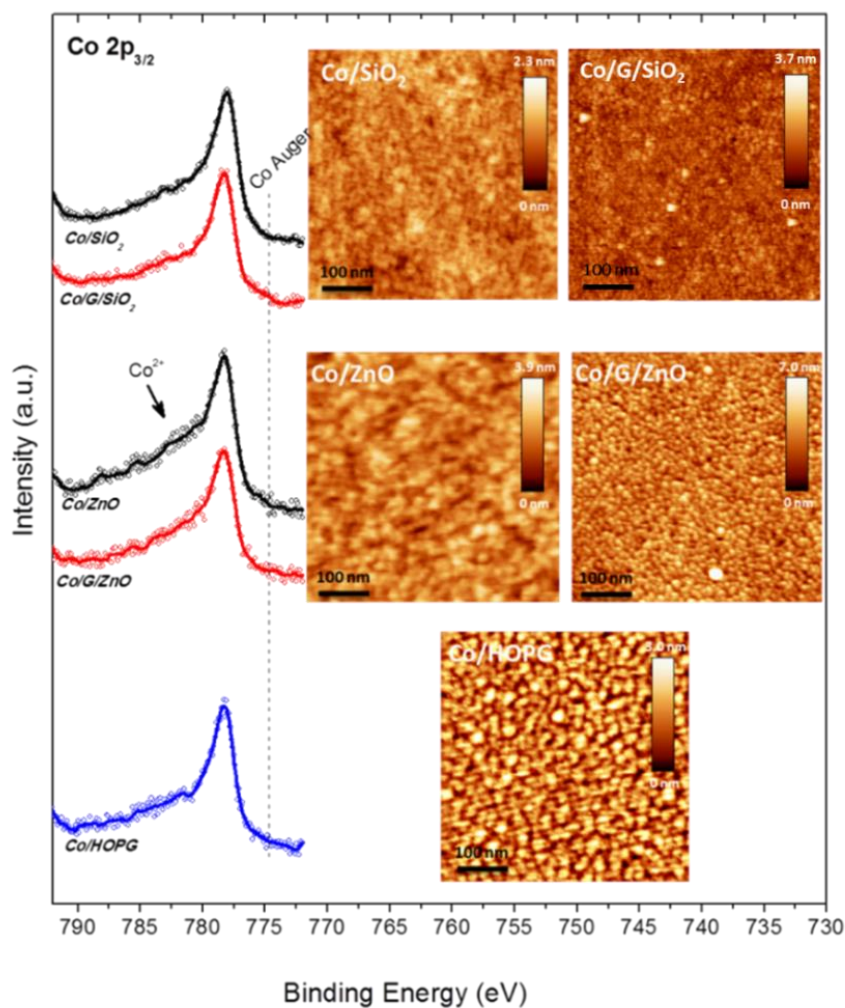


Figure 4 Spectres de Co2p_{3/2} et les images AFM (500 × 500 nm²) de Co (0, 35 nm) déposés sur 5 supports différents

Les résultats AFM (Figure 4) ont montré que Co forme des nanoparticules sur les substrats où une couche de carbone (de graphène ou HOPG) est insérée, ce qui limite l'oxydation de Co par l'O₂ de l'ambiance à des pressions faibles. Cela est dû à la formation d'une couche de CoO à la surface, qui empêche la dissociation et la diffusion de l'oxygène plus profondément dans

les nanoparticules sous des conditions expérimentales appliquées. Au contraire, due à la formation des structures de cobalt aplaties sur SiO₂ et ZnO, l'oxydation par l'oxygène est prouvée plus facile en pression basse. La réduction de Co par H₂ a été fortement affectée par l'interaction métal-support. CoO qui a été créé sur ZnO ne pouvait pas être réduit, en raison de la réaction solide entre Co et ZnO tandis que CoO créé sur SiO₂ pourrait être réduit, mais à très haute température (600 °C). CoO sur carbone pourrait être réduit à très basse température (250 °C).

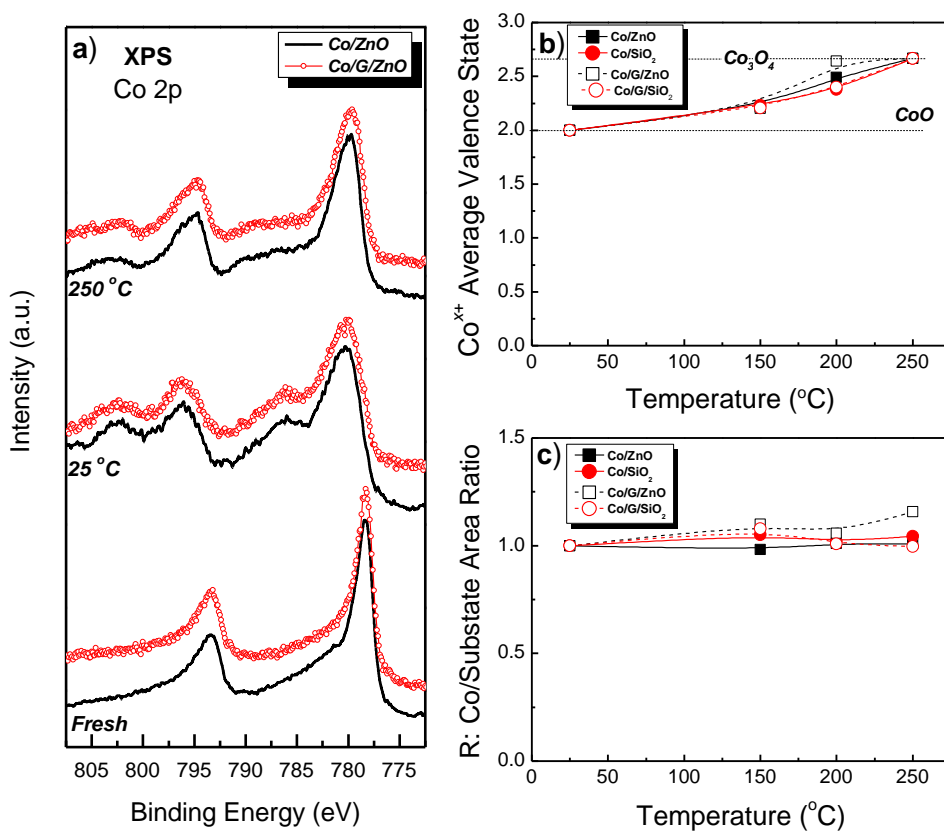


Figure 5 (a) Spectres Co2p des échantillons Co/ZnO et Co/G/ZnO frais et après oxydation dans 7 mbar O₂ à 25 et 250 °C, (b) l'évolution de l'état de valence moyenne (Co^{x+}) et (c) le rapport XPS Co/substrat de l'aire du pic normalisé à sa valeur à la température ambiante, en fonction de la température d'oxydation.

Aux pressions d'O₂ plus élevées (7 mbar), Co est d'abord oxydé à CoO à la température ambiante, et à 250 °C il est oxydé à Co₃O₄, quel que soit le substrat (Figure 5). Néanmoins, la monocouche de graphène a encore un effet fort sur la réduction de Co₃O₄ à une pression d'H₂ de 7 mbar. L'introduction d'une monocouche de graphène entre Co et ZnO ou SiO₂, provoque

la réduction complète de Co en température plus faible par rapport à celle de Co sur ZnO ou SiO₂ (Figure 6). Les résultats Raman ont montré qu'après le traitement à pression basse, le graphène était encore de bonne qualité, peu importe de substrat. Néanmoins, après des traitements sous pressions moyennes, des défauts ont été créés au graphène, en particulier à l'échantillon CoGZnO. Cette étude montre que Co et le substrat agissent comme catalyseurs pour la formation de défauts de graphène pendant les traitements d'oxydation / réduction. En particulier, le nombre de défauts introduits au graphène augmente quand la réactivité entre Co et le substrat d'oxyde augmente (par exemple pour ZnO). Cette partie du travail a montré que la monocouche du graphène pourrait être utilisée comme une couche tampon pour ajuster l'interaction entre Co et le support: elle interdit l'oxydation du CO à pression basse d'O₂, mais facilite la réduction à pressions basses et moyennes.

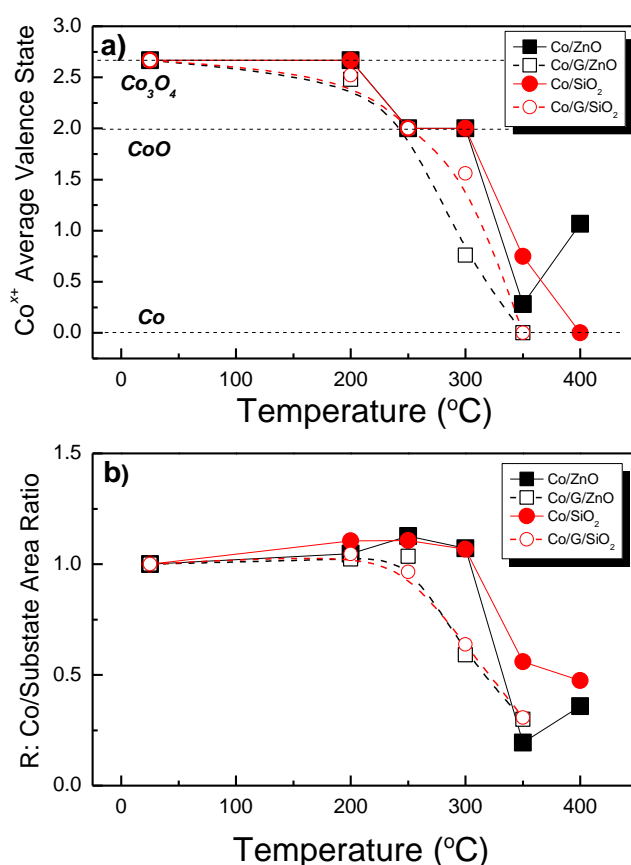


Figure 6 Spectres XPS des échantillons pre-oxydés et mis à 7 mbar H₂ à différentes températures de calcination. (a) L'évolution de l'état de valence moyenne (Co^{x+}) et (b) le rapport de surface de pics Co/substrat normalisé en fonction de la température de calcination.

iii. Modification des propriétés d'oxydo-réduction de Co-Pt par le graphène

Dans le cinquième chapitre, l'effet d'introduction de la monocouche de graphène à l'interaction entre le système bimétallique (Co-Pt) et le support a été étudié. Deux échantillons ont été étudiés: CoPt/ZnO et CoPt/G/ZnO. Les études redox ont été réalisées dans les mêmes conditions que celles du chapitre 4.

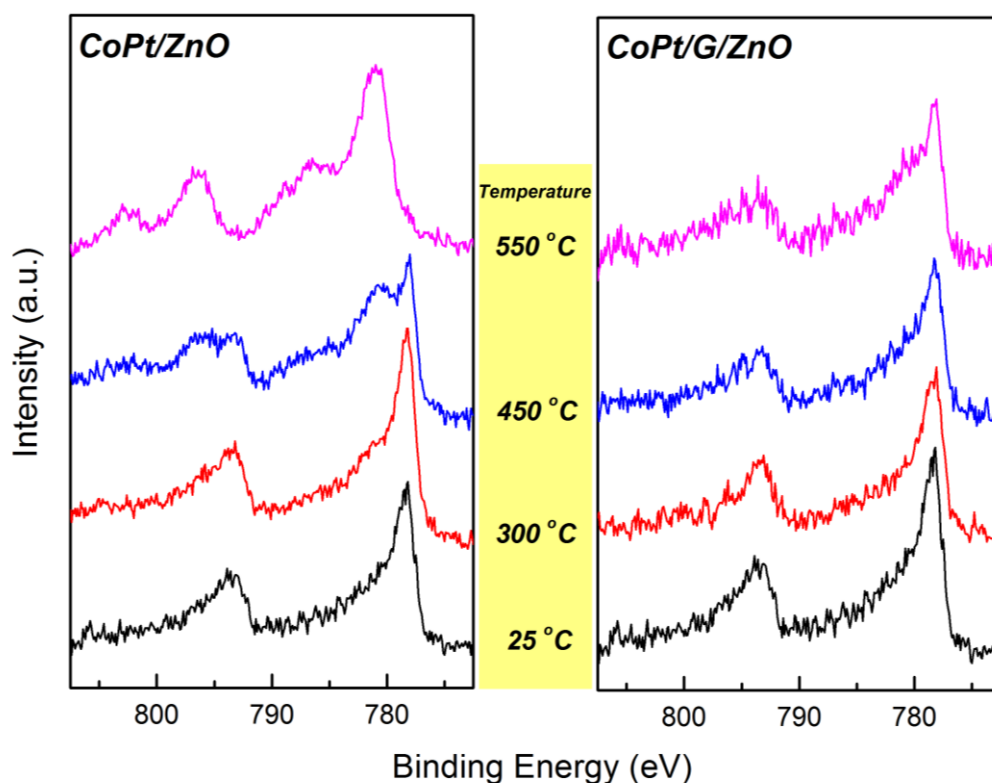


Figure 7 Les spectres XPS de CoPt/ZnO et CoPt/G/ZnO sous UHV en fonction de la température de calcination.

Les images AFM ont montré que le bimétallique Co-Pt forme des particules dont la morphologie ressemble à celle du Co monométallique. Dans ce cas, les résultats d'oxydation/réduction à température basse ont également démontré des tendances similaires avec les expériences de Co monométallique, où l'oxydation du Co sur la couche de graphène a été limitée et sa réduction a été accélérée. Cependant, avec l'addition de la Pt, la température de réduction de tous les échantillons étudiés était inférieure à celle mesurée au Co monométallique. Ceci peut être expliqué par le fait que H_2 est dissocié sur Pt, facilitant ainsi la réduction de Co.^{3,18} En outre, à pressions moyennes, le graphène a également facilité la réduction de CoO dans le système Co-

Pt. Cette partie du travail a prouvé que la monocouche de graphène pourrait être utilisée pour ajuster l'interaction métal-support dans un système plus complexe (Co-Pt).

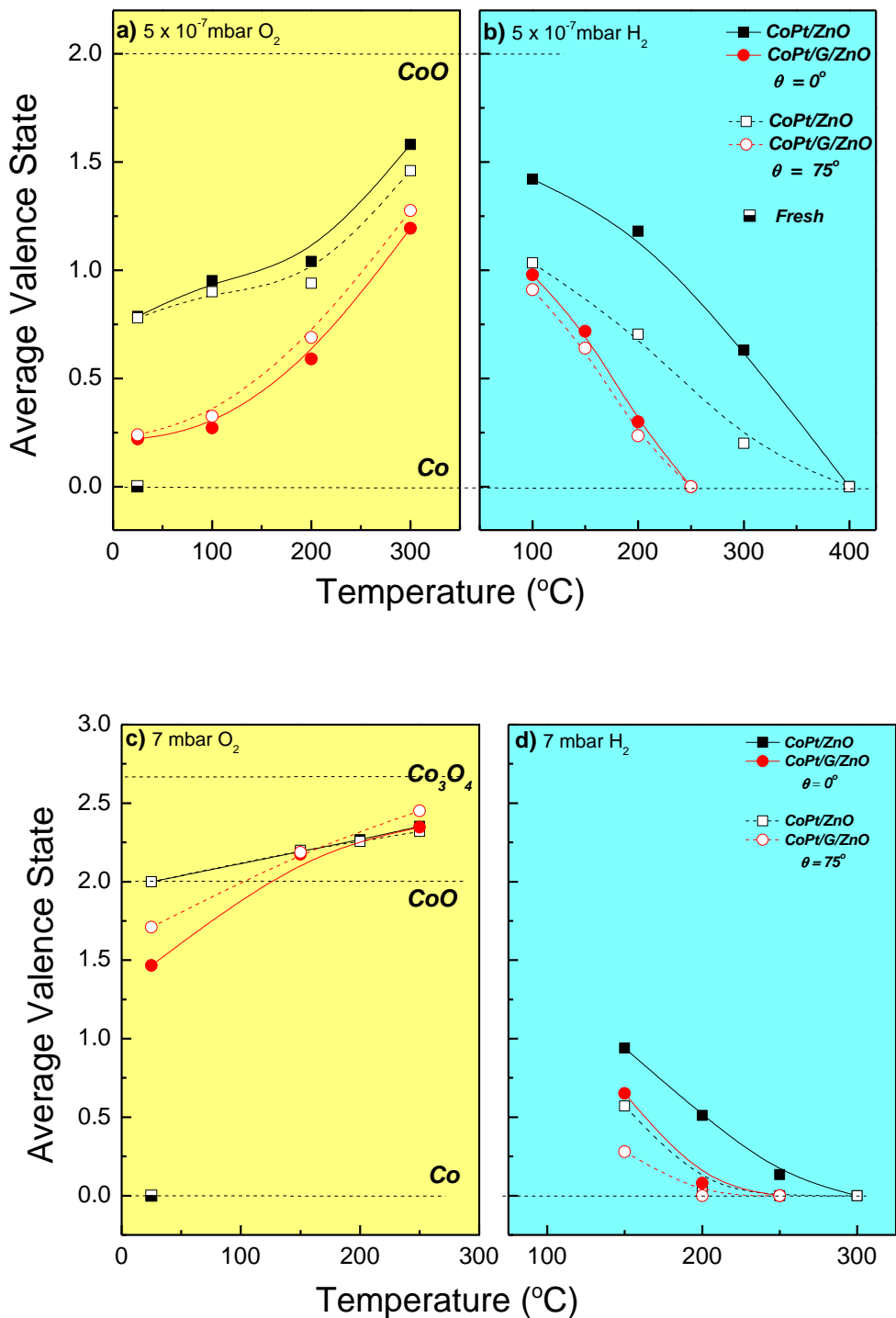


Figure 8 Valence moyenne de Co des CoPt/ZnO et CoPt/G/ZnO sous traitements redox à basse pression (en haut) et à moyenne pression (en bas)

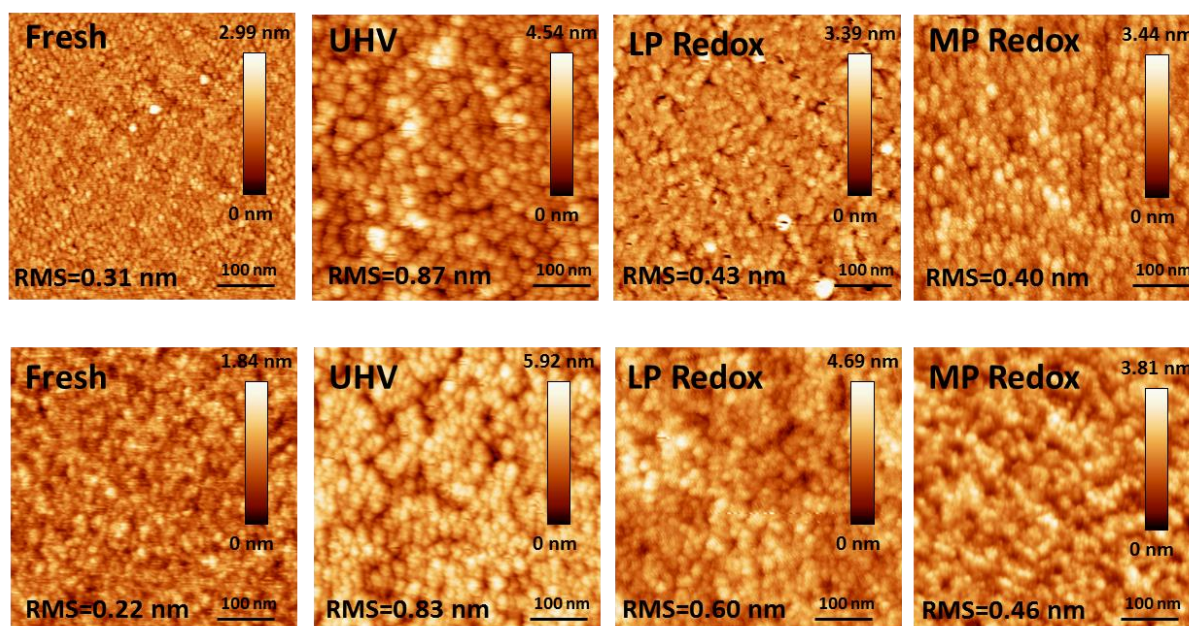


Figure 9 Les images AFM ($500 \times 500 \text{ nm}^2$) de Frais CoPt/ZnO, CoPt/G/ZnO et échantillons après différents traitements

c) Conclusions

Enfin, dans le sixième chapitre, les conclusions générales et les perspectives de ce travail sont données. En général, cette thèse propose une nouvelle approche pour modifier l'interaction métal-support, à savoir en utilisant une monocouche de graphène comme un tampon entre la couche métallique et le support. Les résultats montrent que a) une monocouche de graphène peut protéger Co de l'oxydation par substrats réactifs (tels que ZnO) pendant le recuit sous UHV b) Le graphène peut ajuster l'interaction entre Co-ZnO et Co-SiO₂, en particulier en limitant l'oxydation du Co tandis qu'en facilitant sa réduction c) Une monocouche de graphène peut également modifier l'interaction entre les particules bimétalliques (tels que Co-Pt) et du support. Cette thèse porte sur des catalyseurs modèles, mais elle manifeste les propriétés prometteuses de graphène comme promoteur d'un support efficace aussi pour les catalyseurs techniques. Cela peut inspirer de nouvelles études sur la préparation de supports catalytiques revêtus de graphène dont l'interaction avec les particules de catalyseur est ajustable.

d) Reference

- (1) Heveling, J. Heterogeneous Catalytic Chemistry by Example of Industrial Applications. *J. Chem. Educ.***2012**, 89 (12), 1530–1536.
- (2) Fu, Q.; Wagner, T. Interaction of Nanostructured Metal Overlayers with Oxide Surfaces. *Surf. Sci. Rep.***2007**, 62 (11), 431–498.
- (3) Zheng, F.; Alayoglu, S.; Guo, J.; Pushkarev, V.; Li, Y.; Glans, P.-A.; Chen, J.; Somorjai, G. In-Situ X-Ray Absorption Study of Evolution of Oxidation States and Structure of Cobalt in Co and CoPt Bimetallic Nanoparticles (4 nm) under Reducing (H₂) and Oxidizing (O₂) Environments. *Nano Lett.***2011**, 11 (2), 847–853.
- (4) Liang, Y.; Li, Y.; Wang, H.; Zhou, J.; Wang, J.; Regier, T.; Dai, H. Co₃O₄ Nanocrystals on Graphene as a Synergistic Catalyst for Oxygen Reduction Reaction. *Nat. Mater.***2011**, 10 (10), 780–786.
- (5) Llorca, J.; de la Piscina, P. R.; Dalmon, J.-A.; Sales, J.; Homs, N. CO-Free Hydrogen from Steam-Reforming of Bioethanol over ZnO-Supported Cobalt Catalysts. *Appl. Catal. B Environ.***2003**, 43 (4), 355–369.
- (6) Khodakov, A. Y.; Chu, W.; Fongarland, P. Advances in the Development of Novel Cobalt Fischer-Tropsch Catalysts for Synthesis of Long-Chain Hydrocarbons and Clean Fuels. *Chem. Rev.***2007**, 107 (5), 1692–1744.
- (7) Dalai, A. K.; Davis, B. H. Fischer–Tropsch Synthesis: A Review of Water Effects on the Performances of Unsupported and Supported Co Catalysts. *Appl. Catal. A Gen.***2008**, 348 (1), 1–15.
- (8) Hong, J.; Chernavskii, P. a.; Khodakov, A. Y.; Chu, W. Effect of Promotion with Ruthenium on the Structure and Catalytic Performance of Mesoporous Silica (smaller and Larger Pore) Supported Cobalt Fischer-Tropsch Catalysts. *Catal. Today***2009**, 140 (3-4), 135–141.
- (9) Martin-Luengo, M. A.; Sermon, P. A.; Wang, Y. Reduction and State of Co in Co/ZnO Catalysts: Evidence of a Metal-Support Interaction. *J. Catal.***1992**, 135 (1), 263–268.
- (10) Hyman, M. P.; Martono, E.; Vohs, J. M. Studies of the Structure and Interfacial Chemistry of Co Layers on ZnO(0001). *J. Phys. Chem. C***2010**, 114 (40), 16892–16899.
- (11) Trépanier, M.; Tavasoli, A.; Dalai, A. K.; Abatzoglou, N. Fischer–Tropsch Synthesis over Carbon Nanotubes Supported Cobalt Catalysts in a Fixed Bed Reactor: Influence of Acid Treatment. *Fuel Process. Technol.***2009**, 90 (3), 367–374.

- (12) Xiong, H.; Schwartz, T. J.; Andersen, N. I.; Dumesic, J. A.; Datye, A. K. Graphitic-Carbon Layers on Oxides: Toward Stable Heterogeneous Catalysts for Biomass Conversion Reactions. *Angew. Chemie Int. Ed.* **2015**, *54* (27), 7939–7943.
- (13) Novoselov, K. S.; Fal'ko, V. I.; Colombo, L.; Gellert, P. R.; Schwab, M. G.; Kim, K. A Roadmap for Graphene. *Nature* **2012**, *490* (7419), 192–200.
- (14) Topsakal, M.; Şahin, H.; Ciraci, S. Graphene Coatings: An Efficient Protection from Oxidation. *Phys. Rev. B* **2012**, *85* (15), 155445.
- (15) Kirkland, N. T.; Schiller, T.; Medhekar, N.; Birbilis, N. Exploring Graphene as a Corrosion Protection Barrier. *Corros. Sci.* **2012**, *56*, 1–4.
- (16) Prasai, D.; Tuberquia, J. C.; Harl, R. R.; Jennings, G. K.; Bolotin, K. I. Graphene: Corrosion-Inhibiting Coating. *ACS Nano* **2012**, *6* (2), 1102–1108.
- (17) Nilsson, L.; Andersen, M.; Balog, R.; Lægsgaard, E.; Hofmann, P.; Besenbacher, F.; Hammer, B.; Stensgaard, I.; Hornekær, L. Graphene Coatings: Probing the Limits of the One Atom Thick Protection Layer. *ACS Nano* **2012**, *6* (11), 10258–10266.
- (18) Papaefthimiou, V.; Dintzer, T.; Lebedeva, M.; Teschner, D.; Hävecker, M.; Knop-Gericke, A.; Schlögl, R.; Pierron-Bohnes, V.; Savinova, E.; Zafeirotos, S. Probing Metal–Support Interaction in Reactive Environments: An in Situ Study of PtCo Bimetallic Nanoparticles Supported on TiO₂. *J. Phys. Chem. C* **2012**, *116* (27), 14342–14349.

Chapter 1

Introduction

Chapter 1 Introduction

1.1 Metal-Support interaction in catalysis

1.1.1 Fundamental aspects of metal-support interaction

In 1978, Tauster and co-workers¹ reported that the adsorption of H₂ and CO over titania-supported noble metal catalysts critically depends on the reduction temperature. Using electron microscopy and X-ray diffraction, the authors excluded sintering of the metal particles and indicated the migration of reduced titania species onto the metal as the cause of the decrease in the chemisorption capacity. The authors introduced the term strong metal–support interaction (SMSI) to refer to this phenomenon and since then it has been established as a crucial factor which determines the activity and selectivity of catalysts. Apart from heterogeneous catalysis, metal-support interaction plays a crucial role in many other technology fields, including material science and microelectronics. A thorough understanding of metal-support interaction mechanism has been a great challenge for industry and academia. The basic knowledge about the interaction at the metal-support interface has been addressed in some excellent books and reviews dealing with both experimental and theoretical aspects of the subject.^{2–6} In this work, the problematic of metal-support interaction will be discussed, focusing on its relation to the reduction-oxidation (redox) behavior of metal particles and consequently to catalytic reactions. As supported metal catalysts are used in the majority of heterogeneous catalytic reactions, it is common ground that the metal-support interaction plays a significant role in the general effort to develop novel catalytic materials with improved performance.

Depending on the particular metal–oxide system, the support can influence the metal particles in many different ways, by modifying their morphologies and sizes, by influencing their adsorption properties or even, by changing their oxidation states. At least four mechanisms have been put forward to describe the role of the support to the catalytic behavior of the (supported) metal particles: i) spillover and decoration of the metal particles by support species; ii) adsorption and activation of reaction intermediates over chemically active sites of the support and migration to the metal; iii) modifications of the electronic structure of the metal due to the interaction with the support, referred to the electronic (or ligand) effect and iv) the geometric (or ensemble) effect related to strain effects within the metal structure which have a direct influence on the topography of the atom distribution on the catalysts' surface.⁷ In general,

differentiation between these effects is rarely clear and there is often a contribution from more than one effect. For example, charge transfer between the support and metal aggregates over it, will perturbate the metal's electronic structure. In addition, coverage of metal particles by reduced oxide support species can stabilize the particles' size. Apparently, since many intertwined factors may influence the metal-support interaction, it is very difficult to elucidate its nature by using complex real catalytic systems. Therefore, in this thesis model catalytic systems were used, where several parameters like the support surface, contamination level, deposition method *etc.*, can be controlled during the preparation and the study of the specimens.

1.1.2 Interactions of cobalt with support

Among all sorts of supported metal catalysts, Co catalysts have been widely used for many important reactions, such as Fischer-Tropsch synthesis, ethanol steam reforming reaction and many others. A variety of materials have been tested as substrates in order to support and disperse the active Co metal sites.^{8,9} The Co structure and oxidation state as well as the consequent catalytic activity and stability are significantly influenced by the Co-support interaction. Some examples of Co-support interaction will be elaborated in the following manuscript, where we show how the Co morphologies, the oxidation states and the interactions vary with oxide surface properties. The substrates are categorized by the properties of the support to: i) reducible oxide (ZnO), ii) unreducible oxide (SiO₂) and iii) carbon materials (graphite and graphene).

1.1.2.1 Co on ZnO

ZnO supported Co catalyst has been proven to be one of the best catalysts in ethanol steam reforming reaction.^{8,10,11} However, due to the complexity of working catalysts, the studies of the Co-ZnO interaction are mainly performed on model systems. Termination of ZnO surface and Co overlayer thickness, which will be discussed in detail below, are found to be the most important factors when determining the Co-ZnO interactions.

The epitaxial growth structure, chemical state and thermal stability of Co on the nonpolar ZnO(10 $\bar{1}$ 0) surface have been studied by Su et al^{12,13}. From STM results, they found that Co formed a well-ordered CoO_x (2 × 1) structure at low Co coverage (0.5 monolayer (ML)), while with increasing Co coverage, the surface was converted to a stripe structure (at 0.7-1.0 ML) and further to a cluster structure (at 3.0 ML coverage). It was proposed that the growth process of Co on ZnO(10 $\bar{1}$ 0) followed the 2D-to-3D transition. At the same time, the CoO_x state was

transformed to a Co metallic state as the thickness of deposited Co increased, which also induced an upward band-bending due to the work function difference between Co and ZnO(10 $\bar{1}$ 0). Further studies of the thermal stability of Co on ZnO(10 $\bar{1}$ 0) were carried out by the same group.¹² They found that thermally-induced structural changes were strongly dependent on the Co coverage; a CoO_x (2 × 1) structure was converted to a nanocluster structure, 1.0 ML Co was transformed from striped structure to a rectangular wetting layer structure, and a 3.0 ML thickness nanoclustered Co turned to rectangular islands and chains. The chemical interaction between Co and ZnO(10 $\bar{1}$ 0) during annealing was studied by XPS, which showed that the 1.0 ML Co was maintained at the metallic state up to 800 K.

The Co interaction with the polar oxygen terminated ZnO(000 $\bar{1}$) surface was also investigated by different groups. Law et al.¹⁴ observed a chemical interaction between small deposition amounts (0.1 nm) of Co and ZnO(000 $\bar{1}$) at room temperature, using synchrotron radiation X-ray photoelectron spectroscopy, leading to partial oxidation of Co. This oxidation of Co was attributed to the existence of OH groups on the ZnO(000 $\bar{1}$) surface, since the O-terminated ZnO surface was found to react with residual H₂O and H₂ even in UHV conditions¹⁵ with formation of OH groups. The high annealing temperature (773 K) in UHV led to complete oxidation of Co due to the migration of O ions from the interior of ZnO and/or to the substitution of lattice Zn atoms by Co ions. The Co-ZnO(000 $\bar{1}$) interactions were also investigated with high energy x-rays by Dumont et al.¹⁶ They were not able to observe the oxidation of Co at room temperature, but Co was oxidized through UHV annealing, which was consistent with the results of Law et al.¹⁴ Moreover, they have systematically studied the thermal stability of Co as a function of the annealing temperature and proposed a model of Co - ZnO(000 $\bar{1}$) interaction at various heating stages. As illustrated in Figure 1.1, until the annealing temperature of 700 K, Co remained in the metallic state but in the nanometer scale, the clusters coalesced. Above 700 K, Co started to be oxidized through Zn substitution, and further diffused deeper into the bulk of ZnO(000 $\bar{1}$) at 970 K.

In the work mentioned above, the Co-ZnO(0001) (Zn-terminated) interactions were also reported by Law and coworkers¹⁴ where they found similar chemical interaction between Co/ZnO(0001) and Co/ZnO(000 $\bar{1}$): Co was partially oxidized to Co^{δ+} and further oxidized after UHV annealing on ZnO(0001), however, it was less oxidized when compared with Co on ZnO(000 $\bar{1}$) under the same conditions. The UHV annealing induced Co oxidation on ZnO(0001) was also proved by Hyman et al.¹⁷, where they reported that the oxidation of Co

started at 700 K and the incorporation of Co into ZnO(0001) lattice occurred after 800 K. From the XPS and AFM results, they proposed a layer-by-layer growth mode of Co on ZnO(0001) at 300 K while Co agglomerated to large particles upon heating to 500 K and 700 K, but re-spread when it was oxidized to CoO after 700 K.

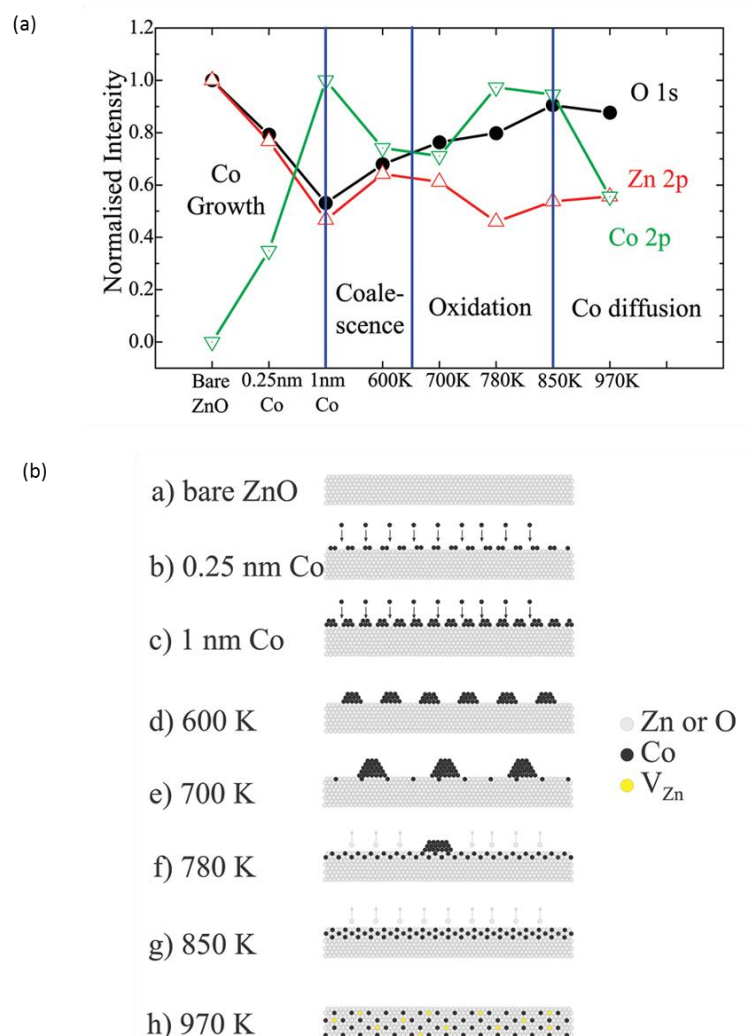


Figure 1.1 (a) Changes in the Zn 2p, O 1s, and Co 2p line intensities at the different stages of the experiment. Zn 2p and O 1s signals are normalized with respect to their value on the bare ZnO surface. Co 2p is normalized for 1 nm Co. (b) Model showing the various stages of the structural modifications during the growth and annealing of the Co/ZnO(0001) system. Reproduced from [16].

Table 1.1 gives an overview of the model system studies of Co-ZnO interaction. It is shown that the Co-ZnO interactions strongly depend on the thickness of Co, the termination of ZnO as well as the population of OH groups on the surface. Nevertheless, strong chemical interactions of Co with different ZnO single crystals have been observed at room temperature and/or after UHV annealing. Moreover, a higher annealing temperature (>800 K) always leads

to the interdiffusion of Co into the ZnO lattice. The strong interactions between Co and ZnO have been found to significantly influence the catalytic reactions. For example, JM Vohs' group has studied the reaction pathways for ethanol reforming on model Co/ZnO(0001) catalysts and found that metallic Co was active for ethoxide decarbonylation, forming CO, H₂ and adsorbed methyl groups. They found that a mixture of Co⁰ and Co²⁺ was active for converting ethoxide groups to acetaldehyde (a critical intermediate to produce H₂ and CO₂) however, CoO was largely unreactive in this reaction. Law and coworkers¹⁸ investigated the temperature programmed desorption (TPD) of ethanol on ZnO(0001) supported Co and CoNi catalysts. During TPD experiments Co was oxidized, increasing the oxygen concentration on the catalysts' surface but by suppressing the overall activity. Due to the strong interactions between Co and ZnO, the formation of unreducible Co species was also recorded in some real working Co-ZnO catalysts.¹⁹⁻²¹

Table 1.1 Summary of Co interactions on ZnO surface

Co/ZnO systems	Co thickness	Interaction@RT	Thermal stability	Structure
Co/ZnO(0001) ¹⁴	0.1 nm	Partial oxidation of Co	Further Oxidation of Co	-
Co/ZnO(0001) ¹⁷	2 ML	Metallic Co	Oxidation at 700 K, Interdiffusion at 850 K	Layer growth, <700K, agglomeration, 700K-800K, re-spread, >800K, diffusion into ZnO bulk
Co/ZnO(000 $\bar{1}$) ¹⁴	0.1 nm	Partial oxidation of Co	Further Oxidation of Co	-
Co/ZnO(000 $\bar{1}$) ¹⁶	0.25-1 nm	Metallic Co	Oxidation of Co at 700 K, Interdiffusion at 850 K	<700K, agglomeration, 700K-850K, cover ZnO, >850K, diffusion into ZnO bulk
Co/ZnO(10 $\bar{1}$ 0) ^{12,13}	0.5-3 ML	Partial oxidation of Co at low coverage (<1.5 nm)	Agglomeration, Interdiffusion	2D-to-3D growth, <600K, agglomeration >600K, agglomeration and diffusion

1.1.2.2 Co on SiO₂

SiO₂ is widely used as a catalyst support. CoSiO₂ catalysts have been used in many industrial reactions, maybe the most important of them being the conversion of hydrogen and carbon monoxide to liquid fuels, the so called Fischer-Tropsch synthesis (FTS). The interaction between Co and SiO₂ is considered to be relatively weak, nevertheless formation of cobalt silicates has been observed during preparation of the catalysts and in the course of the FTS

reaction.^{9,22} The formation of cobalt silicate phase has been always considered as an unwanted effect, since this compound is not active for the FTS reaction. Moreover, even less extended Co-SiO₂ interfacial interaction is expected to influence the Co structure, its stability and consequently the activity of the catalyst. A popular approach to get comprehensive insights about Co-SiO₂ interaction is to develop and study model systems (usually refer to as model catalysts). Since the band gap of bulk SiO₂ is very large (~9.0 eV²³), it is difficult to employ electron spectroscopies to study Co-SiO₂ interfaces with bulk SiO₂ crystals as substrates, because of electron charging effects. Therefore, the studies of Co-SiO₂ interactions often involve SiO₂-films grown on single crystal Si or refractory metal substrates. The SiO₂ film thickness, its surface properties and structures strongly affect the Co-SiO₂ interactions. The details are discussed below.

Co model systems supported on thin layer SiO₂/Si have shown that Co can diffuse through the thin SiO₂ layer towards the SiO₂/Si interface and react with Si to form cobalt silicide.^{24,25} Tung et al²⁴ have found that after annealing of Co/SiO₂ at 500-700 °C, Co diffused through the thin (~0.5-1.5 nm) SiO_x (x < 2) layer and grew uniform CoSi₂ compounds. Co was also reported to penetrate a ~0.3 nm SiO_x layer even at room temperature, followed by formation of a ternary Co-O-Si phase and then a Co-Si solid solution at the interface of SiO_x-Si.²⁵

Co interaction with the native SiO₂ layer on n-type Si(111) wafer has been studied by Čechal et al²⁶. The authors observed Co agglomeration followed by desorption from the SiO₂ surface after annealing in UHV environment. By systematical studies of the Co thermal stability under UHV conditions they addressed that Co (2 nm) formed smooth uniform layers on SiO₂ at room temperature and islands structure at 260-320 °C. Further annealing to temperature higher than 500 °C led to the desorption of Co from the SiO₂ surface, but contrary to the results in ref.[^{24,25}], no diffusion of Co through the native SiO₂ layer was found. Since it is believed that the interdiffusion is facilitated by defects in the SiO₂ layers, such as oxygen vacancies, microchannels, microvoids or pinholes, they proposed that the stoichiometric native SiO₂ could stand up as a diffusion barrier.

In SiO₂ (10-30 nm, amorphous layer) supported Co, chemical interactions between Co and SiO₂ through annealing in air were also found.²⁷ Potoczna-Petru and coworkers²⁷ reported the formation of cobalt oxide after high temperature annealing (1173 to 1273 K) of Co (1 nm) on the SiO₂ surface, which also resulted in wetting and spreading of Co oxides on SiO₂. For the higher loading Co (4 nm) sample they observed the formation of two-dimensional cobalt

orthosilicate (Co_2SiO_4) in the form of crystal flakes. An earlier study by Kondoh et al²⁸ also proposed the formation of Co_2SiO_4 phase after rapid thermal annealing (650-850 °C) of Co (20 nm) on SiO_2 (~150 nm) in air. Furthermore, it is believed that the presence of surface water enhanced the formation of Co_2SiO_4 phase which can be explained by the suggested reaction pathway: $\text{Co} + \bar{\text{O}} \rightarrow \text{CoO}$ and $\text{CoO} + \text{SiO}_2 \rightarrow \text{Co}_2\text{SiO}_4$ (or $2\text{CoO} \cdot \text{SiO}_2$), where foreign $\bar{\text{O}}$ is supplied by surface water. During annealing, the Co thin films agglomerated and formed Co globules that penetrated into SiO_2 .

On planar Co/ SiO_2 /Si(100) model catalyst, formation of Co_2SiO_4 was even observed at low annealing temperature, which was attributed to the high pH condition during preparation.²⁹ In another work of the same group³⁰, cobalt encapsulation by SiO_2 has been verified in the spherical Co/ SiO_2 model system by high-resolution transmission electron microscopy (HRTEM). They prepared spherical Co/ SiO_2 model catalysts with different Co crystallite sizes (4, 13, 28 nm) and found that Co with small crystallites (4 nm) was encapsulated by SiO_2 after H_2 reduction at 500 °C. Encapsulation could prevent the oxidation of Co by $\text{H}_2\text{O}/\text{He}$ mixture up to 400 °C. The authors also noted that encapsulation is not observed on samples with larger Co crystallite sizes (13, 28 nm).

In summary, being an irreducible oxide, SiO_2 is assumed to be relatively inert, however, in certain conditions, Co- SiO_2 systems exhibit strong interactions. Typical chemical interactions such as interdiffusion, alloy formation, redox reaction and encapsulation have been reported. For working Co/ SiO_2 catalysts, the SiO_2 structure (eg. pore size, surface area), the preparation and pretreatment methods also strongly affect the Co- SiO_2 interactions and thus the Co redox property, activity and stability. Therefore, in order to design Co/ SiO_2 with high activity and stability, attention should be paid during preparation of catalysts and during catalytic reactions to avoid undesirable Co- SiO_2 interactions.

1.1.2.3 Co on graphite

When carbon-based materials are used as substrates, metal particles are generally considered to interact weakly with them. The weak interaction between metal-carbon plays a negative role in stabilizing the active metal phase against the loss of surface area, while a positive role in avoiding the formation of unreducible metal-support mixtures (such as metal silicide, metal aluminate when SiO_2 , Al_2O_3 are used as supports). Moreover, due to other advantages of carbon materials, e.g. resistance to acidic or basic media, stabilization at high temperatures, they are

more and more used as support materials in catalysts.^{31,32} Carbon is capable to form many allotropes, such as graphite, graphene, carbon nanotubes, diamond, amorphous carbon etc., which have shown to have quite distinct physical and chemical properties. Since in this thesis we used exclusively planar substrates, only highly oriented pyrolytic graphite (HOPG) and graphene were examined as Co particles substrates.

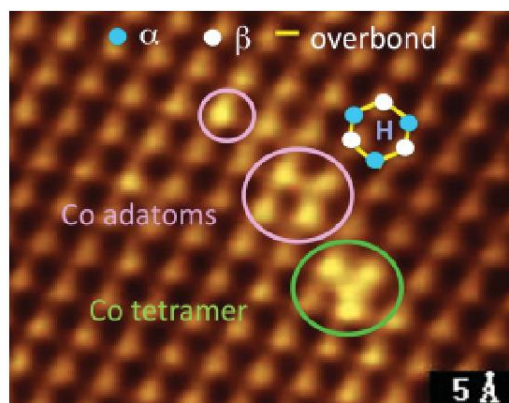


Figure 1.2 Atomic resolution STM image of Co adatoms adsorbed on HOPG. The bright spots encircled and labeled as “Co adatoms” refer to individual Co adatoms that were adsorbed on the β site of the surface graphene layer, whereas those encircled and labeled as “Co tetramer” correspond to a Co tetramer formed by four Co adatoms. Three of these adatoms occupied the β sites and the fourth adatom attached to either the α or the overbond site. The label H indicates the hollow site. From [33]

Since Co interacts weakly with graphite, one of the key issues in theoretical and experimental studies of Co-graphite interaction is the binding sites where Co is attached on the graphite substrate. After having calculated the adsorption energy of Co adatoms and dimers on graphite, it was found that Co adatoms preferred the hole sites (centers of hexagon rings) while the atoms in the dimers lied above a line through the centers of C-C bonds at opposite sides of a ring. However, this result was not well-consistent with a recent STM study of Co on HOPG³³ where Wong et al. proposed that the Co adatoms preferentially adsorbed on the surface graphene carbon sites (β sites) but not the hole sites (see Figure 1.2). The authors attributed the evident discrepancies between theory and experiment to the difficulties associated with correctly modeling Van der Waals forces, and thus binding energies by using DFT.

The morphology of Co particles supported on graphite is another issue studied by many groups, since it is significantly affected by the Co-graphite interaction. Due to the low surface energy of graphite, metals deposited on its surfaces often form physisorbed three-dimensional (3D) islands.³⁴ A 3D growth mode of Co on graphite is a direct consequence of the weak interaction between Co and graphite.^{35,36} Surface contamination or defect sites over graphite

strongly affect these interactions. If the interaction is strong enough, Co adatoms can bind to the graphite surface, reduce their surface diffusion and act as nucleation centers for Co growth.³³ Moreover, on highly contaminated graphite, adsorbed foreign carbon species but not carbon atoms from graphite could act as the Co nucleation sites.^{33,35} Apart from surface diffusion, the intercalation of metal into graphite layers is another possibility of metal-graphite interactions. Although some metals such as lanthanum³⁷, cesium³⁸ are already known as capable of intercalating into graphite, the transition metals, including Co, have never been reported to diffuse into the graphite subsurface.³⁴

1.1.2.4 Co on graphene

Graphene is a single atomic layer of graphite. It was not proved to exist in free-standing state until first exfoliated from graphite by Andre Geim and Kostya Novoselov,³⁹ who were awarded the Nobel Prize in 2010 “for groundbreaking experiments regarding the two-dimensional material graphene”. Graphene has many extraordinary properties, such as high electron mobility, high thermal and mechanical stability etc., some of which exceed those obtained in any other known material or reach the theoretically predicted limits.⁴⁰ Since then, graphene has been at the center of an ever-expanding research area.^{40,41} An introduction of graphene and its preparation methods will be given in *section 1.2*, while this part will be a brief review of previous studies over Co-graphene interaction. Since Co is one of the metals used for the growth of graphene by the CVD method, the graphene/Co interfaces are studied both by theory and experiment. Thus, the Co-graphene interactions will be discussed in two parts: graphene on Co and Co on graphene.

Graphene on cobalt

The lattice constant of the Co(0001) surface is very similar to the free-standing graphene lattice ($a_{\text{graphene}}=2.46 \text{ \AA}$, $a_{\text{Co}}=2.51 \text{ \AA}$), which opens up the possibility of growing stable epitaxial layers without the formation of complex superstructure patterns. Thus, both theoretical and experimental works have been performed to study the graphene interaction with Co(0001) surface. By investigation with STM, a commensurate structure of graphene on Co(0001) has been proved (see Figure 1.3).⁴² Due to the non-equivalence of adjacent carbon atoms in the graphene layer with respect to the underlying Co surface, only every second carbon atom in the graphene’s unit cell can be observed in the STM image (Figure 1.3 a). Thus, one of the two carbon atoms in the graphene is located on top of a Co atom, while the other carbon atom may

be either at an hexagonal close packed hollow site (AB model) or at a face-centered cubic hollow site (AC model) of the cobalt substrate. The experiments and DFT calculations could not distinguish these two models, but they proved that AB and AC models are much more stable than BC model. Scanning tunneling spectroscopy and DFT calculations indicate a strong interaction of the graphene π -states with Co d-states. Other theoretical works also proved this strong chemical interaction between graphene and Co.^{43,44} For comparison, Pt(111), which has a very different lattice constant from graphene (3.92 Å), was also tested as substrate for graphene growth. Graphene on Pt(111) shows moiré domains because of the lattice mismatch. The interaction between graphene and Pt(111) surface is very weak and the electronic structure of graphene is nearly the same as that of a free standing graphene.⁴⁵

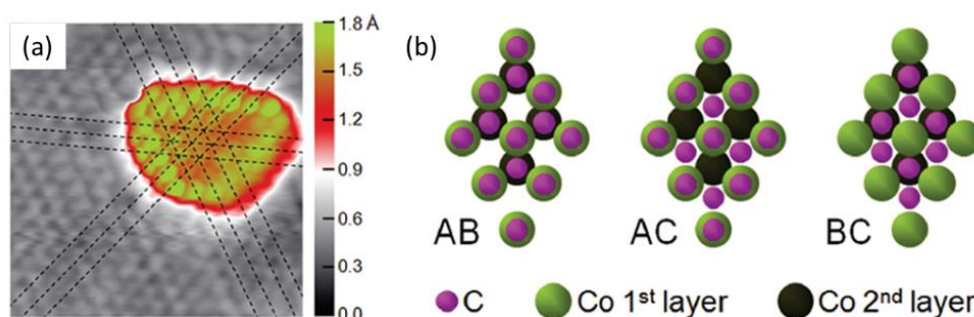


Figure 1.3 (a) Small graphene island on Co(0001) with guidelines matched to the positions of the Co atoms. Different color scales have been adopted for the substrate and the graphene layer. (b) Three structural models for the registry of graphene on Co(0001). Reproduced from [42].

A very recent work⁴⁶ compared the long-term passivation of different metals covered with single layer graphene, where the authors found that the interaction between graphene and the substrates plays a critical role. The strong interaction between graphene and Co prevents the intercalation of oxidizing species along their interface and thus suppresses the oxidation of Co surface, while the weak interaction between graphene and Pt provides a pathway for the intercalation of oxidizing species.

Cobalt on graphene

Apart from the application of grown graphene on Co, graphene supported Co materials have also been applied to many different fields, such as catalysts,^{47,48} supercapacitor⁴⁹ and sensors⁵⁰, which show high performance and potential applications. Fundamental studies help us to well understand the Co-graphene interactions and direct the design of Co-graphene materials.

Similarly to the studies on Co-graphite interactions, there are several theoretical works focusing on the adsorption of metals on graphene.^{51–53} As shown in Figure 1.4, there are three possible adsorption sites on a single layer graphene: the hollow site at the center of a hexagon (H), the bridge site above the C-C bond (B), and the top site right above a carbon atom (T). However, most of the results indicate that on the graphene surface Co adatoms prefer to adsorb on H-type sites.^{51,52,54} The interactions between Co adatoms and graphene are consistent with covalent bonding, and the adsorption is characterized by strong hybridization between Co and graphene electronic states.

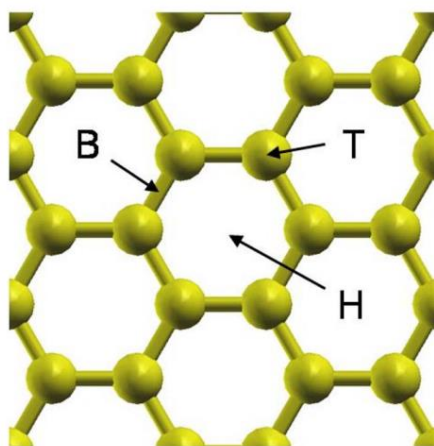


Figure 1.4 Possible adsorption sites of a single adatom onto single-layer graphene: hollow (H), bridge (B), and top (T). Reproduced from^[51].

Co growth morphology has strong effect on the performance of Co-graphene materials. Studies of Co morphology have been carried on graphene grown on Ru, Ir and SiC substrates. In Figure 1.5, Liao et al⁵⁵ showed that Co forms highly dispersed small 3D clusters on graphene moiré on Ru(0001), which was also proved by Poon et al³⁶ that observed the formation of 3D dome-shaped clusters on epitaxial graphene/SiC(0001). The 3D growth mode of Co on graphene is similar to that of Co on graphite, which is driven by the small surface energy of graphene. However, with a pulsed laser deposition (PLD) method, Vo-Van et al⁵⁶ succeeded in getting layer-by-layer grown Co up to ~1.5 nm on a graphene/Ir(111) surface. They believed that it was due to the high instantaneous deposition rate of PLD which led to high nucleation density of smaller clusters in the initial stages of the growth and forced the layer-by-layer growth of Co.

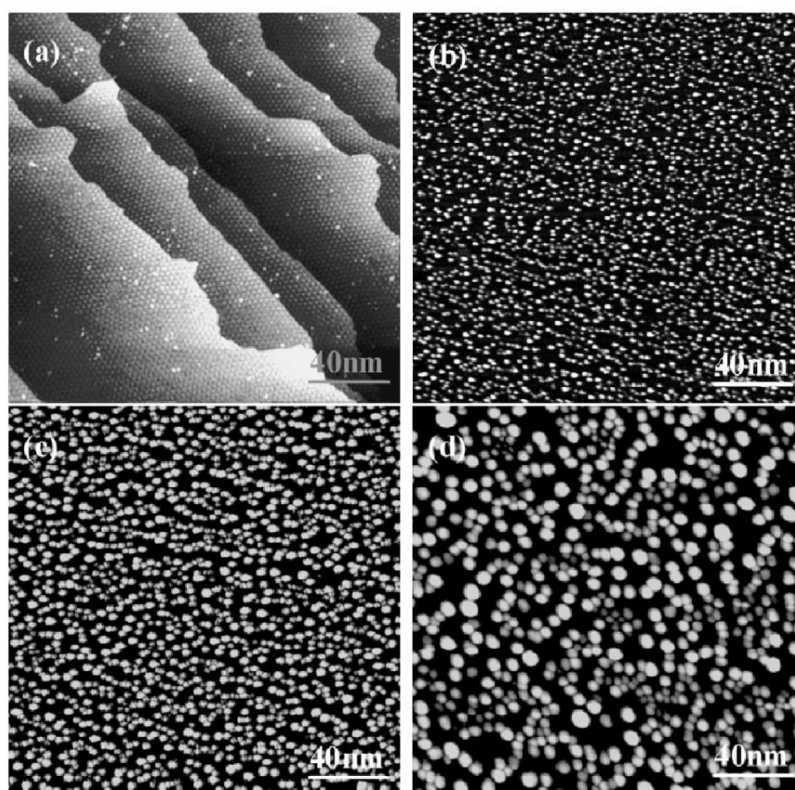


Figure 1.5 STM topographic images ($200 \text{ nm} \times 200 \text{ nm}$) after Co deposition of (a) 0.01, (b) 0.13, (c) 0.70, and (d) 2.5 ML on graphene/Ru(0001) at room temperature. From [55].

As was mentioned above, intercalation of Co into graphite has never been reported, however, Co intercalates at the interface between graphene and its substrate, as has been reported for many supports and summarized in Table 1.2. It was found that the intercalation of Co into graphene/Pt(111) could start even at room temperature and after intercalation the Co 3d states strongly hybridized with graphene.⁵⁷ When it comes to graphene/Ir(111), the intercalation of Co was investigated under various temperatures. At low temperature ($125 \text{ }^\circ\text{C}$), Co preferentially intercalates at regions where graphene has a strong curvature, such as across the substrate step edges and areas with wrinkles. The strong bonding between Co and graphene was also observed after Co intercalation into graphene/Ir(111).^{58,59} Moreover, at a higher annealing temperature (770 K), the intercalated Co can form alloy with the Ir underneath. However, the mechanisms and dynamics of the intercalation processes are still not well understood. One proposed mechanism is that the metal diffuses through the graphene defects which are generated in the contact with the metal followed by the self-healing of graphene C-C bonds.⁶⁰ In addition to this mechanism, Sicot et al⁶¹ suggested that the main intercalation path should be the diffusion through pre-existing lattice defects in graphene, such as vacancies or pentagon-heptagon pairs, which reduce the required energy of trigger intercalation. Another

mechanism proposed by Vlais et al⁶² is that the intercalation path of Co is determined by the strength of the graphene/Ir interaction. This can explain why the substrate step edges and wrinkles are energetically more favorable for intercalation. In the work of de Lima and coworkers,⁶³ it was proposed that all above mechanisms might occur during Co intercalation under SiC epitaxial grown graphene.

Table 1.2 Summary of Co intercalation under graphene

Substrates	Co thickness	Intercalation Temperature	Techniques
Ir(111)	-	200 °C	STM ⁵⁹
	-	Complete at 450 °C	XPS ⁶⁴
	Severl ML	580 - 880 K	AES, LEEM ⁵⁸
	7 ML	570 K	XPS, STM ⁶⁵
	1 ML	125 °C	LEEM ⁶²
Pt(111)	-	Start at RT	STM,STS ⁵⁷
Ru(0001)	0.2 ML	523 K	STM ³⁵
	-	800 K	STM ⁶⁰
SiC	1 - 3 ML	650 °C	STM ⁶³

Annealing of graphene-supported Co not only provokes the intercalation of Co, but also the reaction of Co with graphene. Leong et al⁶⁶ studied the annealing effects to metal-graphene contacts and found a dissolution of carbon from graphene into the metal during annealing. However, this occurred only at the chemisorbed metal-graphene interfaces, such as the interfaces between Ni and Co, but not at the physisorbed interfaces such as Au- and Pt-graphene interfaces. In addition, defects or dangling bonds are required in the initial stage of the chemical reaction, which can be found along the edges of the exfoliated graphene but rarely in the basal plane. On CVD-grown graphene, due to the imperfect lattice and grain boundaries, defect sites can be anywhere throughout the graphene layer. As shown in Figure 1.6, significant amount of defects at the Ni-graphene contact area were introduced by annealing Ni-contacted CVD-graphene at 300 °C, while the as transferred graphene was still in high quality (another example of Co/graphene can be found in the supporting information of Ref.⁶⁶). Low temperature induced chemical reaction (at 100 °C) and the formation of nickel carbide at the interface of deposited Ni and graphene/Ni(111) have been also reported. Chemical reaction could even take place between graphene and deposited metals such as Ti^{67,68}, Pd⁶⁷, Cr⁶⁸ at room temperature, although similar reaction was not observed after Co deposition.⁶⁹ The reason may be due to the

different conditions or graphene qualities used in different works, however, further studies should be considered.

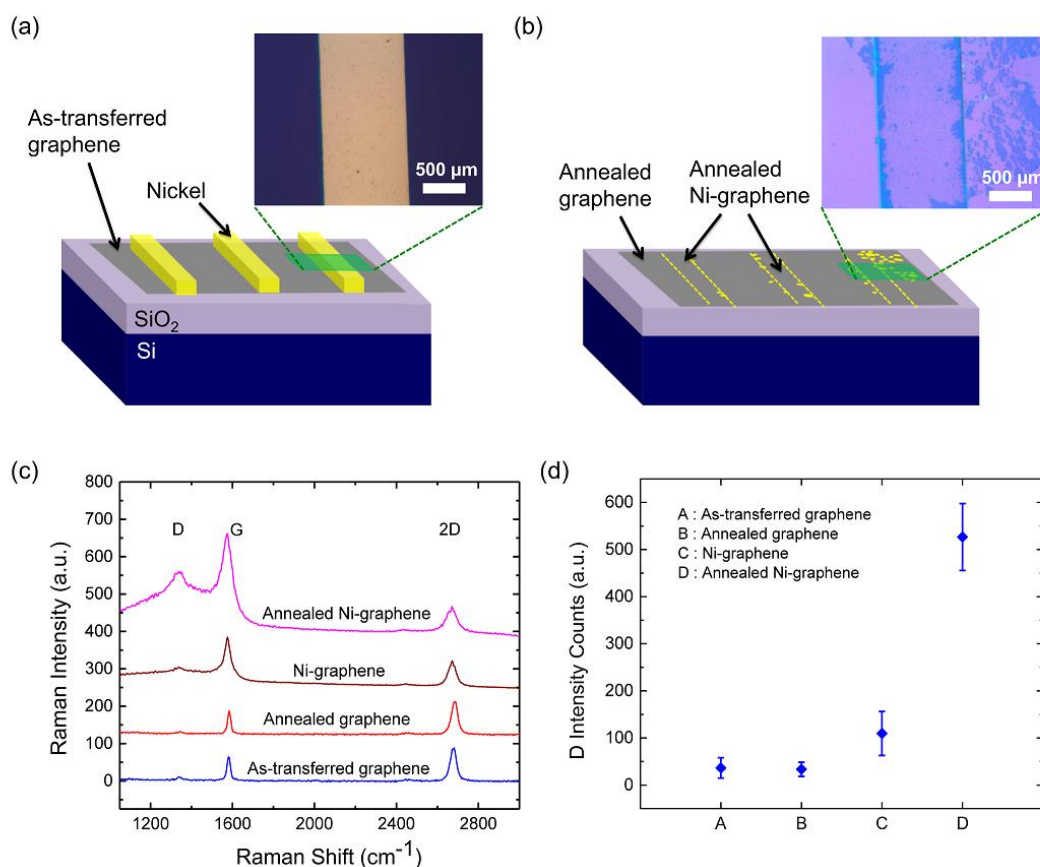


Figure 1.6 Investigation of the annealing effect on Ni-contacted monolayer CVD-grown graphene. (a) Schematic of the sample after annealing, showing several Ni bars deposited on the CVD graphene on a p⁺ Si/SiO₂ substrate. Inset: Optical image of a Ni bar (1 mm wide, 100 nm thick) after 1 h of 300 °C annealing. (b) Schematic of the sample after Ni removal by acid, showing the CVD graphene on a p⁺ Si/SiO₂ substrate with some residual nickel-carbon compound. Inset: Optical image of the marked region. (c) Raman spectra of the CVD graphene sample taken at different positions as indicated. (d) D-peak intensity counts summed over 3600 spectra for four different types of sample as indicated. From [66].

1.2 Modification of Co-support interaction

It is generally accepted that a strong interaction between metal and its support increases the dispersion and leads to the formation of relatively small metal crystallites. In case of catalytic applications, this provides high active surface area, however, can hinder the reducibility of the metal. It is also possible to result in redox reactions at the metal-support interface, encapsulation of the metal by the support and/or the interdiffusion of the metal into the support. In contrast, weak metal-support interactions are likely to prevent interface redox reactions and encapsulation etc., leading to better metal reducibility, but common drawbacks are lower metal

dispersion and severe sintering upon annealing. Therefore, optimizing the metal-support interaction is a crucial issue towards catalysts' design. The metal-support interaction could be determined by the preparation methods, the modifier and the reaction conditions. In this section, modification of Co-support interactions with modifier will be discussed. As it is generally known, the final target of modifying a catalyst is to obtain high activity, selectivity and stability and in that case, each promoter has a specific function for each catalyst and reaction. Thus, the discussion of the modification of Co-support interactions should be based on the specific support and reaction.

1.2.1 Modification of Co-ZnO interactions in steam reforming of ethanol

1.2.1.1 Modification by metals

The role of various oxidation states of cobalt (i.e. metallic Co and Co^{2+}) in steam reforming of ethanol reaction (SRE) has always been a matter of scientific debate. The reaction pathways for ethanol on different model catalysts, including Co/ZnO(0001),¹⁷ Co/YSZ(100),⁷⁰ and Co/CeO₂/YSZ(100)⁷¹ have been studied by Vohs's group and they proposed that both metallic Co and Co^{2+} were active phases for this reaction. However, other works on the SRE under realistic reaction conditions and by controlling the ratio Co and Co^{2+} in catalysts showed that metallic Co was more active than Co^{2+} . Although the debate about the role of Co^{2+} in SRE reaction is far from being closed, it is generally accepted that a high Co^{2+} ratio is detrimental for SRE reaction, since Vohs et al¹⁷ also found that ZnO supported CoO was not active. Thus, high metallic Co ratio is critical for the reaction to proceed.

One strategy for catalyst development consists of the modification of supported Co by adding another metal to form bimetallic crystallites. Bimetallic catalysts often show chemical and electronic properties that are distinct from those of their original metals and offer the opportunity to obtain new catalysts with enhanced selectivity, activity, and stability. Law et al^{14,18} studied ZnO supported Co and NiCo under UHV, O₂ and ethanol conditions and reported the effect of Ni to Co/ZnO model systems under such conditions. According to their results, under UHV annealing condition, the oxidation of Co by ZnO was hampered by Ni addition to Co-ZnO due to the Ni-Co synergetic effects, while after annealing in 1×10^{-6} mbar of O₂, segregation of Co over Ni was observed. The reaction pathway of ethanol was also modified since Ni favors production of methane and cobalt that of acetaldehyde. Homs et al⁷² studied Cu and Ni promoted Co(Na)ZnO catalysts, by HRTEM and they observed the $\text{Co}_{3-x}\text{M}_x\text{O}_4$ mixed oxide particles (M = Ni, Cu) after calcination of the catalysts and CoM alloy after SRE.

Addition of Ni to Co/ZnO improved both the production of hydrogen at low temperature and catalyst stability. The alloy formation was also proved by Llorca and coworkers,^{73,74} that observed the CoFe, CoNi, CoCr, CoCu and CoMn alloys using HRTEM and moreover, they found that the catalysts promoted with Fe, Cr and Mn exhibited a rapid and higher degree of redox exchange between oxidized and reduced Co.

Noble metals, such as Ru,⁷⁵ Rh,⁷⁵ Ir,^{75,76} Pd⁷⁵ and Pt⁷⁷, have also been applied to CoZnO catalysts, but due to their high price, they were added at small amounts as promoters. With the small amount of noble metals, Co oxides are easier to be reduced due to the well-known spillover effect. The mechanism is that noble metals can be easily reduced to the metallic state at much lower temperature than cobalt oxides. Afterwards, hydrogen can be dissociated and activated by the noble metal and in turn, spillover and accelerate the reduction of cobalt oxides. Besides, small amounts of ZnO can also be reduced through the hydrogen spillover effect.^{75,76}

1.2.1.2 Modification by oxides

Oxides are also considered to be potential modifiers for CoZnO catalysts. Al₂O₃ has been used as modifier from low (~ 5wt.%)⁷⁸ to high (> 20 wt.%) loadings.^{79–81} At high Al₂O₃ ratios, spinel phase ZnAl₂O₄ and CoAl₂O₄ were always present on the catalysts,^{79–81} while at low ratios, these phases were not easily distinguished from Co₃O₄.⁷⁸ CoAl₂O₄ could be only partially reduced under the reaction conditions, since its reduction always requires high temperatures (> 700 °C).⁸⁰ Figure 1.7 gives the evidence that highly stable ZnAl₂O₄ phase forms on the catalysts after calcination, reduction and reaction.⁸⁰ According to Krалеva et al⁷⁸, although the reducibility of metal decreased due to the strong metal-support interactions, the catalytic performance in the partial oxidation of ethanol reaction still improved because the obtained metal active sites were in high quality and stable on the ZnAl₂O₄ phase.

Alkalis can be also used to promote CoZnO catalysts. Both K⁸² and Na⁷³ have been already employed as promoters in CoZnO catalysts at a low loading. However, differently from Al₂O₃, alkali-metal oxides do not significantly modify the crystal structure of CoZnO catalysts. The reduction properties of Co were found to be more dependent on the catalysts' preparation method rather than the presence of K (up to 2 wt.%).⁸² In particular, by using a co-precipitation synthesis method, K promoted the reduction to lower temperature, while through citrate method the reduction temperature was not modified by K, possibly due to the incorporation of K into the bulk of the support. For the SRE activity, K had a significant influence on the

catalytic efficiency and acted as a promoter to improve the catalyst stability through inhibiting coke deposition. Similarly as K, addition of 1 wt.% Na to CoZnO also showed higher catalytic activity with respect to the bare CoZnO catalyst, but the microstructure was virtually identical to CoZnO, probably because of the atomically dispersion and the lack of incorporation of Na into the cobalt structure.⁷³

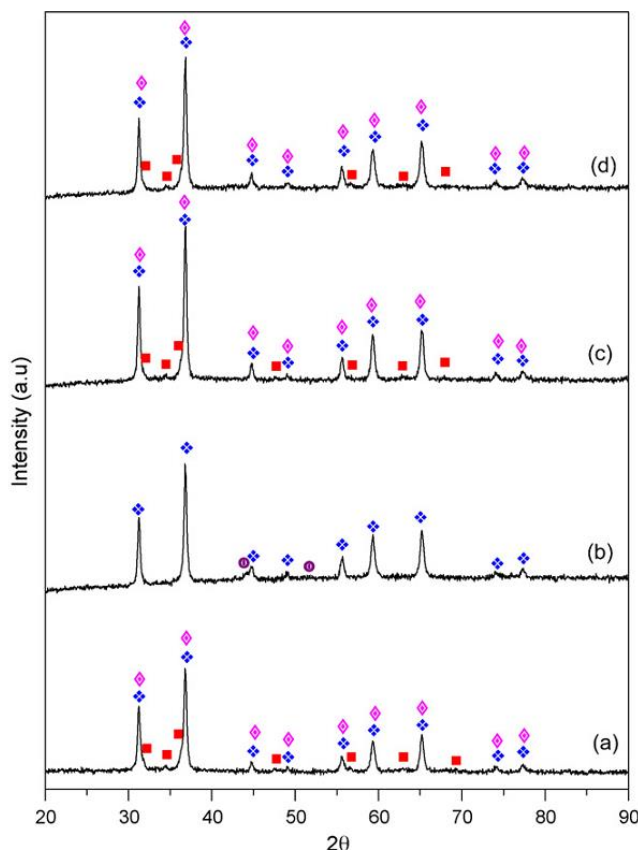


Figure 1.7 XRD patterns of CoZnAl (9 wt.% of Co) catalysts: (a) fresh; (b) reduced; (c) after being used at 500 °C; (d) after being used at 600 °C. \blacklozenge : ZnAl₂O₄, \blacksquare : ZnO, \blacklozenge : CoAl₂O₄, \odot : Co⁰. From [80].

1.2.2 Modification of Co-SiO₂ interactions in Fischer-Tropsch synthesis

1.2.2.1 Modification by noble metals

Noble metals, such as Pt,^{83–85} Pd,⁸³ Ru,^{83,86,87} Re⁸⁴ etc., have been found to have significant effect on the structure and catalytic performance of Co-SiO₂ catalysts in FT synthesis. As has been discussed in 1.1.2.2, at high annealing temperature, the redox reaction between Co and SiO₂ may take place with formation cobalt silicate, which is hardly to be reduced to the active metallic Co.⁹ In this case, addition of noble metals (e.g. Ru) to SiO₂ (MCM-41 and SBA-15 type) supported Co catalysts, could help the formation of reducible phase (Co₃O₄) instead of the barely reducible phase (cobalt silicate) in the calcined catalyst precursors.^{86,87} The typical

XPS results of ref. [86] are shown in Figure 1.8, where monometallic Co catalysts (Co/SBA-15 and Co/MCM-41) show Co 2p_{3/2} peaks at 781.5 and 781.8 eV with obvious shake-up satellite peaks, indicating the presence of the Co²⁺ state in these catalysts. The Co²⁺ peak was attributed to the formation of amorphous cobalt silicate species due to the strong interaction of Co species with the SiO₂ support. For the samples modified with Ru (CoRu/SBA-15 and CoRu/MCM-41), the binding energies of Co 2p_{3/2} peaks at 780.0 and 780.5 eV and the accompanied small satellite peaks, indicate formation of Co₃O₄ species. Thus, addition of only 0.3 wt.% Ru decreases the cobalt-silica interaction and results in the formation of the reducible Co₃O₄ phase.

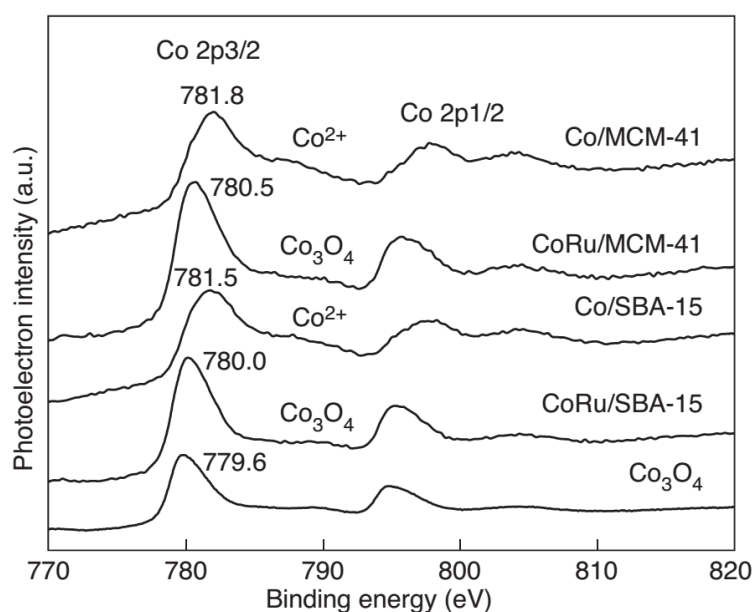


Figure 1.8 XPS spectra of monometallic and Ru- promoted cobalt catalysts supported by MCM-41 (pore size 3.4 nm) and SBA-15 silicas (pore size 4.4 nm). The catalysts contained 10 wt.%Co and 0.3 wt.% Ru in the promoted catalysts. From [87].

Since metallic Co is the active phase in FT synthesis, a pre-reduction treatment is always needed to reduce the calcined catalysts to the metallic state and the noble metals are able to effectively decrease the reduction temperature of cobalt oxide to metallic Co in H₂. For example, metals such as Pt,⁸⁸ Ru,^{83,86} Ir⁸⁹ have been reported to promote the reduction of Co at lower temperature, as mentioned in the previous section, due to the spillover effect. In this case, the lower reduction temperature limits the possibility of cobalt silicate formation. Intermix of cobalt with noble metals can induce formation of cobalt-noble metal bimetallic particles,^{83,90} which can modify the geometric and/or electronic effect of Co-SiO₂ interactions. Besides, noble metals are commonly reported to decrease the crystallite size and increase the dispersion

of Co, however, smaller Co crystallites are easier to be re-oxidized and cause deactivation under FT synthesis conditions.⁹¹⁻⁹³

1.2.2.2 Modification by oxides

Oxides, such as ZrO_2 ,^{9,94} La_2O_3 ,^{9,95} CeO_2 ,^{9,96} MnO ^{9,97} and K_2O ,⁹⁸ have also been employed as FT synthesis promoters for modification of the catalyst texture, Co reducibility, Co dispersion and catalytic performance. For example, ZrO_2 was reported to be able to form a protecting layer to prevent the strong interaction and chemical reaction between Co and SiO_2 during FT synthesis.⁹⁹ Addition of small amount of La^{3+} ($\text{La}/\text{Co} \leq 0.2$) moderates the strong Co- SiO_2 interactions and improves the Co reducibility.¹⁰⁰ However, with high La^{3+} loadings ($\text{La}/\text{Co} \geq 0.5$), the formation of hardly reducible La-Co and Co-Si mixed oxides was observed, because of the higher pH of the impregnating solution. MnO has also been reported to increase the Co reducibility by Tan et al¹⁰¹, but a possible cause of this effect (besides the formation of a protection layer) could be that Mn can scavenge the oxygen present at the Co/ SiO_2 interface allowing Co to remain in the metallic state.

In contrast to noble metals, the modification of Co- SiO_2 interaction by oxides does not always allow lower Co reduction temperatures. Addition of both Ce and K oxides have been observed to hinder the reduction of $\text{Co}^{96,98}$, which, on the other side, has a negative effect on the catalytic activity in FT synthesis.

1.2.3 Modification of Co-Carbon interactions in Fischer-Tropsch synthesis

Carbon materials, such as carbon nanofibers, carbon nanotubes (CNT) and graphene, have drawn considerable attention in catalysis, and these materials with various bonding states and morphologies have been applied in both SRE and FTS. As supports, they have lots of prominent advantages, including high thermal and electrical conductivity, high specific area, resistance to acidic and alkali media and high stability under reaction conditions. However, the surfaces of sp^2 carbons are graphitic, unreactive and hydrophobic, thus they do not offer anchor sites to stabilize the metal particles. As mentioned in 1.1.2.3, Co clusters are physisorbed on the graphite basal planes and only defect and admixture sites strongly interact with Co. Therefore, when carbon materials are used as support for metal nanoparticles, modification of the carbon surface in order to create defects or generate functional groups is required. In this way, the metal nanoparticles could be anchored and stabilized on the carbon surface through strong interactions. Figure 1.9(a) shows a collection of various types of defect sites (heteroatom

doping) on a carbon surface, while Figure 1.9(b) is a brief introduction of different types of functional groups that could be generated on a carbon surface by chemical methods.¹⁰² Upon all these defects and functional groups, the metal-carbon interactions can be tuned.

Acid treatment is one of the simplest ways to modify the carbon surface. In general, with HNO₃ treatment, the caps of closed CNT tubes were opened and the nanotubes were broken to shorter ones. In parallel a lot of defects and functional groups were introduced on the CNT surface. Thus, small Co particles were formed and stabilized on the surface or entered into the nanotubes, which in turn led to high FTS rate.¹⁰³ More recently, not only the liquid phase HNO₃, but also the gas phase HNO₃ was applied to oxidize CNT.¹⁰⁴ In that work, the catalysts supported on oxidized CNT showed higher stability in FTS, possibly due to the stronger anchoring of the Co nanoparticles to the CNT surface. However, higher activity was found on the catalyst with unmodified CNT as support and it was attributed to the existence of *hcp* phase Co in this catalyst.

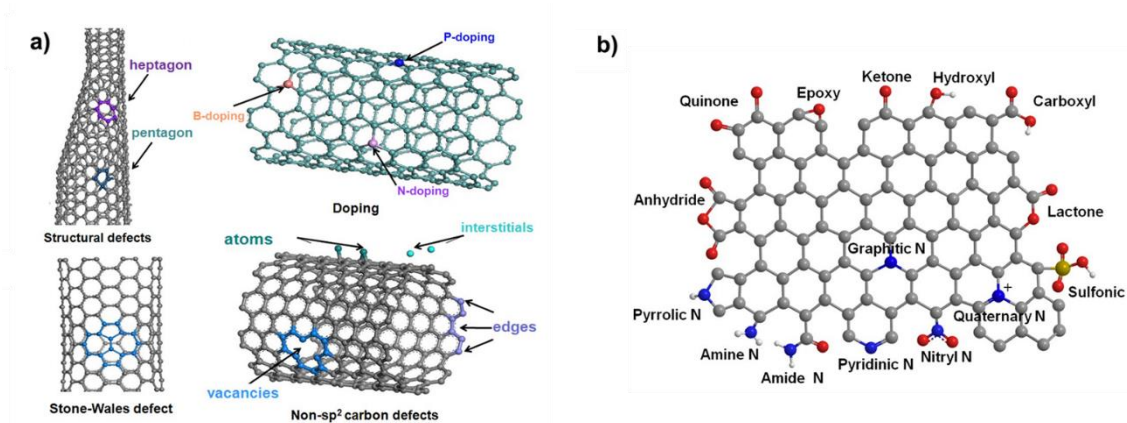


Figure 1.9 (a) Schematic models representing different types of defects and heteroatom dopings on a carbon surface. (b) Schematic models of functional groups on the surface of a nanocarbon. Carbon: gray, nitrogen: blue, oxygen: red, sulfur: dark yellow, hydrogen: white. Reproduced from [102].

Besides HNO₃, there are also some other oxidants used to introduce functional groups on CNT, such as H₂O₂ + O₃, NH₃ and NH₃ H₂O + H₂O₂ etc. Davari et al¹⁰⁵ applied these methods on CNT and the modified CNT was used for supporting Co as FTS catalysts. The authors confirmed that different treatments induced the formation of different functional groups on the support; C=O and carbonyl groups were found in the samples treated with H₂O₂ + O₃ and NH₃ while additionally C-N and N-H were observed for CNT treated by NH₃ H₂O + H₂O₂. They further proved that Co supported on all these three kinds of CNT had stronger metal-carbon

interactions and showed better dispersion, lower reduction temperature and consequently better FTS activity.

Nitrogen doping is another important method to modify carbon materials, being an effective way to tailor the properties of carbon materials and rendering their potential use for various applications.¹⁰⁶ Nitrogen doped mesoporous carbon (NMC) has been tested for FTS where the doped nitrogen, especially sp^2 -type, was proved to act as the heterogeneous site for the nucleation and growth of cobalt species.¹⁰⁷ These nitrogen sites strongly interact with Co nanoparticles, leading to electron transfer from the NMC to CoO particles and also resulting in high dispersion of Co over NMC. During the evaluation of FTS, the product selectivity was observed to shift toward light hydrocarbons due to the formation of small cobalt particles on the N-doped supports.

Graphene has recently attracted intensive attention due to its unique physicochemical properties. It has also several genuine advantages over other carbon allotropes for developing new catalysts (details see Section 1.3). The structure, morphology as well as the quality of graphene materials are significantly influenced by the preparation methods, thus the metal-graphene interactions are mainly determined by the preparation and modification method of graphene. Similarly as for CNTs, graphene can also be modified by HNO_3 , however, more defects and functional groups are being formed as compared with CNT treated under the same conditions.^{108,109} The defects can act as anchoring sites for Co nanoparticles and lead to higher dispersion, smaller particle size, lower reduction temperature and consequently, higher FTS activity and stability.^{108,109} Graphene prepared with other methods have also been applied for FTS catalysts with iron acting as the active metal and the interaction between Fe and graphene was reported to be comparable to Co-graphene. Sun et al¹¹⁰ developed an one-pot hydrothermal synthetic strategy for preparation of metals (Fe, Co, Ni) supported on reduced graphene from graphene oxide and a two-step method was also applied for comparison, see Figure 1.10. They found that after reduction at 723 K for 16 h, Fe on rGO remained highly dispersed showing high activity, selectivity and stability during FTS reaction. They demonstrated that the Fe nanoparticles were anchored by the high amount of defect sites on rGO at elevated temperatures and the FTS activity was strongly influenced by the nature of the carbon support. There are some other studies of Fe on GO by different methods; among them, El-Shall and coworkers¹¹¹ tried the microwave assistant method and other modifiers, such as K and Mn. They found that the defects on graphene acted as favorable nucleation sites for Fe nanoparticles, enhanced Fe-C interaction and improved the formation of an active iron carbide

phase (Fe_5C_2), and at the same time, all studied catalysts gave high activity, selectivity and stability in FTS.

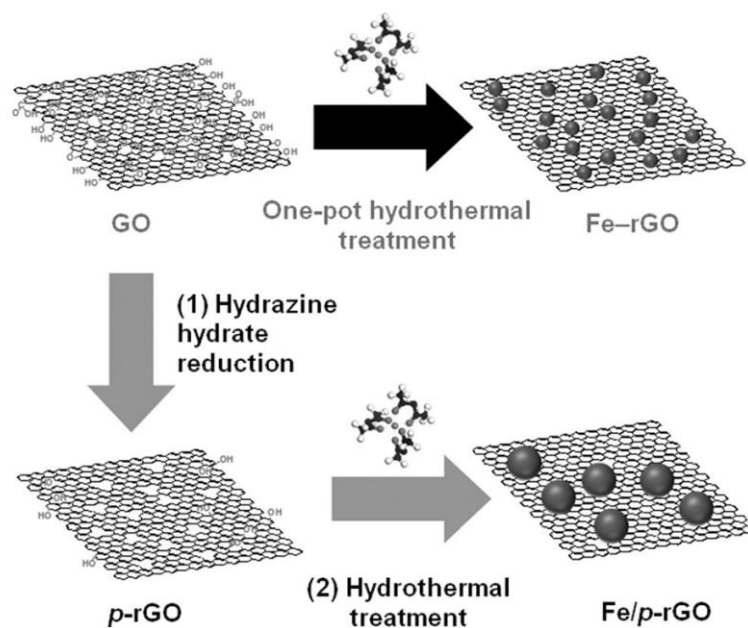


Figure 1.10 Illustration of the one-pot hydrothermal synthetic strategy for the preparation of the Fe-rGO nanohybrid from graphene oxide and $\text{Fe}(\text{acac})_3$ (marked with black arrow). For comparison, the two-step approach for the fabrication of the Fe/p-rGO hybrid material is also illustrated (marked with gray arrows). Reproduced from [110].

As shown above, modification of cobalt-supported catalysts influences a number of catalyst properties and their performance. Noble metals and oxides are the most commonly used promoters for ZnO and SiO_2 supported Co catalysts. The presence of noble metals improves the reducibility and dispersion of Co, and at the same time, it provides new active sites. However, promotion with noble metals significantly increases the cost of the catalysts. When oxides are applied as modifiers, the catalyst properties varies with the different type of oxides, sometimes accompanied with negative effects, such as the increase of the reduction temperature of Co, formation of hardly reduced Co-oxides solid solutions etc. Although carbon based materials interact with Co weakly, modification with defects and functional groups can stabilize Co and improve the catalytic performance. Among all carbon materials, graphene, being a new type of carbon allotropes, has attracted intensive attention, since not only it has intrinsic catalytic properties, but it can also improve the performance of other catalysts by forming functional composites. The application of graphene is mainly determined by the preparation methods and its quality, which will be discussed in detail below.

1.3 Graphene

1.3.1 General introduction of graphene

Graphene is a monolayer of carbon atoms tightly packed in a hexagonal lattice. It is the conceptual building block for graphitic materials, from zero-dimension (0D) fullerenes, to one-dimension (1D) carbon nanotubes, to three-dimension (3D) graphite (Figure 1.11). More than 70 years ago, graphene was theoretically predicted to be unstable and could not exist because two-dimensional (2D) crystal were thermodynamically unstable at finite temperature.^{112,113} Nevertheless, graphene and other 2D crystals were proved to exist on substrates or on graphite tightly bound to another solid surface, as an integral part of larger 3D structures.^{114,115} However, graphene was presumed not to exist in the free state and was believed unstable with respect to the formation of curved structures such as soot, fullerenes and nanotubes.⁴¹ Suddenly, in 2004, Andre Geim and Kostya Novoselov at Manchester University first isolated single-layer graphene from graphite³⁹ and turned free-standing graphene into reality¹¹⁶. This led to an explosion of interest in the academic and industrial community on graphene and graphene-based materials.

The simple “scotch-tape technique”³⁹ for exfoliating graphene is one of the reasons that graphene research progressed so fast since it enables the researchers to obtain high-quality graphene by a relatively easy and cheap method. The very first experiments were carried out on these mechanically exfoliated graphene flakes and focus on their electronic properties.^{39,117,118} The extremely high carrier mobility and an ambipolar field-effect in graphene which have been theoretically predicted for a long time were proved by Novoselov et al³⁹ after they exfoliated graphene. Later, the quantum Hall effect in graphene was observed by Geim’s group and simultaneously by Kim’s group.^{117,118} These extremely promising electronic properties of graphene attracted great research interest. In a short period, many other properties of graphene were measured and found to be superior than other materials, with some of them even reaching the theoretically predicted limits.⁴⁰ The intrinsic electron mobility (μ) of graphene at room temperature was proved to be $\sim 2 \times 10^5 \text{ cm}^2/\text{Vs}$, higher than that of any other known material.^{119,120} The mobility μ of ultraclean suspended graphene can be as high as $250,000 \text{ cm}^2/\text{Vs}$ at low temperature and $120,000 \text{ cm}^2/\text{Vs}$ at 240 K.^{121,122} Besides, graphene was also proved to be the strongest material ever measured, with a Young’s modulus of 1 TPa and intrinsic strength of 130 GPa.¹²³ What’s more, the thermal conductivity of graphene is extraordinarily high at room temperature (its value can be up to $5000 \text{ Wm}^{-1}\text{K}^{-1}$)¹²⁴ and graphene

can sustain extremely high densities of electric current (5×10^8 A/cm², about a million times higher than copper).^{40,125} Finally, even if it is one atom layer thick, graphene is completely impermeable to any gas.¹²⁶

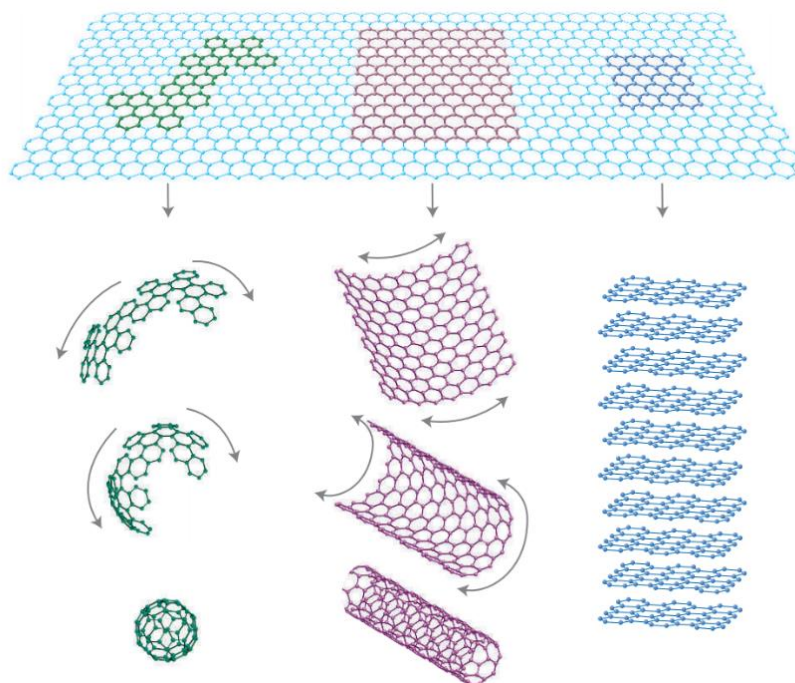


Figure 1.11 Graphene is a 2D building material for carbon materials of all other dimensionalities. From [41].

The superior properties of graphene make it a “*miracle material*”, which is expected to find application to several important fields in the near future. The most exciting potential application of graphene should be in graphene-based electronics. This is not only due to the extraordinary electronic properties of graphene, but also because the Si-based technology is approaching its fundamental limits. The commercial application of graphene as integrated logic circuit seems not to be possible in the next few years since graphene is a conductor but not semiconductor. However, the bandgap engineering in graphene is underway, with the fabrication of graphene nanoribbons,^{127–129} inducing bandgap on bilayer graphene^{130,131} and various modifications by chemical methods^{132,133}. Graphene also meets the requirements of flexible electronics, such as touch screens, e-paper and organic light-emitting diodes (OLEDs) owing to its low sheet resistance and excellent transmittance.^{134,135} Graphene has also been considered for fabrication of high-frequency transistors.^{136–138} The potential application field of graphene goes far beyond electronics and it can be used in almost all the applications that CNT have been utilized and more applications are explored in diverse technology areas based

on its characteristic properties (such as 2D structure, transparent et al.). Those areas include graphene based photonics (photodetectors, optical modulators, mode-locked lasers et al), sensors, composite materials, paints, coating, energy storage, catalysts and even bio-applications.^{40,139,140}

Referring to its application in catalysis, graphene have already been explored as catalytically active centers,¹⁴¹ supporting materials⁴⁷ or one catalyst components for improving catalysts' performance¹⁴². As mentioned above, graphene has several superior and unique properties which endow it with high potential in catalysis. For example, the one-atom thick planar sheet structure of graphene provides it with an extraordinarily large specific surface area (theoretically $2630 \text{ m}^2\text{g}^{-1}$ for a single layer¹⁴³) for loading catalysts. The high conductivity of graphene sheets facilitates the electron transfer for more effective electrocatalysts. The optical transparency and the high electron mobility of graphene make it attractive for new photocatalysts. Other properties, such as high chemical, thermal, optical and electrochemical stability, allow graphene to improve the catalytic stability. To achieve high performance graphene-based catalysts, tailored graphene properties are essential. At the same time, scale up production of graphene is also important for industrial applications. In recent years, various methods have been tried to produce graphene of high quality and/or large scale; the most widely studied methods will be shown below.

1.3.2 Synthesis of Graphene

The quality of graphene is strongly dependent on the preparation method. Some of the superior properties of graphene have been achieved only for high-quality samples (exfoliated graphene)¹¹⁹ and graphene on special substrates like hexagonal boron nitride^{144,145}. For example, the charge mobility of ultraclean suspended graphene can reach $250,000 \text{ cm}^2/\text{Vs}$ ¹¹⁹ while reduced graphene monolayers exhibit a mobility of only $2\sim 200 \text{ cm}^2/\text{Vs}$ ^{146,147} due to the high defect density comparing with the exfoliated graphene. However, for catalytic applications, defects and functional groups on graphene are important and imperative for improved performance.⁴⁷ On the other hand, although the micromechanical cleavage is an effective and reliable method to produce high quality graphene, production yields are extremely low (a few graphene monolayers per mm^2 of substrate area),¹⁴⁶ which significantly limits the application of this method to several technologies. In the last few years, a number of different methods have been used and developed to prepare graphene of various qualities, layers, shape and even dimensions. Here some of the methods which are commonly used are briefly

introduced; more details and methods can be found in the literature^{40,139,140} and references therein.

1.3.2.1 Mechanical exfoliation

This technique involves peeling highly ordered pyrolytic graphite (HOPG) using a scotch tape. Since the first time reported by Geim and coworkers³⁹, it has been considered to be the most effective and reliable method to produce high quality graphene. However, this method is time consuming and produces only randomly placed graphene sheets. The thickness, size and shape of the graphene layer are largely uncontrollable. Thus this method gives a high quality graphene, but due to the above limitations it is most commonly used in the laboratory for fundamental studies of graphene properties. The industrial application of this method is limited by its low production.

1.3.2.2 Chemical exfoliation

Liquid phase exfoliation of graphite is one of the routes to scale up the production of graphene.^{148,149} It is based on exposing graphite to a solvent with surface energy that matches that of graphene. With the help of ultrasounds, graphite breaks up into smaller pieces and the exfoliation occurs more easily. Hernandez et al¹⁴⁸ used N-methyl-pyrrolidone as the solvent and graphite was almost completely exfoliated to a few layer graphite (< 5 layers), with high yield, unoxidized monolayer graphene of ~1 wt%. With further sediment recycling treatments, the yield reached up to 12 wt% of the starting graphite mass. Aqueous solutions with surfactants can also be applied as exfoliation solvents. Lotya et al¹⁴⁹ reported a liquid exfoliation method with water-surfactant (sodium dodecylbenzene sulfonate) as the solvent used to exfoliate graphite, which resulted at more than 40 % of the graphene flakes with < 5 layers and ~3 % consisting of monolayers.

Another related method is the exfoliation of graphite oxide. The graphite oxides are obtained from the oxidation of graphite by strong acids and oxidants through either Brodie,¹⁵⁰ Staudenmaier,¹⁵¹ Hummers method,¹⁵² or some modification of these methods. With the oxygen containing groups, graphite oxide, consisting of a layered structure of ‘graphene oxide’, becomes strongly hydrophilic, which results in the intercalation of water molecules between the layers.¹⁵³ The obtained graphene oxide is electrically insulating due to the oxygen containing groups, so a necessary and important step is to reduce it back to the graphene state by either thermal or chemical methods.

The quality of the graphene derived from chemical exfoliation cannot be as high as that from the mechanical exfoliation method due to the higher density of defects and the residues of surfactant. The resulting graphene flakes may also contain various layers of graphene with uncontrollable shapes. Even so, this kind of graphene can still preserve many properties of the high quality single-layer graphene and can be used in numerous application fields, such as in catalysis, composition materials and coatings. Importantly, these methods are scalable making possible the industrial production of graphene.¹⁵⁴

1.3.2.3 Chemical vapor deposition

Chemical vapor deposition (CVD) has been widely used to grow large-area uniform polycrystalline graphene films.¹⁵⁵ The growth mechanism of graphene using the CVD method is based on the decomposition and the diffusion of the carbon source molecule (such as hydrocarbons) into the metal at high temperature and the segregation of carbon from the sub-surface to the surface of the metal upon the cool down step, since the carbon solubility decreases at low temperature. A variety of transition metals (Ru,¹⁵⁶ Ir,¹⁵⁷ Co,¹⁵⁸ Rh,¹⁵⁹ Ni,^{160,161} Pt,¹⁶² Pd,¹⁶³ Cu,^{161,164,165} Au¹⁶⁶) and alloys (Cu-Ni,^{167,168} Au-Ni,¹⁶⁹ Ni-Mo¹⁷⁰) can be used for graphene growth. Among them, Cu and Ni are the two major substrates for CVD-grown graphene,^{171,172} nevertheless, the graphene growth mechanisms on them are different. Due to the high solubility of carbon in Ni, graphene growth via segregation process is more difficult to control and in this case it forms non-uniform graphene with a thickness distribution of one to a few layers. Graphene growth on Cu is thought to be the surface catalyzed mechanism which results in uniform monolayer graphene.¹⁷³ Graphene sheet of as large as 30 inches has been reported through CVD method over Cu foil substrates.¹⁶⁴

For a number of applications, CVD graphene needs to be transferred from the metal surface to a dielectric surface or other substrate of interest such as plastic foils, glass or SiO₂/Si. Recently, various methods have been used to transfer the as-grown graphene from metallic surfaces onto desired substrates.^{164,174–176} The commonly used process is first to deposit and cure poly(methylmethacrylate) (PMMA) on the graphene surface and then to chemically etch the metal away to obtain free floating PMMA and graphene, which can be transferred onto the desired substrates. Besides of this method, a state-of-the-art roll-to-roll method was applied to transfer a 30 inches graphene from Cu substrate.¹⁶⁴

On the other hand, new CVD methods (plasma-enhanced CVD, metal free CVD) have been developed to synthesize graphene with arbitrary substrates (SiC,¹⁷⁷ SiO₂,¹⁷⁸ sapphire¹⁷⁹) or

without substrates¹⁸⁰, where the complex and expensive transfer step is avoided. However, in order to get high quality graphene with the metal free method, much higher temperature is necessary for cracking the carbon source (such as methane) without the metal catalysis.^{177,179} The plasma enhanced CVD enables the growth of graphene at low temperature which can improve compatibility with modern microelectronic technologies and allow significant energy saving. However, challenges still need to be overcome, like the quality of graphene which is not comparable with that of CVD or exfoliated graphene, and the number of graphene layers which is not well controllable.

To date, CVD graphene films have demonstrated excellent properties: sheet resistances as low as $\sim 125 \Omega \text{ cm}^{-2}$ (ref¹⁶⁴), 97.4 % optical transmittance¹⁶⁴ and a carrier mobility as high as $8800 \text{ cm}^2/\text{V}^{-1}\text{s}^{-1}$ (ref¹⁸¹). Although these values are still far from those obtained from exfoliated single layer graphene, they are nevertheless useful for applications such as flexible and transparent electrodes for solar cells, liquid crystal displays and various high-frequency electronic and optoelectronic devices.¹⁸²

1.3.2.4 Epitaxial growth on silicon carbide

Graphene growth on silicon carbide (SiC) is an alternative preparation technology. The considerable advantage of epitaxial growth over SiC is that insulating SiC substrates do not shunt the current flow in graphene and can be directly applied for electronic devices or components without a transferring step. Under high temperature vacuum annealing conditions, the decomposition of surface SiC is followed by preferential sublimation of Si atoms and subsequent graphitization of the remaining surface carbon atoms.¹³⁰ Generally, high temperature (above 1000 °C) and ultra-high vacuum conditions are used to grow graphene on hexagonal phase silicon carbide (4H-SiC or 6H-SiC).^{183,184} High quality graphene has been obtained from both SiC polar faces i.e. hexagonal SiC, SiC(0001) Si-terminated face (Si-face) and SiC(000 $\bar{1}$) C-terminated face (C-face). However, different epitaxial growth patterns have been observed on different polar faces. On the Si-face, graphene grows in a well-defined orientation, it exhibits regular Bernal stacking, while on C-face, rotational graphene stacking has been observed.^{185,186} This is because of the formation of different interface structures between graphene and bulk SiC during annealing: a well-ordered $(6\sqrt{3} \times 6\sqrt{3})R30^\circ$ phase forms between Si-face and graphene while 2×2 and 3×3 structures form on C-face SiC.¹⁸⁷ The weak interaction between graphene on C-face and the interface preserves the properties of the graphene like a single layer sheet, which leads to a higher mobility of C-face graphene

compared to Si-face graphene.^{185,188} On the other hand, the single orientated interface structure on Si-face can act as a template for graphene growth and leads to the control of graphene thickness on Si-face easier than on C-face.¹⁸⁵

Despite the advantages of this method, the high cost of SiC wafers and the high temperature of the growth conditions are the major drawbacks. Thin layer SiC on Si is considered as a cheaper alternative to SiC wafers and has been tested as the substrate for graphene growth, but further improvement of this method is required.^{189,190} There are also several other methods that have been applied to decrease the graphene growth temperature, for example, nickel assistant,¹⁹¹ continuous electron beam irradiation¹⁹² or fluorocarbon plasma pre-etching.¹⁹³ However, most of them complex the preparation and add extra cost to the production. What's more, the control of graphene layers thickness in the production of larger area graphene and the unintentional doping from the substrate and buffer layers are still areas to be explored.

1.3.2.5 Other methods

A number of other methods have also been used to synthesize graphene, resulting in graphene with different quality and morphologies. Although their readiness level is still not compatible with the methods mentioned above, they have some certain advantages and might open new routes in graphene synthesis. Total synthesis is an exciting way to create high quality graphene nanoribbons (GNRs) with complex structures.^{194,195} Starting from precursor monomers with different structures, the final GNRs show different topologies, width and edge peripheries, which can be designed with atomic precision.¹⁹⁵ However, the main deficiency is the production of only limited quantities of surface-bound GNRs.¹⁹⁶ More recently, long liquid-phase-processable GNRs (> 200 nm) with a well-defined structure were synthesized in solution, a method that can be adapted to prepare GNRs in bulk quantities.¹⁹⁷ Unzipping of carbon nanotubes is another method to get GNRs on a large scale,^{198,199} however, the high price of carbon nanotubes should be considered here. Graphene has been also produced under some special conditions such as flame,^{200–202} continuous wave laser²⁰³ and pulsed laser,²⁰⁴ which are either expensive or not able to produce high quality graphene.

1.3.2.6 Graphene used in this thesis

The specific aim of this work is to study the effect of graphene to the metal-support interaction, notably using “standard” oxide substrates largely employed in catalysis. In order to achieve this, graphene should be in high quality, with the less defects and less functional

groups possible. As shown in Table 1.3 and in Figure 1.12, graphene produced by mechanical exfoliation, CVD and SiC method can meet these requirements. Since graphene will be transferred onto different oxide surface and the main characterization method is XPS, only CVD graphene which could be synthesized in a large scale and is easy to be transferred on substrates is used in this study.

Table 1.3 Properties of graphene obtained by different methods. From^[40].

Method	Crystallite size (mm)	Sample size (mm)	Charge carrier mobility (at ambient temperature) (cm ² /Vs)	Applications
Mechanical exfoliation	>1,000	>1	>2 × 10 ⁵ and >10 ⁶ at low temperature	Research
Chemical exfoliation	≤0.1	Infinite as a layer of overlapping flakes	100 (for a layer of overlapping flakes)	Coatings, paint/ink, composites, transparent conductive layers, energy storage, bioapplications
Chemical exfoliation via graphene oxide	~100	Infinite as a layer of overlapping flakes	1 (for a layer of overlapping flakes)	Coatings, paint/ink, composites, transparent conductive layers, energy storage, bioapplications
CVD	1,000	~1,000	10,000	Photonics, nanoelectronics, transparent conductive layers, sensors, bioapplications
SiC	50	100	10,000	High-frequency transistors and other electronic devices

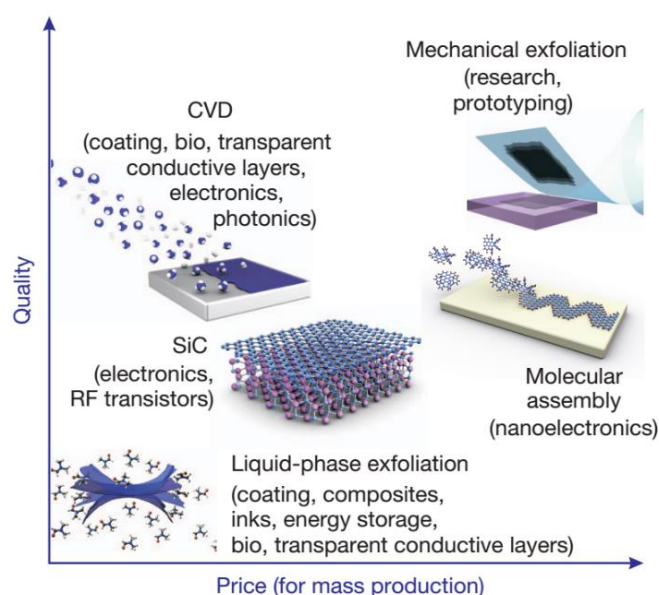


Figure 1.12 There are several methods of mass-production of graphene, which allow a wide choice in terms of size, quality and price for any particular application. From^[40].

1.4 Motivation and outline of the dissertation

Currently, most technical catalysts consist of metal particles supported on porous oxides. The choice of the oxide support is based on diverse criteria including the cost, the toxicity, mechanical properties (e.g. heat dissipation, stability) and more importantly, the nature of its interaction with the metal particles. This interaction is even more pronounced during oxidation and reduction at elevated temperatures, which are essential steps in catalyst's preparation and activation. Upon these treatments, various morphological changes such as sintering, encapsulation, inter-diffusion and alloy formation, can be induced depending on the strength of the metal–support interaction.

Since the important role of the support on the catalytic performance was first realized 35 years ago, almost all catalytic relevant oxide supports have been studied in relation to their interaction with active metals. Recently, carbon based materials (e.g. CNT, carbon black, etc.) are studied as possible substitutes of oxide supports in many catalytic reactions, since they have some certain advantages. Among them, graphene is potentially promising as a catalyst support due to its high mechanical stability, high thermal conductivity and high electron mobility. However, applying single-layer graphene for catalyst support is not practical, since very fast free-standing graphene sheets recombine to form the so-called few-layer graphene. As mentioned above, a number of studies examine the interaction of metal particles with graphene grown over metals and nonmetals such as SiO_2 and SiC , but limited studies focus on other substrates. The motivation of this Ph.D. work is to provide fundamental understanding of the effect of oxide-supported graphene on the metal-support interaction using model catalysts. In order to achieve this object, a comparative study between metal particles directly deposited on bare oxide and graphene-covered oxides is performed and particular focus is given to the impact of the in-between graphene layer in tuning the metal-support interactions.

The studied system consists of Co and Pt-Co directly deposited by electron beam evaporation on bare and graphene covered ZnO, SiO_2 substrates. The choice of these two oxide supports was made based on three main criteria. The first was their relevance in practical applications since both are extensively used as supports for heterogeneous catalysts. The second reason was the knowledge that reducible oxides such as ZnO strongly interact with the metals, while irreducible oxides like SiO_2 are assumed to be relatively inert. Finally, it is relatively easy to fabricate model-planar substrates of these oxides with sufficient electronic conductivity, which is a prerequisite for electron-based analytical methods. On the other hand,

Co is an important transition metal which is widely used in catalysis, but in certain cases it suffers from deactivation due to the strong interaction between Co and the supports (e.g. ZnO and SiO₂). Thus, this work is trying to apply single layer graphene as a buffer layer to modify Co-oxide interaction, with a minimum fingerprint in the macroscopic properties of the catalyst (e.g. thermal conductivity, mechanical properties etc.). The experiments are carried out in three different Ultra High Vacuum (UHV) setups and the surface composition and chemical state are studied mainly by *in-situ* surface techniques such as X-ray photoelectron spectroscopy (XPS) and High resolution electron energy loss spectroscopy (HREELS). In order to get the information of surface morphology and the properties of graphene, *ex-situ* techniques such as Raman spectroscopy (Raman) and atomic force microscopy (AFM) have also been applied.

Specific aim of this thesis is to understand (1) the graphene's effect on the interaction of Co with inert and reactive oxides (2) the modification of the redox properties of Co in the two cases and (3) the stability of graphene in these systems. The details of the above mentioned topics are organized as follows:

Details about the materials preparation, characterization and experimental methods will be given in Chapter 2. The principal theoretic principles of the relevant techniques are also included in the same chapter.

- The investigation of Co nanoparticles supported on ZnO(0001) (Co/ZnO) and on Graphene-ZnO(0001) (Co/G-ZnO) substrates will be demonstrated in Chapter 3. The Co and ZnO interaction was studied *in situ* by annealing the samples in UHV conditions and performing quantitative and chemical surface analysis by XPS.
- Chapter 4 includes the results of oxidation/reduction properties of Co supported on different substrates, including ZnO, Graphene-ZnO, SiO₂, Graphene-SiO₂ and HOPG. The experiments were carried out under low and medium pressure conditions.
- The graphene's effect to the interaction between a bimetallic system (Co-Pt) and the support will be given in Chapter 5.
- Chapter 6 summarizes the results of this thesis and provides an outlook for future research in this area.

1.5 References

- (1) Tauster, S. J.; Fung, S. C.; Garten, R. L. Strong Metal-Support Interactions. Group 8 Noble Metals Supported on Titanium Dioxide. *J. Am. Chem. Soc.* **1978**, *100* (1), 170–175.
- (2) Fu, Q.; Wagner, T. Interaction of Nanostructured Metal Overlayers with Oxide Surfaces. *Surf. Sci. Rep.* **2007**, *62* (11), 431–498.
- (3) Haller, G. L.; Resasco, D. E. Metal-Support Interaction: group VIII Metals and Reducible Oxides. *Adv. Catal.* **1989**, *36*, 173.
- (4) Vayenas, C. G. *Electrochemical Activation of Catalysis: Promotion, Electrochemical Promotion, and Metal-Support Interactions*; Springer Netherlands, 2001.
- (5) Goodman, D. W. Model Studies in Catalysis Using Surface Science Probes. *Chem. Rev.* **1995**, *95* (3), 523–536.
- (6) B.COQ. Metal-Support Interaction in Catalysis. In *Metal-Ligand Interactions in Chemistry, Physics and Biology*; Springer Netherlands, 2000; pp 49–71.
- (7) Mayrhofer, K. J. J.; Blizanac, B. B.; Arenz, M.; Stamenkovic, V. R.; Ross, P. N.; Markovic, N. M. The Impact of Geometric and Surface Electronic Properties of Pt-Catalysts on the Particle Size Effect in Electrocatalysis. *J. Phys. Chem. B* **2005**, *109* (30), 14433–14440.
- (8) Llorca, J.; Homs, N.; Sales, J.; Pilar Ram'irez de la Piscina. Efficient Production of Hydrogen over Supported Cobalt Catalysts from Ethanol Steam Reforming. *J. Catal.* **2002**, *209* (2), 306–317.
- (9) Khodakov, A. Y.; Chu, W.; Fongarland, P. Advances in the Development of Novel Cobalt Fischer – Tropsch Catalysts for Synthesis of Long-Chain Hydrocarbons and Clean Fuels. *Chem. Rev.* **2007**, *107* (5), 1692–1744.
- (10) Llorca, J.; de la Piscina, P. R.; Dalmon, J.-A.; Sales, J.; Homs, N. CO-Free Hydrogen from Steam-Reforming of Bioethanol over ZnO-Supported Cobalt Catalysts. *Appl. Catal. B Environ.* **2003**, *43* (4), 355–369.
- (11) Llorca, J.; Homs, N.; Ramirez de la Piscina, P. In Situ DRIFT-Mass Spectrometry Study of the Ethanol Steam-Reforming Reaction over Carbonyl-Derived Co/ZnO Catalysts. *J. Catal.* **2004**, *227* (2), 556–560.
- (12) Su, S. H.; Chen, H.; Lee, T.; Hsu, Y.; Huang, J. C. A. Thermally Activated Interaction of Co Growth with ZnO(10 $\bar{1}$ 0) Surface. *J. Phys. Chem. C* **2013**, *117*, 17540–17547.

- (13) Su, S. H.; Lai, J. H.; Chen, H.; Lee, T.; Hsu, Y.; Wang, R. L.; Huang, J. C. a. Elucidating the Structure and Chemical State of Co Growth on the ZnO(10 $\bar{1}$ 0) Surface. *J. Phys. Chem. C* **2012**, *116*, 9917–9924.
- (14) Law, Y. T.; Skála, T.; Piš, I.; Nehasil, V.; Vondráček, M.; Zafeiratos, S.; Skala, T.; Pis, I.; Nehasil, V.; Vondracek, M.; et al. Bimetallic Nickel–Cobalt Nanosized Layers Supported on Polar ZnO Surfaces: Metal–Support Interaction and Alloy Effects Studied by Synchrotron Radiation X-Ray Photoelectron Spectroscopy. *J. Phys. Chem. C* **2012**, *116* (18), 10048–10056.
- (15) Wöl, C. The Chemistry and Physics of Zinc Oxide Surfaces. *Prog. Surf. Sci.* **2007**, *82* (2-3), 55–120.
- (16) Dumont, J. a.; Mugumaoderha, M. C.; Ghijsen, J.; Thiess, S.; Drube, W.; Walz, B.; Tolkiehn, M.; Novikov, D.; de Groot, F. M. F.; Sporcken, R. Thermally Activated Processes at the Co/ZnO Interface Elucidated Using High Energy X-Rays. *J. Phys. Chem. C* **2011**, *115* (15), 7411–7418.
- (17) Hyman, M. P.; Martono, E.; Vohs, J. M. Studies of the Structure and Interfacial Chemistry of Co Layers on ZnO(0001). *J. Phys. Chem. C* **2010**, *114* (40), 16892–16899.
- (18) Law, Y. T.; Doh, W. H.; Luo, W.; Zafeiratos, S. A Comparative Study of Ethanol Reactivity over Ni, Co and NiCo-ZnO Model Catalysts. *J. Mol. Catal. A Chem.* **2014**, *381* (0), 89–98.
- (19) Yu, N.; Zhang, H.; Davidson, S. D.; Sun, J.; Wang, Y. Effect of ZnO Facet on Ethanol Steam Reforming over Co/ZnO. *Catal. Commun.* **2016**, *73*, 93–97.
- (20) Chu, X.; Liu, J.; Sun, B.; Dai, R.; Pei, Y.; Qiao, M.; Fan, K. Aqueous-Phase Reforming of Ethylene Glycol on Co/ZnO Catalysts Prepared by the Coprecipitation Method. *J. Mol. Catal. A Chem.* **2011**, *335* (1-2), 129–135.
- (21) Martin-Luengo, M. A.; Sermon, P. A.; Wang, Y. Reduction and State of Co in Co/ZnO Catalysts: Evidence of a Metal-Support Interaction. *J. Catal.* **1992**, *135* (1), 263–268.
- (22) Jablonski, J. M.; Wolcyrz, M.; Krajczyk, L. On Cobalt Silicate Formation during High-Temperature Calcination of Impregnated Cobalt / Silica Catalysts. *J. Catal.* **1998**, *173*, 530–534.
- (23) Min, B. K.; Santra, A. K.; Goodman, D. W. Understanding Silica-Supported Metal Catalysts: Pd/Silica as a Case Study. *Catal. Today* **2003**, *85*, 113–124.
- (24) Tunga, R. T.; Howarda, D. J.; Ohmia, S.; Caymaxa, M.; Maexa, K. Oxide Mediated Epitaxy of CoSi on Silicon. *Appl. Phys. Lett.* **1996**, *68* (June 1996), 3461–3463.

- (25) Gomoyunova, M. V.; Pronin, I. I.; Malygin, D. E.; Gall, N. R.; Vyalikh, D. V.; Molodtsov, S. L. Photoemission Study of Cobalt Interaction with the Oxidized Si(100)2×1 Surface. *Surf. Sci.* **2006**, *600* (12), 2449–2456.
- (26) Čechal, J.; Luksch, J.; Koňáková, K.; Urbánek, M.; Brandejsová, E.; Šikola, T. Morphology of Cobalt Layers on Native SiO₂ Surfaces at Elevated Temperatures: Formation of Co Islands. *Surf. Sci.* **2008**, *602* (15), 2693–2698.
- (27) Krajczyk, L. Spreading of Cobalt Phase and Silicate Formation in Co/SiO₂ Model Catalyst. *Catal. Letters* **2003**, *87* (April), 51–56.
- (28) Kondoh, E.; Donaton, R. a.; Jin, S.; Bender, H.; Vandervorst, W.; Maex, K. Interaction between Co and SiO₂. *Appl. Surf. Sci.* **1998**, *136* (1-2), 87–94.
- (29) Saib, A. M.; Borgna, A.; Loosdrecht, J. Van De; Berge, P. J. Van; Niemantsverdriet, J. W. In Situ Surface Oxidation Study of a Planar Co/SiO₂/Si (100) Model Catalyst with Nanosized Cobalt Crystallites under Model Fischer – Tropsch Synthesis Conditions. *J. Phys. Chem. B* **2006**, *110* (100), 8657–8664.
- (30) Saib, a. M.; Borgna, a.; van de Loosdrecht, J.; van Berge, P. J.; Geus, J. W.; Niemantsverdriet, J. W. Preparation and Characterisation of Spherical Co/SiO₂ Model Catalysts with Well-Defined Nano-Sized Cobalt Crystallites and a Comparison of Their Stability against Oxidation with Water. *J. Catal.* **2006**, *239* (2), 326–339.
- (31) Tavasoli, A.; Sadagiani, K.; Khorashe, F.; Seifkordi, A. A.; Rohani, A. A.; Nakhaeipour, A. Cobalt Supported on Carbon nanotubes—A Promising Novel Fischer–Tropsch Synthesis Catalyst. *Fuel Process. Technol.* **2008**, *89* (5), 491–498.
- (32) Bezemer, G. L.; Bitter, J. H.; Kuipers, H. P. C. E.; Oosterbeek, H.; Holewijn, J. E.; Xu, X.; Kapteijn, F.; Dillen, A J. Van; De Jong, K. P. Cobalt Particle Size Effects in the Fischer –Tropsch Reaction Studied with Carbon Nanofiber Supported Catalysts. *Energy* **2006**, No. 6, 11568–11569.
- (33) Wong, P. K. J.; De Jong, M. P.; Leonardus, L.; Siekman, M. H.; Van Der Wiel, W. G. Growth Mechanism and Interface Magnetic Properties of Co Nanostructures on Graphite. *Phys. Rev. B* **2011**, *84* (5), 1–6.
- (34) Appy, D.; Lei, H.; Wang, C.-Z.; Tringides, M. C.; Liu, D.-J.; Evans, J. W.; Thiel, P. A. Transition Metals on the (0001) Surface of Graphite: Fundamental Aspects of Adsorption, Diffusion, and Morphology. *Prog. Surf. Sci.* **2014**, *89* (3-4), 219–238.
- (35) Poon, S. W.; Pan, J. S.; Tok, E. S. Nucleation and Growth of Cobalt Nanostructures on Highly Oriented Pyrolytic Graphite. *Phys. Chem. Chem. Phys.* **2006**, *8* (28), 3326–3334.

- (36) Poon, S. W.; Wee, A. T. S.; Tok, E. S. Anomalous Scaling Behaviour of Cobalt Cluster Size Distributions on Graphite, Epitaxial Graphene and Carbon-Rich $(6\sqrt{3}\times 6\sqrt{3})R30^\circ$. *Surf. Sci.* **2012**, *606* (21-22), 1586–1593.
- (37) Prudnikova, G. V.; Vjatkin, A. G.; Ermakov, A. V.; Shikin, A. M.; Adamchuk, V. K. Surface Intercalation of Graphite by Lanthanum. *J. Electron Spectros. Relat. Phenomena* **1994**, *68*, 427–430.
- (38) Büttner, M.; Choudhury, P.; Karl Johnson, J.; Yates, J. T. Vacancy Clusters as Entry Ports for Cesium Intercalation in Graphite. *Carbon* **2011**, *49* (12), 3937–3952.
- (39) Novoselov, K. S.; Geim, A. K.; Morozov, S. V.; Jiang, D.; Zhang, Y.; Dubonos, S. V.; Grigorieva, I. V.; Firsov, A. A. Electric Field Effect in Atomically Thin Carbon Films. *Science* **2004**, *306* (5696), 666–669.
- (40) Novoselov, K. S.; Fal'ko, V. I.; Colombo, L.; Gellert, P. R.; Schwab, M. G.; Kim, K. A Roadmap for Graphene. *Nature* **2012**, *490* (7419), 192–200.
- (41) Geim, A. K.; Novoselov, K. S. The Rise of Graphene. *Nat. Mater.* **2007**, *6* (3), 183–191.
- (42) Eom, D.; Prezzi, D.; Rim, K. T.; Zhou, H.; Lefenfeld, M.; Xiao, S.; Nuckolls, C.; Hybertsen, M. S.; Heinz, T. F.; Flynn, G. W. Structure and Electronic Properties of Graphene Nanoislands on Co(0001). *Nano Lett.* **2009**, *9* (8), 2844–2848.
- (43) Gong, C.; Lee, G.; Shan, B.; Vogel, E. M.; Wallace, R. M.; Cho, K. First-Principles Study of Metal–graphene Interfaces. *J. Appl. Phys.* **2010**, *108* (12), 123711.
- (44) Swart, J. C. W.; van Steen, E.; Ciobică, I. M.; van Santen, R. A. Interaction of Graphene with FCC–Co(111). *Phys. Chem. Chem. Phys.* **2009**, *11* (5), 803–807.
- (45) Gao, M.; Pan, Y.; Huang, L.; Hu, H.; Zhang, L. Z.; Guo, H. M.; Du, S. X.; Gao, H. J. Epitaxial Growth and Structural Property of Graphene on Pt(111). *Appl. Phys. Lett.* **2011**, *98* (3), 3–6.
- (46) Weatherup, R. S.; D'Arsié, L.; Cabrero-Vilatela, A.; Caneva, S.; Blume, R.; Robertson, J.; Schlögl, R.; Hofmann, S. Long-Term Passivation of Strongly Interacting Metals with Single-Layer Graphene. *J. Am. Chem. Soc.* **2015**, jacs.5b08729.
- (47) Liang, Y.; Li, Y.; Wang, H.; Zhou, J.; Wang, J.; Regier, T.; Dai, H. Co_3O_4 Nanocrystals on Graphene as a Synergistic Catalyst for Oxygen Reduction Reaction. *Nat. Mater.* **2011**, *10* (10), 780–786.
- (48) Wang, X.; Song, L.; Yang, H.; Xing, W.; Lu, H.; Hu, Y. Cobalt Oxide/graphene Composite for Highly Efficient CO Oxidation and Its Application in Reducing the Fire Hazards of Aliphatic Polyesters. *J. Mater. Chem.* **2012**, *22* (8), 3426.

- (49) O'Hern, S. C.; Boutilier, M. S. H.; Idrobo, J.-C.; Song, Y.; Kong, J.; Laoui, T.; Atieh, M.; Karnik, R.; O'Hern, S. C.; Boutilier, M. S. H.; et al. Selective Ionic Transport through Tunable Subnanometer Pores in Single-Layer Graphene Membranes. *Nano Lett.* **2014**, *14* (3), 1234–1241.
- (50) Cui, L.; Pu, T.; Liu, Y.; He, X. Layer-by-Layer Construction of Graphene/cobalt Phthalocyanine Composite Film on Activated GCE for Application as a Nitrite Sensor. *Electrochim. Acta* **2013**, *88*, 559–564.
- (51) Chan, K. T.; Neaton, J. B.; Cohen, M. L. First-Principles Study of Metal Adatom Adsorption on Graphene. *Phys. Rev. B* **2008**, *77* (23), 1–12.
- (52) Liu, X.; Wang, C. Z.; Yao, Y. X.; Lu, W. C.; Hupalo, M.; Tringides, M. C.; Ho, K. M. Bonding and Charge Transfer by Metal Adatom Adsorption on Graphene. *Phys. Rev. B* **2011**, *83* (23), 235411.
- (53) Sevinçli, H.; Topsakal, M.; Durgun, E.; Ciraci, S. Electronic and Magnetic Properties of 3d Transition-Metal Atom Adsorbed Graphene and Graphene Nanoribbons. *Phys. Rev. B* **2008**, *77* (19), 195434.
- (54) Cao, C.; Wu, M.; Jiang, J.; Cheng, H.-P. Transition Metal Adatom and Dimer Adsorbed on Graphene: Induced Magnetization and Electronic Structures. *Phys. Rev. B* **2010**, *81* (20), 205424.
- (55) Liao, Q.; Zhang, H. J.; Wu, K.; Li, H. Y.; Bao, S. N.; He, P. Nucleation and Growth of Monodispersed Cobalt Nanoclusters on Graphene Moiré on Ru(0001). *Nanotechnology* **2011**, *22* (12), 125303.
- (56) Vo-Van, C.; Kassir-Bodon, Z.; Yang, H.; Coraux, J.; Vogel, J.; Pizzini, S.; Bayle-Guillemaud, P.; Chshiev, M.; Ranno, L.; Guisset, V.; et al. Ultrathin Epitaxial Cobalt Films on Graphene for Spintronic Investigations and Applications. *New J. Phys.* **2010**, *12* (10), 103040.
- (57) Gyamfi, M.; Eelbo, T.; Waśniowska, M.; Wiesendanger, R. Impact of Intercalated Cobalt on the Electronic Properties of Graphene on Pt(111). *Phys. Rev. B* **2012**, *85* (20), 205434.
- (58) Rougemaille, N.; N'Diaye, A. T.; Coraux, J.; Vo-Van, C.; Fruchart, O.; Schmid, A. K. Perpendicular Magnetic Anisotropy of Cobalt Films Intercalated under Graphene. *Appl. Phys. Lett.* **2012**, *101* (14), 142403.
- (59) Decker, R.; Brede, J.; Atodiresei, N.; Caciuc, V.; Blügel, S.; Wiesendanger, R. Atomic-Scale Magnetism of Cobalt-Intercalated Graphene. *Phys. Rev. B* **2013**, *87* (4), 041403.

- (60) Huang, L.; Pan, Y.; Pan, L.; Gao, M.; Xu, W.; Que, Y.; Zhou, H.; Wang, Y.; Du, S.; Gao, H. J. Intercalation of Metal Islands and Films at the Interface of Epitaxially Grown Graphene and Ru(0001) Surfaces. *Appl. Phys. Lett.* **2011**, *99* (16), 10–13.
- (61) Sicot, M.; Leicht, P.; Zusan, A.; Bouvron, S.; Zander, O.; Weser, M.; Dedkov, Y. S.; Horn, K.; Fonin, M. Size-Selected Epitaxial Nanoislands underneath Graphene Moiré on Rh(111). *ACS Nano* **2012**, *6* (1), 151–158.
- (62) Vlaic, S.; Kimouche, A.; Coraux, J.; Santos, B.; Locatelli, A.; Rougemaille, N. Cobalt Intercalation at the Graphene/Iridium(111) Interface: Influence of Rotational Domains, Wrinkles, and Atomic Steps. *Appl. Phys. Lett.* **2014**, *104* (10), 101602.
- (63) de Lima, L. H.; Landers, R.; de Siervo, A. Patterning Quasi-Periodic Co 2D-Clusters underneath Graphene on SiC(0001). *Chem. Mater* **2014**, *26* (14), 4172–4177.
- (64) Vita, H.; Böttcher, S.; Leicht, P.; Horn, K.; Shick, A. B.; M^aca, F. Electronic Structure and Magnetic Properties of Cobalt Intercalated in Graphene on Ir(111). *Phys. Rev. B* **2014**, *90* (16), 165432.
- (65) Drnec, J.; Vlaic, S.; Carlomagno, I.; Gonzalez, C. J.; Isern, H.; Carl^a F.; Fiala, R.; Rougemaille, N.; Coraux, J.; Felici, R. Surface Alloying upon Co Intercalation between Graphene and Ir(111). *Carbon* **2015**, *94*, 554–559.
- (66) Leong, W. S.; Nai, C. T.; Thong, J. T. L. What Does Annealing Do to Metal–Graphene Contacts? *Nano Lett.* **2014**, *14* (7), 3840–3847.
- (67) Gong, C.; McDonnell, S.; Qin, X.; Azcatl, A.; Dong, H.; Chabal, Y. J.; Cho, K.; Wallace, R. M. Realistic Metal–Graphene Contact Structures. *ACS Nano* **2014**, *8* (1), 642–649.
- (68) Iqbal, M. W. Z.; Singh, A. K.; Iqbal, M. W. Z.; Eom, J. Raman Fingerprint of Doping due to Metal Adsorbates on Graphene. *J. Phys. Condens. Matter* **2012**, *24* (33), 335301.
- (69) Wang, W. X.; Liang, S. H.; Yu, T.; Li, D. H.; Li, Y. B.; Han, X. F. The Study of Interaction between Graphene and Metals by Raman Spectroscopy. *J. Appl. Phys.* **2011**, *109* (7), 07C501.
- (70) Martono, E.; Vohs, J. M. Active Sites for the Reaction of Ethanol to Acetaldehyde on Co/YSZ(100) Model Steam Reforming Catalysts. *ACS Catal.* **2011**, *1* (10), 1414–1420.
- (71) Martono, E.; Vohs, J. M. Support Effects in Cobalt-Based Ethanol Steam Reforming Catalysts: Reaction of Ethanol on Co/CeO₂/YSZ(100) Model Catalysts. *J. Catal.* **2012**, *291*, 79–86.
- (72) Homs, N.; Llorca, J.; de la Piscina, P. R. Low-Temperature Steam-Reforming of Ethanol over ZnO-Supported Ni and Cu Catalysts. The Effect of Nickel and Copper Addition to ZnO-Supported Cobalt-Based Catalysts. *Catal. Today* **2006**, *116*, 361–366.

- (73) Casanovas, A.; Roig, M.; De Leitenburg, C.; Trovarelli, A.; Llorca, J. Ethanol Steam Reforming and Water Gas Shift over Co/ZnO Catalytic Honeycombs Doped with Fe, Ni, Cu, Cr and Na. *Int. J. Hydrogen Energy* **2010**, *35* (15), 7690–7698.
- (74) Casanovas, A.; de Leitenburg, C.; Trovarelli, A.; Llorca, J. Ethanol Steam Reforming and Water Gas Shift Reaction over Co–Mn/ZnO Catalysts. *Chem. Eng. J.* **2009**, *154* (1–3), 267–273.
- (75) Cai, W.; Ramírez de la Piscina, P.; Homs, N. Oxidative Steam Reforming of Bio-Butanol for Hydrogen Production: Effects of Noble Metals on Bimetallic CoM/ZnO Catalysts (M=Ru, Rh, Ir, Pd). *Appl. Catal. B Environ.* **2014**, *145*, 56–62.
- (76) Cai, W.; Homs, N.; Ramirez de la Piscina, P. Efficient Hydrogen Production from Bio-Butanol Oxidative Steam Reforming over Bimetallic Co–Ir/ZnO Catalysts. *Green Chem.* **2012**, *14* (4), 1035.
- (77) Chiou, J. Y. Z.; Wang, W. Y.; Yang, S. Y.; Lai, C. L.; Huang, H. H.; Wang, C. Bin. Ethanol Steam Reforming to Produce Hydrogen over Co/ZnO and PtCo/ZnO Catalysts. *Catal. Letters* **2013**, *143*, 501–507.
- (78) Banach, B.; MacHocki, A.; Rybak, P.; Denis, A.; Grzegorzczak, W.; Gac, W. Selective Production of Hydrogen by Steam Reforming of Bio-Ethanol. *Catal. Today* **2011**, *176* (1), 28–35.
- (79) Galetti, A. E.; Gomez, M. F.; Arrua, L. a.; Marchi, A. J.; Abello, M. C. Study of CuCoZnAl Oxide as Catalyst for the Hydrogen Production from Ethanol Reforming. *Catal. Commun.* **2008**, *9* (6), 1201–1208.
- (80) Barroso, M. N.; Gomez, M. F.; Arrúa, L. A.; Abello, M. C. CoZnAl Catalysts for Ethanol Steam Reforming Reaction. *Chem. Eng. J.* **2010**, *158*, 225–232.
- (81) Kraleva, E.; Sokolov, S.; Schneider, M.; Ehrich, H. Support Effects on the Properties of Co and Ni Catalysts for the Hydrogen Production from Bio-Ethanol Partial Oxidation. *Int. J. Hydrogen Energy* **2013**, *38* (11), 4380–4388.
- (82) Banach, B.; Machocki, A. Effect of Potassium Addition on a Long Term Performance of Co–ZnO–Al₂O₃ Catalysts in the Low-Temperature Steam Reforming of Ethanol: Co-Precipitation vs Citrate Method of Catalysts Synthesis. *Appl. Catal. A Gen.* **2015**, *505*, 173–182.
- (83) Sun, S.; Fujimoto, K.; Yoneyama, Y.; Tsubaki, N. Fischer–Tropsch Synthesis Using Co/SiO₂ Catalysts Prepared from Mixed Precursors and Addition Effect of Noble Metals. *Fuel* **2002**, *81* (11–12), 1583–1591.

- (84) Vada, S.; Hoff, A.; AdnaneS, E.; Schanke, D.; Holmen, A. Fischer-Tropsch Synthesis on Supported Cobalt Catalysts Promoted by Platinum and Rhenium. *Top. Catal.* **1995**, 2 (1-4), 155–162.
- (85) Jacobs, G.; Ji, Y.; Davis, B. H.; Cronauer, D.; Kropf, A. J.; Marshall, C. L. Fischer–Tropsch Synthesis: Temperature Programmed EXAFS/XANES Investigation of the Influence of Support Type, Cobalt Loading, and Noble Metal Promoter Addition to the Reduction Behavior of Cobalt Oxide Particles. *Appl. Catal. A Gen.* **2007**, 333 (2), 177–191.
- (86) Hong, J.; Chernavskii, P. a.; Khodakov, A. Y.; Chu, W. Effect of Promotion with Ruthenium on the Structure and Catalytic Performance of Mesoporous Silica (smaller and Larger Pore) Supported Cobalt Fischer-Tropsch Catalysts. *Catal. Today* **2009**, 140 (3-4), 135–141.
- (87) Diehl, F.; Khodakov, A. Y. Promotion of Cobalt Fischer-Tropsch Catalysts with Noble Metals: A Review. *Oil Gas Sci. Technol.* **2009**, 64 (1), 11–24.
- (88) Schanke, D.; Vada, S.; Blekkan, E. A.; Hilmen, A. M.; Hoff, A.; Holmen, A. Study of Pt-Promoted Cobalt CO Hydrogenation Catalysts. *J. Catal.* **1995**, 156 (1), 85–95.
- (89) Okabe, K.; Li, X.; Wei, M.; Arakawa, H. Fischer–Tropsch Synthesis over Co–SiO₂ Catalysts Prepared by the Sol–gel Method. *Catal. Today* **2004**, 89 (4), 431–438.
- (90) Dees, M. J.; Ponec, V. The Influence of Sulfur and Carbonaceous Deposits on the Selectivity and Activity of Pt/Co Catalysts in Hydrocarbon Reactions. *J. Catal.* **1989**, 119 (2), 376–387.
- (91) Hilmen, A. M.; Schanke, D.; Hanssen, K. F.; Holmen, A. Study of the Effect of Water on Alumina Supported Cobalt Fischer–Tropsch Catalysts. *Appl. Catal. A Gen.* **1999**, 186 (1-2), 169–188.
- (92) Jacobs, G.; Patterson, P. M.; Zhang, Y.; Das, T.; Li, J.; Davis, B. H. Fischer–Tropsch Synthesis: Deactivation of Noble Metal-Promoted Co/Al₂O₃ Catalysts. *Appl. Catal. A Gen.* **2002**, 233 (1-2), 215–226.
- (93) Dalai, A. K.; Davis, B. H. Fischer–Tropsch Synthesis: A Review of Water Effects on the Performances of Unsupported and Supported Co Catalysts. *Appl. Catal. A Gen.* **2008**, 348 (1), 1–15.
- (94) Jacobs, G.; Das, T. K.; Zhang, Y.; Li, J.; Racoillet, G.; Davis, B. H. Fischer-Tropsch Synthesis: Support, Loading, and Promoter Effects on the Reducibility of Cobalt Catalysts. *Appl. Catal. A Gen.* **2002**, 233 (1-2), 263–281.

- (95) Lebarbier, V. M.; Mei, D.; Kim, D. H.; Andersen, A.; Male, J. L.; Holladay, J. E.; Rousseau, R.; Wang, Y. Effects of La_2O_3 on the Mixed Higher Alcohols Synthesis from Syngas over Co Catalysts: A Combined Theoretical and Experimental Study. *J. Phys. Chem. C* **2011**, *115* (35), 17440–17451.
- (96) Ernst, B.; Hilaire, L.; Kiennemann, A. Effects of Highly Dispersed Ceria Addition on Reducibility, Activity and Hydrocarbon Chain Growth of a Co/SiO_2 Fischer–Tropsch Catalyst. *Catal. Today* **1999**, *50* (2), 413–427.
- (97) Riedel, T.; Claeys, M.; Schulz, H.; Schaub, G.; Nam, S.-S.; Jun, K.-W.; Choi, M.-J.; Kishan, G.; Lee, K.-W. Comparative Study of Fischer–Tropsch Synthesis with H_2/CO and H_2/CO_2 Syngas Using Fe- and Co-Based Catalysts. *Appl. Catal. A Gen.* **1999**, *186* (1-2), 201–213.
- (98) Huffman, G. P.; Shah, N.; Zhao, J. M.; Huggins, F. E.; Hoost, T. E.; Halvorsen, S.; Goodwin, J. G. In-Situ XAFS Investigation of K-Promoted Co Catalysts. *J. Catal.* **1995**, *151* (1), 17–25.
- (99) Oukaci, R.; Singleton, A. H.; Goodwin, J. G. Comparison of Patented Co F–T Catalysts Using Fixed-Bed and Slurry Bubble Column Reactors. *Appl. Catal. A Gen.* **1999**, *186*, 129–144.
- (100) Haddad; Chen, B.; Goodwin, J. G. Characterization of La^{3+} -Promoted Co/SiO_2 Catalysts. *J. Catal.* **1996**, *51* (0122), 43–51.
- (101) Tan, B. J.; Klabunde, K. J.; Tanaka, T.; Kanai, H.; Yoshida, S. An EXAFS Study of Cobalt-Manganese/Silica Bimetallic Solvated Metal Atom Dispersed (SMAD) Catalysts. *J. Am. Chem. Soc.* **1988**, *110* (18), 5951–5958.
- (102) Zhang, B.; Dang Sheng Su. Probing the Metal – Support Interaction in Carbon-Supported Catalysts by Using Electron Microscopy. *ChemCatChem* **2015**, *110016*, 3639–3645.
- (103) Trépanier, M.; Tavasoli, A.; Dalai, A. K.; Abatzoglou, N. Fischer–Tropsch Synthesis over Carbon Nanotubes Supported Cobalt Catalysts in a Fixed Bed Reactor: Influence of Acid Treatment. *Fuel Process. Technol.* **2009**, *90* (3), 367–374.
- (104) Eschemann, T. O.; Lamme, W. S.; Manchester, R. L.; Parmentier, T. E.; Cognigni, A.; Rønning, M.; de Jong, K. P. Effect of Support Surface Treatment on the Synthesis , Structure , and Performance of Co/CNT Fischer – Tropsch Catalysts. *J. Catal.* **2015**, *328*, 130–138.

- (105) Davari, M.; Karimi, S.; Tavasoli, A.; Karimi, A. Enhancement of Activity , Selectivity and Stability of CNTs-Supported Cobalt Catalyst in Fischer-Tropsch via CNTs Functionalization. *Appl. Catal. A Gen.* **2014**, *485*, 133–142.
- (106) Wang, H.; Maiyalagan, T.; Wang, X. Review on Recent Progress in Nitrogen-Doped Graphene: Synthesis, Characterization, and Its Potential Applications. *ACS Catal.* **2012**, *2* (5), 781–794.
- (107) Yang, Y.; Jia, L.; Hou, B.; Li, D.; Wang, J.; Sun, Y. The Correlation of Interfacial Interaction and Catalytic Performance of N-Doped Mesoporous Carbon Supported Cobalt Nanoparticles for Fischer-Tropsch Synthesis. *J. Phys. Chem. C* **2014**, *118* (1), 268–277.
- (108) Karimi, S.; Tavasoli, A.; Mortazavi, Y.; Karimi, A. Cobalt Supported on Graphene–A Promising Novel Fischer–Tropsch Synthesis Catalyst. *Appl. Catal. A Gen.* **2015**.
- (109) Karimi, S.; Tavasoli, A.; Mortazavi, Y.; Karimi, A. Enhancement of Cobalt Catalyst Stability in Fischer-Tropsch Synthesis Using Graphene Nanosheets as Catalyst Support. *Chem. Eng. Res. Des.* **2015**.
- (110) Sun, B.; Jiang, Z.; Fang, D.; Xu, K.; Pei, Y.; Yan, S.; Qiao, M.; Fan, K.; Zong, B. One-Pot Approach to a Highly Robust Iron Oxide/Reduced Graphene Oxide Nanocatalyst for Fischer-Tropsch Synthesis. *ChemCatChem* **2013**, *5* (3), 714–719.
- (111) Moussa, S. O.; Panchakarla, L. S.; Ho, M. Q.; El-Shall, M. S. Graphene-Supported, Iron-Based Nanoparticles for Catalytic Production of Liquid Hydrocarbons from Synthesis Gas: The Role of the Graphene Support in Comparison with Carbon Nanotubes. *ACS Catal.* **2014**, *4* (2), 535–545.
- (112) Peierls, R. Quelques Propriétés Typiques Des Corps Solides. *Ann. l'institut Henri Poincaré* **1935**.
- (113) Landau, L. Zur Theorie Der Phasenumwandlungen II. *Phys. Z. Sowjetunion* **1937**.
- (114) Evans, J. W.; Thiel, P. A.; Bartelt, M. C. Morphological Evolution during Epitaxial Thin Film Growth: Formation of 2D Islands and 3D Mounds. *Surf. Sci. Rep.* **2006**, *61* (1-2), 1–128.
- (115) Venables, J. A.; Spiller, G. D. T.; Hanbucken, M. Nucleation and Growth of Thin Films. *Reports Prog. Phys.* **1984**, *47* (4), 399–459.
- (116) Novoselov, K. S.; Jiang, D.; Schedin, F.; Booth, T. J.; Khotkevich, V. V; Morozov, S. V; Geim, A. K. Two-Dimensional Atomic Crystals. *Proc. Natl. Acad. Sci. U. S. A.* **2005**, *102* (30), 10451–10453.

- (117) Novoselov, K. S.; Geim, A. K.; Morozov, S. V.; Jiang, D.; Katsnelson, M. I.; Grigorieva, I. V.; Dubonos, S. V.; Firsov, A. A. Two-Dimensional Gas of Massless Dirac Fermions in Graphene. *Nature* **2005**, *438* (7065), 197–200.
- (118) Zhang, Y.; Tan, Y.-W.; Stormer, H. L.; Kim, P. Experimental Observation of the Quantum Hall Effect and Berry's Phase in Graphene. *Nature* **2005**, *438* (7065), 201–204.
- (119) Morozov, S. V.; Novoselov, K. S.; Katsnelson, M. I.; Schedin, F.; Elias, D. C.; Jaszczak, J. A.; Geim, A. K. Giant Intrinsic Carrier Mobilities in Graphene and Its Bilayer. *Phys. Rev. Lett.* **2008**, *100* (1), 11–14.
- (120) Chen, J.-H.; Jang, C.; Xiao, S.; Ishigami, M.; Fuhrer, M. S. Intrinsic and Extrinsic Performance Limits of Graphene Devices on SiO₂. *Nat. Nanotechnol.* **2008**, *3* (4), 206–209.
- (121) Bolotin, K. I.; Sikes, K. J.; Hone, J.; Stormer, H. L.; Kim, P. Temperature-Dependent Transport in Suspended Graphene. *Phys. Rev. Lett.* **2008**, *101* (9), 096802.
- (122) Du, X.; Skachko, I.; Barker, A.; Andrei, E. Y. Approaching Ballistic Transport in Suspended Graphene. *Nat. Nanotechnol.* **2008**, *3* (8), 491–495.
- (123) Lee, C.; Wei, X.; Kysar, J. W.; Hone, J. Measurement of the Elastic Properties and Intrinsic Strength of Monolayer Graphene. *Science* **2008**, *321* (5887), 385–388.
- (124) Balandin, A. A.; Ghosh, S.; Bao, W.; Calizo, I.; Teweldebrhan, D.; Miao, F.; Lau, C. N. Superior Thermal Conductivity of Single-Layer Graphene. *Nano Lett.* **2008**, *8* (3), 902–907.
- (125) Moser, J.; Barreiro, A.; Bachtold, A. Current-Induced Cleaning of Graphene. *Appl. Phys. Lett.* **2007**, *91* (16), 163513.
- (126) Bunch, J. S.; Verbridge, S. S.; Alden, J. S.; van der Zande, A. M.; Parpia, J. M.; Craighead, H. G.; McEuen, P. L. Impermeable Atomic Membranes from Graphene Sheets. *Nano Lett.* **2008**, *8* (8), 2458–2462.
- (127) Han, M.; Özyilmaz, B.; Zhang, Y.; Kim, P. Energy Band-Gap Engineering of Graphene Nanoribbons. *Phys. Rev. Lett.* **2007**, *98* (20), 206805.
- (128) Cai, J.; Pignedoli, C. A.; Talirz, L.; Ruffieux, P.; Söde, H.; Liang, L.; Meunier, V.; Berger, R.; Li, R.; Feng, X.; et al. Graphene Nanoribbon Heterojunctions. *Nat. Nanotechnol.* **2014**, *9* (11), 896–900.
- (129) Chen, Y.-C.; Cao, T.; Chen, C.; Pedramrazi, Z.; Haberler, D.; de Oteyza, D. G.; Fischer, F. R.; Louie, S. G.; Crommie, M. F. Molecular Bandgap Engineering of Bottom-up Synthesized Graphene Nanoribbon Heterojunctions. *Nat. Nanotechnol.* **2015**, *10* (2), 156–160.

- (130) Ohta, T.; Bostwick, A.; Seyller, T.; Horn, K.; Rotenberg, E. Controlling the Electronic Structure of Bilayer Graphene. *Science* **2006**, *313* (5789), 951–954.
- (131) Oostinga, J.; Heersche, H.; Liu, X. Gate-Induced Insulating State in Bilayer Graphene Devices. *Nat. Mater.* **2008**, *7* (2), 151–157.
- (132) Elias, D.; Nair, R.; Mohiuddin, T. Control of Graphene's Properties by Reversible Hydrogenation: Evidence for Graphane. *Science* **2009**, *323* (5914), 610–613.
- (133) Zhan, D.; Yan, J. X.; Ni, Z. H.; Sun, L.; Lai, L. F.; Liu, L.; Liu, X. Y.; Shen, Z. X. Bandgap-Opened Bilayer Graphene Approached by Asymmetrical Intercalation of Trilayer Graphene. *Small* **2015**, *11* (9-10), 1177–1182.
- (134) Wang, J.; Liang, M.; Fang, Y.; Qiu, T.; Zhang, J.; Zhi, L. Rod-Coating: Towards Large-Area Fabrication of Uniform Reduced Graphene Oxide Films for Flexible Touch Screens. *Adv. Mater.* **2012**, *24* (21), 2874–2878.
- (135) Han, T. T.-H.; Lee, Y.; Choi, M.-R. M.; Woo, S. S.-H.; Bae, S.-H.; Hong, B. H.; Ahn, J.-H.; Lee, T.-W. Extremely Efficient Flexible Organic Light-Emitting Diodes with Modified Graphene Anode. *Nat. Photonics* **2012**, *6* (2), 105–110.
- (136) Wu, Y.; Jenkins, K.; Valdes-Garcia, A. State-of-the-Art Graphene High-Frequency Electronics. *Nano Lett.* **2012**, *12* (6), 3062–3067.
- (137) Wu, Y.; Lin, Y.; Bol, A.; Jenkins, K.; Xia, F. High-Frequency, Scaled Graphene Transistors on Diamond-like Carbon. *Nature* **2011**, *472* (7341), 74–78.
- (138) Lin, Y.; Dimitrakopoulos, C.; Jenkins, K. 100-GHz Transistors from Wafer-Scale Epitaxial Graphene. *Science* **2010**, *327* (5966), 662–662.
- (139) Singh, V.; Joung, D.; Zhai, L.; Das, S.; Khondaker, S. I.; Seal, S. Graphene Based Materials: Past, Present and Future. *Prog. Mater. Sci.* **2011**, *56* (8), 1178–1271.
- (140) Aïssa, B.; Memon, N. K.; Ali, A.; Khraisheh, M. K. Recent Progress in the Growth and Applications of Graphene as a Smart Material: A Review. *Front. Mater.* **2015**, *2*, 1–19.
- (141) Qu, L.; Liu, Y.; Baek, J.-B.; Dai, L. Nitrogen-Doped Graphene as Efficient Metal-Free Electrocatalyst for Oxygen Reduction in Fuel Cells. *ACS Nano* **2010**, *4* (3), 1321–1326.
- (142) Zhang, N.; Zhang, Y.; Pan, X.; Yang, M.-Q.; Xu, Y.-J. Constructing Ternary CdS–Graphene–TiO₂ Hybrids on the Flatland of Graphene Oxide with Enhanced Visible-Light Photoactivity for Selective Transformation. *J. Phys. Chem. C* **2012**, *116* (34), 18023–18031.
- (143) Zhou, X.; Qiao, J.; Yang, L.; Zhang, J. A Review of Graphene-Based Nanostructural Materials for Both Catalyst Supports and Metal-Free Catalysts in PEM Fuel Cell Oxygen Reduction Reactions. *Adv. Energy Mater.* **2014**, *4* (8), 1–25.

- (144) Mayorov, A. S.; Gorbachev, R. V.; Morozov, S. V.; Britnell, L.; Jalil, R.; Ponomarenko, L. A.; Blake, P.; Novoselov, K. S.; Watanabe, K.; Taniguchi, T.; et al. Micrometer-Scale Ballistic Transport in Encapsulated Graphene at Room Temperature. *Nano Lett.* **2011**, *11* (6), 2396–2399.
- (145) Dean, C. R.; Young, A. F.; Meric, I.; Lee, C.; Wang, L.; Sorgenfrei, S.; Watanabe, K.; Taniguchi, T.; Kim, P.; Shepard, K. L.; et al. Boron Nitride Substrates for High-Quality Graphene Electronics. *Nat. Nanotechnol.* **2010**, *5* (10), 722–726.
- (146) Gómez-Navarro, C.; Weitz, R. T.; Bittner, A. M.; Scolari, M.; Mews, A.; Burghard, M.; Kern, K. Electronic Transport Properties of Individual Chemically Reduced Graphene Oxide Sheets. *Nano Lett.* **2007**, *7* (11), 3499–3503.
- (147) Feng, H.; Cheng, R.; Zhao, X.; Duan, X.; Li, J. A Low-Temperature Method to Produce Highly Reduced Graphene Oxide. *Nat. Commun.* **2013**, *4*, 1539.
- (148) Hernandez, Y.; Nicolosi, V.; Lotya, M.; Blighe, F. M.; Sun, Z.; De, S.; McGovern, I. T.; Holland, B.; Byrne, M.; Gun'Ko, Y. K.; et al. High-Yield Production of Graphene by Liquid-Phase Exfoliation of Graphite. *Nat. Nanotechnol.* **2008**, *3* (9), 563–568.
- (149) Lotya, M.; Hernandez, Y.; King, P. J.; Smith, R. J.; Nicolosi, V.; Karlsson, L. S.; Blighe, F. M.; De, S.; Wang, Z.; McGovern, I. T.; et al. Liquid Phase Production of Graphene by Exfoliation of Graphite in Surfactant/Water Solutions. *J. Am. Chem. Soc.* **2009**, *131* (10), 3611–3620.
- (150) Brodie, B. Sur Le Poids Atomique Du Graphite. *Ann. Chim. Phys* **1860**.
- (151) Staudenmaier, L. Verfahren Zur Darstellung Der Graphitsäure. *Berichte der Dtsch. Chem. Gesellschaft* **1898**, *31* (2), 1481–1487.
- (152) Hummers, W. S.; Offeman, R. E. Preparation of Graphitic Oxide. *J. Am. Chem. Soc.* **1958**, *80* (6), 1339–1339.
- (153) Park, S.; Ruoff, R. S.; Engineering, M. Chemical Methods for the Production of Graphenes. *Nat. Nanotechnol.* **2009**, *4* (4), 217–224.
- (154) Segal, M. Selling Graphene by the Ton. *Nat. Nanotechnol.* **2009**, *4* (10), 612–614.
- (155) Li, X.; Cai, W.; An, J.; Kim, S.; Nah, J.; Yang, D.; Piner, R.; Velamakanni, A.; Jung, I.; Tutuc, E.; et al. Large-Area Synthesis of High-Quality and Uniform Graphene Films on Copper Foils. *Science* **2009**, *324* (5932), 1312–1314.
- (156) Sutter, P. W.; Flege, J.-I.; Sutter, E. A. Epitaxial Graphene on Ruthenium. *Nat. Mater.* **2008**, *7* (5), 406–411.
- (157) Coraux, J.; N'Diaye, A. T.; Busse, C.; Michely, T. Structural Coherency of Graphene on Ir(111). *Nano Lett.* **2008**, *8* (2), 565–570.

- (158) Ago, H.; Ito, Y.; Mizuta, N.; Yoshida, K.; Hu, B.; Orofeo, C. M.; Tsuji, M.; Ikeda, K.; Mizuno, S. Epitaxial Chemical Vapor Deposition Growth of Single-Layer Graphene over Cobalt Film Crystallized on Sapphire. *ACS Nano* **2010**, *4* (12), 7407–7414.
- (159) Liu, M.; Zhang, Y.; Chen, Y.; Gao, Y.; Gao, T.; Ma, D.; Ji, Q.; Zhang, Y.; Li, C.; Liu, Z. Thinning Segregated Graphene Layers on High Carbon Solubility Substrates of Rhodium Foils by Tuning the Quenching Process. *ACS Nano* **2012**, *6* (12), 10581–10589.
- (160) Chae, S.; Gunes, F.; Kim, K.; Kim, E.; Han, G. Synthesis of Large-Area Graphene Layers on Poly-Nickel Substrate by Chemical Vapor Deposition: Wrinkle Formation. *Adv. Mater.* **2009**, *21* (22), 2328–2333.
- (161) Losurdo, M.; Giangregorio, M. Graphene CVD Growth on Copper and Nickel: Role of Hydrogen in Kinetics and Structure. *Phys. Chem. Chem. Phys.* **2011**, *13* (46), 20836–20843.
- (162) Gao, L.; Ren, W.; Xu, H.; Jin, L.; Wang, Z.; Ma, T.; Ma, L.-P.; Zhang, Z.; Fu, Q.; Peng, L.-M.; et al. Repeated Growth and Bubbling Transfer of Graphene with Millimetre-Size Single-Crystal Grains Using Platinum. *Nat. Commun.* **2012**, *3*, 699.
- (163) An, X.; Liu, F.; Jung, Y. J.; Kar, S. Large-Area Synthesis of Graphene on Palladium and Their Raman Spectroscopy. *J. Phys. Chem. C* **2012**, *116* (31), 16412–16420.
- (164) Bae, S.; Kim, H.; Lee, Y.; Xu, X.; Park, J. Roll-to-Roll Production of 30-Inch Graphene Films for Transparent Electrodes. *Nat. Nanotechnol.* **2010**, *5*, 574–578.
- (165) Wang, Y.; Zheng, Y.; Xu, X.; Dubuisson, E.; Bao, Q. Electrochemical Delamination of CVD-Grown Graphene Film: Toward the Recyclable Use of Copper Catalyst. *ACS Nano* **2011**, *5* (12), 9927–9933.
- (166) Oznuluer, T.; Pince, E.; Polat, E. O.; Balci, O.; Salihoglu, O.; Kocabas, C. Synthesis of Graphene on Gold. *Appl. Phys. Lett.* **2011**, *98* (18), 183101.
- (167) Liu, N.; Fu, L.; Dai, B.; Yan, K.; Liu, X.; Zhao, R.; Zhang, Y.; Liu, Z. Universal Segregation Growth Approach to Wafer-Size Graphene from Non-Noble Metals. *Nano Lett.* **2011**, *11* (1), 297–303.
- (168) Chen, S.; Brown, L.; Levendorf, M.; Cai, W.; Ju, S.-Y.; Edgeworth, J.; Li, X.; Magnuson, C. W.; Velamakanni, A.; Piner, R. D.; et al. Oxidation Resistance of Graphene-Coated Cu and Cu/Ni Alloy. *ACS Nano* **2011**, *5* (2), 1321–1327.
- (169) Weatherup, R. S.; Bayer, B. C.; Blume, R.; Ducati, C.; Baehtz, C.; Schlögl, R.; Hofmann, S. In Situ Characterization of Alloy Catalysts for Low-Temperature Graphene Growth. *Nano Lett.* **2011**, *11* (10), 4154–4160.

- (170) Dai, B.; Fu, L.; Zou, Z.; Wang, M.; Xu, H.; Wang, S.; Liu, Z. Rational Design of a Binary Metal Alloy for Chemical Vapour Deposition Growth of Uniform Single-Layer Graphene. *Nat. Commun.* **2011**, *2*, 522.
- (171) Edwards, R. S.; Coleman, K. S. Graphene Synthesis: Relationship to Applications. *Nanoscale* **2013**, *5* (1), 38.
- (172) Zhang, Y. I.; Zhang, L.; Zhou, C. Graphene and Related Applications. *Acc. Chem. Res.* **2013**, *46*, 2329–2339.
- (173) Li, X.; Cai, W.; Colombo, L.; Ruoff, R. S. Evolution of Graphene Growth on Ni and Cu by Carbon Isotope Labeling. *Nano Lett.* **2009**, *9* (12), 4268–4272.
- (174) Li, X.; Zhu, Y.; Cai, W.; Borysiak, M.; Han, B.; Chen, D.; Piner, R. D.; Colombo, L.; Ruoff, R. S. Transfer of Large-Area Graphene Films for High-Performance Transparent Conductive Electrodes. *Nano Lett.* **2009**, *9* (12), 4359–4363.
- (175) Kim, K. S.; Zhao, Y.; Jang, H.; Lee, S. Y.; Kim, J. M.; Kim, K. S.; Ahn, J.-H.; Kim, P.; Choi, J.-Y.; Hong, B. H. Large-Scale Pattern Growth of Graphene Films for Stretchable Transparent Electrodes. *Nature* **2009**, *457* (7230), 706–710.
- (176) Suk, J. W.; Kitt, A.; Magnuson, C. W.; Hao, Y. F.; Ahmed, S.; An, J. H.; Swan, A. K.; Goldberg, B. B.; Ruoff, R. S. Transfer of CVD-Grown Monolayer Graphene onto Arbitrary Substrates. *ACS Nano* **2011**, *5* (9), 6916–6924.
- (177) Strupinski, W.; Grodecki, K.; Wyszomolek, a.; Stepniowski, R.; Szkopek, T.; Gaskell, P. E.; Grüneis, A.; Haberer, D.; Bozek, R.; Krupka, J.; et al. Graphene Epitaxy by Chemical Vapor Deposition on SiC. *Nano Lett.* **2011**, *11*, 1786–1791.
- (178) Medina, H.; Lin, Y. C.; Jin, C. H.; Lu, C. C.; Yeh, C. H.; Huang, K. P.; Suenaga, K.; Robertson, J.; Chiu, P. W. Metal-Free Growth of Nanographene on Silicon Oxides for Transparent Conducting Applications. *Adv. Funct. Mater.* **2012**, *22* (10), 2123–2128.
- (179) Hwang, J.; Kim, M.; Campbell, D.; Alsalman, H. A.; Kwak, J. Y.; Shivaraman, S.; Woll, A. R.; Singh, A. K.; Hennig, R. G.; Gorantla, S.; et al. Van Der Waals Epitaxial Growth of Graphene on Sapphire by Chemical Vapor Deposition without a Metal Catalyst. *ACS Nano* **2012**, *7* (1), 385–395.
- (180) Dato, A.; Frenklach, M. Substrate-Free Microwave Synthesis of Graphene: Experimental Conditions and Hydrocarbon Precursors. *New J. Phys.* **2010**, *12*, 1–24.
- (181) Chen, B.; Huang, H.; Ma, X.; Huang, L.; Zhang, Z.; Peng, L. How Good Can CVD-Grown Monolayer Graphene Be? *Nanoscale* **2014**, *6* (24), 15255–15261.
- (182) Obraztsov, A. N. Chemical Vapour Deposition: Making Graphene on a Large Scale. *Nat. Nanotechnol.* **2009**, *4* (4), 212–213.

- (183) Hass, J.; de Heer, W. a; Conrad, E. H. The Growth and Morphology of Epitaxial Multilayer Graphene. *J. Phys. Condens. Matter* **2008**, *20* (32), 323202.
- (184) Sprinkle, M.; Siegel, D.; Hu, Y.; Hicks, J.; Tejada, A.; Taleb-Ibrahimi, A.; Le Fèvre, P.; Bertran, F.; Vizzini, S.; Enriquez, H.; et al. First Direct Observation of a Nearly Ideal Graphene Band Structure. *Phys. Rev. Lett.* **2009**, *103* (22), 1–4.
- (185) Hicks, J.; Shepperd, K.; Wang, F.; Conrad, E. H. The Structure of Graphene Grown on the SiC (000 $\bar{1}$) Surface. *J. Phys. D. Appl. Phys.* **2012**, *45* (15), 154002.
- (186) Riedl, C.; Coletti, C.; Starke, U. Structural and Electronic Properties of Epitaxial Graphene on SiC(0001): A Review of Growth, Characterization, Transfer Doping and Hydrogen Intercalation. *J. Phys. D. Appl. Phys.* **2010**, *43* (37), 374009.
- (187) Srivastava, N.; He, G.; Mende, P. C.; Feenstra, R. M.; Sun, Y.; Luxmi. Graphene Formed on SiC under Various Environments: Comparison of Si-Face and C-Face. *J. Phys. D. Appl. Phys.* **2011**, *45* (M1), 21.
- (188) Nemec, L.; Lazarevic, F.; Rinke, P.; Scheffler, M.; Blum, V. Why Graphene Growth Is Very Different on the C Face than on the Si Face of SiC: Insights from Surface Equilibria and the (3 \times 3)-3C-SiC($\bar{1}\bar{1}\bar{1}$) Reconstruction. *Phys. Rev. B* **2015**, *91* (16), 161408.
- (189) Aristov, V. Y.; Urbanik, G.; Kummer, K.; Vyalikh, D. V; Molodtsova, O. V; Preobrajenski, A. B.; Zakharov, A. A.; Hess, C.; Hänke, T.; Büchner, B.; et al. Graphene Synthesis on Cubic SiC/Si Wafers. Perspectives for Mass Production of Graphene-Based Electronic Devices. *Nano Lett.* **2010**, *10* (3), 992–995.
- (190) Ouerghi, A.; Kahouli, A.; Lucot, D.; Portail, M.; Travers, L.; Gierak, J.; Penuelas, J.; Jegou, P.; Shukla, A.; Chassagne, T.; et al. Epitaxial Graphene on Cubic SiC(111)Si(111) Substrate. *Appl. Phys. Lett.* **2010**, *96* (19), 191910.
- (191) Hasegawa, M.; Sugawara, K.; Suto, R.; Sambonsuge, S.; Teraoka, Y.; Yoshigoe, A.; Filimonov, S.; Fukidome, H.; Suemitsu, M. In Situ SR-XPS Observation of Ni-Assisted Low-Temperature Formation of Epitaxial Graphene on 3C-SiC/Si. *Nanoscale Res. Lett.* **2015**, *10* (1), 421.
- (192) Go, H.; Kwak, J.; Jeon, Y.; Kim, S.-D.; Cheol Lee, B.; Suk Kang, H.; Ko, J.-H.; Kim, N.; Kim, B.-K.; Yoo, J.-W.; et al. Low-Temperature Formation of Epitaxial Graphene on 6H-SiC Induced by Continuous Electron Beam Irradiation. *Appl. Phys. Lett.* **2012**, *101* (9), 092105.
- (193) Xu, Y.; Wu, X.; Ye, C.; Deng, Y.; Chen, T.; Ge, S. Growth of Few-Layer Graphene on SiC at Low Temperature with the Fluorocarbon Plasma Pre-Etching. *Thin Solid Films* **2013**, *527*, 65–68.

- (194) Yang, X.; Dou, X.; Rouhanipour, A.; Zhi, L.; Räder, H. J.; Müllen, K. Two-Dimensional Graphene Nanoribbons. *J. Am. Chem. Soc.* **2008**, *130* (13), 4216–4217.
- (195) Cai, J.; Ruffieux, P.; Jaafar, R.; Bieri, M.; Braun, T.; Blankenburg, S.; Muoth, M.; Seitsonen, A. P.; Saleh, M.; Feng, X.; et al. Atomically Precise Bottom-up Fabrication of Graphene Nanoribbons. *Nature* **2010**, *466* (7305), 470–473.
- (196) Hartley, C. S. Graphene Synthesis: Nanoribbons from the Bottom-Up. *Nat. Chem.* **2014**, *6* (2), 91–92.
- (197) Narita, A.; Feng, X.; Hernandez, Y.; Jensen, S. A.; Bonn, M.; Yang, H.; Verzhbitskiy, I. A.; Casiraghi, C.; Hansen, M. R.; Koch, A. H. R.; et al. Synthesis of Structurally Well-Defined and Liquid-Phase-Processable Graphene Nanoribbons. *Nat. Chem.* **2013**, *6* (2), 126–132.
- (198) Jiao, L.; Zhang, L.; Wang, X.; Diankov, G.; Dai, H. Narrow Graphene Nanoribbons from Carbon Nanotubes. *Nature* **2009**, *458* (7240), 877–880.
- (199) Kosynkin, D. V.; Higginbotham, A. L.; Sinitskii, A.; Lomeda, J. R.; Dimiev, A.; Price, B. K.; Tour, J. M. Longitudinal Unzipping of Carbon Nanotubes to Form Graphene Nanoribbons. *Nature* **2009**, *458* (7240), 872–876.
- (200) Li, Z.; Zhu, H.; Wang, K.; Wei, J.; Gui, X.; Li, X.; Li, C.; Fan, L.; Sun, P.; Wu, D. Ethanol Flame Synthesis of Highly Transparent Carbon Thin Films. *Carbon* **2011**, *49* (1), 237–241.
- (201) Li, Z.; Zhu, H.; Xie, D.; Wang, K.; Cao, A.; Wei, J.; Li, X.; Fan, L.; Wu, D. Flame Synthesis of Few-Layered Graphene/graphite Films. *Chem. Commun.* **2011**, *47* (12), 3520–3522.
- (202) Memon, N. K.; Tse, S. D.; Al-Sharab, J. F.; Yamaguchi, H.; Goncalves, A.-M. B.; Kear, B. H.; Jaluria, Y.; Andrei, E. Y.; Chhowalla, M. Flame Synthesis of Graphene Films in Open Environments. *Carbon* **2011**, *49* (15), 5064–5070.
- (203) Wei, D.; Xu, X. Laser Direct Growth of Graphene on Silicon Substrate. *Appl. Phys. Lett.* **2012**, *100* (2), 023110.
- (204) Zhang, H.; Feng, P. X. Fabrication and Characterization of Few-Layer Graphene. *Carbon* **2010**, *48* (2), 359–364.

Chapter 2

Experimental techniques

Chapter 2 Experimental techniques

An overview on the materials, methodology and experimental techniques used in this thesis will be given in this chapter. Most of the experiments were carried out in ultra-high vacuum (UHV), with X-ray photoelectron spectroscopy (XPS) being the primary technique used to study the surface composition and the chemical/oxidation state. Therefore, the principles of this technique will be explicitly discussed in the following part. A number of other characterization techniques were also used, including: Atomic force microscopy (AFM), Raman spectroscopy (Raman), Scanning electron microscopy (SEM), Low-energy ion scattering spectroscopy (LEIS), High Resolution Electron Energy Loss Spectroscopy (HREELS), to study the surface properties, morphologies of the materials and the quality of graphene.

2.1 Materials preparation

2.1.1 Preparation of substrates

The specimens studied in this work can be categorized into two types: 1) Metal particles (Co or CoPt) deposited on the bare planar substrates (SiO_2 , ZnO and highly oriented pyrolytic graphite, HOPG), 2) metal particles (Co or CoPt) deposited on the same substrates after being covered by single-layer graphene. The specimens containing metals directly deposited on oxides (type 1) are mainly used as reference materials for the graphene-based samples. A schematic of sample preparation are shown in Figure 2.1.

The Zn- terminated ZnO(0001)-Zn single crystals (one side polished, $10 \times 10 \times 0.33 \text{ mm}^3$) were purchased from CrysTec[®], GmbH Berlin/Germany and prior to any deposition (either graphene or directly metal particles) their surface was cleaned using a standard routine. This routine consists of Ar^+ sputtering (600 eV, typical sample ion current ca. $2 \mu\text{A}$) for 40 min to remove the surface impurities, followed by annealing at $400 \text{ }^\circ\text{C}$ first in UHV for 8 min and then in $5 \times 10^{-7} \text{ mbar O}_2$ for 2 min to restore the oxygen vacancies and to oxidize residual carbon impurities. This sputtering-annealing procedure was repeated for several cycles until no carbon could be detected by XPS. The SiO_2/Si wafers (p-type doped Si wafer with 300 nm of SiO_2

layer on top, $10 \times 10 \times 0.7 \text{ mm}^3$) were purchased from ACS Material[®], Medford/USA and were cleaned following the same sputtering-annealing procedure as with ZnO samples. The HOPG substrate ($10 \times 10 \times 2 \text{ mm}^3$) was cut and cleaved in air by scotch tape and immediately transferred into the UHV apparatus. It was cleaned by annealing in UHV for several hours at 400 °C to remove the adsorbed contaminations and the absence of foreign species was confirmed by XPS prior to metal deposition.

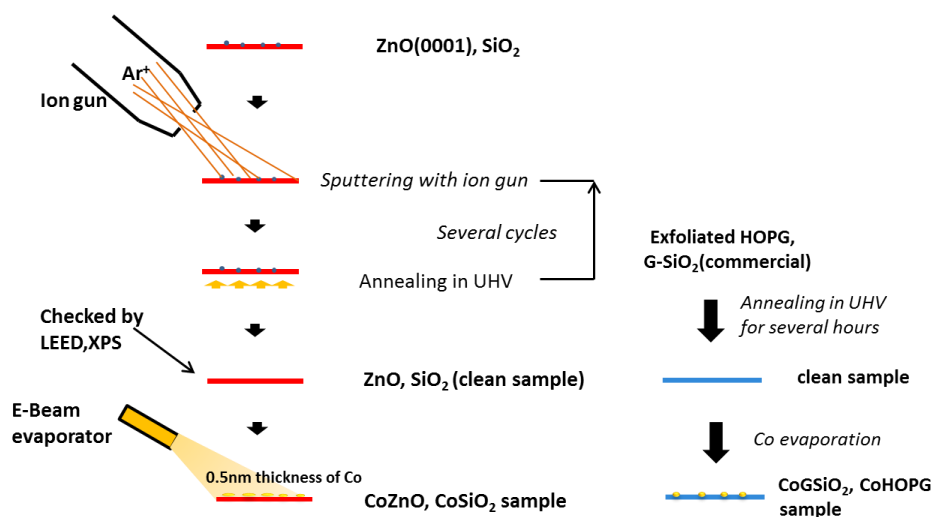


Figure 2.1 Schematic of sample preparation.

CVD-grown single layer graphene was received as a $10 \times 10 \text{ mm}^2$ Trivial Transfer Graphene[®] kit, from ACS Material[®] Medford/USA. Its production was made in four steps: 1) Monolayer graphene was grown on a copper foil, 2) deposition of Poly-methyl methacrylate (PMMA) and cure, 3) Cu removal by etching process, 4) wash of PMMA/Graphene in deionized water¹. This single-layer graphene was then transferred onto the UHV-cleaned ZnO (0001) substrate in air, based on the wetting transfer method previously reported by Suk et. al.² In particular, the single layer graphene sheet protected with a 0.5 μm PMMA layer that was released in deionized water, was “picked up” by the ZnO substrate. After that, the sample was dried under vacuum for 120 min and heated at 150 °C in air for 30 min to enable water evaporation and flattening of the graphene/PMMA film. Then the sample was set into anhydrous ethanol for 240 min to remove the PMMA layer. Ethanol was selected instead of the typically used acetone, to induce minimum modifications on the ZnO support, since it is less aggressive than acetone and evaporates without leaving carbon residues. The residual PMMA was removed by annealing in UHV at 350 °C for several hours and the cleanness of

the sample was verified by XPS. The quality of transferred graphene in each sample was confirmed by Raman spectroscopy.

Single layer graphene on SiO₂/Si substrate was also transferred by wetting transfer method from CVD grown single layer graphene. The difference with the ZnO based samples was that the transfer of graphene was not made in house, but in ACS Material[®] laboratory and the graphene/SiO₂/Si substrates were received as a commercial product. The as-received graphene/SiO₂/Si sample was subjected to a final cleaning step by annealing in UHV for several hours. Finally the quality and the cleanness of graphene were also checked by Raman and XPS.

2.1.2 Metal deposition

2.1.2.1 *Electron beam evaporation of Cobalt and Cobalt Platinum*

Cobalt and cobalt-platinum were directly deposited on the support by electron beam evaporation under UHV conditions. Electron beam evaporation uses an electron beam to melt and vaporize a target material. The metal vapor then expands into vacuum and condenses over the desired substrate. Before metal deposition, all substrates were cleaned as described in section 2.1.1.

A commercial e-beam evaporator (Mantis depositions Ltd., model: QUAD-EV-C) attached to the UHV set-up was used for Co and CoPt evaporation. The evaporator consists of four independent pockets, allowing simultaneous evaporation of up to four materials. The deposition metals (Co and Pt, 2 mm dia. wires 99.99 % purity, MaTeK[®], Germany) are placed opposite to a tungsten filament and a bias voltage of +2 kV is applied between them. When sufficient current is passed through the filament, it reaches the electron emission temperature and a stream of high-energy electrons is drawn from the filament towards the metal rod. The target metal rod is locally heated and evaporated. The pockets are inside a copper shroud which is water cooled to minimize outgassing. A manual shutter was used to control the deposition time and the evaporation rate was measured by integrated metal plates which collect the current of the ionized fraction of the evaporation steam for flux monitoring.

The Co-Pt deposition was performed by simultaneous co-evaporation of the two individual metals. The distance between the source head and the sample was 6 cm to ensure the overlapping of the beam coverage from each evaporation pocket on the target (sample). The thickness of the deposited metals was controlled by varying the deposition time. In order to

control the atomic ratio Co:Pt, the metal vapor flux was adjusted, keeping the same deposition time.

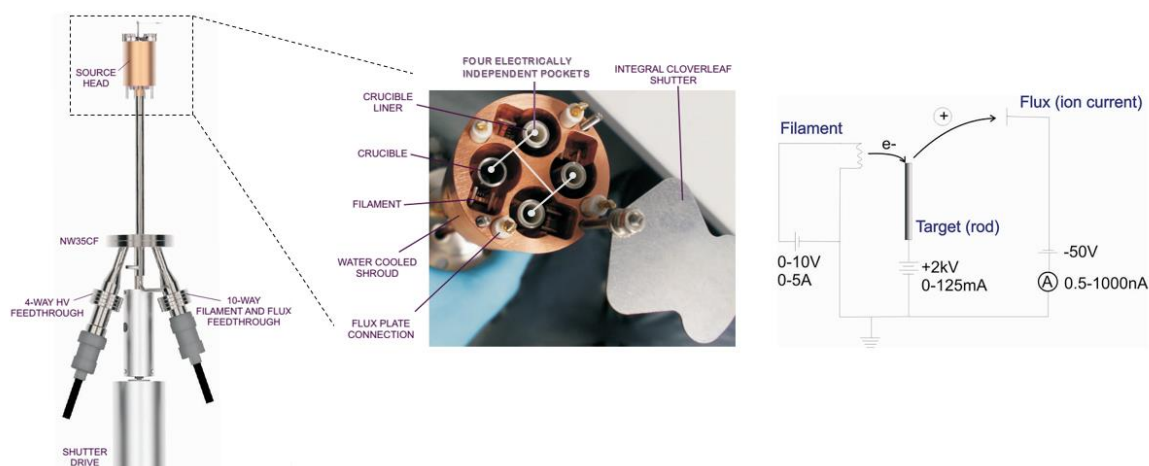


Figure 2.2 The construction and principle of the QUAD-EV-C evaporator. From^[3].

2.2 Characterization Methods

2.2.1 X-ray Photoemission Spectroscopy (XPS)

2.2.1.1 Basic principles

XPS is the principal characterization technique used to study the surface state of all samples in this thesis. XPS is a non-destructive analytical method which can provide information about the chemical state and composition on the surface. It is a rather surface sensitive technique with an average analysis depth between 2 to 5 nm, which is a critical surface region in catalytic reactions.

The principle of XPS is based on the observation that electrons eject from surfaces upon photons irradiation, as shown in Figure 2.3. This phenomenon is called photoelectric effect, and the ejected electrons are called photoelectrons. The kinetic energy (E_k) of these photoelectrons is given by Einstein's equation:

$$E_k = h\nu - E_B - \phi \quad (2.1)$$

where $h\nu$ is the photon energy, E_B is the binding energy of the photoelectron and ϕ is the work function of the sample. Electrical connection between the sample and the electron analyser simplifies this equation to $E_k = h\nu - E_B$.

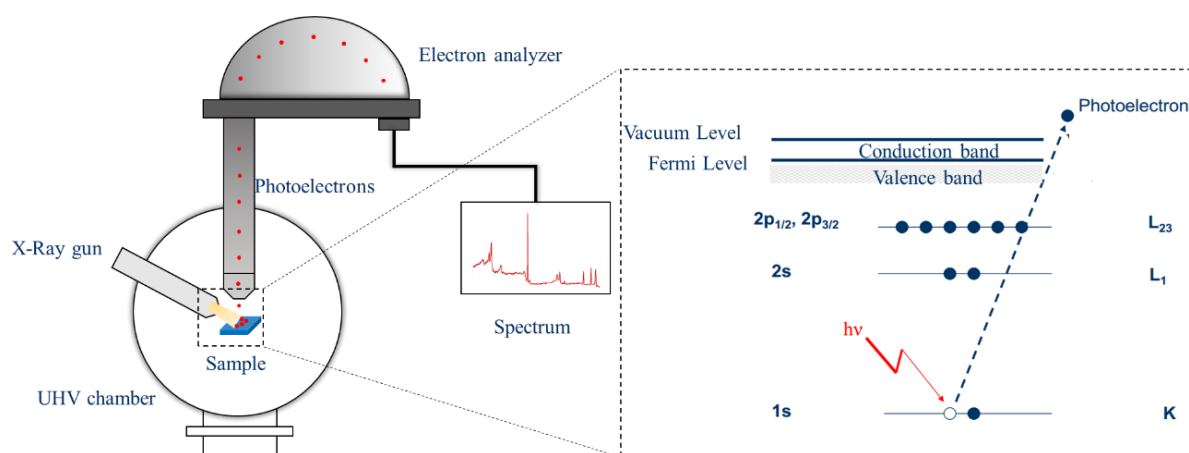


Figure 2.3 Schematic of an XPS system and principle of photoemission process

2.2.1.2 X-ray sources

Dual Al and Mg anode X-ray sources are typically used in lab-based XPS experiments, with X-ray photon energy of 1486.6 eV for Al $K\alpha$ and 1253.6 eV for Mg $K\alpha$. A schematic representation of a dual anode X-ray source is shown in Figure 2.4. X-ray photons with characteristic energy are generated when one of the two filaments (cathode) is heated and the emitted electrons are accelerated by a high voltage (about 15 kV) towards the anode. Inelastic electron-atom collisions on the anode produce an inner-shell ionization and when an electron from a higher level falls into the inner-shell vacancy (core hole) X-rays are generated. However, the core hole can be filled by electrons from other shells, meaning that the produced X-rays will not be monochromatic. If one considers Al for example, when exciting the K-shell (1s) of Al, the hole can be filled from the L_2 or L_3 (2p) sub-shells, leading to $K\alpha_1$ and $K\alpha_2$ lines, which are the most prominent of the X-ray emissions produced, but they tend to be described together as $K\alpha$ X-rays or $K\alpha_{1,2}$ X-rays due to their small energy separation.⁴ Electrons cannot come from the 2s shell, because a change in angular momentum is required in the quantum transition. The next shell with electrons is the valence band ($n = 3$) which gives rise to the widely separated and weak $K\beta$ lines. At the same time, Bremsstrahlung radiation (photons spanning some continuous energy range that arise from the deflection of electrons by surrounding charged particles), and other Auger electron emissions are also produced albeit to much lesser intensities.

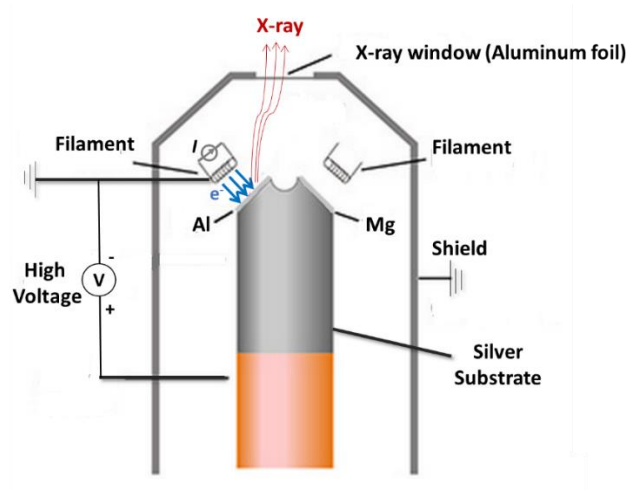


Figure 2.4 Schematic of a dual anode x-ray source.

Due to their low cost and the ease to switch between anode materials, dual Al and Mg anodes X-ray sources are the most commonly used in XPS. However, a wide X-ray line width with satellite lines and the continuum bremsstrahlung background affects the quality of XPS spectrum. In this case, the monochromatic X-ray sources were designed to provide better energy resolution and to remove background caused by satellites and bremsstrahlung. Figure 2.5 shows a schematic of the X-ray monochromator. A quartz single crystal is used to focus the X-rays and diffract an integer number of Al-K α_1 , Ag-L α_1 , Ti-K α_1 , and Cr -K β_1 X-ray wavelength along the direction which satisfies Bragg's law at Theta angle from crystal lattice, namely:

$$n\lambda = 2d \sin \theta \quad (2.2)$$

where n is the diffraction order, λ is the wavelength, d is the crystal atomic spacing, and θ is the angle of diffraction. Since λ of the AlK α_1 and K α_2 X-rays is different, the latter is filtered out. This, combined with a slight concavity introduced into the quartz crystal, results in a focused X-ray beam at the sample surface with a narrower energy spread than possible with a standard source. Both dual anode and monochromatic X-ray sources were used in this thesis, depending on the different UHV apparatus. The details can be found in the experimental part of each chapter.

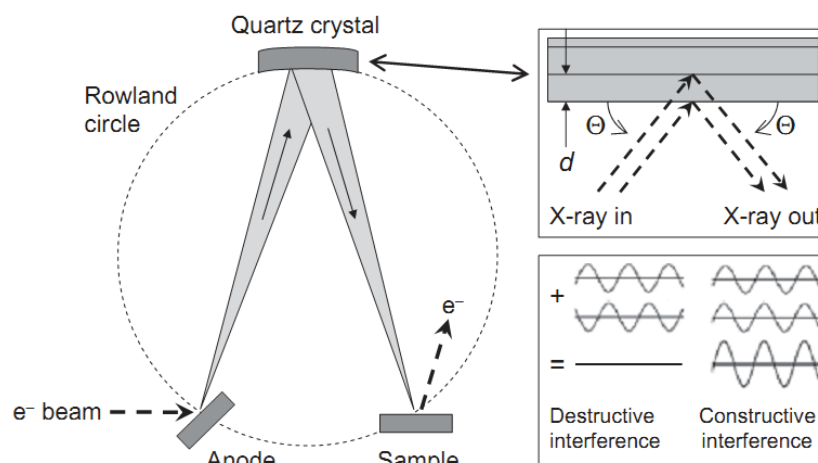


Figure 2.5 Schematic of a monochromatic geometry. From [4].

2.2.1.3 Electron Analyzer and Detector

An electron energy analyzer is used to measure the kinetic energy (E_k) of the emitted photoelectrons. The concentric hemispherical analyzer (CHA), also referred as hemispherical sector analyzer (HSA), is by far the most commonly used energy analyzer for XPS instruments and is also the one involved in this work. A scheme of the CHA is shown in Figure 2.6. It consists of two concentric hemispheres, with radius R_1 (inner hemisphere) and R_2 (outer hemisphere). The two hemispheres are negative polarized with potentials V_1 and V_2 ($V_2 > V_1$). The median equipotential surface between the hemispheres would have a value, V_0 given by:

$$V_0 = (V_1 R_1 + V_2 R_2) / 2R_0 \quad (2.3)$$

where R_0 is the radius of the median equipotential surface.

This means that only the electrons entering through the slit S with selected energy ($E = eV_0$) will follow the trajectory through the analyzer along the median equipotential surface of radius R_0 and will be focused at the exit slit, F. Otherwise, electrons with a kinetic energy not equal to eV_0 will follow a different trajectory and hit on the top or bottom hemisphere. The electrons are usually retarded through the lens system to a constant kinetic energy, commonly referred as pass energy (E_0), before they enter in the hemispheres. This mode is called fixed analyzer transmission (FAT) and it is the most commonly applied mode in XPS.

For the photoelectron detection, channel electron multipliers (CEM) were used. CEM has a horn-shaped continuous dynode structure (see Figure 2.6 right) which is coated in the internal face with an electron-emissive material (such as PbO). The electrons entering the opening of

the channeltron undergo multiple collisions with the channeltron's walls and produce secondary electrons. In this case, these electrons are accelerated into the horn by the potential difference which exists at both ends and at the end channeltrons are capable of electron gains of up to 10^8 .

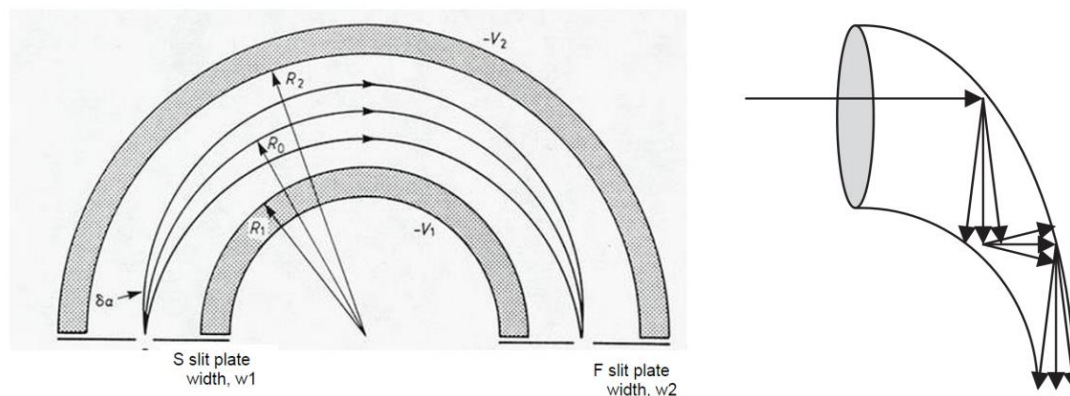


Figure 2.6 Schematic a concentric hemispherical analyzer (left) and channeltron detector (right). From [4].

2.2.1.4 XPS spectrum

By collecting the photoelectrons with the analyzer, multiplying with the detector, counting and analyzing the number of electrons versus its kinetic energy E_k (or binding energy, E_B) distribution, the XPS spectrum is obtained. The spectra over a relatively wide E_B range will give a signature of the elements as a function of their atomic number, thus providing elemental analysis. Moreover, the spectra allow identification of the E_B difference for a particular element present in different local chemical environment (the so-called chemical shift). This E_B difference depends on the initial state and final state of the atom. The initial state effects are induced by chemical bonding with other atoms or ions, while the final state effects are due to perturbation of the electronic structure resulting from photoelectron emission.

As an example, the XPS spectra of Co 2p at different oxidation states of Co are shown in Figure 2.7. The metallic Co spectrum shows two main peaks resulting from the spin-orbit splitting. The spin-orbit splitting arises from the coupling of the magnetic fields set up by an electron spinning around its own axis (defined by m_s) with that of an electron spinning around its nucleus (defined by l),⁴ since the 2p orbital of Co is a non-symmetric orbital ($l=1$) and m_s can have two possible configurations (+1/2 and -1/2), which gives rise to the splitting of two states. The total angular momentum (j , $j=l+m_s$) for p subshell is 3/2 and 1/2, which is shown as two peaks: Co2p_{3/2} and Co 2p_{1/2}, and since the degeneracy of j is $2j+1$, the ratio between the two peaks Co2p_{3/2}/Co 2p_{1/2} is 2/1.

For CoO and Co₃O₄, these two peaks shift to higher binding energy. It is known that the interactions between Co and O atoms which form Co-O chemical bonds depend only on the valence band levels, while the core levels are not directly involved in the bonding process. However, due to the coulomb interaction, the E_B of core electrons result from the attraction of the charged nucleus and the repulsion of the neighboring electrons. Since oxidized cobalt atoms donate electrons to oxygen atoms, the attraction from cobalt nucleus is distributed among fewer electrons per unit volume, and in this case, the binding energy of core electrons increases. Of course one should not overlook the effect of final state effects on the binding energy shifts, which might modify this trend.

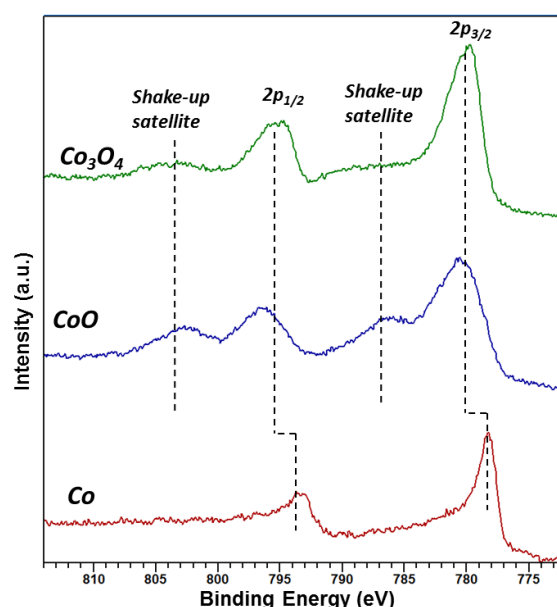


Figure 2.7 XPS spectra of Cobalt at different oxidation state.

The spectrum of CoO also shows additional satellite peaks at higher binding energy. These peaks arise from the shake-up processes which are explained by the transitions of valence electrons to the vacant orbitals above E_F due to photoemission. Since these processes decrease the E_k of the ejected photoelectrons, the satellite peaks appear at higher E_B with respect to the associated main photoelectron peaks by several eV. The high intensity of the satellite peaks of CoO is associated to the high-spin Co²⁺ in the lattice, which allows significant charge-transfer between cobalt 3d⁷ band with neighboring lattice oxygen.⁵ On the other hand, Co₃O₄ has weak satellite peaks. This is explained by the fact that the octahedrally coordinated Co³⁺ states do not contribute to charge transfer and therefore to shake-up processes; the remaining 1/3 Co cations are tetrahedrally coordinated Co²⁺ which give rise to the shake-up peaks of the spectrum.⁶

In this work, in the cases that peaks are overlapping, for example, mixture of CoO and Co₃O₄, the spectrum deconvolution was carried out using reference spectra of pure CoO and Co₃O₄ phases recorded at the same experimental set up. In this case, the peak area and consequently the ratio of the two components can be calculated.

2.2.1.5 Quantification

It is known that, from XPS spectra, the E_B value and the peak shape can provide information on the chemical state of the element. In addition, XPS can also be used for quantification, because the intensity (or area) of XPS peaks is directly related to the elemental stoichiometry of the sample. The XPS peak intensity measured in the experiment not only depends on the quantity of the chemical elements, but is also a function of other factors. In particular, it is related to i) the photoelectron cross section (the probability that photoionization of the certain core level is produced), ii) the inelastic mean free path (IMFP, the mean distance an electron of a specific E_k can travel in a particular solid before it interacts and loses energy to its surroundings), which is in turn related to the material and the photoelectron kinetic energy, iii) the sample morphology and the analyzer parameters and finally iv) the arrangement of the elements within the sample.^{7,8} The latter factor is a bottleneck of XPS results quantification, since appropriate quantification models which represent the sample morphology should be used. Models for various sample morphologies have been described in the literature, but notably their use is complicated by the complex mathematical formulas and more importantly by the need to be fed with exact geometric characteristics of the sample.⁷

In this work two commonly applied and relatively simplified quantification models were used. The metal overlayer thickness I_l , was calculated through quantification of XPS results based on a number of simplifying assumptions,⁹ suitable for flat and homogeneous samples with negligible elastic scattering of photoelectrons. The equation (2.4) reported in Ref⁹ can be utilized to calculate the average thickness of metal overlayer.

$$\frac{I_l}{I_s} = \frac{I_l^\infty}{I_s^\infty} \frac{1 - \exp(-t / \lambda_{in}^l(E_l) \cos \alpha)}{\exp(-t / \lambda_{in}^l(E_s) \cos \alpha)} \quad (2.4)$$

Where I_l and I_s are the photoelectron signal intensities of overlayer (l) and substrate (s), respectively, obtained from the XPS spectra. α is the photoelectron emission angle. The I_l^∞ and I_s^∞ are the signal intensities for infinitely thick layers of overlayer and substrate respectively. These values should be obtained from separate experiments (with the same

measurement conditions), in the same instrument. Alternatively the ratio of I_i^∞ / I_s^∞ can be obtained using theoretically-calculated semi-empirical atomic sensitivity factors reported in the literature. For this thesis the S_x values are obtained from the empirical value given by Wagner et al.¹⁰ (see Table 2.1). The $\lambda'_m(E_l)$ and $\lambda'_m(E_s)$ are the inelastic mean free paths (IMFP) of the photoelectrons from the overlayer and the substrate (with kinetic energy E_l and E_s , respectively) passing through the overlayer (l). The IMFP values are calculated by the TPP-2M equation¹¹, with the aid of QUASES-IMFP-TPP2M software.

Table 2.1 The atomic sensitivity factors used in this thesis¹⁰

Element	Atomic sensitivity factor	
Co	Co 2p	3.8
	Co 2p _{3/2}	2.5
Pt	Pt 4f	4.4
Zn	Zn 2p _{3/2}	4.8
Si	Si 2p	0.27
C	C 1s	0.25
O	O 1s	0.66

These assumptions are reasonable in case of particles on bare oxide substrates. The Co thickness t can be calculated from equation (2.4). According the AFM results, which will be presented in the following chapters, for Co/ZnO or Co/SiO₂, a flat and homogeneous layer structure is observed at least at low temperature. However, when Co is supported on carbon materials, it forms nanoparticles and does not meet the condition of this equation. However, since Co was evaporated under identical conditions (i.e., evaporation flux rate, duration and substrate temperature), the Co amount is assumed to be the same on all the samples.

To calculate the atomic ratio of bimetallic Co-Pt overlayers, a different qualification model assuming that the two components are homogeneously mixed was used:

$$X_M = \frac{\frac{I_M}{I_M^\infty}}{\sum_M \frac{I_M}{I_M^\infty}} \quad (2.5)$$

where X_M is the atomic concentration of metal M, I_M is the XPS peak area of metal M and I_M^∞ is the peak area for infinitely thick layer of M.

Angle resolved XPS measurements were used to detect the depth distribution of elements (within the region of maximum sampling depth). This is due to the fact that the angle between the sample surface normal and the analyzer (take-off angle, θ) adjusts the distance that the photoelectron travel within the solid and therefore the sampling depth (Figure 2.8). In other words, within the same traveling distance λ , the measuring depth (d) varies with θ ($d=\lambda \cos\theta$).

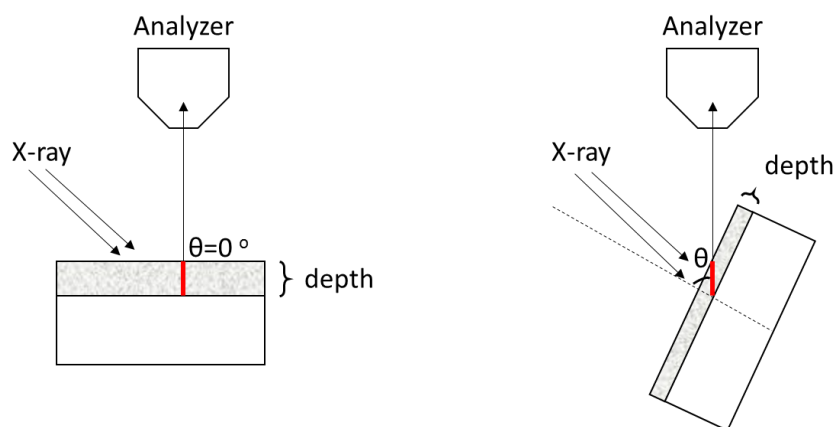


Figure 2.8 A schematic of angle resolved XPS measurement

2.2.2 Raman spectroscopy

Raman spectroscopy is a versatile tool for studying the properties of graphene. It can be used to determine the number and orientation of layers, the quality and types of edge, and the effects of perturbations, such as electric and magnetic fields, strain, doping, disorder and functional groups.¹² Thus, Raman spectroscopy was applied in this work in order to investigate the quality and layer number of graphene and also the graphene stability after various treatments. The principle of Raman spectroscopy is based on the inelastic scattering of monochromatic light. When light is incident on a sample, it may interact with sample atoms or molecules in different manners, such as reflection, adsorption or scattering. During the scattering process, most of the photons are elastically scattered; in this case, the frequency of the incident and scattered light is the same and this process is called Rayleigh scattering. A small amount of photons (only one in every 10^6 - 10^8 incident photons) gains or loses energy during scattering and this inelastic process is the Raman scattering. It consists of two types of scattering; one is named as Stokes–Raman scattering (the scattering light has less energy than the incident light) and the other is referred as anti-Stokes–Raman scattering (the scattering light has more energy than the incident light).¹³

Figure 2.9 shows a simple model of Rayleigh and Raman scattering processes. At room temperature, most molecules are present in the lowest energy vibration state. The virtual states are not real states of the molecule but are created when the laser interacts with the electrons and causes polarization. The energy of these states is determined by the frequency of the light source used.¹⁴ In Rayleigh scattering, when the incident light is absorbed by a molecule, the molecule will be excited to the virtual state and then it will relax and return back to its initial vibrational state by emitting a photon with the same frequency. In Stokes scattering the molecule from the ground vibration state (m) is promoted by the incident light to a virtual state but then returns to a higher vibration state (n) than its initial ground state and the emitted light has lower energy than the incident light. However, due to thermal energy, some molecules may be already present in an excited state (n). If these molecules are excited to a virtual state and then relax back to the ground state (m), energy will be transferred to the scattered photons, which is the so-called anti-Stokes scattering. Since at room temperature most of the molecules are in ground vibration state, the Stokes scattering is the most commonly detected process in Raman measurements.

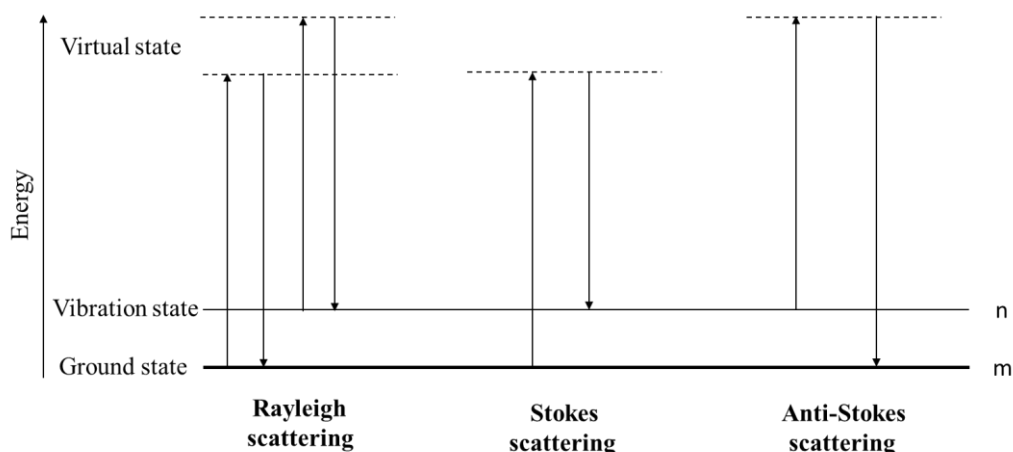


Figure 2.9 Diagram of the Rayleigh and Raman scattering processes.

There are four main components in a Raman spectrometer: excitation source, light collection optics, monochromator and detector (Figure 2.10(a)). In Raman scattering the intensity of the scattering is directly proportional to the power of the incident light. Lasers, which are monochromatic and with strong intensity, is the best excitation source. A good laser source for Raman should has narrow and extremely stable frequency in order to give high quality Raman peaks and not to cause errors in the Raman shift. Since the intensity of Raman scattering is inversely proportional to the forth power of the excitation wavelength, the shorter wavelength of the laser the higher the intensity of Raman scattering.¹⁴ However, high frequency excitation

sources, such as UV, may be absorbed by many compounds and cause the degradation of the sample. So the most common choice is a visible laser source.

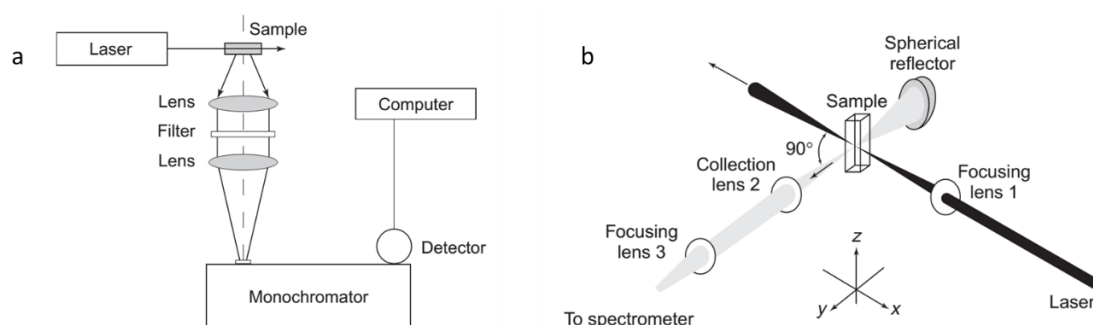


Figure 2.10 Conventional setup (a) and optical system (b) of Raman spectroscopy. From^[13].

In a typical Raman spectrometer, there are three optical devices.¹³ The first is a filter used to remove the plasma laser lines from the outgoing beam which generates Rayleigh scattering with intensity of the order of the Raman intensity. Besides, a spherical microscope objective or a cylindrical lens is needed to focus the laser beam onto the sample. The third device is the collection system (usually consists of two lenses, see Figure 2.10(b)) for recording Raman spectra. Generally, two basic geometries, 90° scattering or 180° scattering, are used in collecting Raman scattering (Figure 2.10(b)). In order to separate the Raman scattering from the other light collected, a monochromator is required. Nowadays the standard configuration is either a triple monochromator or a single monochromator in combination with sharp-cut filters. In a triple monochromator, the first two stages are for Rayleigh stray light rejection, whereas the third monochromator disperses the collected Raman radiation onto a multichannel detector. For the device with a filter (notch filter is widely used), the incident laser light is absorbed by the filter and the scattered light is collected and focused into a monochromator which separates the individual Raman peaks. Then the collected radiation is recorded by a detector, usually a charge-coupled device (CCD). This is a sectored piece of silicon in which each sector is separately addressed to the computer. In this way, it is possible to discriminate each frequency of the scattered light and therefore construct a Raman spectrum.¹⁴

In this thesis, Raman spectra were acquired at room temperature and atmosphere conditions with a micro-Raman spectrometer (Horiba LabRam Aramis), with excitation wavelength at 532 nm. A $100\times$ objective was used to focus the excitation laser to an approximately $1\ \mu\text{m}$ spot with a laser power less than 1 mW to avoid heating and damage of the sample.

2.2.3 Low energy ion scattering (LEIS)

Low-energy ion scattering (LEIS), also called ion scattering spectroscopy (ISS), is a surface analytical technique with supreme surface sensitivity, normally used for characterizing the elemental composition of the outermost surface layer.

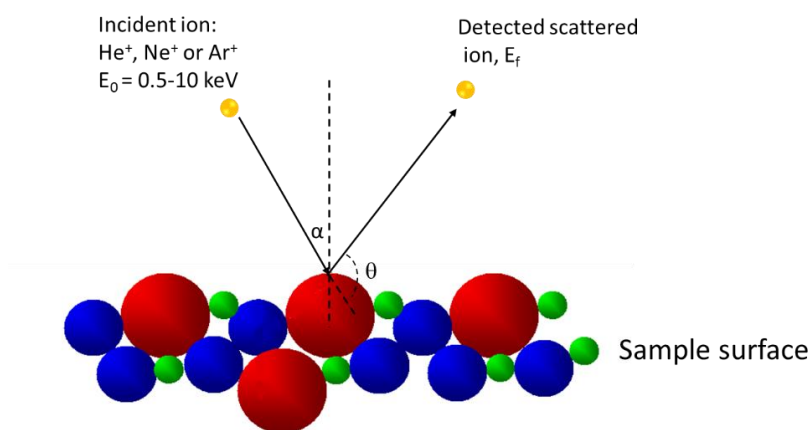


Figure 2.11 Experimental geometry of LEIS.

In a LEIS experiment (see Figure 2.11) the surface under investigation is bombarded with noble gas ions (He⁺, Ne⁺ or Ar⁺) with energy (E_0) between 0.5 - 3 keV. The ion beam is directed on the sample surface with an incident angle α ; typically smaller than 60 °.¹⁵ The ions collide with atoms on the sample surface and backscatter from the sample with kinetic energy (E_f) (at a scattering angle θ ; usually 140 °), typically measured with a CHA analyser. Generally the kinetic energy E_f is smaller than E_0 due to the momentum and energy transfer between the incident ions and surface atoms. E_f is dependent on the scattering angle (θ), the incident ion energy (E_0) and the masses of the incident (m_1) and the scattering (m_2) atoms, which can be calculated from the following equation:

$$\frac{E_f}{E_0} = \left(\frac{\cos \theta \pm \sqrt{\left(\frac{m_2}{m_1}\right)^2 - \sin^2 \theta}}{1 + \frac{m_2}{m_1}} \right)^2 \quad (2.6)$$

In an experiment, θ is normally a constant for a given instrument, m_1 is a known value for the source atom and E_0 is also fixed. Thus, it becomes obvious that E_f is a unique function of m_2 . Therefore, by measuring kinetic energy E_f , the mass of the surface atoms m_2 can be determined and this leads to the illustration of the element composition of the outermost surface layer.

For the LEIS measurements in this work, an IQE 11/35 (SPECS) ion source and He⁺ as incident ions were adopted. The incident energy was typically 750 eV and the scattering angle was 130°.

2.2.4 High resolution electron energy loss spectroscopy (HREELS)

High resolution electron energy loss spectroscopy (HREELS) is based on measuring the electron energy loss due to the inelastic scattering of these electrons with the sample. When an electron beam interacts with the sample surface, the electrons might lose energy by several paths including core level ionizations, valence-level excitations, plasmon losses, or vibrational excitations. HREELS usually takes advantage of small electron losses in the range of 10⁻³ eV to 1 eV. These losses are induced due to interactions with the vibrational modes of the adsorbed molecules or the surface phonons of the substrate. Thus, it is a complementary method to infrared spectroscopy and plays an important role in studies of model catalysts.^{16,17} In this thesis, the HREELS studies were carried out in the UHV multi-chamber analytical system (Prevac, Poland) in Lublin, Poland. The R4000 (Scienta) hemispherical electron energy analyzer and a monochromatic ELS 5000 (LK Technologies) electron gun with LaB6 cathode. The HREELS spectra were acquired in a specular geometry using a 14.069 eV incident electron beam directed 22.5 ° from the surface normal.

2.2.5 Atomic force microscopy (AFM)

An atomic force microscope (AFM) is one type of scanning probe microscopes (SPM), which allows investigating the local properties of solid surfaces with high spatial resolution.¹⁸ The AFM instruments are widely applied to measure the surface roughness (i.e. topography) as well as the mechanical (e.g. stiffness), electrical and magnetic properties of surfaces. The great virtue of this technique to other SPM methods (e.g. scanning tunneling microscopy, STM) is that it can be equally applied for electron conductive and isolating samples.

Figure 2.12(a) shows a photograph of the AFM (NTMDT Aura) used in this thesis and its main components. The working principle of AFM is shown in Figure 2.12(b). The AFM probe is made of an elastic cantilever with a sharp tip at the end. A laser beam is focused on the back of the cantilever and is reflected to a four-section split photodiode. The sample (or the probe) is mounted on a piezoelectric scanner, which allows precise control of its position in plane and vertical directions. The probe is brought into close proximity with the sample and as the sample moves the cantilever bends due to attractive forces between the tip and the surface (such as

Van der Waals force, electrostatic forces etc.). The deflection of the cantilever causes slight changes in the direction of the reflected laser beam, influencing the current produced by the photodiode. By using atomic sharp tips and nm scaled samples the movement of the photodiode current is directly proportional to the surface features.

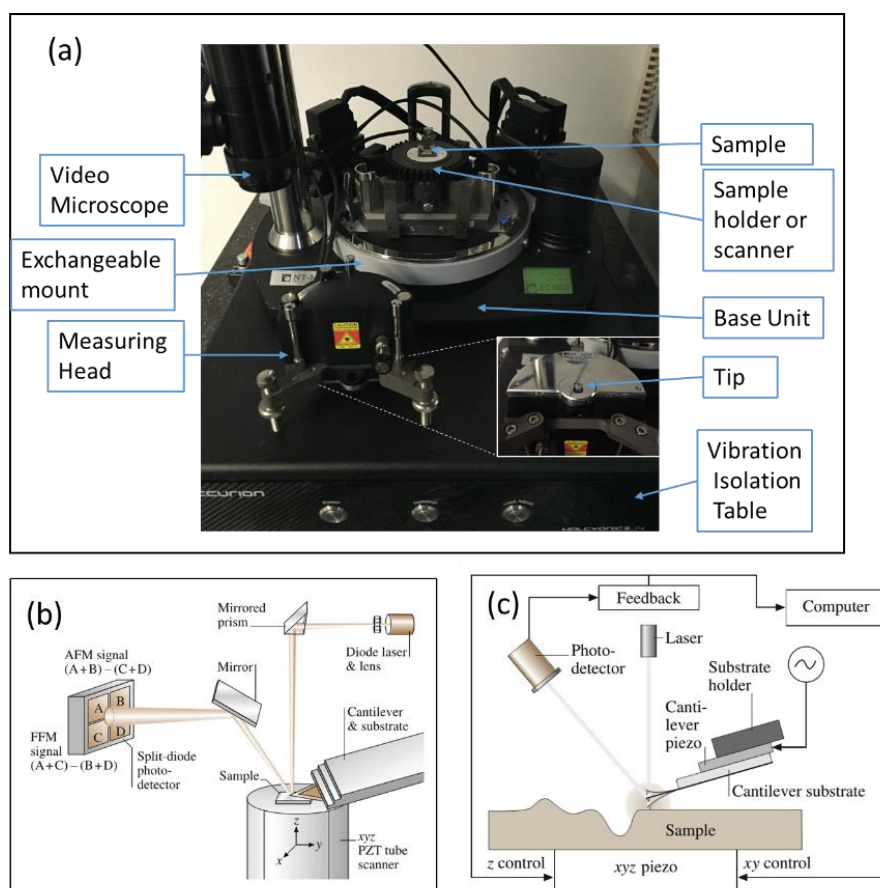


Figure 2.12 (a) Photograph of the AFM used in this thesis (NTEGRA Aura system). Principle of AFM measurement (b) and Schematic of tapping mode measurement (c), reproduced from [19].

AFM instruments can acquire images by three different methods: contact mode (also called static mode), non-contact mode and tapping mode (also called intermittent contact, AF mode or vibrating mode).

a) Contact mode

In contact mode, the tip is in direct contact with the surface and the AFM can be operated in both constant height and constant force modes. At constant force mode, a feedback system can be used to control the bending of the cantilever at a constant value and consequently, the interaction force as well. Thus the recorded voltage on the scanner Z-electrode reflects the surface topography. At constant height mode, the probe moves at an average height above the

sample and the bending of the cantilever is proportional to the applied force and consequently to the sample surface features. A drawback of contact mode is the direct physical contact of the tip with the sample. As the tip scans over the sample, the normal force and the substantial frictional force can damage the sample and the tip, hence distort the resulting data. Thus the contact techniques are practically not suitable for soft samples such as organic thin films and biological materials.

b) Non-contact mode

In the noncontact mode, the tip and the sample are in close proximity, but not in direct contact. The cantilever oscillates at its resonant frequency with small amplitude (about 1-10 nm). When the tip approaches the surface, the cantilever is affected by an additional force (van der Waals forces, or other long-range forces) and the resonance frequency is decreased. This decrease can be detected by the optical system and feedback to the instrument electronics, which recompense this change and maintain a constant oscillation amplitude or frequency by adjusting the average distance between the tip and sample. The topographic image of the sample surface can be obtained by measuring this distance at each point. In order to detect the slight difference of amplitude and phase of oscillation in non-contact mode, high sensitivity and stability of feedback are required. Moreover, under ambient conditions, most sample surfaces are covered by a layer of contamination which consists of water vapor and nitrogen. In this case, the tip will oscillate above the adsorbed layer and image both the sample surface and the layer. If the forces of this layer are higher than the range of van der Waals force between the tip and the sample surface, the image cannot be representative of the surface topography.

c) Tapping mode

In tapping mode, the cantilever is forced to oscillate near a resonance frequency similar to the non-contact mode, but the amplitude of this oscillation is higher, at about 10-100 nm. During scanning, the interaction forces, including elastic force and long range forces (van der Waals forces, electrostatic forces etc.), affect the oscillation amplitude like in the non-contact mode. Moreover, the changes in the oscillation amplitude can be detected and recorded with the help of a feedback system (Figure 2.12(b)). In tapping mode, the applied force is always vertical and there are significantly less lateral forces, so it is not distractive to the surface and can be used for soft surfaces. Compared to the non-contact mode, since the tip can approach close enough to the sample during tapping, the short-range forces will be detectable even with a liquid surface contamination under atmospheric conditions.

In this work, all of the AFM images were obtained under tapping mode at ambient conditions. A NTEGRA aura system from NT-MDT is utilized. The PPP-NCHR tips from NANOSENSORS with radius less than 10 nm are chosen for measuring.

2.2.6 Scanning Electron microscopy (SEM)

SEM is a common technique for the examination of the sample morphology. An electron beam is scanned on the sample and signals derived from electron interaction or scattering with the sample surface are recorded. Figure 2.13a shows various phenomena occurring when the incident electron beam interacts with the sample. The information depth extends from less than 100 nm to around 5 μm depending on the energy of the incident electrons, the atomic number, the density of the sample and the type of detected electrons (Figure 2.13b). The depth increases at high beam energy, small atomic number and small sample density. The SEM system used in this work was a JEOL 6700F microscope. The samples were fixed on the sample holder with graphite tape.

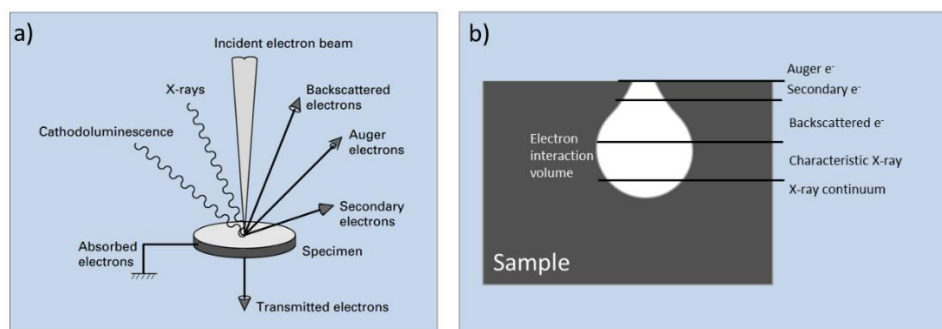


Figure 2.13(a) Signals generated by the electron interaction²⁰ and (b) generated regions

2.3 UHV experimental apparatuses

In this work, XPS measurements were conducted in three UHV experimental set-ups. Two of them are located in the *Surface Analysis Laboratory (SAL)* of the *Institut de chimie et procédés pour l'énergie, l'environnement et la santé (ICPEES)* in Strasbourg, while the third one is at the *Faculty of Chemistry of the University of Maria Curie-Skłodowska* Lublin, Poland. The first two equipment will be described below, while the equipment in Poland is a commercial multichamber UHV (PREVAC[®]) and the details can be found elsewhere²¹.

a) UHV system for low pressure studies

Figure 2.14 shows the UHV system for low pressure studies. This UHV system consists of three chambers: a load-lock chamber, a preparation chamber and an analysis chamber. The

preparation chamber is equipped with Ar^+ sputtering gun for sample cleaning and the e-beam evaporator for metal deposition. The analysis chamber is equipped with a dual anode ($\text{AlK}\alpha$ and $\text{MgK}\alpha$) X-ray source, an ultraviolet source, a 1-channel CHA VG Clam-2 electron analyzer, a gas/vapor doser and a differentially pumped mass spectrometer (see Figure 2.14). In this thesis, experiments were performed using $\text{Al K}\alpha$ source and an X-ray incident angle of 30° with respect to the sample. The emission angle of the photoelectrons was fixed to 15° to the normal of the sample's surface. The photoelectrons were detected by using a pass energy of 20 eV for all of the high resolution spectra (and 50 eV for the survey scan). The analysis chamber is equipped with a 4-axis manipulator with heating and liquid- N_2 cooling capabilities. The sample was mounted on a PTS 1200 EB/C-K Mo sample holder (PREVAC[®]) and could be heated either by the resistance mode of a tungsten filament or by electron bombardment mode heating (for temperatures higher than 300°C). In order to study the low pressure oxidation/reduction properties of the samples, the O_2/H_2 gas was manually introduced by leak valves to the analysis chamber and the pressure was monitored by an ion gauge. In all of the low pressure redox studies, the O_2 and H_2 pressure were controlled at 5×10^{-7} mbar.

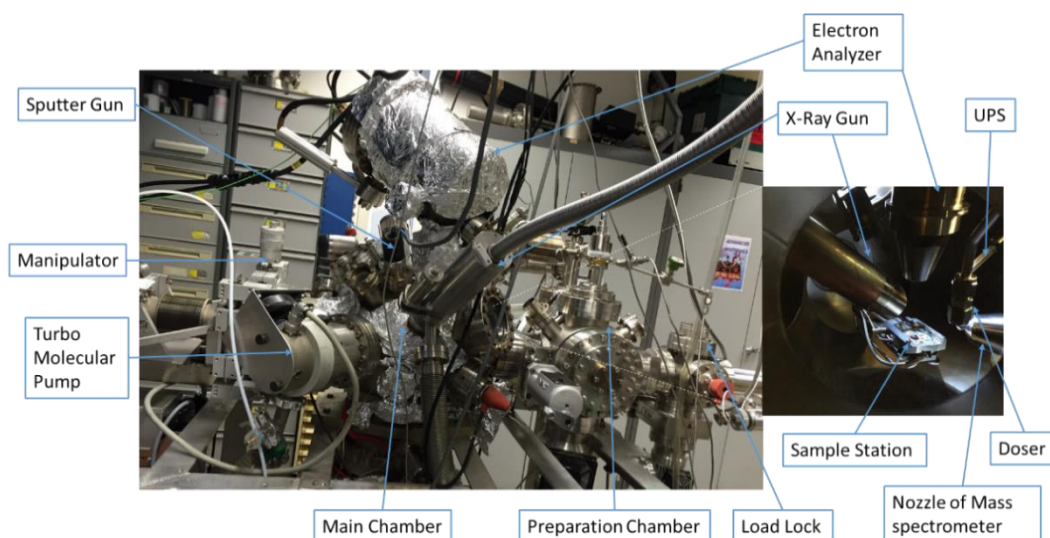


Figure 2.14 The UHV system used in the low pressure studies.

b) UHV system for medium pressure studies

The medium pressure studies were performed in the VSW UHV system (see Figure 2.15). Beside the load-lock chamber, preparation chamber and analysis chamber, it is also equipped with a high pressure chamber which is connected to the load-lock. The volume of the high pressure chamber is ~ 1 L, a capacitance gauge (Pfeifer Vacuum CMR 362) and a gas regular valve (Pfeifer Vacuum RVC 300) are installed to supply a constant pressure and/or gas flow.

Samples were mounted on a sample holder able to operate both under vacuum and high pressure conditions (Omnivac). The holder is equipped with a ceramic heater and a thermocouple directly attached on the side of the sample. During the medium pressure experiments, a 7 mbar pressure and 40 mbarl/s gas flow were applied for all the experiments. After the sample was treated in O₂/H₂ in this chamber, the gas could be pump out and the sample was transferred into the UHV chamber through the load-lock without exposure it in the air.

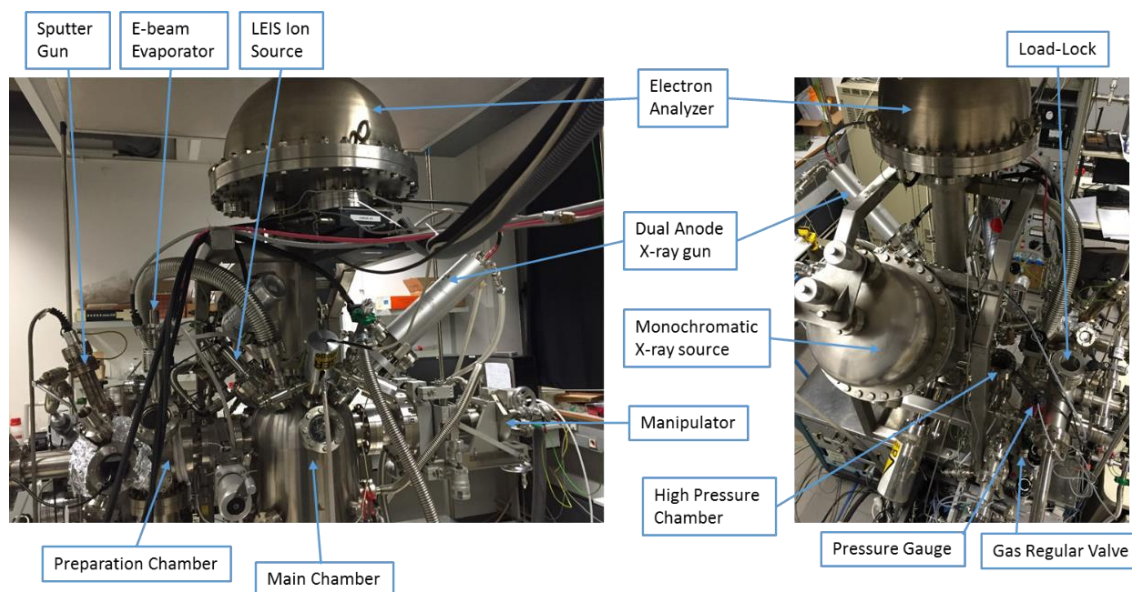


Figure 2.15 Photograph of the VSW UHV system at two different directions.

The preparation chamber is equipped with Ar⁺ sputtering gun for sample cleaning and the e-beam evaporator for metal deposition. The analysis chamber is equipped with an ultraviolet source for UPS, an IQE 11/35 (SPECS) ion source for LEIS, a VSW Class WA hemispherical electron analyzer (150 mm radius) with a multi-channeltron detector and two X-ray sources for XPS. One of the X-ray sources is a non-monochromatic dual anode (Al K α and MgK α) X-ray source and the other one is a monochromatic Al K α source. In this work, the monochromatic Al source (1486.6 eV; anode operating at 240 W) is chosen for high resolution spectra. The X-ray incident angle is 45° with respect to the sample and two emission angles of the photoelectrons are chosen which are 0° and 75° to the normal of the sample surface. The photoelectrons were detected by using pass energy of 44 eV for all of the high resolution spectra (and 90 eV for the survey scan).

2.4 References

- (1) Graphene on SiO₂ Substrate <http://www.acsmaterial.com/product.asp?cid=88&id=106> (accessed Oct 17, 2015).
- (2) Suk, J. W.; Kitt, A.; Magnuson, C. W.; Hao, Y. F.; Ahmed, S.; An, J. H.; Swan, A. K.; Goldberg, B. B.; Ruoff, R. S. Transfer of CVD-Grown Monolayer Graphene onto Arbitrary Substrates. *ACS Nano* **2011**, 5 (9), 6916–6924.
- (3) Mantis Deposition Ltd / ebeamvaporator <http://www.mantisdeposition.com/ebeamvaporator> (accessed Oct 17, 2015).
- (4) Heide, P. Van der. *X-Ray Photoelectron Spectroscopy: An Introduction to Principles and Practices*; 2011.
- (5) Moses, A. W.; Flores, H. G. G.; Kim, J.-G.; Langell, M. A. Surface Properties of LiCoO₂, LiNiO₂ and LiNi_{1-x}Co_xO₂. *Appl. Surf. Sci.* **2007**, 253 (10), 4782–4791.
- (6) Vaz, C. A. F.; Prabhakaran, D.; Altman, E. I.; Altman, E. I.; Henrich, V. E. Experimental Study of the Interfacial Cobalt Oxide in Co₃O₄/α-Al₂O₃(0001) Epitaxial Films. *Spectroscopy* **2009**, 3 (0001), 1–8.
- (7) Mohai, M. XPS MultiQuant: Multimodel XPS Quantification Software. *Surf. Interface Anal.* **2004**, 36 (8), 828–832.
- (8) Moulder, J. F.; Stikle, W. F.; Sobol, P. E.; Bomben, K. D. *Handbook of X-Ray Photoelectron Spectroscopy*; Chastain, J., Roger C. King, J., Eds.; Physical Electronics, Inc., 1995.
- (9) Powell, C. J.; Jablonski, A. Progress in Quantitative Surface Analysis by X-Ray Photoelectron Spectroscopy: Current Status and Perspectives. *J. Electron Spectros. Relat. Phenomena* **2010**, 178-179, 331–346.
- (10) Wagner, C. D.; Davis, L. E.; Zeller, M. V.; Taylor, J. A.; Raymond, R. H.; Gale, L. H. Empirical Atomic Sensitivity Factors for Quantitative Analysis by Electron Spectroscopy for Chemical Analysis. *Surf. Interface Anal.* **1981**, 3 (5), 211–225.
- (11) Tanuma, S.; Powell, C. J.; Penn, D. R. Calculations of Electron Inelastic Mean Free Paths. V. Data for 14 Organic Compounds over the 50-2000 eV Range. *Surf. Interface Anal.* **1994**, 21 (3), 165–176.
- (12) Ferrari, A. C.; Basko, D. M. Raman Spectroscopy as a Versatile Tool for Studying the Properties of Graphene. *Nat. Nanotechnol.* **2013**, 8 (4), 235–246.
- (13) Popp, J.; Kiefer, W. *Raman Scattering, Fundamentals*; 2006.

- (14) Smith, E.; Dent, G. *Modern Raman Spectroscopy: A Practical Approach*; John Wiley & Sons, 2013.
- (15) BRONGERSMA, H.; DRAXLER, M.; DERIDDER, M.; BAUER, P. Surface Composition Analysis by Low-Energy Ion Scattering. *Surf. Sci. Rep.* **2007**, 62 (3), 63–109.
- (16) Soriaga, M. P.; Chen, X.; Li, D.; Stickney, J. L. High Resolution Electron Energy-Loss Spectroscopy. In *Applications of physical methods to inorganic and bioinorganic chemistry*; Scott, R. A., Lukehart, C. M., Eds.; WILEY, 2007; pp 499–529.
- (17) Wang, H.; Chu, P. K. Surface Characterization of Biomaterials. In *Characterization of Biomaterials*; Bandyopadhyay, A., Bose, S., Eds.; Elsevier Inc., 2013; p 131.
- (18) Mironov, V. L. *The Fundamentals of Scanning Probe Microscopy*; 2004.
- (19) Bhushan, B. *Nanotribology and Nanomechanics*; Bhushan, B., Ed.; Springer-Verlag: Berlin/Heidelberg, 2005.
- (20) Jeol USA. SEM: Scanning Electron Microscope A to Z.; 2009; pp 3–30.
- (21) Spektroskopia elektronowa (XPS) <http://www.lab.umcs.lublin.pl/xps.php> (accessed Jan 12, 2016).

Chapter 3

**Investigation of Co interaction with
bare, and graphene-covered, ZnO
substrates in UHV conditions**

Chapter 3 Investigation of Co interaction with bare, and graphene-covered, ZnO substrates in UHV conditions¹

3.1 Introduction

It is generally accepted that the morphology and the electronic properties of supported overlayers are strongly influenced by the interaction with the substrate.^{1–3} Traditionally, supports like graphite, SiO₂, and Al₂O₃ are considered highly stable and relatively inert, while oxides such as TiO₂ and ZnO are known to have a strong influence on the structural and chemical characteristics of the deposited overlayer. In many applications, both the bulk (volume) and surface characteristics of the support are equally important. Bulk characteristics influence properties such as the mechanical stability, thermal and electric conductivity, photon absorption properties, and so on, while surface characteristics control the chemistry at the metal/support interface. For example, both the energy gap (bulk property) and the surface reactivity govern the performance of photocatalytic materials.⁴ In general, the surface and the bulk properties of supports are interconnected, and it is very difficult to modify one without influencing the other.

Graphene is considered as an attractive supporting material for metal clusters due to its unique electronic, structural, and chemical characteristics.^{2,5–12} In addition, graphene has been explored as an ultrathin barrier to protect different metals, such as Cu,^{13,14} Cu/Ni,¹⁴ Ag,¹⁵ Fe,¹⁶ and so on, from corrosion in air, H₂O₂ and electrochemical environments. In all above studies, metals or relatively inert oxides were used as the supporting material of graphene layers. The effect of graphene on reactive oxide supports, which are known to interact actively with metal overlayers, has not been explored so far. In this work we demonstrate a new perspective of single-layer graphene as an interlayer that can dramatically influence the metal–support interaction. This is a potentially novel and stimulating application of graphene since it can act as a transparent, ultrathin, electron conductive, promoter/mediator of the substrate chemical properties.

¹ This chapter is a reproduction of the published paper on *J. Phys. Chem. Lett.*, 2014, 5 (11), pp 1837–1844⁶⁹.

3.2 Experimental methods

Materials and Synthesis

In this Chapter, ZnO(0001) and single layer graphene covered ZnO(0001) (named as G-ZnO) were prepared as substrates for investigating the cobalt-support interactions. Cobalt evaporation was carried out at room temperature with a rate of 0.01 nm/sec for a period of 50 sec and at background pressure $< 8 \times 10^{-9}$ mbar. For the flash heating treatments the temperature increase ramp rate was 1 °C/sec. After each temperature treatment the sample was cooled down to room temperature where spectroscopic data were recorded. Details of sample preparation can be found in Chapter 2, section 2.1.

Characterization methods

Raman spectra were recorded at room temperature and at atmospheric conditions by a Horiba spectrometer LabRam. A 532 nm laser was used as excitation energy with power energy of 0.93 mW and a fluence of $2.25 \text{ mW } \mu\text{m}^{-2}$. The morphology of the samples was investigated by the atomic force microscopy (AFM). Measurements were carried out at ambient conditions with NanoScope V (Bruker-Veeco) operated in the tapping mode, which is low-invasive and recommended for the surface of soft materials.

XPS and HREELS experiments were conducted in two ultrahigh vacuum (UHV) chambers with background pressure $< 2 \times 10^{-9}$ mbar, equipped with hemispherical electron analysers and a dual anode (Al K α and Mg K α) X-ray source and standard surface preparation facilities (ion sputter gun, LEED optics etc.).¹⁷ In one of the UHV setup (VG Microtec, Strasbourg) the analysis area of the samples was maximized (*ca.* $8 \times 8 \text{ mm}^2$) in order to get representative information of large spatial area of the sample. The second UHV multi-chamber analytical system (Prevac, Poland) was also equipped, among others, with theR4000 (Scienta) hemispherical electron energy analyzer and a monochromatic ELS 5000 (LK Technologies) electron gun with LaB6 cathode for the High Resolution Electron Energy Loss Spectroscopy (HREELS). The HREELS spectra were acquired in a specular geometry using a 14.069 eV incident electron beam directed 22.5 ° from the surface normal.

3.3 Results and discussion

3.3.1 Characterization of ZnO and Graphene-ZnO substrates

Figure 3.1 shows Raman and X-ray photoelectron spectroscopy (XPS) C 1s results recorded after transferring the PMMA/graphene film onto ZnO and PMMA dissolution, abbreviated as G-ZnO. Both characterizations indicate spectral features due to traces of PMMA residues that were not totally removed by the ethanol treatment.^{18,19} Deconvolution of the C 1s XPS peak using previously described PMMA C 1s spectrum^{19,20} reveals that the residue PMMA signal is about 30 % of the overall C 1s peak (in some transfer attempts, the residue PMMA signal could reach up to 70 %). This indicates that ethanol can effectively dissolve the majority of the PMMA layer, yet some PMMA residues remain after this procedure.^{21,22} Quantitative XPS calculations assuming the typical layer model²³ estimate the overall thickness of the carbon layer to be 1.5 ± 0.5 nm or roughly about 5 atomic layers (estimated carbon thickness 0.3 nm). For comparison, we immersed the bare ZnO crystal (without PMMA/graphene) into liquid ethanol, and we found that the signal of the C 1s peak due to residual species was 4 times lower, while the C 1s peak position was shifted to higher energies by about 1 eV (Figure 1b, second from bottom). This observation shows that graphene/PMMA can be clearly differentiated from residual carbon species in the C 1s spectrum. Annealing the sample at 350 °C in UHV for 1 h effectively removes the PMMA traces as indicated by the disappearance of the PMMA fingerprint peaks in both Raman and XPS spectra (Figure 3.1a,b). The thickness of the carbon layer after annealing was estimated by XPS about 0.5 nm, compatible with the expected thickness of single-layer graphene.

The quality of the transferred graphene was characterized by Raman spectroscopy, which is an efficient method to conclude about the number of graphene sheets and their structural order.^{24–28} The main features of the Raman spectrum of graphene are the so-called G and 2D bands at about 1580 and 2700 cm^{-1} , respectively, while an additional bands around 1350 cm^{-1} (D band) is observed in disordered or defective graphene. The narrow symmetric 2D band and the relatively low G-to-2D band intensity ratio shown in Figure 3.1a can be used as a safe indicator of single-layer graphene.^{25,28} In addition, the low intensity of the D band ($\sim 1350 \text{ cm}^{-1}$) suggests that the graphene layer transferred on ZnO has a quite low defect density. Comparison of the Raman spectra of the G-ZnO sample before and after annealing in UHV shows that annealing has effectively removed the PMMA related spectral features, without introducing new defects on the graphene layer (the D band remains small).

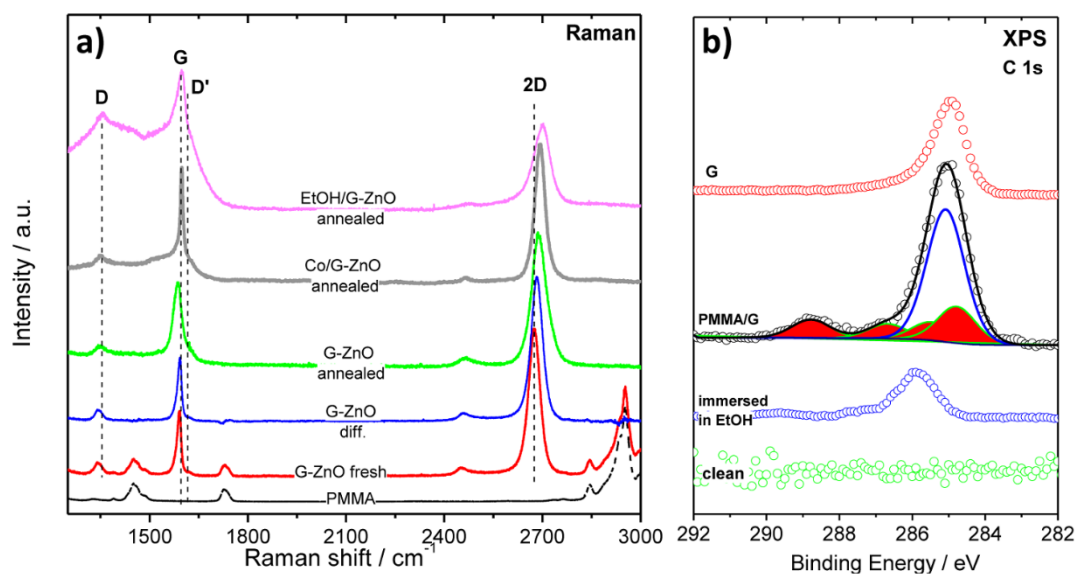


Figure 3.1 (a) Raman spectra of PMMA and G-ZnO samples before and after annealing as well as after cobalt deposition and ethanol exposure cycles, the blue line (G-ZnO diff.) derives after subtraction of PMMA to G-ZnO spectrum. (b) From bottom to top: XPS C 1s core level spectra of the clean bare ZnO (0001) substrate, after immersion in ethanol bath, after graphene transfer, after vacuum annealing.

Surface phonons were examined using high-resolution energy-loss spectroscopy (HREELS). The clean ZnO (0001) surface (lower portion of Figure 3.2a) is characterized by surface optical phonons at 67, 134, and 200 meV due to long-range surface lattice vibrations.^{29,30} After transfer of the graphene layer and UHV annealing, the surface phonons of ZnO are completely screened. Instead, a weak shoulder at about 40 meV and a very broad structure centered at about 165 meV appeared (indicated by arrows in Figure 3.2a), similar to previous reports from graphene sheets on SiC.³¹ The addition of graphene can influence the HREELS spectra in two ways: either by efficiently screening the ZnO substrate phonons or by inducing new features in the spectrum, for example due to the coupling of substrate phonons with plasmons from the graphene layer.^{32,33} Full screening of the ZnO phonon features in the HREELS spectrum has been reported after deposition of thick metal overlayers on ZnO, e.g., 3 and 20 atomic layers for Pt²⁹ and Cu³⁰, respectively. The presented HREELS spectra confirm the effective coverage of ZnO by graphene but cannot be conclusive about the effect of graphene on ZnO surface phonons. Overall, as compared to metals, single-layer graphene can be a very efficient, thermally stable material to screen the ZnO surface phonons.

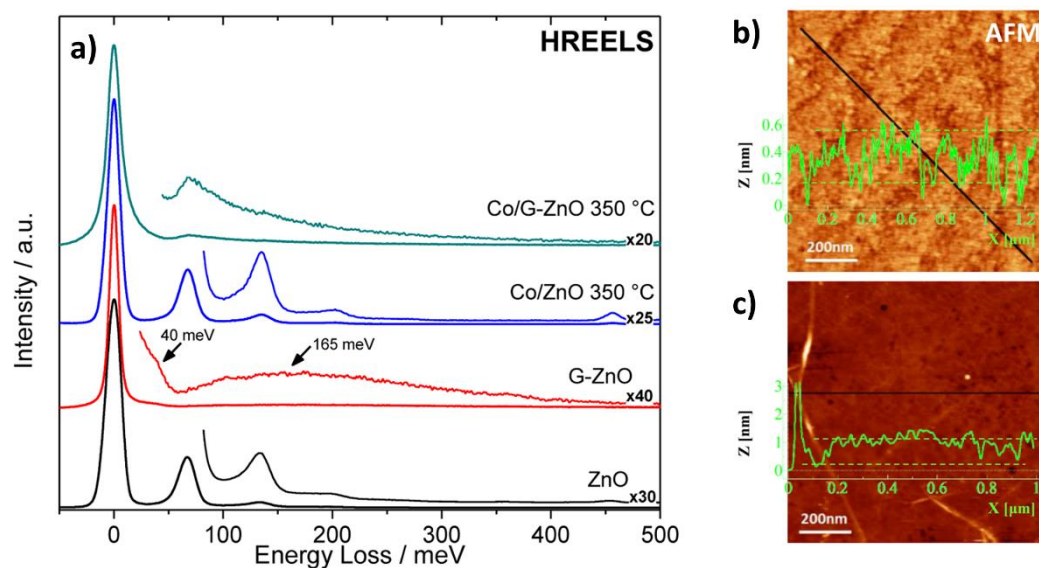


Figure 3.2 (a) From bottom to top: HREELS spectra of ZnO, G-ZnO, Co/ZnO, and Co/G-ZnO after annealing at 350 °C. (b) Tapping-mode AFM topographic images of clean bare ZnO and (c) G-ZnO samples. The line profiles along the lines depicted in the AFM images are superimposed in the figures.

The morphology of the sample surface was analyzed by atomic force microscopy (AFM). A typical AFM image and a line profile of the ZnO (0001) substrate after cleaning in UHV are shown in Figure 3.2b. The step-and-terrace structure can be observed with a step height of about 0.25 nm corresponding to a half lattice parameter of the unit cell of Co .³⁴ In the AFM topographic image of the G-ZnO sample (Figure 3.2c), the layer is continuous and flat (root-mean-squared (RMS) roughness ~ 0.5 nm), although some wrinkles and small tears can be seen. As derived by the line profile curve superimposed in Figure 3.2c, the height of the graphene layer is about 1 nm compatible with a monolayer thickness for AFM measurements under atmospheric conditions.^{35,36} We should mention here that, although the theoretical thickness of single-layer graphene is 0.35 nm, the thickness of graphene in the AFM measurements can vary from 0.4 to 1 nm due to the chemical contrast between graphene and the substrate and the specific settings of the AFM instruments.^{37,38}

3.3.2 Graphene's effect to the Co-ZnO interactions

Cobalt, at coverage of about 0.5 nm, or 2 equivalent layers, was evaporated onto annealed G-ZnO substrates in UHV at room temperature (abbreviated as Co/G-ZnO). For comparison, cobalt was also evaporated on a bare, clean ZnO substrate (abbreviated as Co/ZnO) under identical conditions (i.e., evaporation flux rate, duration and substrate temperature). Figure 3.3a,b compares the evolution of the Co 2p XPS peaks of Co deposited on ZnO and G-ZnO substrates as a function of the annealing temperature. Up to 100 °C, the sharp Co 2p_{3/2} peak at

778.3 eV indicates the metallic Co state (Co^0)^{17,39} for both substrates. However, upon further annealing, the evolution of the Co 2p_{3/2} spectrum in the two substrates is considerably different. In particular, on bare ZnO, and starting from 200 °C, the intensity of metallic Co 2p_{3/2} peak at 778.3 eV decreases and is gradually replaced by a component at 780.6 eV, which is typical for CoO^{17,39,40} (Figure 3.3a). It is interesting to note that, under the conditions examined, the oxidation is limited to CoO and does not proceed further to the more thermodynamically stable Co₃O₄ phase.⁴¹ This result is in agreement with previous studies reporting that when Co/ZnO is annealed in vacuum, a solid state reaction takes place at the interface inducing cobalt oxidation.^{17,39,42} In contrast, annealing of the Co/G-ZnO sample does not cause any evident effect to the Co 2p_{3/2} peak shape, which remains identical to that of metallic Co even after annealing at 350 °C. These results clearly show that the addition of graphene affects the metal–support interaction by preventing Co oxidation by ZnO. Apparently, the oxidation of Co by ZnO necessitates oxygen transport through a common interface between the two materials or substitution of Zn by Co ions in the ZnO oxide lattice. Defect free graphene acts as a physical barrier for the in-diffusion of Co while, as has been described previously, is impermeable toward oxygen,^{43,44} which elucidates the observed resistance of Co to oxidation. This description accounts not only for areas that graphene is in physical contact with the support but also for curved graphene areas, since in both cases the Co–ZnO interaction is prohibited.

The XPS intensity ratio between Co 2p and Zn 2p photoelectron peaks ($I_{\text{Co}}/I_{\text{Zn}}$) is indicative of the cobalt dispersion on the substrate^{45,46} and as such, can be used to qualitatively report about the morphological changes of cobalt overlayer upon annealing. In Figure 3.3c, a plot of the normalized $I_{\text{Co}}/I_{\text{Zn}}$ is presented as a function of the annealing temperature for both Co/ZnO and Co/G-ZnO samples. Comparison of the $I_{\text{Co}}/I_{\text{Zn}}$ ratio in the two samples indicates very similar values up to 200 °C, but significant deviation above this temperature. In particular, the decrease of $I_{\text{Co}}/I_{\text{Zn}}$ observed up to 200 °C indicates that less Co but more ZnO substrate is exposed. This can be explained by Co particle agglomeration and/or by increase of their contact angle with the support. At temperatures higher than 200 °C, the $I_{\text{Co}}/I_{\text{Zn}}$ ratio of the G-ZnO substrate continues to decrease monotonically, indicating that agglomeration carries on as the temperature increases. On the contrary, on bare ZnO the ratio increases above 200 °C, showing redispersion of cobalt. It is evident that upon annealing the Co overlayer on bare ZnO, cobalt is oxidized to CoO and spreads out over the ZnO surface, while over G-ZnO agglomeration of cobalt is observed.

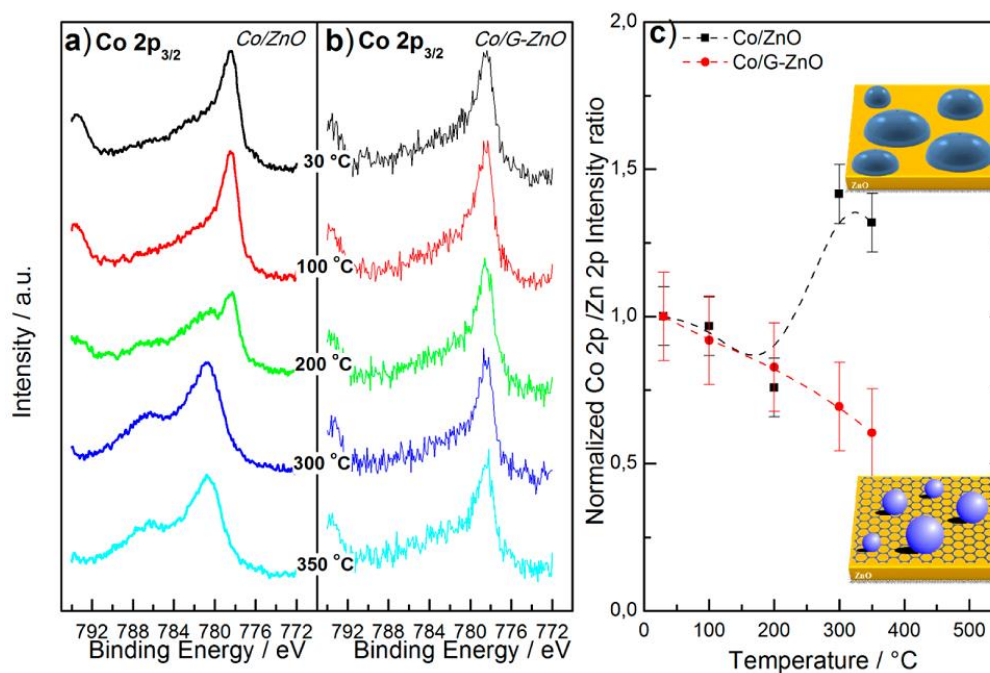


Figure 3.3 XPS spectra of (a) Co/ZnO and (b) Co/G-ZnO upon annealing at different temperatures. (c) Variation of the normalized XPS Co 2p/Zn 2p intensity ratios with temperature for Co/ZnO and Co/G-ZnO samples. To facilitate the comparison, the Co 2p/Zn 2p intensity ratio is normalized to the initial ratio at 30 °C. The error bars represent the data scattering as the deviation of the mean value obtained in three repeated experiments. A graphical representation of the cobalt particles' morphology after annealing at the higher temperature is included.

The surface morphology of the Co/ZnO and Co/G-ZnO samples before and after annealing was further studied by AFM. The surface of the fresh Co-ZnO sample (Figure 3.4a) is relatively flat and continuous, but becomes rougher than that of clean ZnO (Figure 3.2b) and individual particles can be seen. After annealing Co-ZnO at 350 °C (Figure 3.4b) the surface of this sample becomes more flat, with as RMS roughness of 0.35 nm and an average height of 1.3 nm. As anticipated, the morphology of the Co deposit on the G-ZnO substrate is significantly different (Figure 3.4c). Co forms highly dispersed homogeneous particles on the G-ZnO surface. The Co–Co cohesive energy and the Co–C dissociation energy are the key parameters that define the energetics of Co morphology on G-ZnO. The Co–C dissociation energy has been reported to be about 155 kJ/mol,⁴⁷ and the cohesive energy of Co in a bulk crystal is about 423 kJ/mol.⁴⁸ However, one cannot simply compare the cohesive energy of Co bulk crystals with the Co–C bond energy. Considering the size, shape, and structure of the Co nanoparticles in our case, and based on the surface–area–difference (SAD) model,^{7,49} the Co-Co cohesive energy could be computed using: $E_{coh} = E_b(1 - \frac{3p\alpha d_{hkl}}{D})$, where E_b is the cohesive energy

(absolute value) of the bulk crystal; p is the parameter used in determining the coherence between the nanocrystals and the matrix; α is related to the shape of nanocrystals; d_{hkl} is the interplanar distance of (hkl) ; and D is the size of the nanocrystal. For Co bulk crystal, E_b has been reported to be 423 kJ/mol. From Figure 3.4c, the Co nanoclusters are found to be spherical with nanocrystal size (D) \sim 10 nm, and for spherical nanoparticles $\alpha = 1$. It is also well known that nanoparticles tend to adopt low index surface planes to lower the total surface energy. Therefore, we assume Co nanoparticles are surrounded by (0001) crystal planes. So, assuming that spherical Co nanoparticles ($\alpha = 1$) with (0001) crystal planes on the surface grow on graphene with a non-coherent interface ($p = 1$), the E_{coh} is about 395 kJ/mol. This value is much higher than the Co–C dissociation energy. Hence, formation of 3D particles is favored for Co on graphene.⁷ After annealing, formation of larger Co aggregates is observed in the AFM image (Figure 3.4d), as is also deduced by the reduction of the I_{Co}/I_{Zn} ratio in the XPS results.

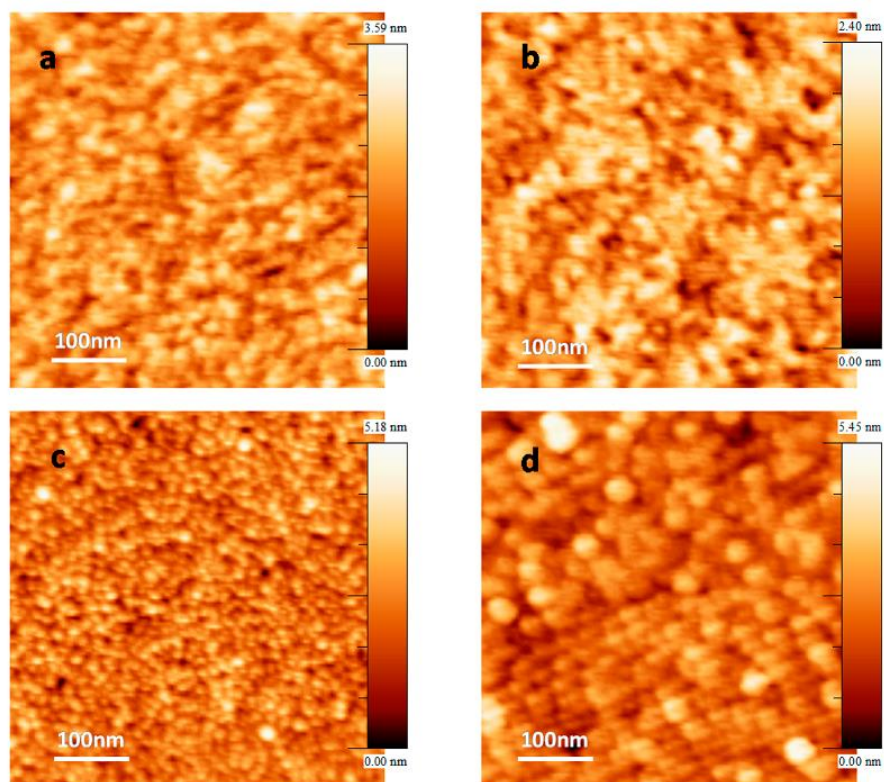


Figure 3.4 Tapping-mode AFM topographic images ($500 \times 500 \text{ nm}^2$) of (a) fresh Co/ZnO, (b) Co/ZnO after annealing at 350 °C, (c) fresh Co/G-ZnO and (d) Co/G-ZnO after annealing at 350 °C

In the HREELS spectrum recorded on Co/ZnO after annealing (Figure 3.2a), the loss features at 67 and 134 cm^{-1} due to ZnO substrate areas are clearly visible. In the presence of the graphene interlayer, after annealing, a very weak signal at about 70 meV coincides well with the more intense ZnO phonon and might come from uncovered ZnO areas within the grain

boundaries of graphene nanocrystals. The minor contribution of this peak to the overall HREELS signal confirms the effective screening of ZnO phonon losses by graphene, even after cobalt deposition and annealing.

3.3.3 The stability of graphene

Having shown the important influence of graphene interlayer on the Co–ZnO interaction, we discuss the stability of the graphene layer upon UHV thermal treatment. As has been shown earlier, the frequency, the width, and the relative intensities of Raman peaks are sensitive to the strain, the number of defects, and the charge doping within the graphene layer.^{22,50–52} In Figure 3.1a, the Raman spectra of G-ZnO and Co/G-ZnO samples after annealing at 350 °C are shown. In addition, the position and the full width at half-maximum (fwhm) of the G and 2D bands are summarized in Table 1, along with the intensity ratios between the main Raman bands. The I_D/I_G band intensity ratio has been used to estimate the defect density of the graphene layer.⁵¹ In general, higher I_D/I_G ratios are indicative of higher degree of defects. The relatively low I_D/I_G ratios before and after annealing shown in Table 3.1, suggest a low defect density that is not significantly affected by the cobalt deposition and the heating treatment. It has been reported that deposition of metals such as Pd,⁵³ Ti,⁵³ Ni⁵⁴ and Co⁵⁴ on graphene can induce defects sites due to the chemical interaction between metals and graphene. However, in our case, the low defect density of graphene might be attributed to the relatively low deposition amount and the short duration time as well as the flash annealing condition.

Table 3.1 The G band and 2D band FWHM and positions and the intensity ratios for G-ZnO under various treatments (estimated error $\pm 1.5 \text{ cm}^{-1}$).

Sample	Position G (cm^{-1})	G FWHM (cm^{-1})	Position 2D (cm^{-1})	2D FWHM (cm^{-1})	Intensity ratio I_D/I_G	Intensity ratio I_{2D}/I_G
G-ZnO	1591	17	2676	44	0,15	2,26
G-ZnO annealed	1586	33	2689	58	0,10	1,72
Co/G-ZnO annealed	1598	11	2693	40	0,10	1,30
EtOH+G-ZnO annealed	1587	67	2698	43	0,64	0,49

Apart from the defects, Raman peaks can be informative about the mechanical strain within the graphene nanocrystallites. It has been proposed that mechanical strain induces a larger Raman shift of the 2D peak compared to that of the G band, followed by increase in the peak's fwhm.²⁶ On the basis of this argument and of the information presented Table 3.1, we can

deduce that annealing at 350 °C induces more strain within graphene as compared to the fresh G-ZnO sample. Indeed, the relative position of the 2D and G peaks is enlarged by 19 cm⁻¹, while the 2D peak fwhm becomes broader than that of the fresh G-ZnO sample by 30 %. Although defects and strain phenomena are usually interconnected,⁵⁵ we propose that the interaction between the graphene layer and ZnO is accountable for the observed strain since, as mentioned above, the defect density remains the same.

In the case of Co/G-ZnO, the Raman spectrum is characterized by an upshift in the G position and a significant decrease of its fwhm. In addition, the I_{2D}/I_G ratio is further decreased. Previous studies have shown that such spectral modifications are induced by the electrical doping of graphene.^{22,58} The type of doping can be determined from the relative shifts between the G and 2D bands. In particular, the upshift of the G band position and the downshift of the 2D band indicates n-doping of graphene, whereas the upshift of both G and 2D bands implies p-doping.⁵⁷ As shown in Table 3.1, both the G and the 2D bands upshift compared to G-ZnO sample, suggesting an electron withdrawn from graphene toward the cobalt adlayer and therefore p-type (hole) doped graphene. Of course one cannot exclude the possibility of charge transfer interaction with the ZnO support, catalyzed by the presence of the cobalt overlayer.

It is interesting to note here that previous studies reporting that when gold nanoparticles are attached on graphene, there is electron charge transfer from graphene to the Au particles.^{8,60} However, DFT calculations predicted the reverse trend for cobalt, i.e. charge transfer from Co to graphene and n-type graphene doping,^{59,60} which comes in contradiction our experimental results. Since the Raman measurements were carried out at atmosphere condition, supported Co nanoparticles should be oxidized immediately after exposure in air. Thus, unlike metallic Co where electrons are transferred towards graphene, for oxidized cobalt electrons are transferred from graphene to CoO. This leads to the p-type dope of graphene, which has also observed in other works.⁶¹

Recently it was suggested that, apart from Raman spectra, the C 1s binding energy shifts can be used in order to evaluate charge transfer phenomena between graphene and substrate or overlayer structures.^{14,61,62} However, here we did not observe any binding energy shift in the C 1s spectra of graphene before and after cobalt deposition and annealing (the spectra were identical within the experimental error of ±0.1 eV). There are two possible reasons that can explain the stability of the C 1s binding energy in our work. First, it is likely that the charge doping of cobalt in graphene is lower, compared to the other cases and therefore the shift of C

1s peak is much smaller and difficult to observe. According to Dahal et al.⁶² the C 1s core level shift of graphene in contact with a metal is correlated with the work function of the metal. In particular, graphene doping from metals with work function around 5 eV is limited and do not induce any binding energy shift to the C 1s peak. This can explain the absence of the C 1s binding energy shift in our case, since the work function of cobalt is reported to be around 5 eV.⁶⁴ Another possible reason is the influence of the final state effects on the binding energy shifts. We recall that the binding energy measured in a photoemission experiment does not directly reflect the state of the atom before photoemission (initial state), but is also affected by the redistribution of all surrounding electrons after photoemission in order to screen the core hole (final state effects). The effectiveness of the core hole screening depends not only on the particular element (intra-atomic screening), but also on the surrounding environment, i.e., atom co-ordination number and interaction with the support (extra-atomic screening). Therefore, it is possible that the magnitude of the C 1s peak shift upon doping is influenced by differences in the final state effects among different systems, and might be not a safe indicator of the charge doping.

The stability of graphene layer on ZnO was also tested upon ethanol exposure/desorption cycles in the UHV chamber. The Raman spectra recorded after three repeated ethanol exposure/desorption cycles show significant increase of the I_D/I_G intensity ratio along with a considerable broadening of the G and D bands (see Figure 3.1a and Table 3.1). Similar Raman spectra features have been recently ascribed to significant structural disorder of graphene due to the formation of defects.⁶⁵ Figure 3.5 shows the optical microscopy (OM) images and the corresponding Raman spectra of G-ZnO after ethanol exposure/desorption. From the OM images, it can be seen that the initially intact graphene layer was fragmented in smaller graphene flakes of 5 to 20 μm size after ethanol exposure. In addition, micro-Raman measurements in points with different OM image contrast confirm the presence of micro-boundaries, where the ZnO substrate is not covered by graphene. The micro-Raman results are also supported by the decrease of the C 1s to Zn 2p signal ratio after ethanol exposure (see Figure 3.6). This is a quite remarkable result, since graphene is generally considered to be chemically inert to the interaction with gases. In addition, liquid ethanol was used for the removal of the PMMA layer without producing significant defect density (see Figure 3.5a). This indicates that during the desorption cycles ethanol reacts with graphene, possibly with dangling carbon bonds at the edge/boundaries of graphene introducing defects.

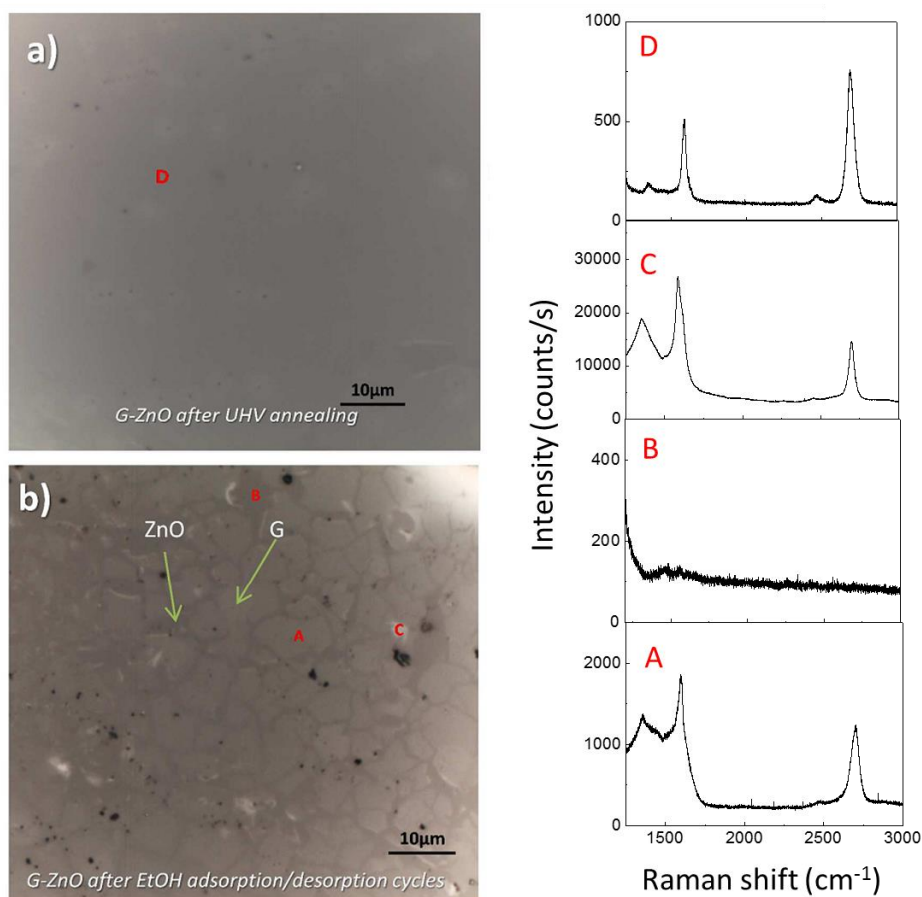


Figure 3.5 Optical microscopy images of (a) G-ZnO sample after annealing in UHV and (b) G-ZnO sample after annealing in UHV and 3 repeated ethanol exposure/desorption cycles. Raman measurements in points A, B, C and D shown in the Figures. (a) and (b) are included.

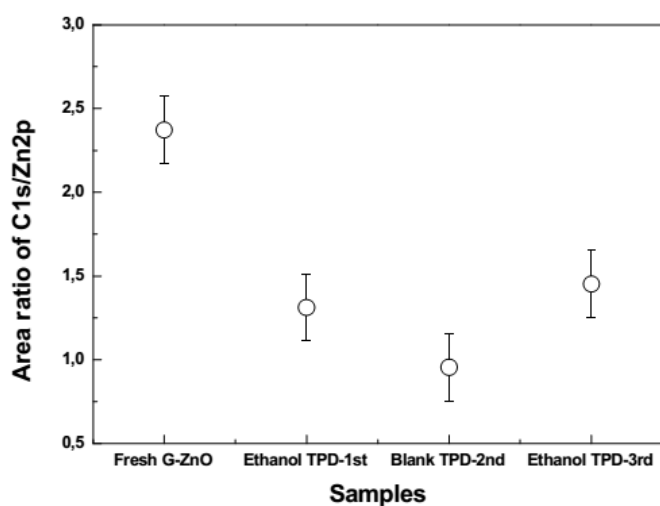


Figure 3.6 The evolution of the XPS C 1s to Zn 2p intensity ratio of G-ZnO sample exposed to ethanol at - 150 °C and subsequently annealed up to 350 °C.

The results presented above can inspire new strategies to control the metal–support interaction in applications where the surface modification without the influence of the bulk characteristics of a material is required. This can be directly applicable in heterogeneous catalytic reactions where strong interaction between the active phase and the support has been blamed for the catalysts' deactivation. For example, cobalt on oxide supports is used in two industrially relevant reactions, namely, the carbonylation of glycerol and the Fischer–Tropsch process. In both cases, strong metal support interaction induces formation of mixed cobalt-support oxides, which are difficult to reduce and cause irreversible deactivation.^{66,67} Using a model system we show here that graphene can prevent diffusion phenomena at the metal/oxide interface upon thermal treatment and eventually suppresses metal oxidation. Apparently, in industrial applications, easily scalable preparation methods of the graphene/oxide interface should be used, like, for example, via graphene oxide precursors,⁶⁸ while the stability of graphene under reaction conditions should be improved. However, cobalt/graphene and graphene/ZnO composite materials are already investigated for optoelectronic, photocatalytic, electrochemical and many other applications. In general, we believe that the results presented here do not concern only the particular Co–ZnO interface, but might be of broad interest in applications where metal–oxide or oxide–graphene interfaces play a key role.

3.4 Conclusions

Summarizing, CVD-grown single layer graphene was transferred onto ZnO(0001) and subsequently Co was deposited in order to investigate the effect of graphene interlayer on the Co–ZnO interaction. It is shown that graphene could effectively prevent the oxidation of Co by the ZnO support and decrease cobalt dispersion. Raman results indicated graphene was in p-type doping upon Co deposition and UHV annealing, but relatively low defect density.

3.5 References

- (1) Stakheev, A. Y.; Kustov, L. . Effects of the Support on the Morphology and Electronic Properties of Supported Metal Clusters: Modern Concepts and Progress in 1990s. *Appl. Catal. A Gen.* **1999**, *188* (1-2), 3–35.
- (2) Zhou, W.-P.; Yang, X.; Vukmirovic, M. B.; Koel, B. E.; Jiao, J.; Peng, G.; Mavrikakis, M.; Adzic, R. R. Improving Electrocatalysts for O₂ Reduction by Fine-Tuning the Pt-Support Interaction: Pt Monolayer on the Surfaces of a Pd₃Fe(111) Single-Crystal Alloy. *J. Am. Chem. Soc.* **2009**, *131* (35), 12755–12762.
- (3) Fujitani, T.; Nakamura, J. The Chemical Modification Seen in the Cu/ZnO Methanol Synthesis Catalysts. *Appl. Catal. A Gen.* **2000**, *191* (1-2), 111–129.
- (4) Kanan, D. K.; Carter, E. A. Band Gap Engineering of MnO via ZnO Alloying: A Potential New Visible-Light Photocatalyst. *J. Phys. Chem. C* **2012**, *116* (18), 9876–9887.
- (5) Zhou, H.; Qui, C.; Liu, Z.; Yang, H.; Hu, L.; Li, J.; Gu, C.; Sun, L. Thickness-Dependent Morphologies of Gold on N-Layer Graphenes. *J. Am. Chem. Soc.* **2010**, *132* (3), 944–946.
- (6) Liu, L.; Chen, Z.; Wang, L.; Stolyarova, P.; Elena; Taniguchi, T.; Watanabe, K.; Polyakova Stolyarova, E.; Taniguchi, T.; Watanabe, K.; et al. Slow Gold Adatom Diffusion on Graphene: Effect of Silicon Dioxide and Hexagonal Boron Nitride Substrates. *J. Phys. Chem. B* **2012**, *117* (16), 4305–4312.
- (7) Zhou, Z.; Gao, F.; Goodman, D. W. Deposition of Metal Clusters on Single-Layer graphene/Ru(0001): Factors That Govern Cluster Growth. *Surf. Sci.* **2010**, *604* (13-14), L31–L38.
- (8) Kamat, P. V. Graphene-Based Nanoarchitectures. Anchoring Semiconductor and Metal Nanoparticles on a Two-Dimensional Carbon Support. *J. Phys. Chem. Lett.* **2010**, *1* (2), 520–527.
- (9) Sutter, E.; Albrecht, P.; Wang, B.; Bocquet, M.-L.; Wu, L.; Zhu, Y.; Sutter, P. Arrays of Ru Nanoclusters with Narrow Size Distribution Templated by Monolayer Graphene on Ru. *Surf. Sci.* **2011**, *605* (17-18), 1676–1684.
- (10) Wintterlin, J.; Bocquet, M.-L. Graphene on Metal Surfaces. *Surf. Sci.* **2009**, *603* (10-12), 1841–1852.
- (11) Sutter, E.; Wang, B.; Albrecht, P.; Lahiri, J.; Bocquet, M.-L.; Sutter, P. Templating of Arrays of Ru Nanoclusters by Monolayer graphene/Ru Moirés with Different Periodicities. *J. Phys. Condens. Matter* **2012**, *24* (31), 314201.

- (12) Coy-Diaz, H.; Addou, R.; Batzill, M. Interface between Graphene and SrTiO₃ (001) Investigated by Scanning Tunneling Microscopy and Photoemission. *J. Phys. Chem. C* **2013**, *117* (40), 21006–21013.
- (13) Chen, S.; Brown, L.; Levendorf, M.; Cai, W.; Ju, S.-Y.; Edgeworth, J.; Li, X.; Magnuson, C. W.; Velamakanni, A.; Piner, R. D.; et al. Oxidation Resistance of Graphene-Coated Cu and Cu/Ni Alloy. *ACS Nano* **2011**, *5* (2), 1321–1327.
- (14) Singh Raman, R. K.; Chakraborty Banerjee, P.; Lobo, D. E.; Gullapalli, H.; Sumandasa, M.; Kumar, A.; Choudhary, L.; Tkacz, R.; Ajayan, P. M.; Majumder, M. Protecting Copper from Electrochemical Degradation by Graphene Coating. *Carbon* **2012**, *50* (11), 4040–4045.
- (15) Zhao, Y.; Xie, Y.; Hui, Y. Y.; Tang, L.; Jie, W.; Jiang, Y.; Xu, L.; Lau, S. P.; Chai, Y. Highly Impermeable and Transparent Graphene as an Ultra-Thin Protection Barrier for Ag Thin Films. *J. Mater. Chem. C* **2013**, *1* (32), 4956–4961.
- (16) Kang, D.; Kwon, J. Y.; Cho, H.; Sim, J.-H.; Hwang, H. S.; Kim, C. S.; Kim, Y. J.; Ruoff, R. S.; Shin, H. S. Oxidation Resistance of Iron and Copper Foils Coated with Reduced Graphene Oxide Multilayers. *ACS Nano* **2012**, *6* (9), 7763–7769.
- (17) Law, Y. T.; Doh, W. H.; Luo, W.; Zafeirotos, S. A Comparative Study of Ethanol Reactivity over Ni, Co and NiCo-ZnO Model Catalysts. *J. Mol. Catal. A Chem.* **2014**, *381* (0), 89–98.
- (18) Thomas, K. J.; Sheeba, M.; Nampoore, V. P. N.; Vallabhan, C. P. G.; Radhakrishnan, P. Raman Spectra of Polymethyl Methacrylate Optical Fibres Excited by A 532 Nm Diode Pumped Solid State Laser. *J. Opt. A-Pure Appl. Opt.* **2008**, *10* (5), 55303.
- (19) Babanov, Y. A.; Nemtsova, O. M. M.; Kamensky, I. Y. Y.; Mikhailova, S. S. S. The Determination of the True Profile of XPS Line by Regularization Method: I. Mathematical Algorithm and Numerical Simulations. *J. Electron Spectros. Relat. Phenomena* **2010**, *182* (3), 90–96.
- (20) Fulghum, J. E. Recent Developments in High Energy and Spatial Resolution Analysis of Polymers by XPS. *J. Electron Spectros. Relat. Phenomena* **1999**, *100* (1-3), 331–355.
- (21) Nathawat, R.; Kumar, A.; Acharya, N. K.; Vijay, Y. K. XPS and AFM Surface Study of PMMA Irradiated by Electron Beam. *Surf. Coatings Technol.* **2009**, *203* (17-18), 2600–2604.
- (22) Lin, Y.-C.; Lu, C.-C.; Yeh, C.-H.; Jin, C.; Suenaga, K.; Chiu, P.-W. Graphene Annealing: How Clean Can It Be? *Nano Lett.* **2012**, *12* (1), 414–419.

- (23) Briggs, D.; Seah, P. *Practical Surface Analysis: Auger and X-Ray Photoelectron Spectroscopy*; Wiley, 1990; Vol. 1.
- (24) Suzuki, S.; Orofeo, C. M.; Wang, S. M.; Maeda, F.; Takamura, M.; Hibino, H. Structural Instability of Transferred Graphene Grown by Chemical Vapor Deposition against Heating. *J. Phys. Chem. C* **2013**, *117* (42), 22123–22130.
- (25) Casiraghi, C.; Pisana, S.; Novoselov, K. S.; Geim, A. K.; Ferrari, A. C. Raman Fingerprint of Charged Impurities in Graphene. *Appl. Phys. Lett.* **2007**, *91* (23), 233108.
- (26) Ni, Z.; Wang, Y.; Yu, T.; Shen, Z. Raman Spectroscopy and Imaging of Graphene. *Nano Res.* **2008**, *1* (4), 273–291.
- (27) Machado, B. F.; Serp, P. Graphene-Based Materials for Catalysis. *Catal. Sci. Technol.* **2012**, *2* (1), 54–75.
- (28) Malard, L. M. M.; Pimenta, M. A. A.; Dresselhaus, G.; Dresselhaus, M. S. S. Raman Spectroscopy in Graphene. *Phys. Rep.* **2009**, *473* (5-6), 51–87.
- (29) Petrie, W. T.; Vohs, J. M. Interaction of Platinum Films with the (0001) and (0001) Surfaces of ZnO. *J. Chem. Phys.* **1994**, *101* (9), 8098–8107.
- (30) Qiu, H.; Gallino, F.; Di Valentin, C.; Wang, Y. Shallow Donor States Induced by In-Diffused Cu in ZnO: A Combined HREELS and Hybrid DFT Study. *Phys. Rev. Lett.* **2011**, *106* (6), 066401.
- (31) Liu, Y.; Willis, R. F.; Emtsev, K. V.; Seyller, T. Plasmon Dispersion and Damping in Electrically Isolated Two-Dimensional Charge Sheets. *Phys. Rev. B* **2008**, *78* (20), 201403.
- (32) Koch, R. J.; Seyller, T.; Schaefer, J. A. Strong Phonon-Plasmon Coupled Modes in the Graphene/silicon Carbide Heterosystem. *Phys. Rev. B* **2010**, *82* (20), 201413.
- (33) Tanuma, S.; Powell, C. J.; Penn, D. R. Calculations of Electron Inelastic Mean Free Paths. V. Data for 14 Organic Compounds over the 50-2000 eV Range. *Surf. Interface Anal.* **1994**, *21* (3), 165–176.
- (34) Maki, H.; Ichinose, N.; Ohashi, N.; Haneda, H.; Tanaka, J. The Lattice Relaxation of ZnO Single Crystal (0001) Surface. *Surf. Sci.* **2000**, *457* (3), 377–382.
- (35) Lotya, M.; Hernandez, Y.; King, P. J.; Smith, R. J.; Nicolosi, V.; Karlsson, L. S.; Blighe, F. M.; De, S.; Wang, Z.; McGovern, I. T.; et al. Liquid Phase Production of Graphene by Exfoliation of Graphite in Surfactant/Water Solutions. *J. Am. Chem. Soc.* **2009**, *131* (10), 3611–3620.

- (36) Nemes-Incze, P.; Osváth, Z.; Kamarás, K.; Biró, L. P. Anomalies in Thickness Measurements of Graphene and Few Layer Graphite Crystals by Tapping Mode Atomic Force Microscopy. *Carbon* **2008**, *46* (11), 1435–1442.
- (37) Ferrari, A. C.; Meyer, J. C.; Scardaci, V.; Casiraghi, C.; Lazzeri, M.; Mauri, F.; Piscanec, S.; Jiang, D.; Novoselov, K. S.; Roth, S.; et al. Raman Spectrum of Graphene and Graphene Layers. *Phys. Rev. Lett.* **2006**, *97* (18), 187401.
- (38) Xu, K.; Cao, P.; Heath, J. R. Graphene Visualizes the First Water Adlayers on Mica at Ambient Conditions. *Science* **2010**, *329* (5996), 1188–1191.
- (39) Law, Y. T.; Skála, T.; Piš, I.; Nehasil, V.; Vondráček, M.; Zafeiratos, S.; Skala, T.; Pis, I.; Nehasil, V.; Vondracek, M.; et al. Bimetallic Nickel–Cobalt Nanosized Layers Supported on Polar ZnO Surfaces: Metal–Support Interaction and Alloy Effects Studied by Synchrotron Radiation X-Ray Photoelectron Spectroscopy. *J. Phys. Chem. C* **2012**, *116* (18), 10048–10056.
- (40) Zafeiratos, S.; Dintzer, T.; Teschner, D.; Blume, R.; Hävecker, M.; Knop-Gericke, A.; Schlögl, R.; Haevecker, M.; Knop-Gericke, A.; Schloegl, R. Methanol Oxidation over Model Cobalt Catalysts: Influence of the Cobalt Oxidation State on the Reactivity. *J. Catal.* **2010**, *269* (2), 309–317.
- (41) Ha, D.-H. D.-H.; Moreau, L. M.; Honrao, S.; Hennig, R. G.; Robinson, R. D. The Oxidation of Cobalt Nanoparticles into Kirkendall-Hollowed CoO and Co₃O₄: The Diffusion Mechanisms and Atomic Structural Transformations. *J. Phys. Chem. C* **2013**, *117* (27), 14303–14312.
- (42) Hyman, M. P.; Martono, E.; Vohs, J. M. Studies of the Structure and Interfacial Chemistry of Co Layers on ZnO(0001). *J. Phys. Chem. C* **2010**, *114* (40), 16892–16899.
- (43) Topsakal, M.; Şahin, H.; Ciraci, S. Graphene Coatings: An Efficient Protection from Oxidation. *Phys. Rev. B* **2012**, *85* (15), 155445.
- (44) Bunch, J. S.; Verbridge, S. S.; Alden, J. S.; van der Zande, A. M.; Parpia, J. M.; Craighead, H. G.; McEuen, P. L. Impermeable Atomic Membranes from Graphene Sheets. *Nano Lett.* **2008**, *8* (8), 2458–2462.
- (45) Hess, C.; Tzolova-Mueller, G.; Herbert, R.; Tzolova-Muller, G.; Herbert, R. The Influence of Water on The Dispersion of Vanadia Supported on Silica SBA-15: A Combined XPS and Raman Study. *J. Phys. Chem. C* **2007**, *111* (26), 9471–9479.
- (46) Venezia, A. M. X-Ray Photoelectron Spectroscopy (XPS) for Catalysts Characterization. *Catal. Today* **2003**, *77* (4), 359–370.

- (47) Martin, B. D.; Finke, R. G. Cobalt-Carbon Homolysis and Bond Dissociation Energy Studies of Biological Alkylcobalamins: Methylcobalamin, Including a.g.toreq.1015 Co-CH₃ Homolysis Rate Enhancement at 25.degree. Following One-Electron Reduction. *J. Am. Chem. Soc.* **1990**, *112* (6), 2419–2420.
- (48) Domenicano, A.; Hargittai, I. *Strength from Weakness: Structural Consequences of Weak Interactions in Molecules, Supramolecules, and Crystals*; Springer Netherlands, 2002.
- (49) Qi, W. H.; Wang, M. P.; Zhou, M.; Hu, W. Y. Surface-Area-Difference Model for Thermodynamic Properties of Metallic Nanocrystals. *J. Phys. D. Appl. Phys.* **2005**, *38* (9), 1429–1436.
- (50) Suk, J. W.; Kitt, A.; Magnuson, C. W.; Hao, Y.; Ahmed, S.; An, J.; Swan, A. K.; Goldberg, B. B.; Ruoff, R. S. Transfer of CVD-Grown Monolayer Graphene onto Arbitrary Substrates. *ACS Nano* **2011**, *5* (9), 6916–6924.
- (51) Canc, L. G.; Jorio, A.; Ferreira, E. H. M.; Stavale, F.; Achete, C. A.; Capaz, R. B.; Moutinho, M. V. O.; Lombardo, A.; Kulmala, T. S.; Ferrari, A. C. Quantifying Defects in Graphene via Raman Spectroscopy at Different Excitation Energies. *Nano Lett.* **2011**, *11* (8), 3190–3196.
- (52) Wang, S. M.; Qiao, L.; Zhao, C. M.; Zhang, X. M.; Chen, J. L.; Tian, H. W.; Zheng, W. T.; Han, Z. B.; Bae, S.; Kim, H.; et al. A Growth Mechanism for Graphene Deposited on Polycrystalline Co Film by Plasma Enhanced Chemical Vapor Deposition. *New J. Chem.* **2013**, *37* (5), 1616–1622.
- (53) Gong, C.; McDonnell, S.; Qin, X.; Azcatl, A.; Dong, H.; Chabal, Y. J.; Cho, K.; Wallace, R. M. Realistic Metal–Graphene Contact Structures. *ACS Nano* **2014**, *8* (1), 642–649.
- (54) Leong, W. S.; Nai, C. T.; Thong, J. T. L. What Does Annealing Do to Metal–Graphene Contacts? *Nano Lett.* **2014**, *14* (7), 3840–3847.
- (55) Blanc, N.; Jean, F.; Krasheninnikov, A. V.; Renaud, G.; Coraux, J. Strains Induced by Point Defects in Graphene on a Metal. *Phys. Rev. Lett.* **2013**, *111* (8), 85501.
- (56) Das, A.; Pisana, S.; Chakraborty, B.; Piscanec, S.; Saha, S. K.; Waghmare, U. V.; Novoselov, K. S.; Krishnamurthy, H. R.; Geim, A. K.; Ferrari, A. C.; et al. Monitoring Dopants by Raman Scattering in an Electrochemically Top-Gated Graphene Transistor. *Nat. Nanotechnol.* **2008**, *3* (4), 210–215.
- (57) Lee, J.; Novoselov, K. S. K.; Shin, H. S. H. Interaction between Metal and Graphene: Dependence on the Layer Number of Graphene. *ACS Nano* **2011**, *5* (1), 608–612.

- (58) Luo, Z.; Somers, L. A.; Dan, Y.; Ly, T.; Kybert, N. J.; Mele, E. J.; Johnson, A. T. C.; Charlie Johnson, A. T. Size-Selective Nanoparticle Growth on Few-Layer Graphene Films. *Nano Lett.* **2010**, *10* (3), 777–781.
- (59) Khomyakov, P. a.; Giovannetti, G.; Rusu, P. C.; Brocks, G.; Van Den Brink, J.; Kelly, P. J. First-Principles Study of the Interaction and Charge Transfer between Graphene and Metals. *Phys. Rev. B* **2009**, *79* (19), 1–12.
- (60) Liu, X.; Wang, C. Z.; Yao, Y. X.; Lu, W. C.; Hupalo, M.; Tringides, M. C.; Ho, K. M. Bonding and Charge Transfer by Metal Adatom Adsorption on Graphene. *Phys. Rev. B* **2011**, *83* (23), 235411.
- (61) Huang, X. L.; Wang, R. Z.; Xu, D.; Wang, Z. L.; Wang, H. G.; Xu, J. J.; Wu, Z.; Liu, Q. C.; Zhang, Y.; Zhang, X. B. Homogeneous CoO on Graphene for Binder-Free and Ultralong-Life Lithium Ion Batteries. *Adv. Funct. Mater.* **2013**, *23* (35), 4345–4353.
- (62) Dahal, A.; Addou, R.; Coy-Diaz, H.; Lallo, J.; Batzill, M. Charge Doping of Graphene in Metal/graphene/dielectric Sandwich Structures Evaluated by C-1s Core Level Photoemission Spectroscopy. *APL Mater.* **2013**, *1* (4), 042107.
- (63) Zhang, L.; Ye, Y.; Cheng, D.; Pan, H.; Zhu, J. Intercalation of Li at the Graphene/Cu Interface. *J. Phys. Chem. C* **2013**, *117* (18), 9259–9265.
- (64) Haag, N.; Steil, S.; Großmann, N.; Fetzer, R.; Cinchetti, M.; Aeschlimann, M. Tailoring the Energy Level Alignment at the Co/Al₂O₃ Interface by Controlled Cobalt Oxidation. *Appl. Phys. Lett.* **2013**, *103* (25), 251603.
- (65) O’Hern, S. C.; Boutilier, M. S. H.; Idrobo, J.-C.; Song, Y.; Kong, J.; Laoui, T.; Atieh, M.; Karnik, R.; O’Hern, S. C.; Boutilier, M. S. H.; et al. Selective Ionic Transport through Tunable Subnanometer Pores in Single-Layer Graphene Membranes. *Nano Lett.* **2014**, *14* (3), 1234–1241.
- (66) Koo, H.-M.; Lee, B. S.; Park, M.-J.; Moon, D. J.; Roh, H.-S.; Bae, J. W. Fischer–Tropsch Synthesis on Cobalt/Al₂O₃-Modified SiC Catalysts: Effect of Cobalt–alumina Interactions. *Catal. Sci. Technol.* **2014**, *4* (2), 343–351.
- (67) Rubio-Marcos, F.; Calvino-Casilda, V.; Bañares, M. A.; Fernandez, J. F. Control of the Interphases Formation Degree in Co₃O₄/ZnO Catalysts. *ChemCatChem* **2013**, *5* (6), 1431–1440.
- (68) Gong, Y.; Meng, X.; Zou, C.; Yao, Y.; Fu, W.; Wang, M.; Yin, G.; Huang, Z.; Liao, X.; Chen, X. A Facile One-Pot Synthesis of Yolk-Shell ZnO Microsphere–graphene Composite Induced by Graphene Oxide. *Mater. Lett.* **2013**, *106*, 171–174.

- (69) Luo, W.; Doh, W. H.; Law, Y. T.; Aweke, F.; Ksiazek-sobieszek, A.; Sobieszek, A.; Salamacha, L.; Skrzypiec, K.; Machocki, A.; Zafeiratos, S. Single-Layer Graphene as an Effective Mediator of the Metal–Support Interaction. *J. Phys. Chem. Lett.* **2014**, *5*, 1837–1844.

Chapter 4

Influence of graphene interlayer on the redox properties of oxides supported Co particles

Chapter 4 Influence of graphene interlayer on the redox properties of oxides supported Co particles

4.1 Introduction

Cobalt is a transition metal which is employed as a catalyst in a variety of important chemical reactions. Notably, it is a selective Fischer–Tropsch synthesis (FTS) catalyst, which is an industrial process to convert synthesis gas (CO and H₂) to synthetic liquid fuels and valuable chemicals.^{1,2} In recent years, cobalt-based catalysts are gaining extensive interest in reactions using hydrocarbon reforming to produce renewable fuels.^{3,4} For most of their catalytic applications cobalt particles are supported on suitable supports, typically metal oxides, with the aim to increase their dispersion and enhance their stability at aggressive catalytic reaction conditions (usually high temperature and pressure). The role of the support, and in particular of the cobalt-support interaction on the catalytic properties, remains an open question, even if it is widely acknowledged that the support affects the cobalt particle size, reducibility and stability.⁵ For example, in FTS reaction Al₂O₃ support is considered crucial for the formation of small cobalt particles, but on the other hand it deteriorates the catalytic performance by formation of inactive cobalt species, such as cobalt aluminates, which are difficult to reduce.⁶ Catalytic supports based on silicon oxide are considered to have a relatively weak interaction with Co, forming rather large cobalt particles which are easier to reduce as compared to the smaller ones.^{1,7} However in some cases, under extreme reaction conditions formation of inactive cobalt silicates is unavoidable.¹ ZnO is another commonly used support for cobalt-based catalysts, with potentially promising applications in alcohol oxidation and reforming for hydrogen production^{8,9} and recently for FTS reaction as well¹⁰. During ethanol steam reforming reaction ZnO has been reported to strongly interact and oxidize Co, while diffusion of cobalt into ZnO lattice at high temperature is also possible.^{8,11}

Carbon-based materials, such as carbon nanotubes and carbon fibers, are studied as possible substitutes of oxide supports in many catalytic reactions, since they promote the oxidation stability of the metal and have some certain advantages such as high thermal conductivity. However, it is difficult to prepare pelletized carbon materials with high mechanical stability¹² and the high cost of CNTs is also a major problem.¹³ Graphene is potentially promising as a catalyst support due to its high mechanical stability, high thermal conductivity and high

electron mobility. Nonetheless, free-standing single-layer graphene is often corrugated and wrinkled in unpredictable ways, or even recombines to form the so-called *few-layer graphene*. This will unavoidably affect its unique properties and calls for suitable supports where the 2D nature of graphene can be constrained.

Graphene-protected oxides could be a good compromise for a new class of catalytic supports combining the desirable macroscopic properties of oxides (thermal stability, microstructure etc.), and the metal-support interaction of carbon-based materials. The interaction of metal particles with graphene grown over metals^{14–16} and nonmetals such as SiO₂^{17–19} and SiC^{20–22} has been reported, even so very limited studies focus on catalytic-relevant oxide substrates.¹⁴ In chapter 3, we have shown that single layer graphene can dramatically influence the interaction between Co and ZnO²³ and protect Co from being oxidized by ZnO upon vacuum annealing. In the work presented in this chapter, we deposit cobalt over graphene on planar ZnO and SiO₂ substrates and perform a comparative study of its redox properties upon near ambient pressure O₂ and H₂ gas exposure. The motivation behind this work is to describe the effect of oxide-supported graphene on the metal-support interaction using model systems resembling realistic catalysts.

4.2 Experimental Methods

4.2.1 Materials

The substrates used for cobalt deposition can be categorized in bare planar oxide substrates (SiO₂, ZnO(0001)), the same substrates being covered by single-layer graphene (G/SiO₂, G/ZnO) and highly oriented pyrolytic graphite (HOPG), which will be used as the bulk reference of graphene. Samples for low pressure study were deposited with Co for a period of 5 min and with a constant evaporation rate of 0.07 nm/min, while the deposition condition for medium pressure study was 10 min with a rate of 0.08 nm/min. Details of sample preparation can be found in Chapter 2, section 2.1.

The cobalt overlayer thickness was calculated through quantification of XPS results based on a number of simplifying assumptions,²⁴ suitable for flat and homogeneous samples with negligible elastic scattering of photoelectrons (please referring to section 2.2.1.5). The calculated values are shown in Table 4.1. It will be shown in the AFM results that Co forms relatively flat layer on ZnO and SiO₂ which meets the assumptions of the calculation. On G/ZnO, G/SiO₂ and HOPG, Co forms nanoparticle structure, in this case, this method will

underestimate the Co thickness. However, since Co was evaporated under identical conditions (i.e., evaporation flux rate, duration and substrate temperature), the Co amount is assumed to be the same.

Table 4.1 Calculated Co thickness.

Samples	Co/ZnO	Co/SiO ₂	Co/G/ZnO	Co/G/SiO ₂	Co/HOPG
Co thickness for Low pressure study (nm)	0.32	0.35	0.17	0.16	0.14
Co thickness for Medium pressure study (nm)	0.80	0.79	0.48	0.54	-

4.2.2 Characterization

The low pressure redox experiments and the XPS measurements were carried out in the UHV system described in Chapter 2, section 2.3. The sample was mounted on a molybdenum sample holder (see Figure 4.1a) which could be heated either by the resistance mode of a tungsten filament or by electron bombardment mode heating (for temperatures higher than 300 °C). Experiments were performed using Al K α source and X-ray photoelectron spectra were recorded at normal (0 degrees) and at grazing (80 degrees) take-off angles. Oxygen and hydrogen exposure of samples was carried out in the main chamber by leak valves and the pressure was monitored by an ion gauge. Each oxidation temperature was kept for 0.5 h while flash annealing was used for the reduction step.

The medium pressure redox study and X-ray photoelectron spectroscopy (XPS) measurements were carried out in the VSW UHV setup (base pressure 1×10^{-9} mbar) (see Chapter 2, section 2.3). A monochromated Al K α X-ray source (1486.6 eV; anode operating at 240 W) was used as the incident radiation. The oxidation/reduction treatments were carried out in 1 liter volume flow-through an ambient pressure reactor attached to the UHV setup. Samples were mounted on the sample holder which was designed to be able to work under high pressure conditions (see Figure 4.1b). Each oxidation/reduction step was performed by annealing for 30 min at various temperatures in 7 mbar O₂ or H₂ with a leak rate of 40 mbar l/s, respectively. Subsequently the sample was cooled at room temperature in gas, pumped down to 5×10^{-8} mbar and was immediately transferred under vacuum into the analysis chamber for characterization.

The oxidation state of cobalt is represented here by the average valence state x (Co ^{$x+$}). These values are computed from the areas of Co₃O₄, CoO and Co components, obtained by deconvolution of the overall Co 2p spectra, under the assumption that the atomic sensitivity factors are the same for all states. This represents valence states x of 2.67, 2 and 0 for Co₃O₄,

CoO and Co respectively. The Co/substrate peak area ratio (R) was calculated using the integrated XPS peak area of Co 2p and that of the more intense substrate peak (Zn 2p and Si 2p for ZnO and SiO₂, respectively), normalized to the atomic sensitivity factors²⁵. In case of graphene-coated oxides, the C 1s signal was also admeasured with the substrate signal. A reference Co/ZnO (0001) sample was investigated by Near-edge X-ray absorption fine structure spectroscopy (NEXAFS) at the ISISS beam line at Helmholtz Zentrum, Berlin.²⁶ The sample was measured in the total electron yield (TEY) mode after 2 hours treatment at 320 °C in 0.3 mbar H₂.

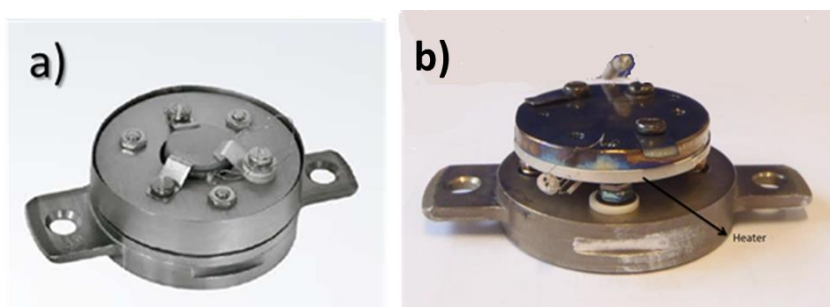


Figure 4.1 The two type of sample holders used for the a) UHV and low pressure gas exposure and b) medium pressure gas exposure experiments.

Raman spectra were acquired at room temperature and atmospheric conditions using a micro-Raman spectrometer (Horiba LabRam), with excitation wavelength of 532 nm. A 100× objective was used to focus the excitation laser to an approximately 1 μm spot with a laser power of less than 1 mW to avoid heating and damage the sample. Scanning electron microscopy (SEM) measurements were performed using Jeol JSM-6700F (Japan) electron microscope at accelerating voltage of 10 kV. The morphology of the samples was mainly investigated by an AFM microscope (NTEGRA Aura from NT-MDT) at ambient conditions and under tapping mode operation.

4.3 Results and discussion. Part I: low pressure redox behavior

4.3.1 Characterization of the *as-prepared* samples

The quality of graphene layer after transfer and before cobalt deposition was verified by Raman spectroscopy and SEM microscopy (*please refer to supporting information in appendices*). These results show that graphene layer is flat and uniform with some instinct bilayer islands and some wrinkles. Consequently cobalt was evaporated in vacuum over the various supports using identical conditions. *In situ* X-ray photoelectron spectroscopy (XPS) and *ex situ* atomic force microscopy (AFM) were used to probe the chemical state and the morphology of cobalt deposit prior to any treatment (Figure 4.2). For all samples the XPS Co 2p_{3/2} peak at 778.2 eV is asymmetric (c.a. 782 eV) due to the energy loss features and has a shoulder to the low energy side assigned to the Co L₃M₄₅M₄₅ Auger signal.²⁷ Comparison of the XP data shows great similarities in the spectra of oxide and carbon supported cobalt. A slightly enhanced intensity around 782 eV in the case of the Co/ZnO sample, proposes a superimposition of ionic Co²⁺ features which appear in this region, however the low intensity of the peak does not allow a reliable quantification of this feature.

The AFM topography images on bare SiO₂ and ZnO substrates show the formation of a uniform Co layer which follows the locally high and low features of the substrate.²⁸ This indicates that the initial Co deposition process on oxides approximates that of a layer by layer growth mode in agreement with previous studies.^{23,29} On the contrary on carbon substrates cobalt forms individual, homogeneously-dispersed, nanoparticles with an estimated average particle size of ~10 nm on G/ZnO and G/SiO₂ and ~16 nm on HOPG. The enhanced mobility of cobalt adatoms over the carbon support as compared to oxides is accountable for the cobalt nanoparticles formation, in accordance with previous studies of cobalt on graphene and amorphous carbon supports.^{23,30,31} Liu et al¹⁷ found that the diffusion constant of an Au adatom over a single layer graphene supported on SiO₂ is ~800 times higher compared to that for graphite, which was attributed to the higher local surface roughness of SiO₂ and the less reactive of HOPG surface. Notably, graphene-supported Co forms smaller particles than HOPG, which indicates differences in the Co adatoms diffusion in the two cases. This is correlated with previous studies of Au¹⁸, Ag³² and Pd¹⁹ on graphene which have shown that the metal particle morphology depends on the number of graphene layers, (i.e. the fewer the graphene layers, the smaller the metal particle size) due to the lower diffusion barrier on multi-layer graphene. Here we show that Co morphologies on oxide, graphene and HOPG substrates

show different diffusion behavior, even if the interaction between Co and graphene is stronger than that of Au.³³

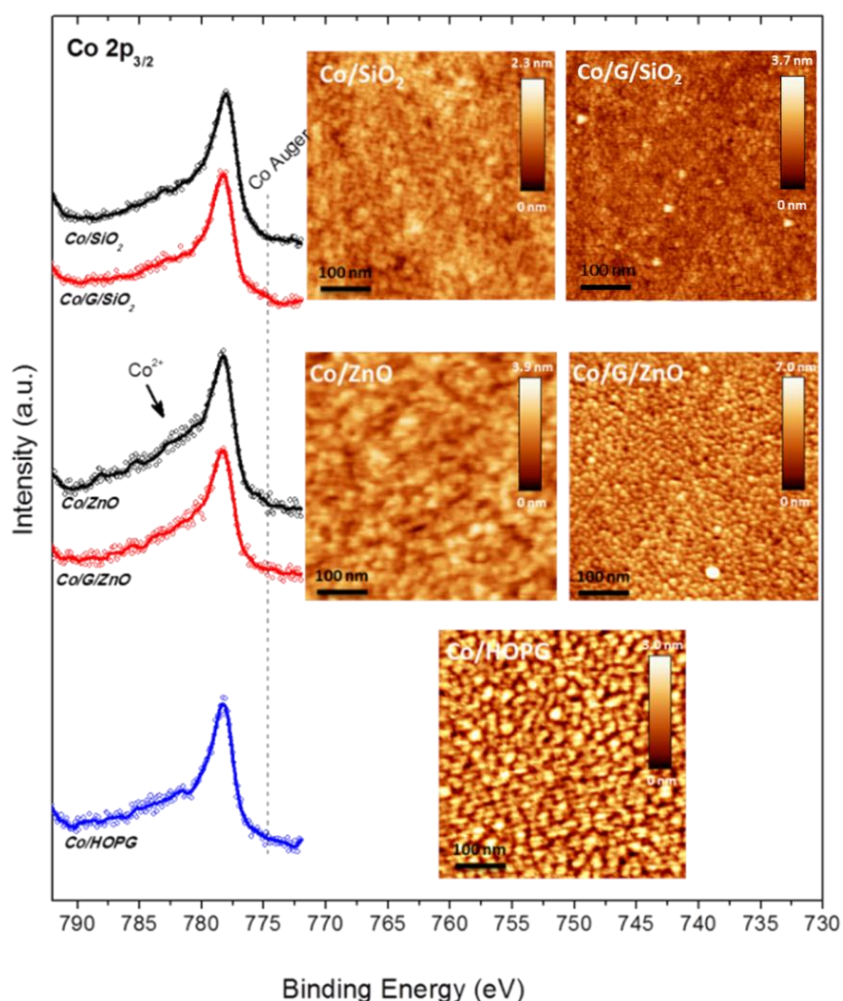


Figure 4.2 Co $2p_{3/2}$ XPS spectra and tapping mode AFM topographic images ($500 \times 500 \text{ nm}^2$) of 0.35 nm Co deposited under vacuum on 5 different supports at room temperature.

4.3.2 Oxidation and reduction at 5×10^{-7} mbar

A set of Co $2p_{3/2}$ XPS spectra obtained from 0.35 nm cobalt deposited on ZnO and G/ZnO substrates and consequently exposed to 5×10^{-7} mbar O_2 and H_2 is shown in Figure 4.3 a. For a complete series of spectra of all samples as a function of the annealing temperature please refer to *supporting information in appendices*. In O_2 the Co $2p_{3/2}$ spectrum is broad indicating the superposition of spectral features due to more than one cobalt oxidation states. Peak fitting using reference peaks suggests that cobalt is partially oxidized to a mixture of CoO (with a Co^{2+} peak at 780.6 eV) and metallic Co^0 (with a component at 778.2 eV). Simple comparison of the Co $2p_{3/2}$ spectra on the two supports reveals that cobalt on G/ZnO is less oxidized than on the ZnO support. Comparison of the Co $2p_{3/2}$ peaks in the maximum annealing temperature

in H₂ shows significant differences in the two substrates. In particular, over G/ZnO oxidized cobalt is fully reduced to Co⁰ while on the contrary over ZnO cobalt is oxidized even further to the CoO face.

The portion of metallic and CoO components in the Co 2p XPS spectrum can provide information on the average valence distribution of Co cations on the surface. The variation of the average Co valence as a function of the annealing temperature in O₂ and H₂ can be seen in Figure 4.3b. There is a clear difference in the Co valence evolution between oxide and carbon supports both in O₂ and H₂ exposure. In O₂ cobalt on bare oxides (ZnO, SiO₂) is oxidized to a large extent (around 1.7 at 100 °C), while on carbon substrates the oxidation is limited (about 1 at 100 °C). Ionic cobalt is formed already at room temperature oxygen exposure and increases only slightly upon higher temperature oxidation (100 °C).

The reduction of CoO in H₂ depends very much from the support, with carbon substrates dramatically decreasing the reduction temperature. Besides there are also distinct differences between bare ZnO and SiO₂ supports. In particular, on ZnO reduction of CoO starts at 150 °C and continues up to 250 °C, while above this temperature Co starts to re-oxidize up to formation of 100 % CoO at 350 °C. On the other hand on SiO₂ support CoO is gradually reduced with temperature, up to complete reduction to Co at 600 °C. In Chapter 3, we have shown that Co can be oxidized by ZnO substrate during UHV annealing due to the solid state reaction at the interface. Thus, annealing of Co/ZnO in low pressure H₂ combines two parallel processes: a reduction reaction by gas phase H₂ up to 250 °C and a dominant oxidation interfacial interaction with the ZnO support at higher temperature. In the case of SiO₂ support the interfacial oxidation does not occur and cobalt oxide is reduced either by gas phase H₂ or by thermal simple decomposition. As in the case of oxidation, carbon-based samples (Co/G/ZnO, Co/G/SiO₂ and Co/HOPG) exhibit similar characteristics in reducing environment. In particular, in H₂ effective reduction of CoO to metallic Co occurs already at 250 °C.

Figure 4.3c shows the evolution of the peak area ratio between Co 2p and the more intense substrate peak (Si 2p, Zn 2p and C 1s (for HOPG)) as a function of the annealing temperature. This Co/substrate ratio is indicative of the surface cobalt amount and therefore shrinkage, agglomeration or diffusion of cobalt into the substrate, will decrease it.³⁴ In order to facilitate the comparison among the samples, all ratios are normalized according to their initial ratio. As is evident, the peak area ratio follows the evolution of the Co valence presented in Figure 4.3b. Namely, in all samples the ratio decreases with temperature, with an exception of Co/ZnO,

where re-oxidation above 250 °C is accompanied by an increase of the ratio. One can anticipate that the higher temperature enhances the kinetics of surface diffusion and favors particles agglomeration, while oxidation of Co on ZnO in H₂ creates flat particles and re-establishment of the original particle morphology.

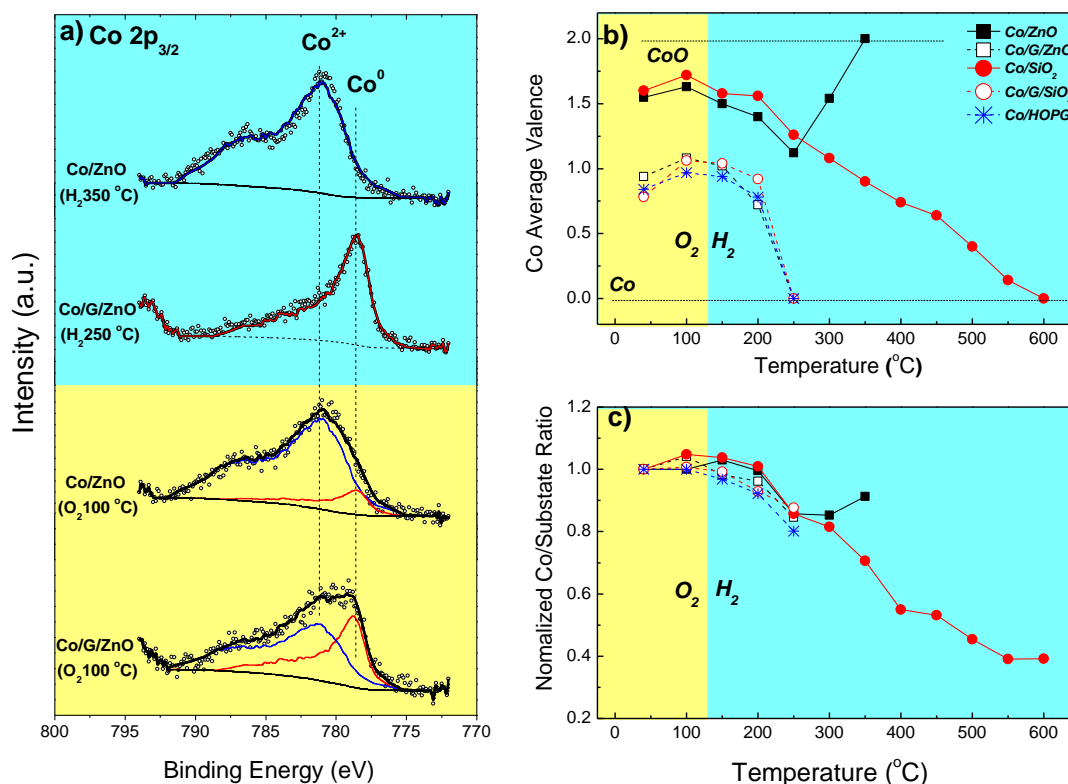


Figure 4.3 The Co 2p_{3/2} spectra of Co/ZnO and Co/G/ZnO samples after O₂ (yellow) and H₂ (cyan) exposure at characteristic temperatures b. The Co average valence and c. the normalized Co/substrate peak area ratio as a function of the annealing temperature. Two different regions indicate *annealing* in 5×10^{-7} mbar O₂ and in 5×10^{-7} mbar H₂, respectively.

The qualitative XPS finding regarding modification of Co particles morphology upon annealing can be confirmed from the AFM images taken after oxidation/reduction treatment (Figure 4.4). On SiO₂, Co is organized in small and dense nanoparticle arrays of about 10 nm size, confirming the XPS results of Figure 4.3c, which show intense agglomeration after the high temperature redox treatment. On the contrary on ZnO, cobalt overlayer remains flat and particles are not possible to be distinguished, within the lateral resolution of the instrument. The flat cobalt layer is also justified by the XPS results which indicated oxidation of cobalt to CoO that has previously reported to form relatively flat layers on ZnO²³. In the case of carbon-based samples, cobalt keeps the homogeneously dispersed nanoparticles morphology observed

in the fresh samples (Figure 4.2), however the size of the nanoparticles after the redox treatments is enlarged in accordance with the observed decrease in the Co/substrate XPS intensity ratio shown in Figure 4.3c. Comparison of the cobalt morphology on graphene and HOPG substrates indicates that graphene-supported cobalt forms in general smaller cobalt particles. This probably reflects the differences in the Co-substrate interaction, which favors cobalt mobility on the HOPG support and thus its agglomeration to bigger particles. It also indicates that although oxidation and reduction of Co on graphene and HOPG process in a similar way, smaller Co particles are maintained on graphene at all treatment stages.

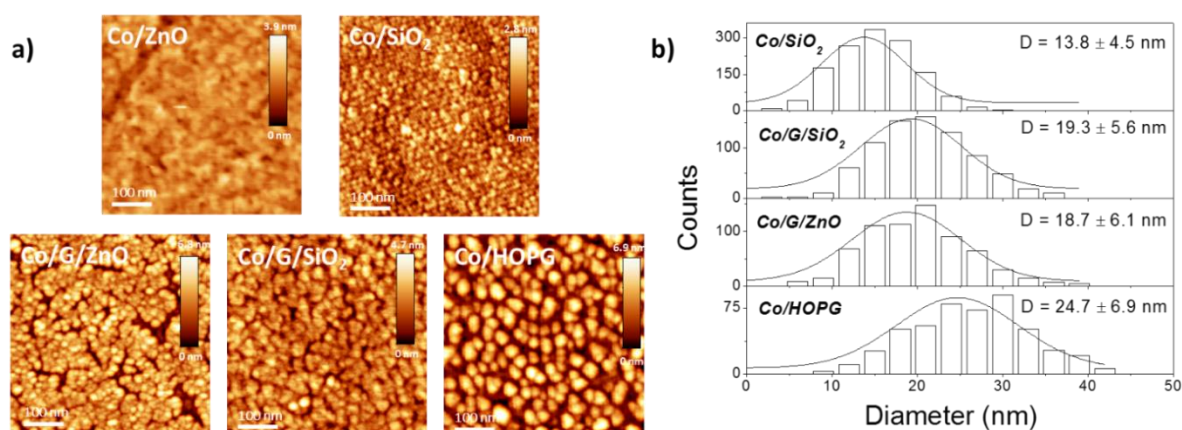


Figure 4.4 (a) Top view, tapping mode AFM topographic images ($500 \times 500 \text{ nm}^2$) of Co deposited on 5 different substrates after the high temperature redox treatment and (b) The histograms of Co particle diameter for the samples with particle structure.

4.3.3 Comparison of normal and grazing angle XPS

XPS measurements of Co $2p_{3/2}$ at 2 different take-off angles (normal and grazing) were employed to address the distribution of different cobalt oxidation states within the cobalt particles. For relatively flat and dense cobalt particles the effective escape depth λ of photoelectrons change with the take-off angle θ , affecting the sampling depth d of the XPS measurement according to:^{35,36} $d = 3\lambda \cos\theta$. Thus assuming an average λ of Co 1.4 nm ³⁷, by varying the θ from 0° to 80° degrees the effective sampling depth (or information depth) changes from 4.2 nm at 0° to about 0.7 nm at 80° . Figure 4.5a shows characteristic Co $2p_{3/2}$ spectra of partly oxidized cobalt particles supported on ZnO and HOPG at normal and grazing take-off angles. Comparison of the ionic (Co^{2+}) and metal (Co^0) cobalt components of the spectra in the two take-off angles shows a different tendency for the two substrates. In particular, at grazing angle measurements, the Co^{2+} component is enhanced on HOPG but declines on ZnO-supported cobalt. The behavior described above is reproduced at Figure 4.5b

which shows the % atomic fraction of Co^{2+} ions calculated by deconvolution of the Co 2p spectrum in two components (Co^{2+} and Co^0) for normal (0°) and grazing (80°) take-off angles. Several oxidation degrees of cobalt supported on HOPG and bare oxides, obtained after O_2 treatments up to 100°C , are included in the graph. As shown above cobalt oxidation on carbon-based supports proceeds in a similar manner therefore the results on HOPG are representative also for graphene covered oxides. In the graph of Figure 4.5b, homogenous distribution of Co^{2+} ions in the volume of cobalt particles should not give any difference in the two collection angles, therefore the experimental points should coincide with the diagonal line of the graph. On the contrary, in case of preferential localization of Co^{2+} ions on the surface or the subsurface of cobalt particles, the experimental points should be above or below the diagonal line, respectively.

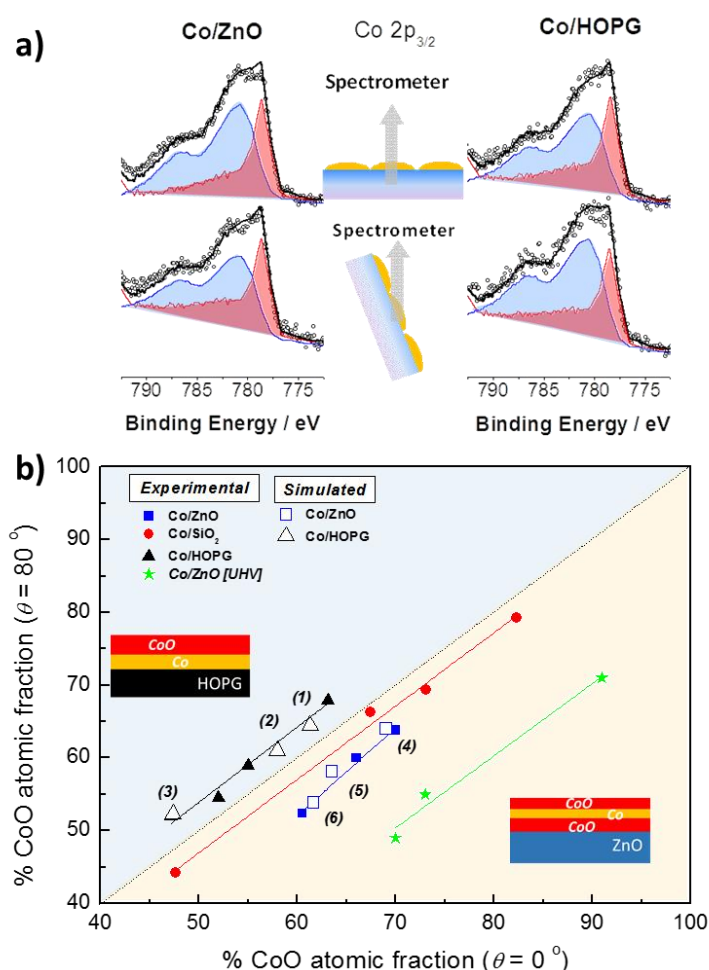


Figure 4.5 XPS measurement and SESSA simulation of supported cobalt oxidation state (O_2 pressure = 5×10^{-7} mbar, temperature $\leq 100^\circ\text{C}$) under two different take-off angles (0° and 80°). (a) XPS spectra of Co/ZnO and Co/HOPG, (b) Experimental and simulated % CoO atomic fraction under two take-off angles and (inset) simulation models of Co/ZnO and Co/HOPG. The star points in (b) represent of Co oxidation by ZnO under UHV annealing condition, recorded as a reference.

As shown in Figure 4.5, in the case of Co on HOPG, the CoO atomic fraction is systematically higher at 80 ° as compared to 0 ° degrees measurements, while for Co/ZnO the trend is reversed. This means that on carbon substrates, oxidized cobalt is preferentially located at the surface of the particles, while on the contrary, on ZnO, a considerable amount of cobalt oxide at the subsurface, likely at the interface with the support, is noted. For comparison, the ARXPS results of Co oxidized by ZnO under the UHV annealing condition²³ is also shown in Figure 4.5, where this difference is even more pronounced. Since ZnO but not O₂ is the oxygen source in in UHV, it is obvious that Co is oxidized from the interface of Co and ZnO. Moreover on SiO₂ support the experimental points are very close to the diagonal line, suggesting than in this case Co²⁺ ions are relatively homogenously distributed within cobalt nanoparticles.

To further illustrate the surface composition as given by the angle-resolved XPS measurements, we use the SESSA^{38,39} software to simulate the ARXPS measurement. A schematic representation of the employed arrangement models is shown in the inset of Figure 4.5b. Based to the XPS results, layer structure was chosen for Co/ZnO simulation with a metallic Co layer sandwiched between two CoO layers. For Co/HOPG, we assumed that oxidation is exclusively at the surface and a layered arrangement was used with a CoO surface layer over metallic Co. The CoO fractions of several different cobalt oxidation states were simulated at take-off angles of 0 ° and 80 ° for several layer thicknesses in order to approach the experimental points. These values are shown in Figure 4.5b as open squares and triangles. In addition the thicknesses of each layer used to calculate these points are shown in Table 4.2. It is clear that the simulated values are in good accordance with the experimental results, confirming the differences in the oxidation behavior of Co on ZnO and carbon surface.

Apparently the arrangement model employed to calculate the thicknesses shown in Table 4.2 is simplified since do not take into account important characteristics of the cobalt layer structure (e.g. surface roughness, particles of different sizes etc.). However can be used in order to draw some qualitative information about the cobalt overlayer morphology in the two sample types. As expected, at higher oxidation degree of Co/HOPG the thickness of CoO surface layer grows (from point 3 to 1) followed by decrease of Co layer underneath (since the overall cobalt amount is stable). On the other hand for Co/ZnO, growth of the surface CoO layer (from point 6 to 4) is followed by a parallel growth of the subsurface CoO in contact with ZnO. This is justified since cobalt oxidation from both oxidation sources (surface and subsurface) is favored at higher temperature.

Table 4.2 The layer thicknesses used in SESSA simulation software for the calculation of the points in Figure 1.5b. The employed arrangement models used in the simulation are inserted in Figure 1.5b. The overall layer thickness was kept constant ($\pm 6\%$) and the thickness of each individual layer was varied in order to obtain values similar to the experimental fraction.

	Co/HOPG		Co/ZnO			
	Layer thickness (Å)		Layer thickness (Å)			
Points in Figure 4.5b	1 st layer (CoO)	2 nd layer (Co)	Points in Figure 4.5b	1 st layer (CoO)	2 nd layer (Co)	3 rd layer (CoO)
(1)	2.75	2	(4)	1.5	1.25	2.3
(2)	2.5	2.2	(5)	1.4	1.4	2.05
(3)	1.9	2.5	(6)	1.3	1.5	2

4.3.4 Stability of the graphene layer under redox treatments

The Raman spectra of SiO₂ and ZnO supported graphene as well as of HOPG samples both just after Co evaporation and after the redox treatment are shown in Figure 4.6. The main features of the Raman spectrum around 1600 and 2700 cm⁻¹ are due to G and 2D bands of graphene. The additional spectral feature for graphene samples at ~1350 cm⁻¹ is assigned to the D band, which is absent in the disorder-free graphene and requires defects for its activation by a single-phonon intervalley scattering process. The appearance of this peak indicates that some defects were introduced into the graphene film during preparation and cobalt deposition, while the redox treatments partly increase their number but notably do not destroy graphene.

The peak intensity ratio (I_D/I_G) is about 0.35 for both Co/G/SiO₂ and Co/G/ZnO after redox treatment. The relatively low I_D/I_G ratio suggests that the majority of the defects are due to graphene edges and sub-domain boundaries,⁴⁰ possibly caused by the different thermal expansion coefficients between graphene and the substrates. However, considering the reaction of Co with graphene during deposition and annealing⁴¹ (also will be shown in Figure 4.7), a small amount of other kind of defects (such as vacancies) is also possible. As expected, there is no D band on the spectrum of the Co/HOPG sample because in that case Raman spectra are due to the inner layers of the sample and are not sensitive to the surface defects.⁴²

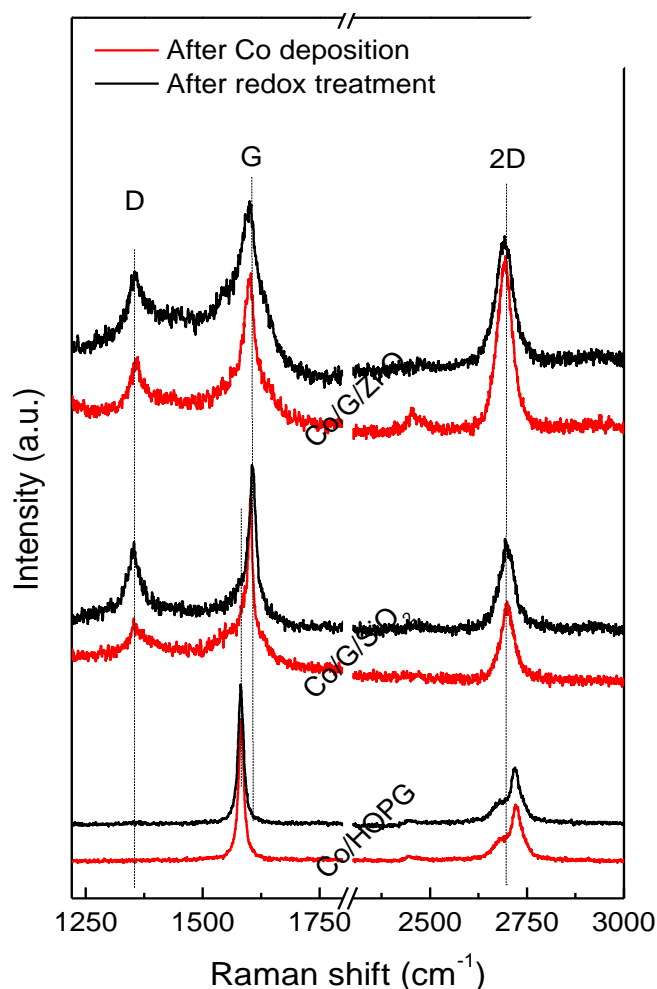


Figure 4.6 Raman spectra for Co/G/ZnO Co/G/SiO₂ and Co/HOPG before (red lines) and after (black lines) the redox treatment

4.3.5 Discussion

According to the above interpretation, the valence and morphology of cobalt are interconnected and are both strongly affected by the substrate. On ZnO and SiO₂, Co forms a relatively flat layer structure which is easier to be oxidized. Angle measurements show that cobalt oxide is mainly at the interface between Co and ZnO, SiO₂. On carbon substrate, cobalt is organized in nanoparticles which are only partially oxidized in oxygen from the outer surface. This indicates that the graphene interlayer between Co and substrate could adjust the morphology of Co and consequently change the oxidation properties. According to the mechanism of cobalt oxidation by gas phase oxygen,^{43,44} dissociatively adsorbed oxygen diffuses into the Co layer in order to establish a quasi-octahedral ligand field with formation of CoO. Since Co forms nanoparticles on G/ZnO, G/SiO₂ and HOPG, after a layer of CoO is formed, dissociation and deeper diffusion of oxygen into the core of the nanoparticles is limited

by the low temperature slow kinetics. Thus, only the outer layer part of Co is oxidized to CoO for the carbon-based sample.

Freund et al^{45,46} has reported the preferential oxidation of Pd at its interface with Fe₃O₄ support, in accordance with our observations of Co oxidation on ZnO and SiO₂. Oxidation of Co might occur by direct transfer/spillover of oxygen species from the support to the nanoparticles. An alternative explanation is oxidation by surface OH on ZnO. Formation of OH groups have been previously reported on polar ZnO surfaces prepared under UHV conditions due to the adsorption of residual H₂ or H₂O, which are always present in the UHV environment, on the ZnO surface.^{47,48} Oxidation of Co by the OH groups on ZnO(0001) has been observed at a low Co loading (0.1 nm)⁴⁹; this could be a driving force for interface CoO formation and it can also explain the higher oxidation degree of Co at the interface of Co and ZnO than SiO₂.

The reduction of CoO is mainly influenced by its interaction with the support especially at elevated temperatures. Co has strong chemical interaction with ZnO which leads to its oxidation to CoO even in the presence of H₂ (at least for the low exposure pressures used here). With a single interlayer of graphene, reduction of CoO in H₂ is considerably facilitated, since the single graphene layer can efficiently block the transfer of oxygen from ZnO to Co.²³ Under the same conditions, an extent solid reaction between Co and SiO₂ is not observed, however the complete reduction temperature of CoO is as high as 600 °C. Notably, even in the case of SiO₂ where there is no oxidative solid state reaction between cobalt and the support, graphene really facilitates reduction. Although the cause of the reduction temperature difference is not clear, one should note that the Co-C interaction is lower than Co-SiO₂, which might have an effect on the reduction temperature. Another possibility might be the very small size of CoO NPs over SiO₂ which is more resistant to reduction as we have shown previously.⁵⁰ What is interesting is that the oxide substrate beneath the graphene layer (ZnO or SiO₂) has no pronounced effect to the redox process.

4.4 Results and discussion. Part II: medium pressure redox

4.4.1 The as-prepared samples

The quality of the graphene layer transferred on the oxide substrates before and after cobalt deposition is demonstrated by the Raman spectra shown in Figure 4.7a. The two intense peaks, the G band at 1580 cm^{-1} and 2D band at $\sim 2700\text{ cm}^{-1}$, are due to the in-plane vibrational (E_{2g}) mode and the two phonon intervalley double resonance scattering of graphene,^{51,52} respectively. The narrow symmetric 2D band and the relatively low G/2D band intensity ratio can be used as safe indicators of single-layer graphene formation.⁵¹ The C 1s XPS spectra shown in Figure 4.7b, consist of a single asymmetric component at 284.8 eV, shifted of about 0.4 eV higher than that of the HOPG samples measured in the same setup, in agreement with previous reports.^{53,54}

After cobalt deposition and prior to any treatment, two additional features at $\sim 1350\text{ cm}^{-1}$ and 1625 cm^{-1} appear in the Raman spectrum. The peak at 1350 cm^{-1} is assigned to the D band and is activated due to a single-phonon intervalley process due to the presence of defects at the graphene lattice (edges, vacancies etc.). The other one, known as D' band, is activated by an intervalley scattering process, which also requires defects. It is therefore evident that vacuum deposition of 0.8 nm of cobalt at room temperature induces defects on the graphene layer. The C 1s spectra after cobalt deposition show the appearance of a new peak feature at the low binding energy side of the main peak. The binding energy of this new component at 283.7 eV is characteristic for carbon dissolved in metals,⁵⁵ i.e. carbide formation. This proposes a plausible mechanism for the creation of defects observed after cobalt deposition on graphene; a chemical interaction takes place at the interface of Co and graphene through a carbon dissolution-precipitation mechanism. This interaction is responsible for the formation of local defects on graphene, in its contact with the Co overlayer and can be possibly enhanced while annealing.⁴¹ However, chemical interaction and defect formation can be also responsible for the creation of anchor sites of the cobalt particles on graphene, which in turn may stabilize their size and morphology.

The intensity ratio of D and D' peaks can be used to describe the distinctive nature of the defects over graphene.⁵⁶ In particular, the $I_D/I_{D'}$ ratio changes from ~ 13 for sp^3 -carbon, to ~ 7 for vacancy-like defects and down to 3.5 for boundary-like defects with low defect concentration. The $I_D/I_{D'}$ ratios for Co/G/SiO₂ and Co/G/ZnO were calculated to be 4.89 and 4.62, respectively, possibly due to a mixture of boundary-like defects and vacancy-like defects.

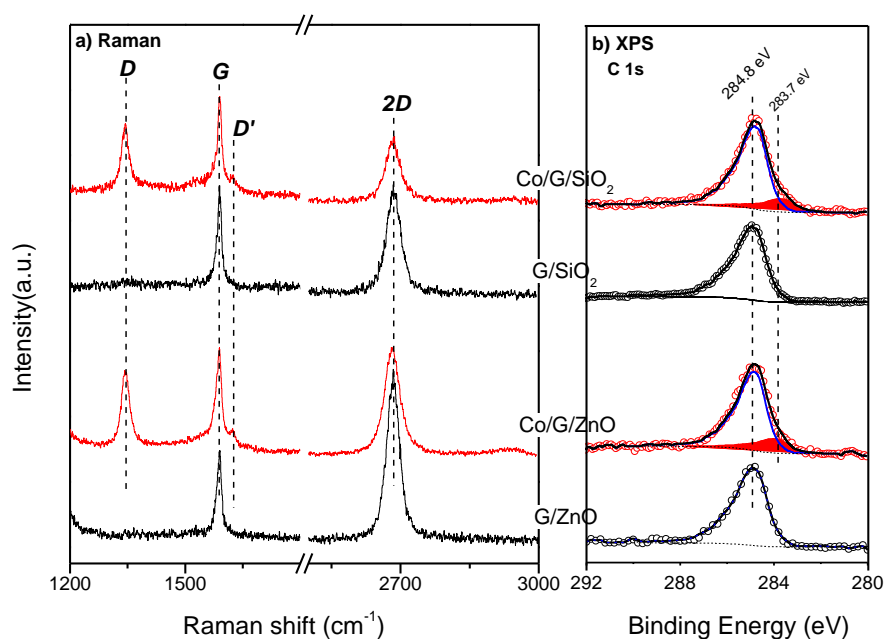


Figure 4.7 (a) Raman and (b) C 1s XPS spectra of graphene transferred on SiO₂ and ZnO substrates before and after vacuum deposition of 0.8 nm cobalt at room temperature.

Topography AFM images are used to probe the morphology of the cobalt deposit over the supports prior to any treatment (Figure 4.8). After deposition on the ZnO surface, Co forms a relatively flat layer, which indicates that the initial cobalt deposition process approximates the layer by layer growth mode.^{23,29,57} The surface morphology of Co/SiO₂ is quite similar with that of the Co/ZnO sample, i.e. a uniform Co layer is formed²⁸ and locally follows the high and low features on the SiO₂. On the contrary over G/ZnO and G/SiO₂ supports, cobalt seems to form individual, homogeneously-dispersed, nanoparticles. The enhanced mobility of cobalt adatoms over the carbon support is accountable for the cobalt nanoparticles formation, in accordance with previous studies of cobalt on graphene and amorphous carbon supports.^{30,23,31} Comparison with the AFM images in Figure 4.2, where 0.35 nm Co was deposited on each substrate, reveals that the deposition of a higher amount (0.8 nm) of Co does not significantly change the surface morphology.

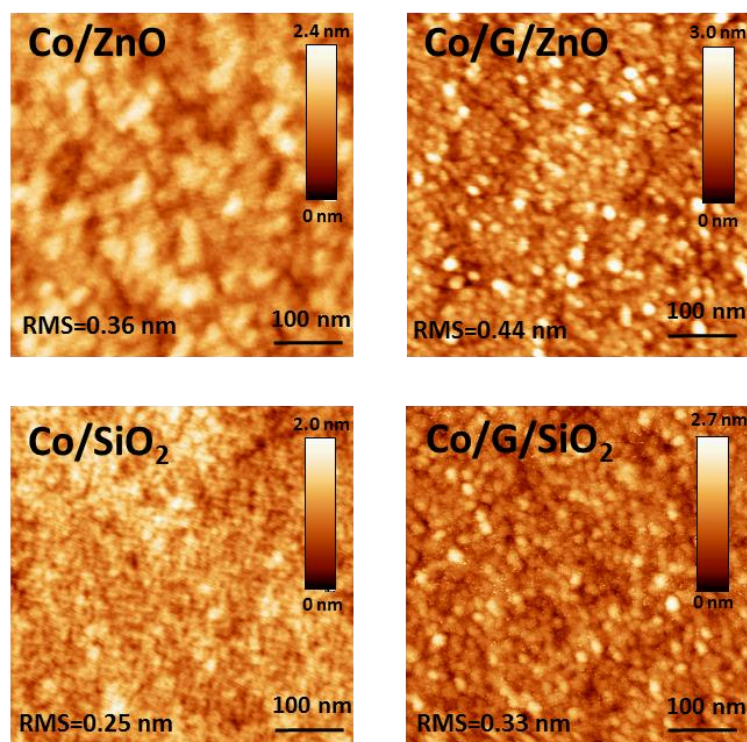


Figure 4.8 Tapping mode AFM topographic images ($500 \times 500 \text{ nm}^2$) of 0.8 nm Co deposited on four different supports before any treatment. The RMS values of the surface roughness are given in each figure.

4.4.2 Annealing in O_2 ambient

The Co $2p_{3/2}$ XPS spectra of the fresh Co/ZnO and Co/G/ZnO substrates after O_2 treatment at various temperatures are shown in Figure 4.9. The spectra recorded over SiO_2 -supported Co particles under identical conditions are presented in *supporting information in appendices*. The Co 2p peak appears at 778.3 eV just after preparation (*fresh*) indicating that the as-prepared cobalt is initially metallic. After exposure in 7 mbar O_2 at room temperature the main Co $2p_{3/2}$ peak is shifted at 780.4 eV and is accompanied with an intense satellite at the high BE side that is typical for CoO formation.⁸ Increasing the temperature to 250 °C induces a shift of the Co $2p_{3/2}$ peak at 779.8 eV while the satellite peak broadens and becomes less intense. These features are characteristic of spinel bulk-like Co_3O_4 .²⁶ The spectra recorded on bare and graphene-protected ZnO look very similar, pointing to a comparable oxidation behavior in the two cases. The evolution of the cobalt oxidation state during the O_2 treatment, as deduced by the analysis of the Co 2p XPS spectra, is represented in Figure 4.9b by the average valence state Co^{+x} (an example of peak deconvolution can be found in *supporting information in appendices*). In this graph it is evident that apart from small differences observed at 200 °C, the substrate has almost no impact on the oxidation process. This suggests that cobalt oxide

formation is kinetically and thermodynamically favored under the current oxidation conditions (pressure and temperature) and is not notably influenced by the morphological differences of the cobalt layer observed in the AFM images of Figure 4.8.

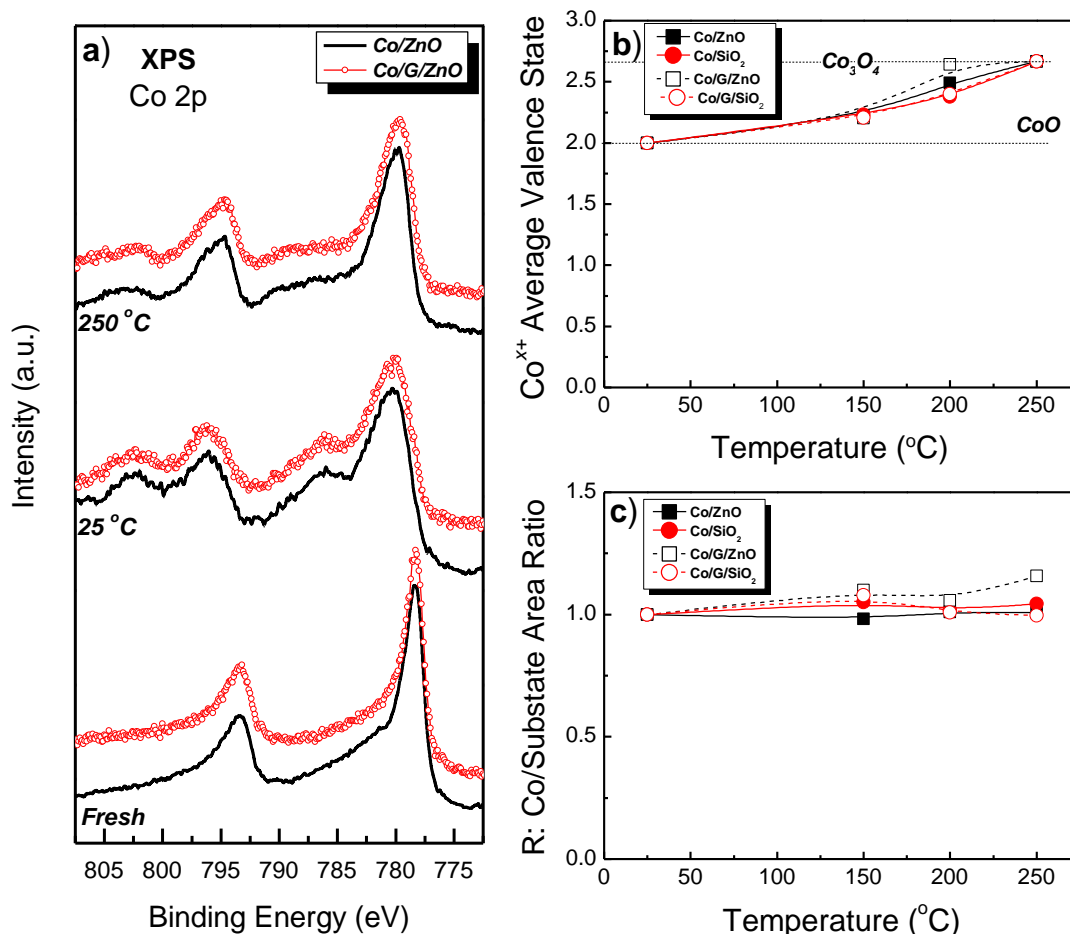


Figure 4.9 (a) Co 2p XPS spectra acquired from fresh Co/ZnO and Co/G/ZnO samples and after oxidation in 7 mbar O₂ at 25 and 250 °C, (b) evolution of the Co average valence state (Co^{x+}) and (c) the Co/substrate XPS peak area ratio normalized to its room temperature value, as a function of the oxidation temperature.

Changes in the cobalt surface area at each annealing stage can be monitored by following the modification of the Co 2p to the substrate XPS peak area ratio. This ratio is influenced by changes in the cobalt particles morphology and size, diffusion of cobalt into the substrate or migration of foreign species over it. In Figure 4.9c it is shown that the Co/substrate peak area ratio is practically constant over all substrates, even if a small increase is observed on G/ZnO at the maximum annealing temperature (250 °C). This increase might be caused by flattening of the initially round cobalt particles due to improved wetting of the substrate induced by oxidation.⁵⁷ However, the general trend of Figure 4.9c is that during the oxidative annealing process cobalt nearly retains its morphology, while migration or bulk diffusion phenomena should be neglected based on the above arguments.

4.4.3 Annealing in H₂ ambient

The reduction of supported Co₃O₄ particles at various annealing temperatures in 7 mbar H₂ is studied next. The cobalt average valence state and the Co to substrate intensity ratio are presented in Figure 4.10. The evolution of Co^{x+} in Figure 4.10a indicates that in all cases, Co₃O₄ follows a two-step reduction process: Co₃O₄ → CoO → Co in agreement with previous reports.^{58,59} However, the reduction temperature of cobalt oxide is significantly influenced by the substrate. In particular, cobalt oxide supported on graphene is being reduced at lower temperature as compared to that on the oxide substrates. This counts for both reduction steps (Co₃O₄ → CoO and CoO → Co) and in addition the Co^{x+} value is systematically lower on G/ZnO than on G/SiO₂. The variations in the reduction temperature of cobalt oxide can be a direct consequence of differences in the cobalt particle size, which in turn is associated with the strength of the cobalt/support interaction. Overall, results in Figure 4.10a clearly indicate that the graphene layer on both ZnO and SiO₂ decreases the activation energy of Co₃O₄ → CoO and CoO → Co transitions.

The AFM images in Figure 4.8 combined with the XPS results in Figure 4.9c, suggested that the morphology of the cobalt particles on ZnO and SiO₂ is more flat as compared to that on the graphene substrates. Carbon materials are considered to be inert support materials which have little interaction with Co⁶⁰ and therefore the reduction of Co oxides on the carbon material should be easier than on ZnO and SiO₂. In general, higher reduction temperatures are necessary in order to reduce Co oxides supported on strongly interacting surfaces.^{61,62} The Co-SiO₂ interaction is relatively weak compared to the Co-ZnO one, thus Co can be completely reduced at 400 °C, while on bare ZnO cobalt re-oxidizes at 400 °C. This result seems surprising keeping in mind the highly reducing gas atmosphere of 7 mbar H₂ used in this experiment. Note that the Co 2p photoelectron peak is not sensitive to the different crystal structures of cobalt monoxide,^{26,50} therefore NEXAFS measurements were performed to distinguish between tetrahedrally and octahedrally coordinated Co²⁺ ions. The Co L edge NEXAFS spectra measured at Co/ZnO (0001) samples after treatment at 360 °C in 0.2 mbar H₂ (shown in *supporting information in appendices*) have clear characteristics of tetrahedrally coordinated Co²⁺ ions. As has been described previously,⁶³ Co²⁺ ions can enter into the wurtzite ZnO lattice and substitute Zn²⁺ ions forming a mixed CoZnO_x spinel phase. Therefore one can claim that at higher annealing temperature a strong interaction takes place at the Co-ZnO interface, which leads to a mixed CoZnO_x oxide formation. This is consistent with our previous results in Chapter 3, where we have shown that oxidation of Co by the ZnO single crystalline support

can take place upon vacuum annealing through a solid state reaction: $\text{Co} + \text{ZnO} \rightarrow \text{CoO} + \text{Zn}$.^{23,49} Besides, recently we reported the formation of a mixed $\text{Zn}_{1-x}\text{Co}_x\text{O}$ oxide for cobalt nanoparticles supported on ZnO nanowires. This oxide was unreducible in 0.2 mbar H_2 at temperatures as high as 400 °C.²⁶ The present study shows that oxidation at cobalt/ZnO is a general property of this interface, with little influence of the gas phase environment.

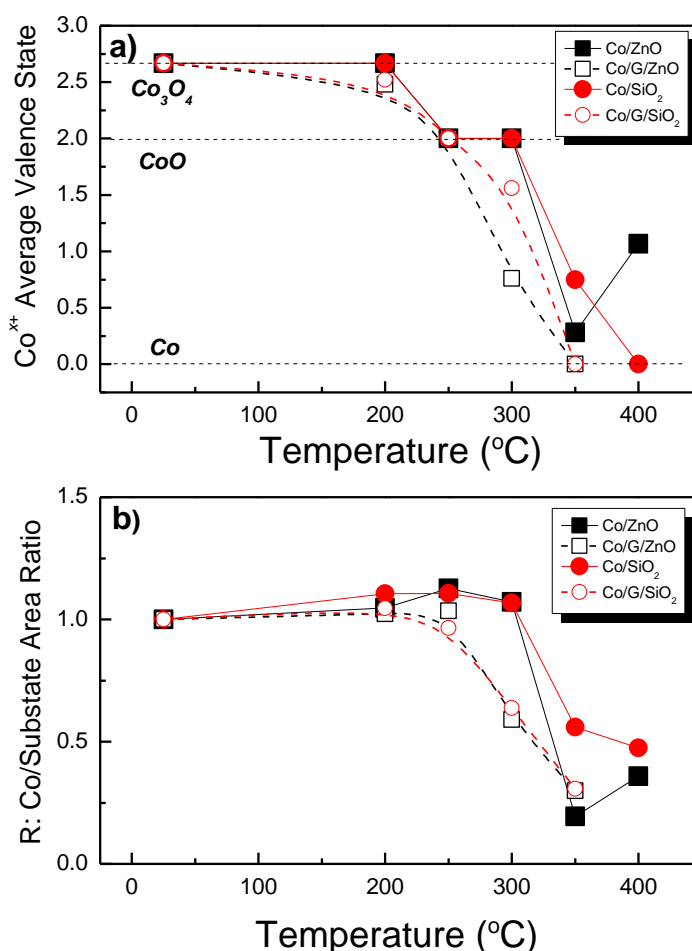


Figure 4.10 XPS results of oxidized samples in 7 mbar H_2 at various annealing temperatures. (a) Evolution of the Co average valence state (Co^{x+}) and (b) the normalized Co/substrate peak area ratio as a function of the annealing temperature

Figure 4.10b shows the evolution of cobalt to substrate peak area ratio as a function of temperature after the H_2 treatment. During the reduction of Co_3O_4 to CoO (200 °C for graphene and 250 °C for bare oxides), the Co/substrate ratios for all samples are almost stable, indicating insignificant changes of cobalt particles' morphology at this stage. At higher temperature, CoO is reduced to Co and the Co/substrate area ratio gradually decreases pointing to significant loss of the cobalt surface area. This reflects the coalesce and shrinkage of Co particles during the reduction process.^{37,64} It is interesting to note that in the case of ZnO substrate at 400 °C the

ratio increases again following the re-oxidation of cobalt by the support, which implies a re-dispersion process of Co at the ZnO surface.^{23,57}

The AFM images (Figure 4.11) confirm that the surface morphology is strongly modified by the redox treatment as compared to the fresh samples. The high root mean square roughness (RMS) values indicate that in all cases cobalt particles grown in size. The average Co particle diameter as estimated by the AFM image analysis (Figure 4.11) is about 19 nm for Co supported on G/ZnO and G/SiO₂, 18 nm for Co/ZnO and 13 nm for Co/SiO₂. The particles size differences in the AFM images are in accordance with the observed modifications in the XPS intensity ratios shown in Figure 4.10.

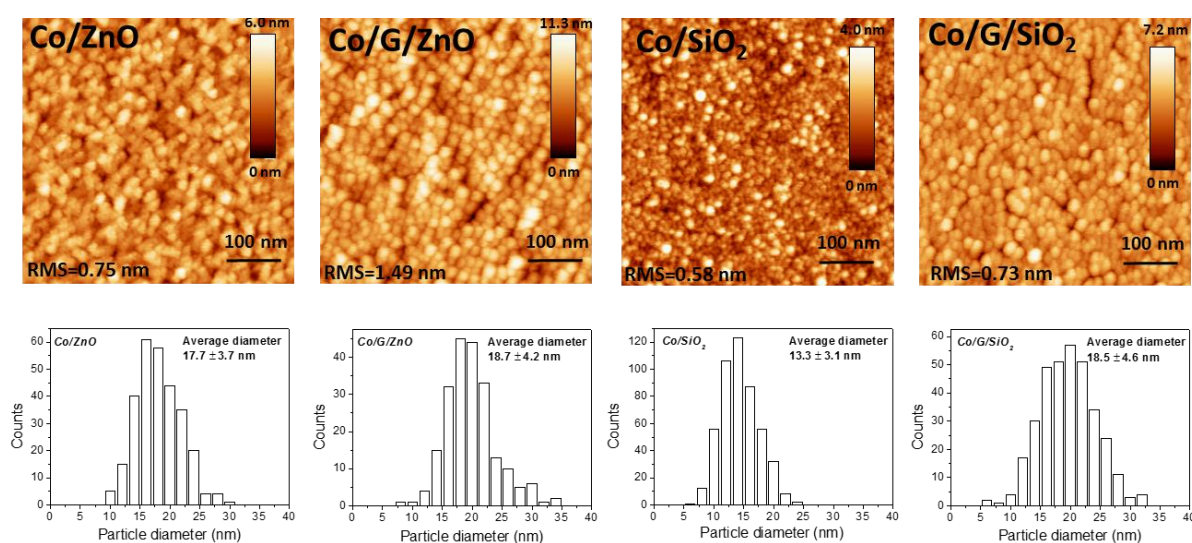


Figure 4.11(Top) Tapping mode AFM topographic images ($500 \times 500 \text{ nm}^2$) of 0.8 nm Co deposited on four different supports after the oxidation/reduction treatment. (Bottom) Histograms for the Co particles diameter distribution obtained by analysis of the above AFM images.

The ratio R_{redox}/R_{fresh} between the fresh (R_{fresh}) and redox treated (R_{redox}) samples can be used to estimate the degree of Co particles agglomeration. Particularly lower R_{redox}/R_{fresh} ratio corresponds to higher agglomeration (lower surface area) of cobalt due to the redox treatment. The experimental R_{redox}/R_{fresh} ratios shown in Figure 4.12 imply that graphene-supported cobalt loose more surface area during redox treatment as compared to the oxide substrates. To quantify this, we simulate the R_{redox}/R_{fresh} ratio employing SESSA software.^{38,39} The simulation model consists of Co islands on planar substrate with different particle size (volume) and density (see supporting information in appendices). The average diameter and height of Co nanoparticles found by the AFM image analysis were used as a base to simulate the R_{redox}/R_{fresh} ratio after the redox treatments. Then the distribution of cobalt on the fresh samples was

estimated so as the theoretical and experimental R_{redox}/R_{fresh} ratios are converging. As shown by the schematics in Figure 4.12, the high surface diffusivity of cobalt on graphene, due to the weaker Co-graphene interaction causes the growth of cobalt to bigger particles after treatment. Although the XPS simulation seems to underestimate the cobalt particles size as compared to the AFM images, it clearly suggests that graphene-supported cobalt forms less dense and bigger particles as compared to the oxide-supported.

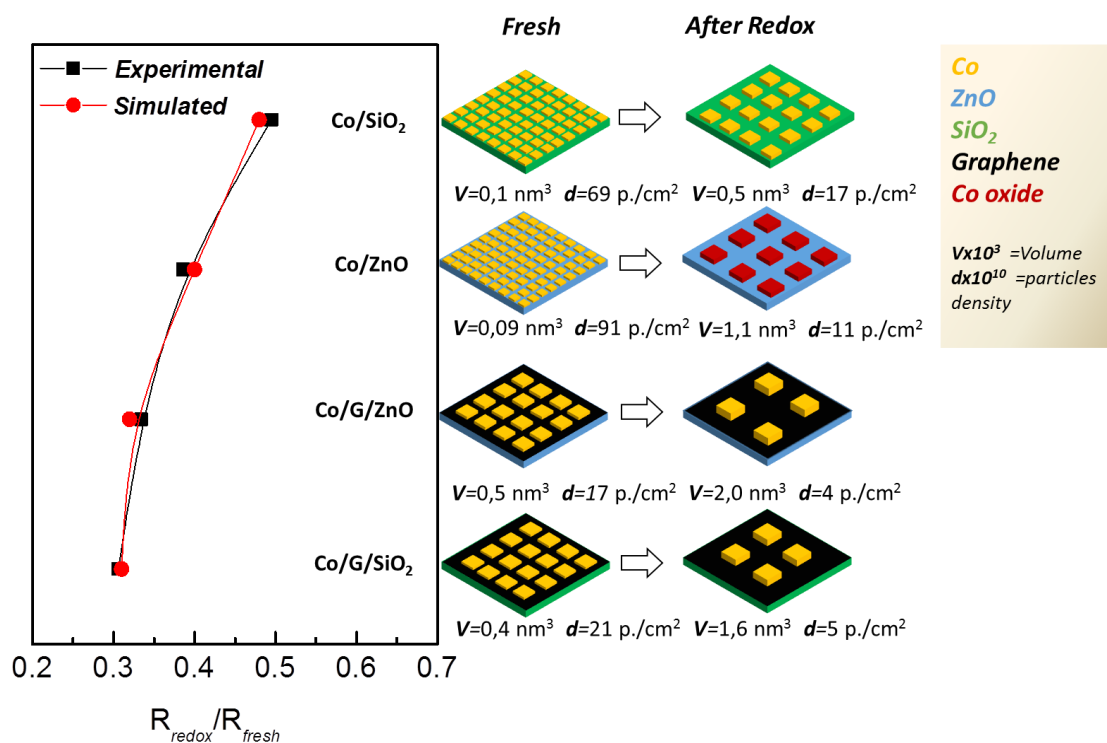


Figure 4.12 Comparison of simulated and experimental XPS intensity ratios of four different samples and schematic representation of the samples morphology (particle volume ($\times 10^3$ nm³), V and particles density ($\times 10^{10}$ particles per cm²), d) is determined by the theoretical simulation of the XPS intensity ratios.

On the whole, the above presented data show that in 7 mbar O₂ Co oxidation proceeds independently from the substrate, while on the contrary reduction of Co oxides in H₂ is determined by it. In general graphene improves the reducibility of cobalt oxide as compared to the bare oxide supports. This indicates that one can tune the metal support interaction by inserting a graphene interlayer, thus changing the morphology of the supported metal and also the oxidation/reduction properties.

4.4.4 Stability of the graphene layer under redox treatments

As shown in Figure 4.7, prior to any treatment, a number of defects are created on the graphene layer due to cobalt deposition. The Raman spectra of Co/G/SiO₂ and Co/G/ZnO after

redox treatments are shown in Figure 4.13. For both samples the intense D and D' band, along with the appearance of a weak peak near 2920 cm^{-1} (D + D' band) indicate highly defective graphene. Figure 4.13 also includes Raman spectra from different sample regions notably bilayer-graphene island (abbreviated as: BL-Co/G/ZnO and BL-Co/G/SiO₂) and graphene areas at the corner of the sample which were protected from cobalt deposition by the mounting clip (abbreviated as: G/ZnO and G/SiO₂). The different regions are indicated in the optical images of the samples shown in Figure 4.13c and d. The overlapping G and D' bands are deconvoluted with Lorentzian line shapes and the calculated I_D/I_G intensity ratio is shown in Table 4.3. This ratio can be used to estimate the average inter-defect distance (L_D) and the defect density (n_D) according to empirical relations presented by Cançado et al:⁶⁵

$$L_D^2(\text{nm}^2) = (1.8 \pm 0.5) \times 10^{-9} \lambda_L^4 \left(\frac{I_D}{I_G}\right)^{-1} \quad (4.1)$$

$$n_D(\mu\text{m}^{-2}) = \frac{(1.8 \pm 0.5)}{\lambda_L^4} \times 10^{14} \left(\frac{I_D}{I_G}\right) \quad (4.2)$$

where λ_L is the excitation wavelength in nm (532 nm in our case). These formulas were deduced from Raman spectra of ion-bombarded samples but should be valid for other type of point defects in the limit of $L_D \geq 10$ nm and at visible excitation wavelengths. As shown in Table 4.3 the defect density, n_D , of graphene after the redox treatment increases considerably on single layer areas, while the bilayer graphene areas proved to be more resistant, with lower n_D . This is consistent with literature observations, which have shown that bilayer graphene is more resistant to oxidization⁶⁶ and hydrogenation⁶⁷ than single layer graphene. In addition, the sample areas without cobalt were even more stable showing a very low intensity of the D peak. This observation supports the results of Figure 4.7 and suggests that Co plays a catalytic role on the introduction of defects in graphene.

The intensity ratio of D and D' peaks in Table 4.3 can be used to describe the distinctive nature of the defects over graphene.⁵⁶ In particular, the $I_D/I_{D'}$ ratio changes from ~ 13 for sp³-carbon, to ~ 7 for vacancy-like defects and down to 3.5 for boundary-like defects with low defect concentration. The $I_D/I_{D'}$ ratio for Co/G/SiO₂ and Co/G/ZnO just after cobalt deposition was calculated to be 4.9 and 4.6, respectively, pointing to a mixture of both boundary-like and vacancy-like defects. After redox treatments, the $I_D/I_{D'}$ ratios for both samples dramatically decrease to 2-3, however this should not be taken as an indication of boundary-like defects since at highly disordered state the defects are so many and so close to each other that the information about the geometry of the single defect cannot be given from such analysis.⁵⁶

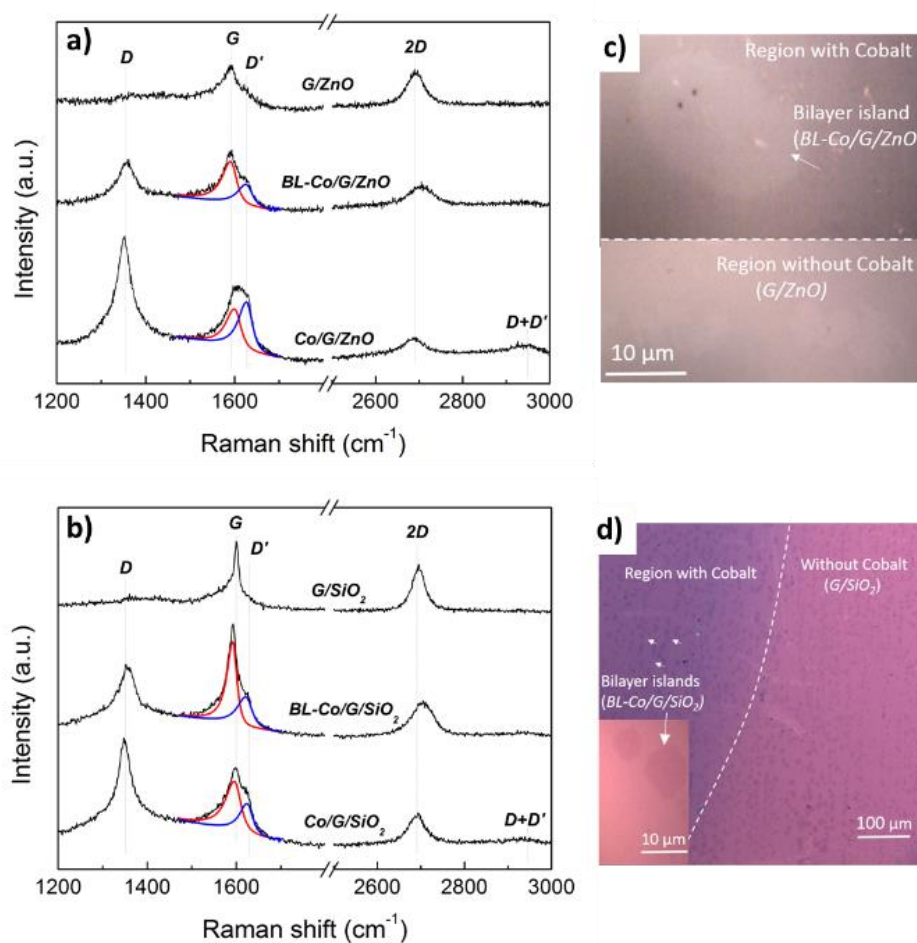


Figure 4.13 Raman spectra at different regions for (a) Co/G/ZnO and (b) Co/G/SiO₂ after 7 mbar redox treatment. The spectra are fitted with Lorentzian line shapes.

Even so, other features of Raman spectra can provide some additional information about the graphene state. Ferrari and Robertson^{65,68} proposed that the amorphization of graphene proceeds in two stages: first from crystalline to the nanocrystalline (Stage 1) and then towards mainly sp² amorphous carbon (Stage 2). The Raman spectral features in Figure 4.13 (high intensity of D peak, the appearance of D + D' peak as well as the overlapping of G and D' peak) indicate that after redox treatment the amorphization process of the graphene samples is still at Stage 1. In addition, the calculated L_D values for the redox treated Co/G/ZnO and Co/G/SiO₂ in Table 4.3 are 7.6 nm and 9.0 nm, respectively. Considering that the proposed experimental error of the empirical relations is ~ 30 %, ⁶⁵ these L_D values are still in the range limit of the formulas and they are also in consistence with Stage 1, since the transition between Stage 1 and 2 is usually observed at L_D ≈ 2–5 nm.^{56,65} Overall the analysis of the Raman spectra shows that breaking of sp² C-C bonds, after cobalt deposition and redox treatment, gradually disassemble the macroscopic single graphene crystal into nanometer sized graphene nanocrystallites.⁶⁹

Table 4.3 Intensity ratio, average interdefect distance and defect density of Co/G/ZnO and Co/G/SiO₂ after redox treatment

Samples		Intensity ratio I _D /I _G	Intensity ratio I _D /I _{D'}	Average interdefect distance L _D (nm)	Defect density n _D (nm)
Samples after Co deposition	Co/G/ZnO	0.67	4.89	14.6	1513
	Co/G/SiO ₂	0.77	4.62	13.7	1723
Samples after redox treatments	Co/G/ZnO (single layer)	2.50	2.27	7.6	5617
	BL-Co/G/ZnO (bilayer island)	0.83	1.67	13.2	1865
	Co/G/SiO ₂ (single layer)	1.77	2.87	9.0	3977
	BL-Co/G/SiO ₂ (bilayer island)	0.61	1.68	15.4	1370

Comparison of the Raman spectra between Co/G/ZnO and Co/G/SiO₂ shows that ZnO-supported graphene has more defects after redox than that of SiO₂, for all 3 area-types. This suggests that apart from cobalt overlayer the stability of graphene is also influenced by the support⁷⁰. Problems in the stability of graphene on ZnO substrates has been recently raised under UV radiation, where graphene decomposes photocatalytically.⁷¹ Here we show that under high temperature redox treatments, the ZnO support can also deteriorate graphene's quality by creating a number of defects, phenomenon which is accelerated by the catalytic role of the metal overlayer (here cobalt). Certainly since defects on graphene can also act as anchor sites for metal particles or for dopants and even as active sites for reactions,⁷² modification of graphene in controlled environments might be deliberately performed for some applications.

Raman spectroscopy provides information about the graphene structure, while XPS is sensitive to the oxidation state of graphene layer after the treatment. On the top part of Figure 4.14, some characteristic C 1s spectra at various stages of Co/G/SiO₂ sample treatment are shown. These spectra are dominated by the C 1s peak at 284.8 eV due to graphene, but two additional components due to Co-diluted carbon (283.7 eV) and oxidized carbon species (288.4 eV) can be easily distinguished. The evolution of these carbon species in the course of the gas treatments is presented in the bottom graphs of Figure 4.14. Since both graphene samples gave very similar results, the average of the two is shown. Prior to gas exposure (open symbols), an amount of diluted carbon is found, while upon annealing in O₂ diluted carbon disappears and oxidized carbon species are developed. The later reaches a maximum at 250 °C in O₂ but in H₂ is gradually vanishing. What is interesting is that at higher H₂ annealing temperature, the

diluted carbon component does not reappear, even if cobalt overlayer is completely reduced to metallic cobalt (Figure 4.10).

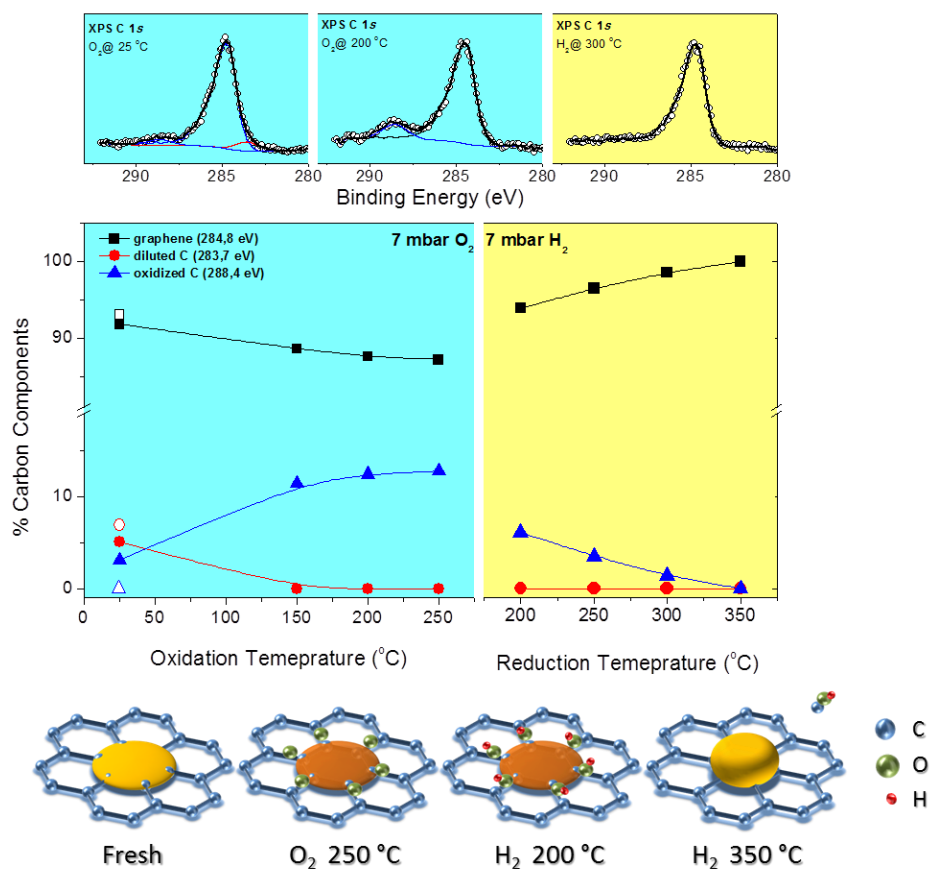


Figure 4.14 (Top) Characteristic C 1s XPS spectra recorded at various stages of the Co/G/SiO₂ sample treatment. **(Middle)** Evolution of the carbon components derived by deconvolution of the C 1s XPS spectra as a function of temperature during the oxidation and reduction treatments. **(Bottom)** Schematic representation of the suggested mechanism responsible for formation of graphene defects in contact with cobalt during the redox treatment.

Based on these results one can speculate the mechanism of graphene quality deterioration over cobalt covered areas upon the redox treatment (bottom part of Figure 4.14). In particular cobalt particles locally dilute carbon atoms of graphene lattice, making these atoms vulnerable to oxidation in O₂ atmosphere. In H₂, or at high temperature, oxidized carbon species volatile C-O and/or C-O-H compounds, leaving behind defective graphene layer in the vicinity of cobalt particles. This mechanism is consistent with the observation highly defective graphene only in cobalt covered areas of the sample. In addition it explains the absence of diluted carbon species in the C 1s XPS spectra after cobalt reduction in hydrogen, since the carbon atoms around cobalt particles are already consumed.

4.5 Conclusions

In summary, the effect of graphene on the redox properties and morphologies of cobalt supported on ZnO and SiO₂ has been studied. It was shown that with a graphene layer on the oxides, fresh deposited Co morphology changes from flat layer structure to nanoparticle structure. Under low pressure condition, the graphene layer in-between of Co and the substrates limits the oxidation of Co but facilitates the reduction of Co. ARXPS proves that the oxidation of Co on bare substrates is preferentially provoked from the subsurface while on the carbon material substrates it comes from the surface of the Co nanoparticles. Small amount of defects were detected by Raman spectroscopy after Co deposition and redox treatment.

Under medium pressure conditions, graphene does not significantly affect the oxidation properties of Co under the medium pressure oxidation condition. However, in the reduction condition, graphene protects Co from the solid reaction with ZnO and facilitates the reduction reactions of Co₃O₄ to CoO and of CoO to Co, compared with that on both ZnO and SiO₂ bare substrates. In addition, the Raman results suggested that after redox treatment, graphene was in the nanocrystalline form on both substrates. On the basis of these data, it is evident that graphene can modify the supported Co morphology and improve the hydrogen reduction properties of Co oxides.

4.6 References

- (1) Khodakov, A. Y.; Chu, W.; Fongarland, P. Advances in the Development of Novel Cobalt Fischer – Tropsch Catalysts for Synthesis of Long-Chain Hydrocarbons and Clean Fuels. *Chem. Rev.* **2007**, *107* (5), 1692–1744.
- (2) Iglesia, E. Design, Synthesis, and Use of Cobalt-Based Fischer-Tropsch Synthesis Catalysts. *Appl. Catal. A Gen.* **1997**, *161* (1-2), 59–78.
- (3) Turner, J.; Sverdrup, G.; Mann, M. K.; Maness, P.-C.; Kroposki, B.; Ghirardi, M.; Evans, R. J.; Blake, D. Renewable Hydrogen Production. *Int. J. Energy Res.* **2008**, *32* (5), 379–407.
- (4) Llorca, J.; Homs, N.; Sales, J.; de la Piscina, P. R. Efficient Production of Hydrogen over Supported Cobalt Catalysts from Ethanol Steam Reforming. *J. Catal.* **2002**, *209* (2), 306–317.
- (5) Fu, T.; Li, Z. Review of Recent Development in Co-Based Catalysts Supported on Carbon Materials for Fischer–Tropsch Synthesis. *Chem. Eng. Sci.* **2015**, *135*, 3–20.
- (6) Oh, J.-H.; Bae, J. W.; Park, S.-J.; Khanna, P. K.; Jun, K.-W. Slurry-Phase Fischer–Tropsch Synthesis Using Co/ γ -Al₂O₃, Co/SiO₂ and Co/TiO₂: Effect of Support on Catalyst Aggregation. *Catal. Letters* **2009**, *130* (3-4), 403–409.
- (7) Girardon, J.-S.; Quinet, E.; Griboval-Constant, A.; Chernavskii, P. A.; Gengembre, L.; Khodakov, A. Y. Cobalt Dispersion, Reducibility, and Surface Sites in Promoted Silica-Supported Fischer–Tropsch Catalysts. *J. Catal.* **2007**, *248* (2), 143–157.
- (8) Law, Y. T.; Doh, W. H.; Luo, W.; Zafeiratos, S. A Comparative Study of Ethanol Reactivity over Ni, Co and NiCo-ZnO Model Catalysts. *J. Mol. Catal. A Chem.* **2014**, *381* (0), 89–98.
- (9) Llorca, J.; de la Piscina, P. R.; Dalmon, J.-A.; Sales, J.; Homs, N. CO-Free Hydrogen from Steam-Reforming of Bioethanol over ZnO-Supported Cobalt Catalysts. *Appl. Catal. B Environ.* **2003**, *43* (4), 355–369.
- (10) Marin, R. P.; Kondrat, S. A.; Davies, T. E.; Morgan, D. J.; Enache, D. I.; Combes, G. B.; Taylor, S. H.; Bartley, J. K.; Hutchings, G. J. Novel Cobalt Zinc Oxide Fischer–Tropsch Catalysts Synthesised Using Supercritical Anti-Solvent Precipitation. *Catal. Sci. Technol.* **2014**, *4* (7), 1970–1978.
- (11) Dumont, J. A.; Mugumaoderha, M. C.; Ghijsen, J.; Thiess, S.; Drube, W.; Walz, B.; Tolkiehn, M.; Novikov, D.; de Groot, F. M. F.; Sporken, R. Thermally Activated

- Processes at the Co/ZnO Interface Elucidated Using High Energy X-Rays. *J. Phys. Chem. C* **2011**, *115* (15), 7411–7418.
- (12) Xiong, H.; Schwartz, T. J.; Andersen, N. I.; Dumesic, J. A.; Datye, A. K. Graphitic-Carbon Layers on Oxides: Toward Stable Heterogeneous Catalysts for Biomass Conversion Reactions. *Angew. Chemie Int. Ed.* **2015**, *54* (27), 7939–7943.
- (13) Su, D. S.; Perathoner, S.; Centi, G. Nanocarbons for the Development of Advanced Catalysts. *Chem. Rev.* **2013**, *113* (8), 5782–5816.
- (14) Liu, X.; Han, Y.; Evans, J. W.; Engstfeld, A. K.; Behm, R. J.; Tringides, M. C.; Hupalo, M.; Lin, H.-Q.; Huang, L.; Ho, K.-M.; et al. Growth Morphology and Properties of Metals on Graphene. *Prog. Surf. Sci.* **2015**, *90* (4), 397–443.
- (15) Zhou, Z.; Gao, F.; Goodman, D. W. Deposition of Metal Clusters on Single-Layer graphene/Ru(0001): Factors That Govern Cluster Growth. *Surf. Sci.* **2010**, *604* (13-14), L31–L38.
- (16) Drnec, J.; Vlais, S.; Carlomagno, I.; Gonzalez, C. J.; Isern, H.; Carlà F.; Fiala, R.; Rougemaille, N.; Coraux, J.; Felici, R. Surface Alloying upon Co Intercalation between Graphene and Ir(111). *Carbon* **2015**, *94*, 554–559.
- (17) Liu, L.; Chen, Z.; Wang, L.; Polyakova(Stolyarova), E.; Taniguchi, T.; Watanabe, K.; Hone, J.; Flynn, G. W.; Brus, L. E. Slow Gold Adatom Diffusion on Graphene: Effect of Silicon Dioxide and Hexagonal Boron Nitride Substrates. *J. Phys. Chem. B* **2012**, *117* (16), 4305–4312.
- (18) Zhou, H.; Qui, C.; Liu, Z.; Yang, H.; Hu, L.; Li, J.; Gu, C.; Sun, L. Thickness-Dependent Morphologies of Gold on N-Layer Graphenes. *J. Am. Chem. Soc.* **2010**, *132* (3), 944–946.
- (19) Zhou, H.; Yu, F.; Yang, H.; Qiu, C.; Chen, M.; Hu, L.; Guo, Y.; Yang, H.; Gu, C.; Sun, L. Layer-Dependent Morphologies and Charge Transfer of Pd on N-Layer Graphenes. *Chem. Commun.* **2011**, *47* (33), 9408–9410.
- (20) Poon, S. W.; Wee, A. T. S.; Tok, E. S. Anomalous Scaling Behaviour of Cobalt Cluster Size Distributions on Graphite, Epitaxial Graphene and Carbon-Rich $(6\sqrt{3}\times 6\sqrt{3})R30^\circ$. *Surf. Sci.* **2012**, *606* (21-22), 1586–1593.
- (21) Hershberger, M. T.; Hupalo, M.; Thiel, P. A.; Tringides, M. C. Growth of fcc(111) Dy Multi-Height Islands on 6H-SiC(0001) Graphene. *J. Phys. Condens. Matter* **2013**, *25* (22), 225005.
- (22) Hupalo, M.; Binz, S.; Tringides, M. C. Strong Metal Adatom-Substrate Interaction of Gd and Fe with Graphene. *J. Phys. Condens. Matter* **2011**, *23* (4), 045005.

- (23) Luo, W.; Doh, W. H.; Law, Y. T.; Aweke, F.; Ksiazek-sobieszek, A.; Sobieszek, A.; Salamacha, L.; Skrzypiec, K.; Machocki, A.; Zafeiratos, S. Single-Layer Graphene as an Effective Mediator of the Metal–Support Interaction. *J. Phys. Chem. Lett.* **2014**, *5*, 1837–1844.
- (24) Powell, C. J.; Jablonski, A. Progress in Quantitative Surface Analysis by X-Ray Photoelectron Spectroscopy: Current Status and Perspectives. *J. Electron Spectros. Relat. Phenomena* **2010**, *178-179*, 331–346.
- (25) Briggs, D.; Seah, P. *Practical Surface Analysis: Auger and X-Ray Photoelectron Spectroscopy*; Wiley-VCH, Weinheim, Germany, 1990; Vol. 1.
- (26) Turczyniak, S.; Luo, W.; Papaefthimiou, V.; Ramgir, N. S.; Haevecker, M.; Machocki, A.; Zafeiratos, S. A Comparative Ambient Pressure X-Ray Photoelectron and Absorption Spectroscopy Study of Various Cobalt-Based Catalysts in Reactive Atmospheres. *Top. Catal.* **2015**, *5* (2), 532–542.
- (27) Fierro, G.; Jacono, M. Lo; Inversi, M.; Dragone, R.; Porta, P. TPR and XPS Study of Cobalt–copper Mixed Oxide Catalysts: Evidence of a Strong Co–Cu Interaction. *Top. Catal.* **2000**, *10* (1-2), 39–48.
- (28) Čechal, J.; Luksch, J.; Koňáková, K.; Urbánek, M.; Brandejsová, E.; Šíkola, T. Morphology of Cobalt Layers on Native SiO₂ Surfaces at Elevated Temperatures: Formation of Co Islands. *Surf. Sci.* **2008**, *602* (15), 2693–2698.
- (29) Su, S. H.; Lai, J. H.; Chen, H.; Lee, T.; Hsu, Y.; Wang, R. L.; Huang, J. C. A. Elucidating the Structure and Chemical State of Co Growth on the ZnO(10 $\bar{1}$ 0) Surface. *J. Phys. Chem. C* **2012**, *116*, 9917–9924.
- (30) Liao, Q.; Zhang, H. J.; Wu, K.; Li, H. Y.; Bao, S. N.; He, P. Nucleation and Growth of Monodispersed Cobalt Nanoclusters on Graphene Moiré on Ru(0001). *Nanotechnology* **2011**, *22* (12), 125303.
- (31) Lucas, S.; Colomer, J. F.; Bittencourt, C.; Moskovkin, P.; Moreau, N. Surface Phenomena Involved in the Formation of Co Nanoparticles on Amorphous Carbon and SiO₂ Deposited by Magnetron Sputtering. *Appl. Phys. A Mater. Sci. Process.* **2010**, *99* (1), 125–138.
- (32) Huang, C.-W.; Lin, H.-Y.; Huang, C.-H.; Shiue, R.-J.; Wang, W.-H.; Liu, C.-Y.; Chui, H.-C. Layer-Dependent Morphologies of Silver on N-Layer Graphene. *Nanoscale Res. Lett.* **2012**, *7* (1), 618.

- (33) Liu, X.; Wang, C. Z.; Hupalo, M.; Lu, W. C.; Tringides, M. C.; Yao, Y. X.; Ho, K. M. Metals on Graphene: Correlation between Adatom Adsorption Behavior and Growth Morphology. *Phys. Chem. Chem. Phys.* **2012**, *14* (25), 9157.
- (34) Werner, W. S. M.; Chudzicki, M.; Smekal, W.; Powell, C. J. Interpretation of Nanoparticle X-Ray Photoelectron Intensities. *Appl. Phys. Lett.* **2014**, *104* (24), 243106.
- (35) Jablonski, A.; Powell, C. J. The Electron Attenuation Length Revisited. *Surf. Sci. Rep.* **2002**, *47* (2-3), 33–91.
- (36) Burrell, M. C.; Butts, M. D.; Derr, D.; Genovese, S.; Perry, R. J. Angle-Dependent XPS Study of Functional Group Orientation for Aminosilicone Polymers Adsorbed onto Cellulose Surfaces. *Appl. Surf. Sci.* **2004**, *227* (1-4), 1–6.
- (37) Castner, D. G.; Watson, P. R.; Chan, I. Y. X-Ray Absorption Spectroscopy, X-Ray Photoelectron Spectroscopy, and Analytical Electron Microscopy Studies of Cobalt Catalysts. 2. Hydrogen Reduction Properties. *J. Phys. Chem.* **1990**, *94* (2), 819–828.
- (38) Werner, W. S. M. Electron Transport in Solids for Quantitative Surface Analysis. *Surf. Interface Anal.* **2001**, *31* (3), 141–176.
- (39) Smekal, W.; Werner, W. S. M.; Powell, C. J. Simulation of Electron Spectra for Surface Analysis (SESSA): A Novel Software Tool for Quantitative Auger-Electron Spectroscopy and X-Ray Photoelectron Spectroscopy. *Surf. Interface Anal.* **2005**, *37* (11), 1059–1067.
- (40) Malard, L. M. M.; Pimenta, M. A. A.; Dresselhaus, G.; Dresselhaus, M. S. S. Raman Spectroscopy in Graphene. *Phys. Rep.* **2009**, *473* (5-6), 51–87.
- (41) Leong, W. S.; Nai, C. T.; Thong, J. T. L. What Does Annealing Do to Metal–Graphene Contacts? *Nano Lett.* **2014**, *14* (7), 3840–3847.
- (42) Martins Ferreira, E. H.; Moutinho, M. V. O.; Stavale, F.; Lucchese, M. M.; Capaz, R. B.; Achete, C. a.; Jorio, A. Evolution of the Raman Spectra from Single-, Few-, and Many-Layer Graphene with Increasing Disorder. *Phys. Rev. B* **2010**, *82* (12).
- (43) Matsuyama, T.; Ignatiev, A. LEED-AES Study of the Temperature Dependent Oxidation of the Cobalt (0001) Surface. *Surf. Sci.* **1981**, *102*, 18–28.
- (44) Benitez, G.; Carelli, J. L.; Heras, J. M.; Viscido, L. Interaction of Oxygen with Thin Cobalt Films. *Langmuir* **1996**, *12* (1), 57–60.
- (45) Schalow, T.; Laurin, M.; Brandt, B.; Schauermaun, S.; Guimond, S.; Kühlenbeck, H.; Starr, D. E.; Shaikhutdinov, S. K.; Libuda, J.; Freund, H.-J. Oxygen Storage at the Metal/oxide Interface of Catalyst Nanoparticles. *Angew. Chemie Int. Ed.* **2005**, *44* (46), 7601–7605.

- (46) Schalow, T.; Brandt, B.; Starr, D. E.; Laurin, M.; Shaikhutdinov, S. K.; Schauer mann, S.; Libuda, J.; Freund, H.-J. Size-Dependent Oxidation Mechanism of Supported Pd Nanoparticles. *Angew. Chemie Int. Ed.* **2006**, *45* (22), 3693–3697.
- (47) Lauritsen, J. V.; Porsgaard, S.; Rasmussen, M. K.; Jensen, M. C. R.; Bechstein, R.; Meinander, K.; Clausen, B. S.; Helveg, S.; Wahl, R.; Kresse, G.; et al. Stabilization Principles for Polar Surfaces of ZnO. *ACS Nano* **2011**, *5* (7), 5987–5994.
- (48) Wölfl, C. The Chemistry and Physics of Zinc Oxide Surfaces. *Prog. Surf. Sci.* **2007**, *82* (2-3), 55–120.
- (49) Law, Y. T.; Skála, T.; Piš, I.; Nehasil, V.; Vondráček, M.; Zafeiratos, S.; Skala, T.; Pis, I.; Nehasil, V.; Vondracek, M.; et al. Bimetallic Nickel–Cobalt Nanosized Layers Supported on Polar ZnO Surfaces: Metal–Support Interaction and Alloy Effects Studied by Synchrotron Radiation X-Ray Photoelectron Spectroscopy. *J. Phys. Chem. C* **2012**, *116* (18), 10048–10056.
- (50) Papaefthimiou, V.; Dintzer, T.; Dupuis, V.; Tamion, A.; Tournus, F.; Hillion, A.; Teschner, D.; Hävecker, M.; Knop-Gericke, A.; Schlögl, R.; et al. Nontrivial Redox Behavior of Nanosized Cobalt: New Insights from Ambient Pressure X-Ray Photoelectron and Absorption Spectroscopies. *ACS Nano* **2011**, *5* (3), 2182–2190.
- (51) Ferrari, A. C.; Meyer, J. C.; Scardaci, V.; Casiraghi, C.; Lazzeri, M.; Mauri, F.; Piscanec, S.; Jiang, D.; Novoselov, K. S.; Roth, S.; et al. Raman Spectrum of Graphene and Graphene Layers. *Phys. Rev. Lett.* **2006**, *97* (18), 187401.
- (52) Ferrari, A. C.; Basko, D. M. Raman Spectroscopy as a Versatile Tool for Studying the Properties of Graphene. *Nat. Nanotechnol.* **2013**, *8* (4), 235–246.
- (53) Zhou, M.; Pasquale, F. L.; Dowben, P. A.; Boosalis, A.; Schubert, M.; Darakchieva, V.; Yakimova, R.; Kong, L.; Kelber, J. A. Direct Graphene Growth on Co₃O₄(111) by Molecular Beam Epitaxy. *J. Phys. Condens.* **2012**, *24*, 072201.
- (54) Lin, C.-Y.; Shiu, H.-W.; Chang, L.-Y.; Chen, C.-H.; Chang, C.-S.; Chien, F. S.-S. Core-Level Shift of Graphene with Number of Layers Studied by Microphotoelectron Spectroscopy and Electrostatic Force Microscopy. *J. Phys. Chem. C* **2014**, *118* (43), 24898–24904.
- (55) Gong, C.; McDonnell, S.; Qin, X.; Azcatl, A.; Dong, H.; Chabal, Y. J.; Cho, K.; Wallace, R. M. Realistic Metal–Graphene Contact Structures. *ACS Nano* **2014**, *8* (1), 642–649.
- (56) Eckmann, A.; Felten, A.; Mishchenko, A.; Britnell, L.; Krupke, R.; Novoselov, K. S.; Casiraghi, C. Probing the Nature of Defects in Graphene by Raman Spectroscopy. *Nano Lett.* **2012**, *12* (8), 3925–3930.

- (57) Hyman, M. P.; Martono, E.; Vohs, J. M. Studies of the Structure and Interfacial Chemistry of Co Layers on ZnO(0001). *J. Phys. Chem. C* **2010**, *114* (40), 16892–16899.
- (58) Luo, W.; Jing, F.-L.; Yu, X.-P.; Sun, S.; Luo, S.-Z.; Chu, W. Synthesis of 2-Methylpyrazine Over Highly Dispersed Copper Catalysts. *Catal. Letters* **2012**, *142* (4), 492–500.
- (59) Jacobs, G.; Chaney, J. A.; Patterson, P. M.; Das, T. K.; Davis, B. H. Fischer–Tropsch Synthesis: Study of the Promotion of Re on the Reduction Property of Co/Al₂O₃ Catalysts by in Situ EXAFS/XANES of Co K and Re LIII Edges and XPS. *Appl. Catal. A Gen.* **2004**, *264* (2), 203–212.
- (60) Bezemer, G. L.; Bitter, J. H.; Kuipers, H. P. C. E.; Oosterbeek, H.; Holewijn, J. E.; Xu, X.; Kapteijn, F.; Dillen, A. J. Van; Jong, K. P. De. Cobalt Particle Size Effects in the Fischer–Tropsch Reaction Studied with Carbon Nanofiber Supported Catalysts. *J. Am. Chem. Soc.* **2006**, *128* (6), 3956–3964.
- (61) Jacobs, G.; Das, T. K.; Zhang, Y.; Li, J.; Racoillet, G.; Davis, B. H. Fischer-Tropsch Synthesis: Support, Loading, and Promoter Effects on the Reducibility of Cobalt Catalysts. *Appl. Catal. A Gen.* **2002**, *233* (1-2), 263–281.
- (62) Jacobs, G.; Ji, Y.; Davis, B. H.; Cronauer, D.; Kropf, A. J.; Marshall, C. L. Fischer–Tropsch Synthesis: Temperature Programmed EXAFS/XANES Investigation of the Influence of Support Type, Cobalt Loading, and Noble Metal Promoter Addition to the Reduction Behavior of Cobalt Oxide Particles. *Appl. Catal. A Gen.* **2007**, *333* (2), 177–191.
- (63) Liu, X.-C.; Shi, E.-W.; Chen, Z.-Z.; Chen, B.-Y.; Huang, W.; Song, L.-X.; Zhou, K.-J.; Cui, M.-Q.; Xie, Z.; He, B.; et al. The Local Structure of Co-Doped ZnO Films Studied by X-Ray Absorption Spectroscopy. *J. Alloys Compd.* **2008**, *463* (1-2), 435–439.
- (64) Khodakov, A. Y.; Griboval-Constant, A.; Bechara, R.; Villain, F. Pore-Size Control of Cobalt Dispersion and Reducibility in Mesoporous Silicas. *J. Phys. Chem. B* **2001**, *105* (40), 9805–9811.
- (65) Canc, L. G.; Jorio, A.; Ferreira, E. H. M.; Stavale, F.; Achete, C. A.; Capaz, R. B.; Moutinho, M. V. O.; Lombardo, A.; Kulmala, T. S.; Ferrari, A. C. Quantifying Defects in Graphene via Raman Spectroscopy at Different Excitation Energies. *Nano Lett.* **2011**, *11* (8), 3190–3196.
- (66) Liu, L.; Ryu, S.; Tomasik, M. R.; Stolyarova, E.; Jung, N.; Hybertsen, M. S.; Steigerwald, M. L.; Brus, L. E.; Flynn, G. W. Graphene Oxidation : Thickness-Dependent Etching and Strong Chemical Doping. *Nano Lett.* **2008**, *8* (7), 1965–1970.

- (67) Ryu, S.; Han, M. Y.; Maultzsch, J.; Heinz, T. F.; Kim, P.; Steigerwald, M. L.; Brus, L. E. Reversible Basal Plane Hydrogenation of Graphene. *Nano Lett.* **2008**, *8* (12), 4597–4602.
- (68) Ferrari, A. C. Raman Spectroscopy of Graphene and Graphite: Disorder, Electron–phonon Coupling, Doping and Nonadiabatic Effects. *Solid State Commun.* **2007**, *143*, 47–57.
- (69) Krauss, B.; Lohmann, T.; Chae, D. H.; Haluska, M.; Von Klitzing, K.; Smet, J. H. Laser-Induced Disassembly of a Graphene Single Crystal into a Nanocrystalline Network. *Phys. Rev. B* **2009**, *79* (16), 1–9.
- (70) Zhang, Z.; Yin, J.; Liu, X.; Li, J.; Zhang, J.; Guo, W. Substrate-Sensitive Graphene Oxidation. *J. Phys. Chem. Lett.* **2016**, 867–873.
- (71) Mun, D.; Lee, J.; Bae, S.; Kim, T. Photocatalytic Decomposition of Graphene over a ZnO Surface under UV Irradiation. *Phys. Chem. Chem. Phys.* **2015**, *17* (2), 15683–15686.
- (72) Zhang, B.; Su, D. S. Probing the Metal – Support Interaction in Carbon- Supported Catalysts by Using Electron Microscopy. *ChemCatChem* **2015**, *7*, 3639–3645.

Chapter 5

Interaction of bimetallic PtCo layers with bare and graphene-covered ZnO (0001) supports

Chapter 5 Interaction of bimetallic PtCo layers with bare and graphene-covered ZnO (0001) supports

5.1 Introduction

Bimetallic catalysts have been proposed to be one of the most promising classes of catalysts in several applications such as fuel cells and hydrocarbon reforming reactions.¹⁻³ In comparison to their monometallic counterparts, bimetallic catalysts have superior performance in several catalytic reactions, not only due to the combination of the properties associated with the two metals but also because of synergistic effects. However, the surface composition and oxidation state may vary during the catalytic reaction which will complicate the understanding of reaction mechanisms. For example, in reactive gas phase, preferential adsorption of reactant molecules will induce the rearrangement of surface atoms, which consequently influences the surface morphology, structure and the oxidation state.^{4,5} Since high temperature is necessary for many reactions, heat treatment induced surface segregation makes the bimetallic system more complex.^{1,6} In addition, in the case of supported bimetallic catalysts, the support properties can also determine the tendency of surface segregation due to the different interactions between metals and the support. The effect of the support is more pronounced when the strong metal-support interaction (SMIS) occurs between metals and reducible oxides supports, where metals with low work functions (i.e. Na, K and Al) may be oxidized by the support (i.e. TiO₂ and ZnO) and metals with high work functions (i.e. Pt, Pd and Au) may be encapsulated. In many cases, the surface state of the bimetallic catalysts are under the influence of a combination of these factors and it is difficult to establish the structure-property relationship.

In the previous chapters, we have shown that the graphene interlayer can significantly modify the Co-support interactions and the redox properties of Co. This part of work is a step forward in the comprehension of graphene's effect to the bimetallic-support interaction. Based on the previous results, Co-Pt bimetallic was studied due to its potential applications in many catalytic reactions, such as Fischer-Tropsch synthesis,⁷ CO oxidation^{6,8} and electrochemical reactions^{9,10}. This part of work can assist in the understanding of bimetallic-support interactions and the designing of new catalysts materials.

5.2 Experimental part

Sample preparation.

Two substrates are used in this study: Zn terminated ZnO(0001) and graphene covered ZnO(0001) (named as G/ZnO). Cobalt and platinum were evaporated under UHV on clean ZnO and G/ZnO substrates, using a commercial e-beam evaporator (Mantis depositions Ltd., model: QUAD-EV-C) attached to the UHV set-up. In order to control the atomic ratio between Co:Pt, the metal vapor flux was adjusted to keep the same deposition time. The base pressure during deposition was better than 1×10^{-8} mbar and the two metals were deposited using pre-calibrated vapour fluxes. For the experiments described here we used 5 min deposition time with Co and Pt deposition rates of 0.06 nm/min and 0.02 nm/min, respectively. Under these conditions, the overall PtCo loading is estimated of about 0.4 nm and the Co:Pt ratio was kept at 3:1 (0.3 nm Co/0.1 nm Pt) for all the samples studied in this thesis. Details of sample preparation can be found in Chapter 2, section 2.1.

Characterization methods.

Vacuum and low pressure redox treatments were performed in the VSW ultra-high vacuum (UHV) system described in the experimental part of this thesis. During the UHV studies, the samples were flash-heated at the set temperature with a rate of 60 °C/min. For the low pressure redox study, oxygen and hydrogen exposure of samples was carried out in the main chamber by leak valves and the pressure was monitored at 5×10^{-7} mbar by an ion gauge. Each oxidation temperature was kept for 0.5 h while flash annealing was used for the reduction step.

Medium pressure redox studies were carried out in a high pressure chamber attached on the VSW UHV system. The procedure used in this part of work was identical to these described in Chapters 4. In detail, each oxidation/reduction step was performed by annealing for 30 min at various temperatures in 7 mbar O₂ or H₂ with a leak rate of 40 mbar l/s respectively. Subsequently the sample was cooled down in the gas, pumped in UHV pressure and transferred to the UHV XPS analysis chamber, without being exposed to the atmosphere. A monochromatic AlK α source was used for the XPS analysis. Two different photoelectron take off angles (angle between electron analyzer and sample surface nominal) were chosen to probe different depth of the sample: a $\theta = 0^\circ$ take off angle (by default) which probes more of the bulk and a $\theta = 75^\circ$ take off angle which is more surface sensitive.

The low energy ion scattering spectroscopy (LEIS) measurements were performed with an IQE 11/35 (SPECS®) ion source using He⁺ as incident ion. The incident energy was typically 750 eV and the scattering angle was 130 °.

Raman measurements were performed with a micro-Raman spectrometer (Horiba LabRam Aramis), with excitation wavelengths of 532 nm. The laser was focused with a 100× objective lens to an approximately 1 μm spot, with a laser power of 1 mW to avoid heating and damage to the sample. The morphology of the samples was investigated at ambient conditions using a NTEGRA aura AFM microscope from NT-MDT. The AFM topography images were obtained at tapping mode using PPP-NCHR tips from NANOSENSORS with radius less than 10 nm.

5.3 Results and discussion

5.3.1 UHV annealing

Initially the interaction of the bimetallic layer with each substrate was investigated by annealing in UHV, thus without the presence of reactive gas phase atmosphere. Figure 5.1 compares the Co 2p XPS peaks of CoPt/ZnO and CoPt/G/ZnO at various annealing temperatures. Up to 300 °C, the sharp Co 2p_{3/2} peak at 778.3 eV indicates the metallic Co state for both samples. However, upon further annealing, the evolution of the Co 2p spectrum in the two samples is considerably different. In particular for CoPt/ZnO, as the temperature increases, the initial spectrum is modified to a component at 780.6 eV and a shake-up satellite peak at 785.0 eV, which is typical for CoO. This observation is in agreement with the results presented in Chapter 3. There it was shown that when monometallic Co supported on ZnO was annealed in vacuum, a solid state reaction took place at the interface inducing cobalt oxidation. However there is a significant difference between the monometallic and bimetallic deposit, regarding the temperature that this reaction occurs. In particular, the addition of Pt significantly increases the oxidation temperature of cobalt from 200 °C (for monometallic Co) to 450 °C (for PtCo).

On the contrary, annealing of CoPt/G/ZnO does not cause evident effect to the Co 2p spectrum, which remains almost stable up to 450 °C. Only a minor CoO peak contribution could be observed as a shoulder at 780.6 eV at 550 °C. This indicates that the single layer graphene affects the interaction between bimetallic CoPt overlayer and the ZnO support by preventing the oxidation of Co from ZnO. At 550 °C, the slight oxidation of Co might be induced by the intercalation of small amount of Co which is directly in contact with ZnO through the defects of the graphene layer (see 5.3.5).

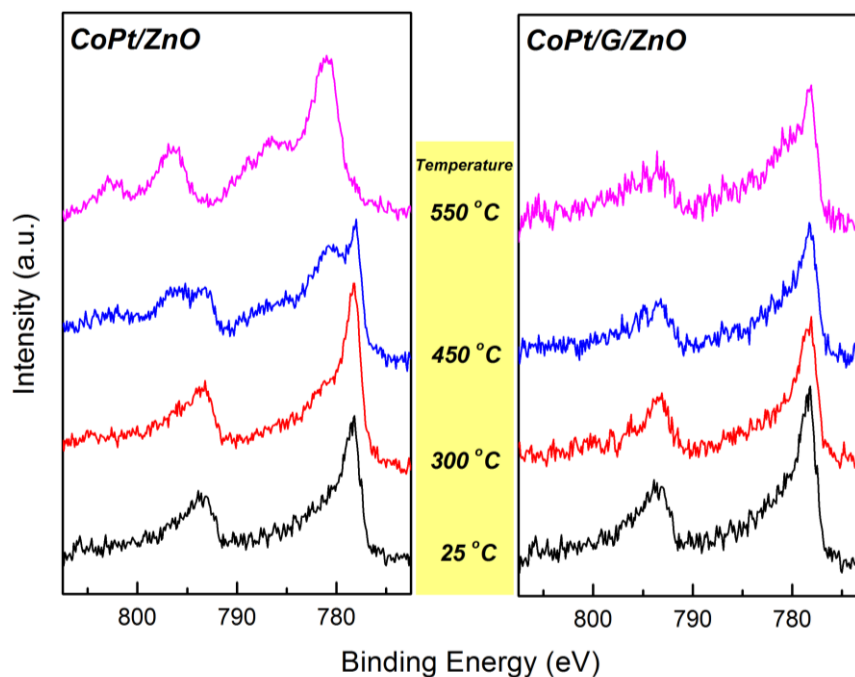


Figure 5.1 XPS spectra of CoPt/ZnO and CoPt/G/ZnO after annealing in UHV at various temperatures.

The evolution of the cobalt oxidation state as a function of temperature can be followed by the average cobalt valence state shown in Figure 5.2b. This ratio was obtained after deconvolution of the Co 2p spectra in two components (metallic Co and CoO) using reference spectra curves as explained in the previous chapters. In order to distinguish potential segregation between the two cobalt oxidation states, measurements from normal (0° degrees) and grazing (75° degrees) photoelectron takeoff angles are included. We recall that a higher take-off angle provides information of less depth, given that there is no spherical symmetry of the particles (e.g. spheres on planar substrate). A characteristic example of spectra recorded on the same sample at 2 different angles is given in Figure 5.2a.

The differences in the oxidation state of cobalt in the PtCo overlayer in the two samples are evident. It is also clear that for both substrates the amount of CoO is systematically lower at 75° as compared to the 0° measurements. This difference shows that metallic cobalt is located preferentially on the surface of the PtCo particles (the metallic Co peak component is enhanced at 75° degrees takeoff angle measurements which are more surface sensitive) with more CoO into their interior.

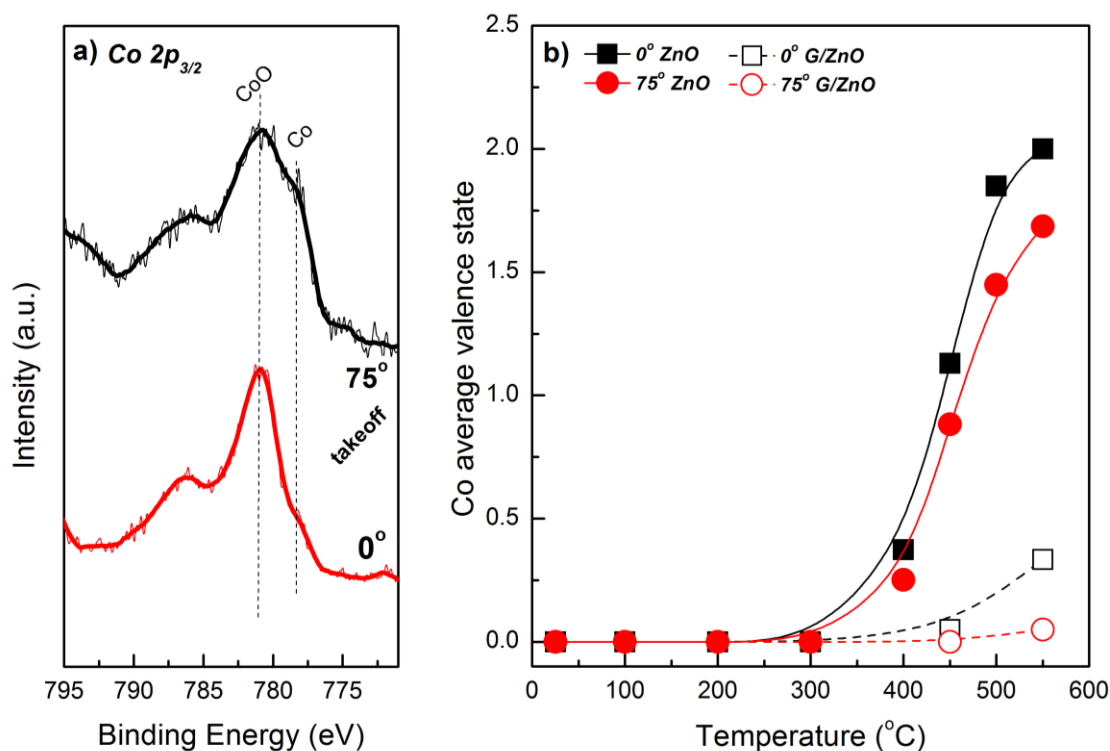


Figure 5.2 a) Characteristic Co $2p_{3/2}$ spectra recorded in two takeoff photoelectron emission angles on PtCo/ZnO after UHV annealing at 500 °C, b) the evolution of cobalt average valence state for CoPt/ZnO and CoPt/G/ZnO samples as a function of the annealing temperature. The measurements were acquired at two different photoelectron takeoff angles ($\theta = 0$ and 75°).

We turn now our attention to the Pt 4f spectra (*not shown*). Apart from some changes in their intensity, the shape and binding energy of the Pt 4f peaks are identical for both substrates and remain unaffected after the annealing treatments. This indicates that on both samples platinum remains in the metallic state upon annealing, which is not surprising since it is well-known that platinum, as compared to cobalt, is very difficult to get oxidized by the gas phase.

The XPS intensity ratio of Co to Pt (Figure 5.3) is indicative of Co and Pt mixing within the PtCo overlayer. In addition, changes of the Co/Pt ratio can be used to evaluate the preferential surface segregation of the alloy constituents upon the annealing treatment. As shown in Figure 5.3, before 400 °C, the $I_{\text{Co}}/I_{\text{Pt}}$ ratios on both substrates decrease gradually, indicating a higher agglomeration rate of Co than Pt and/or segregation of Pt on top of Co. At higher annealing temperatures, the continuous decreasing trend of $I_{\text{Co}}/I_{\text{Pt}}$ ratio for CoPt/GZnO implies that Co and Pt maintain a similar aggregation tendency. However, an opposite tendency is shown in Figure 5.3 for CoPt/ZnO, where the $I_{\text{Co}}/I_{\text{Pt}}$ ratio rises up after 400 °C. As has been shown in Figure 5.2b, after annealing at 400 °C, Co on CoPt/ZnO is partly oxidized to CoO. We have shown in the previous chapters that cobalt oxidation is followed by spread out of Co over the

support, which is reflected in the increase of Co to support intensity ratio.^{11,12} However, since Pt does not have as intense interaction with the ZnO support (absence of Pt oxides) as cobalt, it migrates and coalescences in a higher degree at higher temperature. This will have a direct effect on the $I_{\text{Co}}/I_{\text{Pt}}$ ratio which will increase, as shown in Figure 5.3.

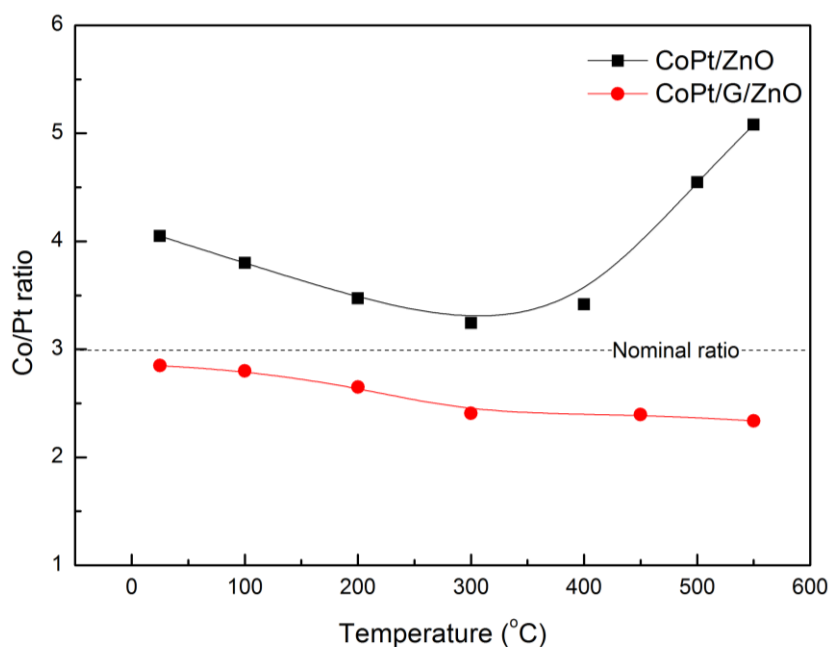


Figure 5.3 Variation of the Co 2p/Pt 4f intensity ratios for CoPt/ZnO and CoPt/G/ZnO samples as a function of the annealing temperature in UHV.

As has been shown in Figure 5.1b, after annealing at 350 °C, Co on CoPt/ZnO is partly oxidized to CoO. As revealed in the previous chapters, cobalt oxidation is followed by spread out of Co over the support, which is reflected in the increase of Co to support XPS intensity ratio.^{11,12} However, as shown in Figure 5.2, the direction of cobalt oxide migration is from inwards (close to the interface with ZnO) towards the surface of the particles. It seems that cobalt oxidation displaces Pt atoms from the surface leading to the increase of the Co/Pt ratio shown in Figure 5.3. This is in accordance with the well-known tendency of Co oxides to migrate toward the surface and covering Pt.^{13,14,8} The reason is likely that since Co has higher oxygen affinity than Pt, it tends to combine with O₂, which will drive Co atoms to migrate to the surface when bimetallic CoPt particles are exposed to an O₂ atmosphere. However, when CoPt/ZnO sample is annealed in UHV conditions, the oxygen source comes from the ZnO substrate which is found underneath the CoPt. In this case, Co moves to the interface of CoPt and ZnO to get oxidized and thus it leaves Pt at the outer surface.

The low energy ion scattering spectroscopy (LEIS) results can be used as an ultimate surface sensitive method to distinguish the composition of the outermost surface layer of the samples. As shown in Figure 5.4, Pt, Zn and Co related peaks can be distinguished in the LEIS spectrum according to their characteristic scattered He ions kinetic energy. It is evident that the LEIS spectrum of the fresh PtCo/ZnO sample (at 25 °C) is dominated by the Pt signal, which suggests the presence of Pt on the surface. The presence of the Zn signal indicates that the ZnO surface is not completely covered by Co and Pt, but there are areas of the ZnO support that remain uncovered. This is reasonable, taking into account that the deposition amount of metals is only ~ 0.4 nm.

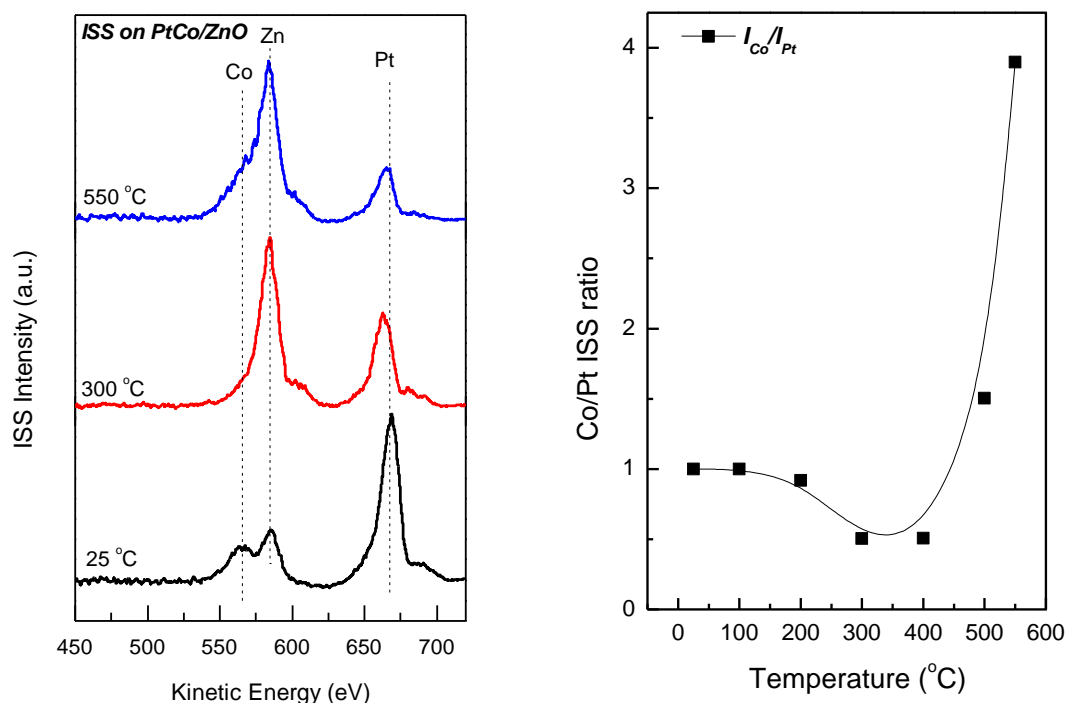


Figure 5.4. Characteristic low energy ion scattering spectroscopy spectra (LEIS) of CoPt/ZnO samples annealed in UHV at the indicated temperatures. The figure to the right shows the Co to Pt ratio obtained after deconvolution of the ISS spectra, as a function of the UHV annealing temperature. Please note that the data are not normalized to the ISS cross sections of each element therefore should be interpreted qualitatively.

Upon annealing at intermediate temperature (300 °C), the Zn peak intensity increases considerably, which is consistent with agglomeration of the PtCo layer and uncovering of the support area. Of course one cannot exclude that part of the Zn signal is derived from the Zn support ions which spillover the PtCo layer during annealing. In addition, the Co peak almost disappears. Finally at the higher annealing temperature (550 °C), the increase of the Zn peak

signal continues, but the cobalt related signal re-appears. These observations can be easily followed in the Co/Pt ratios obtained by the deconvolution of the LEIS peaks which are also consistent with the XPS results of Figure 5.3.

5.3.2 Low pressure redox

The effect of single layer graphene to the initial stages of reduction and oxidation of bimetallic CoPt was studied next. In order to do so, CoPt/ZnO and CoPt/G/ZnO samples were exposed consecutively at low pressure (5×10^{-7} mbar) of O₂ and H₂ in the UHV chamber and the evolution of the oxidation state as a function of temperature was studied *in situ*. In Figure 5.5, the Co average valence for CoPt/ZnO and CoPt/G/ZnO at two different takeoff angles is plotted versus the annealing temperature for O₂ and consequently for H₂ atmosphere. We should recall that the deposition conditions and the initial sample state (before gas exposure) were almost identical to those of the UHV annealing experiments shown in the previous paragraph.

As expected, the general trend of oxidation and reduction is the same for both substrates. In particular, Co is gradually oxidized to CoO in O₂ and reduced back to metallic Co in H₂, while Pt oxidation state is not affected under the employed conditions. However, the Co oxidation and reduction rate, as well as the angle measurements show significant differences between bare and graphene-covered ZnO substrates. As can be clearly seen in Figure 5.5, as soon as the samples are exposed to O₂ atmosphere, oxidation of Co on ZnO is much more pronounced as compared to that on graphene. With the temperature increase, the Co oxidation state at different depths shows a significant deviation; Co on ZnO is preferentially oxidized from the subsurface while Co on G/ZnO is oxidized more towards the outer surface.

Preferential oxidation of noble metals at their interface with oxide substrates has been reported by several groups.¹⁵⁻¹⁷ Freund *et al*^{15,16} reported the preferential oxidation of Pd at the Pd /Fe₃O₄ interface and they suggested that the Pd oxide film is stabilized by the strong interaction with the iron oxide support. In addition, when Au/ZnO nanorods were oxidized at 200 °C, higher oxidation state of Au was observed at the interface with ZnO due to the Au-O-Zn interaction. The affinity of cobalt to oxygen species is of course much higher than that of gold, and cobalt has been reported to get oxidized even under UHV conditions by residual OH groups attached on ZnO.¹⁸ In Chapter 4 we observed this phenomenon also for the Co/ZnO sample. Although the details of the preferential oxidation of Co at the interface of Co and ZnO

are still unclear, the Co-ZnO interaction should be the driving force. With a single layer graphene in-between, this Co-ZnO interaction is blocked, together with the interfacial oxidation, rationalizing the higher CoO ratio at the outer surface of CoPt/G/ZnO in Figure 5.5a. At 300 °C, Co on both substrates is partially oxidized to CoO, with ~75 % CoO on CoPt/ZnO and ~60 % CoO on CoPt/G/ZnO. Since Co oxidation started from dissociative adsorption of oxygen and was followed by diffusion of oxygen into the Co layer in order to establish a quasi-octahedral ligand field and then formation of CoO, one can presume that adsorption and/or diffusion of oxygen is easier on CoPt/ZnO than CoPt/G/ZnO.

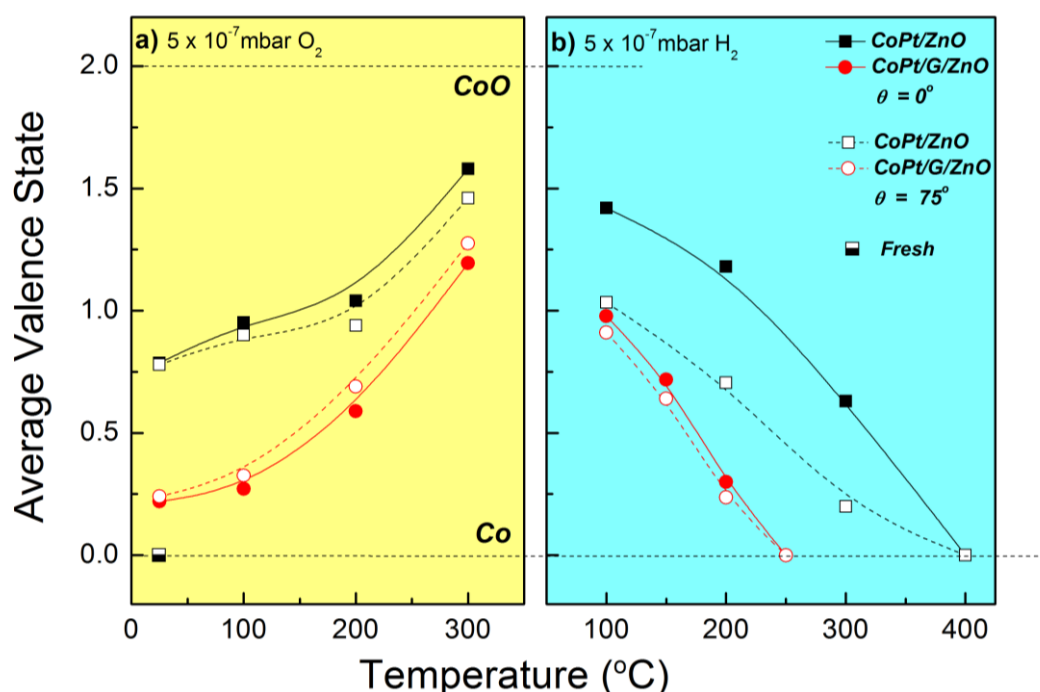


Figure 5.5 Co average valence state of CoPt/ZnO and CoPt/G/ZnO samples during the low pressure redox treatments. The initial oxidation states (just after UHV deposition) are represented by the two colors point.

Under H_2 exposure, CoO for both samples starts to reduce from 100 °C and is completely reduced to metallic Co at higher temperature. However, due to the weak interaction between Co and G/ZnO, reduction of CoO on G/ZnO is much easier than that of CoO on ZnO. It should be noticed that, on both substrates, CoO reduction is more enhanced at the outer surface. This is not unexpected since the reduction medium (H_2 in the gas phase) adsorbs and diffuses from the outer towards the interior of the PtCo overlayer.

Figure 5.6 shows the variation of the I_{Co}/I_{Pt} ratio with the oxidation/reduction temperature for both CoPt/ZnO and CoPt/G/ZnO. As shown also for the UHV annealed sample, the initial Co/Pt ratio differs in each sample. In particular, for graphene supported CoPt the initial ratio is

close to the nominal one, while for the ZnO supported sample it is higher, suggesting a higher surface exposure of cobalt. This might be the effect of segregation of Co over Pt in mixed PtCo particles or may reflect mostly separated Pt and Co particles with lower contact angle of Co on ZnO (thus higher surface area). The latter scenario can be justified by the well manifested strong interaction between Co and ZnO, which drives Co to wet the ZnO surface.

In O₂, the I_{Co}/I_{Pt} ratio for both samples increases with temperature, however this increase is more evident at the G/ZnO substrate, while at the maximum temperature (300 °C), both samples converge to the same I_{Co}/I_{Pt} ratio. This suggests that the remixing of the PtCo overlayer upon annealing in low pressure O₂, is due to the segregation of Co on the surface of Pt (increase of I_{Co}/I_{Pt}), which is more pronounced on G/ZnO. As mentioned in the previous part, exposure of bimetallic CoPt in O₂ atmosphere would drive Co atoms to migrate on top of Pt and get oxidized to CoO. Please note that, although Co on ZnO is easier to be oxidized as the oxidation degree is always found higher than Co on G/ZnO, the segregation of CoO on Pt is less significant, as is shown in Figure 5.6 as a tender increasing trend of I_{Co}/I_{Pt}.

Comparison of Figure 5.5 and Figure 5.6 shows that in the case of G/ZnO there is a close relation between the cobalt oxidation state and its surface segregation over Pt. In particular, on G/ZnO, a steep increase of the cobalt average valence as a function of temperature is followed by an equally steep increase of the I_{Co}/I_{Pt} ratio. On the contrary, for ZnO, the increase of the Co average valence state especially above 100 °C is accompanied by an almost stable I_{Co}/I_{Pt} ratio. This indicates that oxidation and surface segregation might be governed by different mechanisms in the two cases. This information should be combined with 2 additional facts; first is the differences observed between the two samples at the normal and grazing take off angle measurements (higher Co surface valence for G/ZnO, but lower for ZnO as compared to the subsurface, shown in Figure 5.5) and second is the higher oxidation state of cobalt in the case of ZnO as compared to G/ZnO. Based on the above arguments one can conclude that in the case of ZnO, cobalt oxidation is taking place not only from the gas phase O₂, but also at the interface, due to the interaction with the support. As was also mentioned in the case of monometallic Co, oxidation by ZnO will drive CoO towards the interface with the support rather than to the surface over Pt.

Reduction of CoO in H₂, partly cancels cobalt segregation and drives metallic Co to re-mix with Pt, as is shown by the decrease of I_{Co}/I_{Pt} ratio observed for both substrates. Reduction of Co oxides on CoPt/ZnO is similar to that on CoPt/G/ZnO, leading to the alloying of Co and Pt,

and after complete reduction at 400 °C, $I_{\text{Co}}/I_{\text{Pt}}$ almost recovers to its original ratio. It has been reported that Pt facilitates Co reduction in bimetallic PtCo structures (nanoparticle or layer structure), due to the hydrogen activation and spillover effect from Pt to Co which facilitates reduction of Co.^{3,13,19} This is clearly reflected by the low reduction temperature as compared to monometallic samples. The effect of Pt is more evident on the bare ZnO substrate, since the reduction of cobalt is complete, even if it requires relatively higher temperature. Please recall the results presented in Chapter 4 for monometallic cobalt, which have shown inability to reduce Co ions in H_2 . Another promising effect of graphene (apart from the ease in reduction) is its ability to restore the $I_{\text{Co}}/I_{\text{Pt}}$ ratio close to the nominal one after reduction. This result suggests remixing of CoPt and the reversibility of the dealloying process observed in O_2 at least during a single redox cycle.

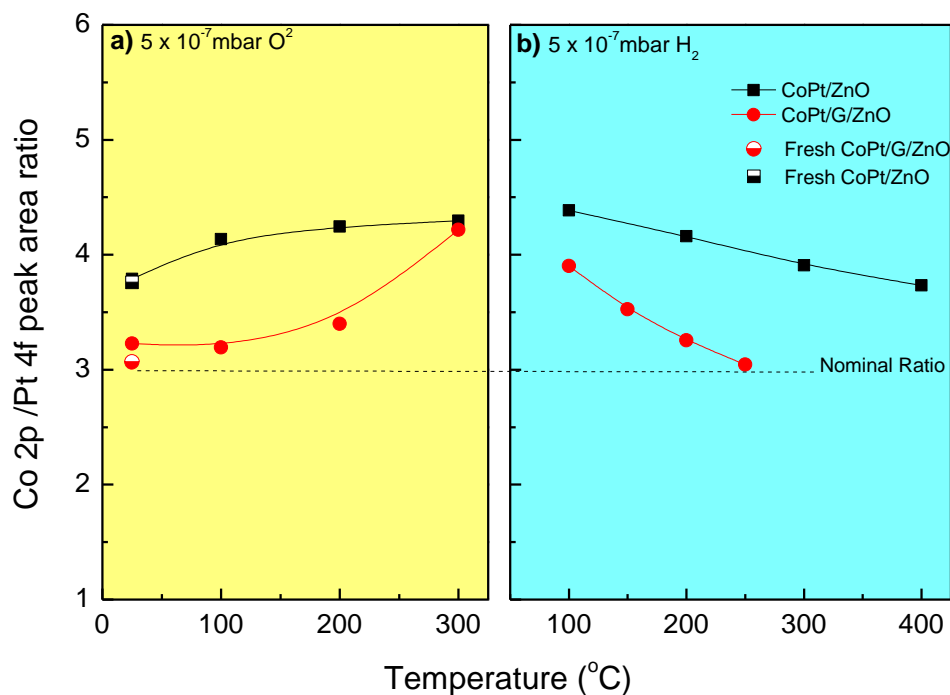


Figure 5.6 Variation of the XPS Co 2p/Pt 4f intensity ratios for CoPt/ZnO and CoPt/G/ZnO samples under 5×10^{-7} mbar O_2/H_2 conditions. The initial ratios (just after UHV deposition) are represented by the two colors points.

5.3.3 Medium pressure conditions

Studies under UHV and low pressure conditions helped us to understand graphene's effect to the CoPt and ZnO interaction as well as the Co redox properties at the initial stages of oxidation. However, usually real catalytic conditions involve exposure at higher gas pressure (atmospheric or even higher). Traditionally in surface science studies, it is difficult to correlate

results obtained at low vacuum conditions with real world catalysis which is usually referred as the “*pressure gap*” problem. To deal with this question we carried out medium pressure (7 mbar) redox studies on CoPt/ZnO and CoPt/G/ZnO. However, we should note that, in contrast with the low pressure studies, the presented results are not obtained *in situ*, but in a *quasi in situ* mode as described in the experimental part in Chapter 2.

The Co average valence of CoPt/ZnO and CoPt/G/ZnO during the medium pressure redox treatments is shown in Figure 5.7. Compared to low pressure oxidation, it is clear that higher O₂ pressure is much more effective to cobalt oxidation.²⁰ However, even under these conditions, a small portion of Co on G/ZnO is still in the metallic state after room temperature oxidation. With the temperature increase, Co on both substrates becomes partially oxidized and at 250 °C, the Co₃O₄ ratio reaches ~50 % for both samples. This implies that under high temperature and high pressure oxygen conditions, diffusion of oxygen is no longer the determining step of the Co oxidation reaction. Comparison with the monometallic Co samples presented in Chapter 4, can lead to the conclusion that Pt hinders cobalt oxidation at the medium O₂ pressure. A closer look at the oxidation state at different analysis depths shows that Co on ZnO is homogeneously oxidized while oxidation of Co on G/ZnO is still more evident at the outer surface. This implies that even at 7 mbar O₂ the subsurface interaction has probably still an effect on cobalt oxidation. This is of course much less evident in the spectroscopic results due to the higher oxidation degree of cobalt and validates our choice to study metal/substrate interaction at different pressure regimes.

The reduction of supported cobalt oxides in 7 mbar H₂ as a function of the annealing temperature is shown in Figure 5.7b. As is evident, after treatment at 150 °C most of cobalt oxide is already reduced. Cobalt oxide supported over graphene is reduced at relatively lower temperature as compared to the ZnO-supported one, as is typically observed in all samples and at all conditions studied in this thesis. Compared to the medium pressure reduction results of monometallic Co/ZnO shown in Chapter 4, we can find that with the addition of Pt, Co on ZnO can be completely reduced instead of forming a Co_xZn_{1-x}O mixed oxide phase. In addition, angle measurements showed for both samples that the reduced cobalt signal is predominately enhanced on the surface, indicating that reduction proceeds from the surface toward the core of PtCo overlayer.

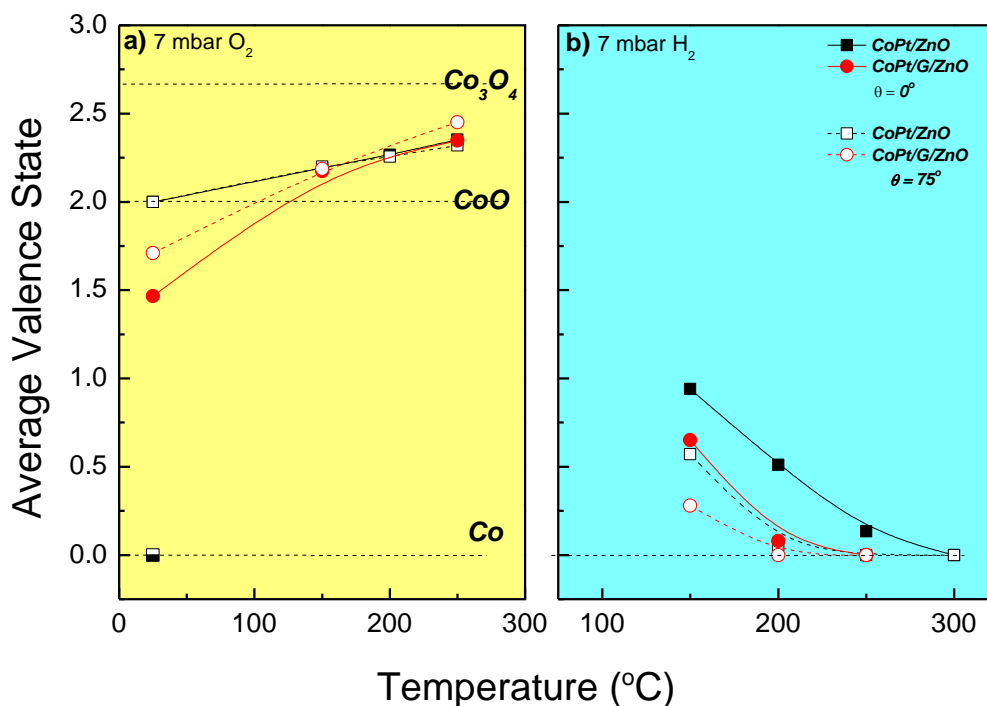


Figure 5.7 Co average valence state of CoPt/ZnO and CoPt/G/ZnO during the medium pressure redox treatments. The initial oxidation states (just after UHV deposition) are represented by the two colors point.

We turn now our attention on the oxidation state of Pt. In contrast to the UHV and low pressure conditions, oxidation of Pt is observed under medium pressure oxidation conditions. The deconvolution of Pt 4f XPS spectra for both samples is shown in Figure 5.8. The evolution of Pt oxidation state as a function of temperature after Pt 4f peak deconvolution is shown in Figure 5.9. The Pt 4f_{7/2} for both freshly prepared CoPt/ZnO and CoPt/G/ZnO is found at ~71.6 eV, in agreement with the literature values for PtCo alloys.^{21,22} Annealing of CoPt/G/ZnO in O₂ up to 150 °C does not influence the main Pt 4f peak. Besides, an additional peak at higher binding energy (72.6 eV) is observed after oxidation at 250 °C. This peak can be safely assigned to PtO formation according to literature reports.²³ In the case of CoPt/ZnO, ~9 % of the total amount of Pt is oxidized to PtO already at room temperature, while this fraction further increases to 19 % after oxidation at 150 °C. When the temperature rises to 250 °C, a higher oxidation state of Pt, located at ~ 74.2 eV, is clearly shown at the XPS spectrum. This new feature is in consistence with further oxidation of PtO to PtO₂.^{23,24}

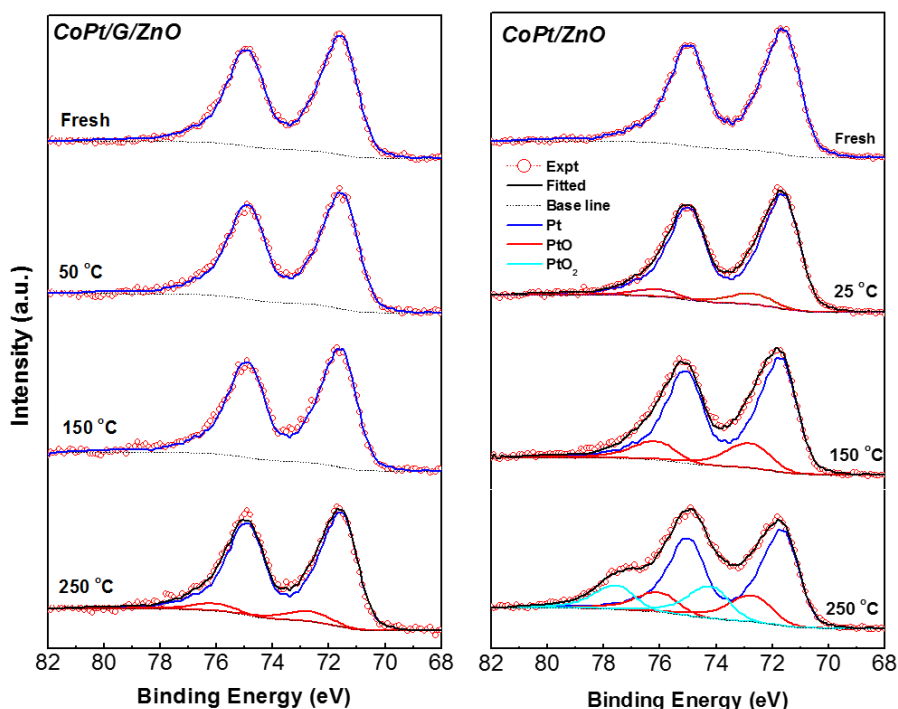


Figure 5.8 The Pt 4f XPS spectra under various oxidation temperatures for CoPt/ZnO and CoPt/GZnO. Deconvolution of the main spectra to metal and oxidized Pt components is included.

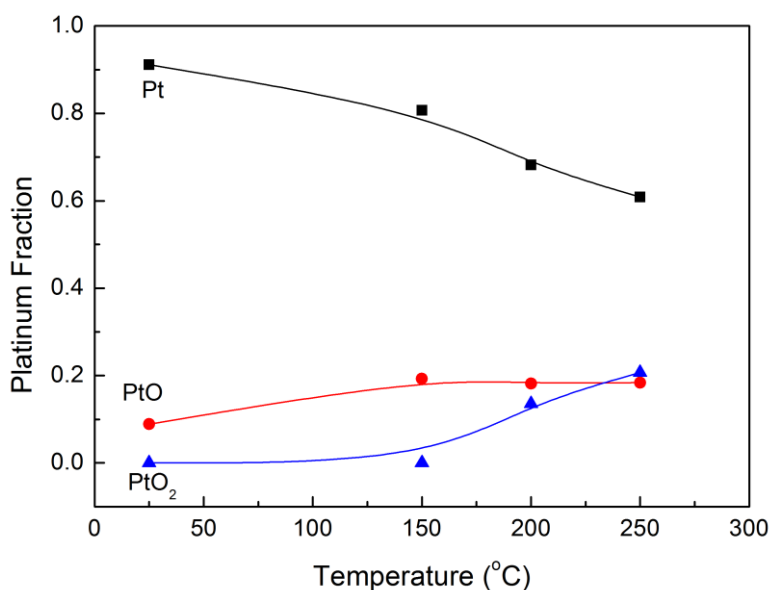


Figure 5.9 Evolution of the various Pt oxidation states as a function of temperature. The results were obtained after deconvolution of the Pt 4f spectra recorded on CoPt/ZnO sample during medium pressure oxidation.

Oxidation of Au at the interface of Au and ZnO, at 200 °C and O₂ ambient, has been reported before and was attributed to Au-O-Zn interaction.¹⁷ Ceria is also known to stabilize Pt oxides by formation of Pt-Ce-O species.^{25,26} In our case, we could not observe any clear difference in

the angle dependent measurements, therefore it is difficult to attribute the location of Pt oxides as surface or as subsurface. Unfortunately neither the mechanism of Pt oxidation on ZnO can be pointed out unambiguously. However, since the only difference between the two samples is the substrate, we presume that ZnO plays an important role in Pt oxidation. Therefore, under the medium pressure oxidation conditions, although Co oxidation states on both substrates are similar, Pt is hardly oxidized on CoPt/G/ZnO due to the effect of graphene. These results indicate that Pt oxidation is facilitated on bare ZnO in accordance with the trend observed for cobalt. It is also worth noting that this is not a direct support effect since it was not observed at lower pressure or UHV experiments, but probably ZnO indirectly affects the redox properties of Pt, for example due to the influence of the PtCo mixing arrangement.

Figure 5.10 shows the I_{Co}/I_{Pt} ratio as a function of redox temperature. Just after deposition, and before gas exposure, the I_{Co}/I_{Pt} ratio for G/ZnO was close to the nominal one, while cobalt surface segregation was observed in the case of ZnO. This is in accordance with the samples discussed before.

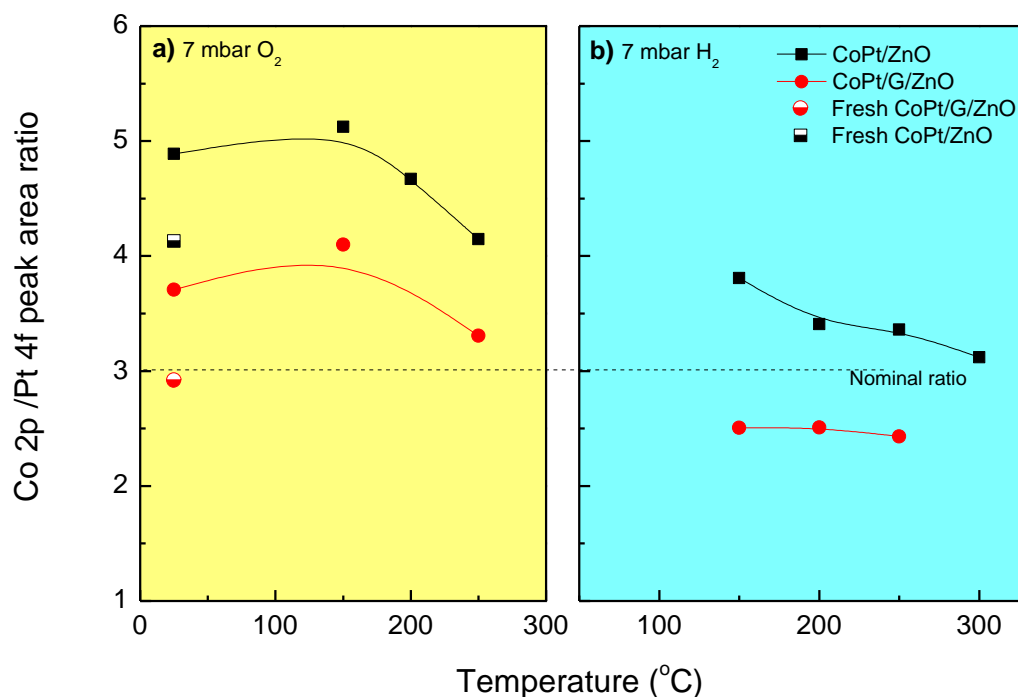


Figure 5.10 Variation of the normalized XPS Co 2p/Pt 4f intensity ratios with oxidation/reduction temperature for CoPt/ZnO and CoPt/G/ZnO samples under 7 mbar O_2/H_2 . The initial oxidation states (just after UHV deposition) are represented by the two colors point.

After oxygen exposure at room temperature there is an abrupt increase of this ratio, while after that the I_{Co}/I_{Pt} ratios of both samples follow a similar trend during oxidation. Up to 150

°C, the $I_{\text{Co}}/I_{\text{Pt}}$ ratio increases suggesting re-dispersion of Co after oxidation and/or enrichment of CoO on top of Pt. However, at higher temperature (250 °C), the $I_{\text{Co}}/I_{\text{Pt}}$ ratio decreases, which could be explained by the oxidation of Pt and mixing of Pt and Co oxides.

During the reduction process in H_2 , Pt oxides on both substrates were readily reduced in the first annealing step (*not shown*). Co oxides on CoPt/G/ZnO are also mostly reduced after 150 °C. Concerning the $I_{\text{Co}}/I_{\text{Pt}}$ intensity ratio, after a significantly decrease due to the reformation of CoPt alloy, the ratio remains almost constant until Co is completely reduced. For CoPt/ZnO, Co reduction is slower than that of CoPt/G/ZnO, thus the $I_{\text{Co}}/I_{\text{Pt}}$ ratio shows a tender decreasing trend.

5.3.4 Morphology of supported bimetallic Co-Pt

The morphology study of all the samples fresh and after the redox treatments was carried out by AFM on tapping mode under atmospheric conditions. As shown in Figure 5.11, the as-deposited CoPt/G/ZnO sample shows highly dispersed nanoparticle structure which is in consistence with the morphology observed for monometallic Co in the previous chapters. Therefore as in these cases, a 3D growth mode of CoPt on graphene is proposed. After UHV annealing, much larger particles are shown in the AFM images. This is due to the dynamic coalescence of smaller particles driven by their enhanced mobility caused by the high temperature. The low and medium pressure redox treated samples show similar surface roughness and particle size. Since both samples are reduced at 250 °C, this demonstrates that the annealing temperature is the primary cause for the agglomeration of CoPt particles and the gas pressure plays a secondary role.

Freshly deposited CoPt forms a relatively flat structure on ZnO with the root mean square roughness (RMS) of 0.22 nm. After UHV annealing, CoPt on ZnO also shows nanoparticle structure similar to that of CoPt/G/ZnO. This is quite interesting since from the XPS results, after UHV annealing, Co is oxidized and then re-dispersed on ZnO. However, it should be noticed that the final Co/Zn ratio did not recover to the initial value, moreover, Pt/Zn ratio also decreased (*not shown*). The LEIS data also shows that more ZnO surface is exposed after UHV annealing. This means that as compared to the fresh deposited samples, CoPt is agglomerated. After low and medium pressure redox treatments, both Co and Pt are in the metallic state and agglomeration is manifested by the rougher particle structure on ZnO surface. These AFM

images also reflect that the surface roughness of CoPt on ZnO is mainly dependent on the final annealing temperature.

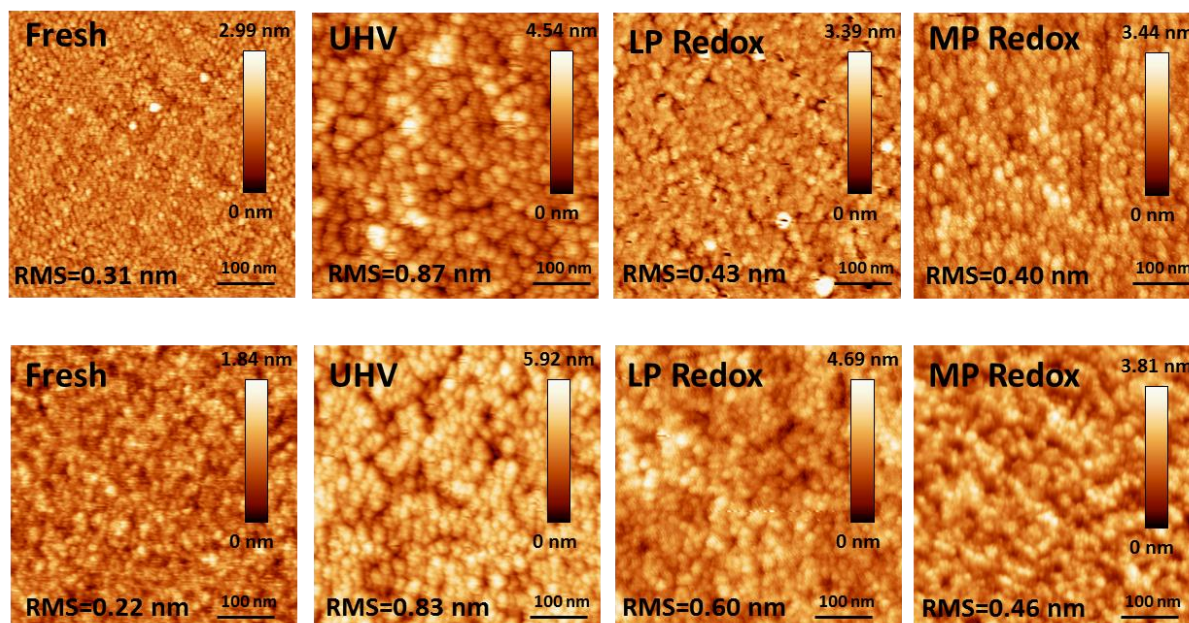


Figure 5.11 AFM images of CoPt/G/ZnO and CoPt/ZnO samples after various treatments. *Top row:* CoPt/G/ZnO and *bottom row:* CoPt/ZnO. From left to right are the samples: after CoPt deposition, UHV annealing, low pressure redox and medium pressure redox treatments.

5.3.5 Quality of Graphene

Figure 5.12 presents the representative micro-Raman spectra of graphene collected from the pristine and redox treated samples. The peaks width (fwhm) and their intensity ratios are summarized in Table 5.1. The spectrum of pristine graphene shows sharp G (1585 cm^{-1}) and 2D (2690 cm^{-1}) peaks with peak intensity ratio $I_{2D}/I_G = 1.60$, indicating that single layer graphene was successfully transferred on to ZnO without detectable amount of defects, like in the previous samples. After CoPt deposition, a low intensity D peak at 1350 cm^{-1} appears, implying that deposition of Co-Pt introduced a relatively small amount of defects.

Although Pt is reported to bound weakly on graphene through physisorbed interactions, cobalt is chemisorbed on graphene and therefore its interaction is expected to be stronger than that of Pt. Metals such as Ti^{27,28}, Pd²⁷, Cr²⁸ which have chemisorbed interaction with graphene were found to form a strong bond with it and introduce defects immediately just after deposition. Therefore, during Co-Pt deposition, chemical reaction may occur at the Co-graphene interface as for example the dissolution of carbon from graphene into the metal

volume.²⁹ It is expected that the high temperature annealing process that follows will enhance this process.²⁹

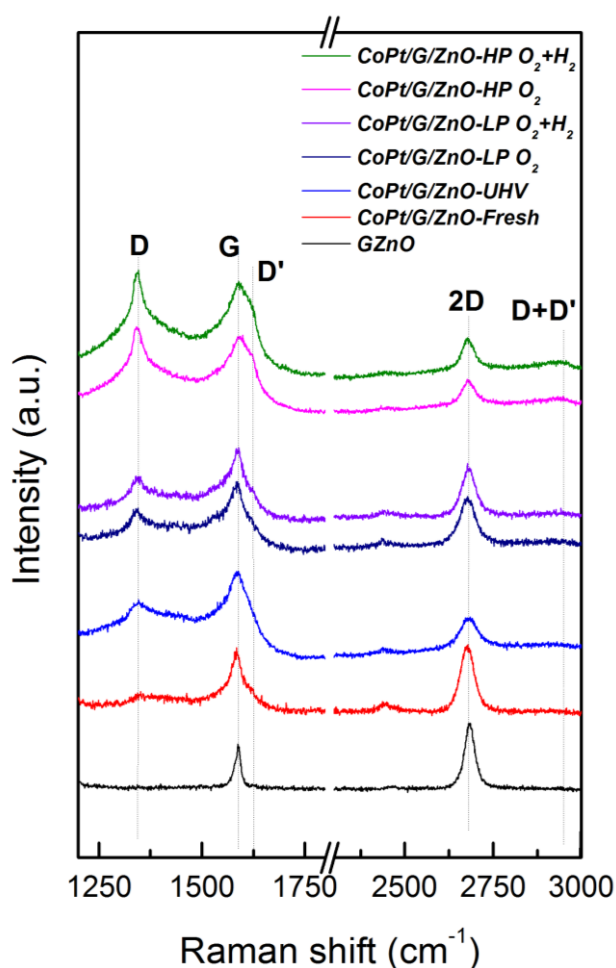


Figure 5.12 Raman spectra of graphene on fresh CoPt/G/ZnO samples and after various treatments.

As shown in Figure 5.12 and Table 5.1, after UHV annealing at 550 °C, a significantly higher intensity ratio of I_D/I_G (0.50) and a much broader 2D peak ($\text{fwhm} = 61.2 \text{ cm}^{-1}$) are found. This indicates that more defects are introduced to graphene due to enhanced interface interactions. We have to mention here that the role of ZnO in the creation of defects on graphene should not be ignored. The degradation of graphene by the ZnO support has been observed in Chapter 4. Compared to the graphene spectrum of the freshly deposited CoPt/G/ZnO sample, after low pressure oxidation treatment the samples show similar 2D peak width but higher I_D/I_G ratio, signifying that this step partly increases the amount of defects. However, a further reduction step has no evident effect on the graphene quality, which might be due to the relatively low reduction temperature (250 °C) and/or the hydrogen conditioning. Additionally, graphene is less defective after low pressure oxidation and reduction than after

UHV treatment. This means that higher annealing temperature (550 °C) is more critical than the redox conditions (5×10^{-7} mbar) in creating defects.

Table 5.1 The peak intensity ratios and the 2D peak fwhm of CoPt/G/ZnO sample under various treatments.

Samples	I _D /I _G	I _{2D} /I _G	2D (fwhm/cm ⁻¹)
GZnO	0	1.60	32.3
CoPt/G/ZnO (Fresh depposited)	0.36	1.42	45.6
CoPt/G/ZnO (After UHV 550 °C)	0.50	0.37	61.1
CoPt/G/ZnO (5×10^{-7} mbar O₂, 300 °C)	0.45	0.67	46.4
CoPt/G/ZnO (5×10^{-7} mbar redox)	0.48	0.65	45.3
CoPt/G/ZnO (7 mbar O₂, 250 °C)	1.01	0.36	46.2
CoPt/G/ZnO (7 mbar redox)	1.05	0.37	45.3

The Raman spectrum of CoPt/G/ZnO after oxidation under 7 mbar O₂ shows much higher peak intensity of both D and D' and an additional D+D' peak at 2920 cm⁻¹ appears. This implies that medium pressure oxidation introduced more defects to graphene than the low pressure conditions. However, the treatment pressure has no evident effect on the quality of the remaining graphene islands.

5.4 Conclusions

This chapter reports the study of the effect of graphene interlayer on the arrangement and the redox behavior of bimetallic PtCo overlayers. Graphene influences the arrangement between Pt and Co and favors their intermixing. On the other hand, bare ZnO enhances Co and Pt separation. This arrangement has a direct influence on the redox properties of PtCo; graphene supported PtCo overlayers are much more resistant to oxidation in O₂ but more susceptible to reduction under H₂.

5.5 References

- (1) Liao, H.; Fisher, A.; Xu, Z. J. Surface Segregation in Bimetallic Nanoparticles: A Critical Issue in Electrocatalyst Engineering. *Small* **2015**, *11* (27), 3221–3246.
- (2) Xin, H. L.; Alayoglu, S.; Tao, R.; Genc, A.; Wang, C. M.; Kovarik, L.; Stach, E. A.; Wang, L. W.; Salmeron, M.; Somorjai, G. A.; et al. Revealing the Atomic Restructuring of Pt-Co Nanoparticles. *Nano Lett.* **2014**, *14* (6), 3203–3207.
- (3) Borgna, A.; Anderson, B. G.; Saib, A. M.; Bluhm, H. Pt-Co/SiO₂ Bimetallic Planar Model Catalysts for Selective Hydrogenation of Crotonaldehyde. *J. Phys. Chem. B* **2004**, *108* (46), 17905–17914.
- (4) Newton, M. A.; Belver-Coldeira, C.; Martínez-Arias, A.; Fernández-García, M. Dynamic in Situ Observation of Rapid Size and Shape Change of Supported Pd Nanoparticles during CO/NO Cycling. *Nat. Mater.* **2007**, *6* (7), 528–532.
- (5) Penuelas, J.; Andreatza, P.; Andreatza-Vignolle, C.; Tolentino, H. C. N.; De Santis, M.; Mottet, C. Controlling Structure and Morphology of CoPt Nanoparticles through Dynamical or Static Coalescence Effects. *Phys. Rev. Lett.* **2008**, *100* (11), 1–4.
- (6) Xu, H.; Fu, Q.; Guo, X.; Bao, X. Architecture of Pt-Co Bimetallic Catalysts for Catalytic CO Oxidation. *ChemCatChem* **2012**, *4* (10), 1645–1652.
- (7) Schanke, D.; Vada, S.; Blekkan, E. A.; Hilmen, A. M.; Hoff, A.; Holmen, A. Study of Pt-Promoted Cobalt CO Hydrogenation Catalysts. *J. Catal.* **1995**, *156* (1), 85–95.
- (8) Xu, X.; Fu, Q.; Wei, M.; Wu, X.; Bao, X. Comparative Studies of Redox Behaviors of Pt-Co/SiO₂ and Au-Co/SiO₂ Catalysts and Their Activities in CO Oxidation. *Catal. Sci. Technol.* **2014**, *4* (9), 3151.
- (9) Huang, Q.; Yang, H.; Tang, Y.; Lu, T.; Akins, D. L. Carbon-Supported Pt-Co Alloy Nanoparticles for Oxygen Reduction Reaction. *Electrochem. Commun.* **2006**, *8* (8), 1220–1224.
- (10) Liu, L.; Pippel, E.; Scholz, R.; Gösele, U. Nanoporous Pt-Co Alloy Nanowires: Fabrication, Characterization, and Electrocatalytic Properties. *Nano Lett.* **2009**, *9* (12), 4352–4358.
- (11) Luo, W.; Doh, W. H.; Law, Y. T.; Aweke, F.; Ksiazek-sobieszek, A.; Sobieszek, A.; Salamacha, L.; Skrzypiec, K.; Machocki, A.; Zafeiratos, S. Single-Layer Graphene as an Effective Mediator of the Metal-Support Interaction. *J. Phys. Chem. Lett.* **2014**, *5*, 1837–1844.

- (12) Hyman, M. P.; Martono, E.; Vohs, J. M. Studies of the Structure and Interfacial Chemistry of Co Layers on ZnO(0001). *J. Phys. Chem. C* **2010**, *114* (40), 16892–16899.
- (13) Papaefthimiou, V.; Dintzer, T.; Dupuis, V.; Tamion, A.; Tournus, F.; Teschner, D.; Hävecker, M.; Knop-Gericke, A.; Schlögl, R.; Zafeiratos, S. When a Metastable Oxide Stabilizes at the Nanoscale: Wurtzite CoO Formation upon Dealloying of PtCo Nanoparticles. *J. Phys. Chem. Lett.* **2011**, *2* (8), 900–904.
- (14) Papaefthimiou, V.; Dintzer, T.; Lebedeva, M.; Teschner, D.; Hävecker, M.; Knop-Gericke, A.; Schlögl, R.; Pierron-Bohnes, V.; Savinova, E.; Zafeiratos, S. Probing Metal–Support Interaction in Reactive Environments: An in Situ Study of PtCo Bimetallic Nanoparticles Supported on TiO₂. *J. Phys. Chem. C* **2012**, *116* (27), 14342–14349.
- (15) Schalow, T.; Laurin, M.; Brandt, B.; Schauermaun, S.; Guimond, S.; Kuhlenbeck, H.; Starr, D. E.; Shaikhutdinov, S. K.; Libuda, J.; Freund, H.-J. Oxygen Storage at the Metal/oxide Interface of Catalyst Nanoparticles. *Angew. Chem. Int. Ed. Engl.* **2005**, *44* (46), 7601–7605.
- (16) Schalow, T.; Brandt, B.; Starr, D. E.; Laurin, M.; Shaikhutdinov, S. K.; Schauermaun, S.; Libuda, J.; Freund, H.-J. Size-Dependent Oxidation Mechanism of Supported Pd Nanoparticles. *Angew. Chem. Int. Ed. Engl.* **2006**, *45* (22), 3693–3697.
- (17) Liu, X.; Liu, M.-H.; Luo, Y.-C.; Mou, C.-Y.; Lin, S. D.; Cheng, H.; Chen, J.-M.; Lee, J.-F.; Lin, T.-S. Strong Metal-Support Interactions between Gold Nanoparticles and ZnO Nanorods in CO Oxidation. *J. Am. Chem. Soc.* **2012**, *134* (24), 10251–10258.
- (18) Law, Y. T.; Doh, W. H.; Luo, W.; Zafeiratos, S. A Comparative Study of Ethanol Reactivity over Ni, Co and NiCo-ZnO Model Catalysts. *J. Mol. Catal. A Chem.* **2014**, *381* (0), 89–98.
- (19) Zheng, F.; Alayoglu, S.; Guo, J.; Pushkarev, V.; Li, Y.; Glans, P.-A.; Chen, J.; Somorjai, G. In-Situ X-Ray Absorption Study of Evolution of Oxidation States and Structure of Cobalt in Co and CoPt Bimetallic Nanoparticles (4 nm) under Reducing (H₂) and Oxidizing (O₂) Environments. *Nano Lett.* **2011**, *11* (2), 847–853.
- (20) Chernavskii, P. a.; Pankina, G. V.; Chernavskii, a. P.; Peskov, N. V.; Afanas'ev, P. V.; Perov, N. S.; Tennov, V. a.; Lunin, V. V. The Kinetics of Low-Temperature Oxidation of Cobalt Nanoparticles on a Carbon Carrier. *Russ. J. Phys. Chem.* **2006**, *80* (9), 1475–1480.
- (21) Lee, Y.; Lim, K.; Chung, Y.; Whang, C.; Jeon, Y. XPS Core-Level Shifts and XANES Studies of Cu–Pt and Co–Pt Alloys. *Surf. Interface Anal.* **2000**, *30*, 475–478.

- (22) Vasquez, Y.; Sra, A. K.; Schaak, R. E. One-Pot Synthesis of Hollow Superparamagnetic CoPt Nanospheres. *J Am Chem Soc* **2005**, *127* (36), 12504–12505.
- (23) Jiang, Z.-Z.; Wang, Z.-B.; Chu, Y.-Y.; Gu, D.-M.; Yin, G.-P. Ultrahigh Stable Carbon Riveted Pt/TiO₂-C Catalyst Prepared by in Situ Carbonized Glucose for Proton Exchange Membrane Fuel Cell. *Energy Environ. Sci.* **2011**, *4* (3), 728.
- (24) Abe, Y.; Kawamura, M.; Sasaki, K. Preparation of PtO and α -PtO₂ Thin Films by Reactive Sputtering and Their Electrical Properties. *Jpn. J. Appl. Phys.* **1999**, *38* (Part 1, No. 4A), 2092–2096.
- (25) Werdinius, C.; Österlund, L.; Kasemo, B. Nanofabrication of Planar Model Catalysts by Colloidal Lithography: Pt/Ceria and Pt/Alumina. *Langmuir* **2003**, *19* (2), 458–468.
- (26) Österlund, L.; Kielbassa, S.; Werdinius, C.; Kasemo, B. Reactivity of Pt/ceria and Pt/alumina Planar Model Catalysts Prepared by Colloidal Lithography. *J. Catal.* **2003**, *215*, 94–107.
- (27) Gong, C.; McDonnell, S.; Qin, X.; Azcatl, A.; Dong, H.; Chabal, Y. J.; Cho, K.; Wallace, R. M. Realistic Metal–Graphene Contact Structures. *ACS Nano* **2014**, *8* (1), 642–649.
- (28) Iqbal, M. W. Z.; Singh, A. K.; Iqbal, M. W. Z.; Eom, J. Raman Fingerprint of Doping due to Metal Adsorbates on Graphene. *J. Phys. Condens. Matter* **2012**, *24* (33), 335301.
- (29) Leong, W. S.; Nai, C. T.; Thong, J. T. L. What Does Annealing Do to Metal–Graphene Contacts? *Nano Lett.* **2014**, *14* (7), 3840–3847.

Chapter 6

Summary, general conclusion and perspectives

Chapter 6 Summary, general conclusion and perspectives

6.1 General conclusion

Understanding the interaction between metals and oxides is essential to determine the performance of metal/oxide catalysts in chemical reactions. One central issue of concern in employing oxide supported metal catalysts is the ability of rational design of new catalysts so as to control this interaction. In this work, we focus on the effect of graphene, a recently developed very promising material, on the metal-oxide support interaction. For this reason a model system, based on monometallic and bimetallic cobalt over single layer graphene-coated oxide supports, was designed and fabricated. The effect of graphene to the cobalt-oxides interaction under various environments is explored. The combination of *in-situ* surface techniques (such as XPS, HREELS etc.) and ex-situ techniques (such as AFM and Raman) allowed us to investigate the effects of graphene to the physical properties of the supported Co materials, i.e. surface composition, morphology and the chemical state. Experiments under various pressure reduction (H_2) and oxidation (O_2) environments helped us to understand the modification of the Co redox properties by graphene.

In chapter 3, we describe how graphene was successfully transferred onto ZnO(0001) surface through the wetting transfer method. The high quality of transferred graphene was proved by Raman and AFM. Co nanoparticles on ZnO (Co/ZnO) and Graphene-ZnO (Co/G/ZnO) were prepared under vacuum and their interaction with the supports was studied *in situ* by annealing the samples in the UHV and the results were interpreted by performing quantitative and chemical surface analysis by XPS. AFM images showed that freshly deposited Co formed highly dispersed nanoparticles on G/ZnO and a relatively flat layer structure on ZnO. Annealing of Co/ZnO in UHV proved that Co can be oxidized by ZnO starting from 200 °C, and be completely oxidized to CoO at 300 °C through the solid reaction ($Co + ZnO \rightarrow CoO + Zn$). In contrast, Co on G/ZnO maintained the metallic state even after annealing at 350 °C. The results indicate that the single layer graphene acts as a physical barrier for the in-diffusion of Co and it's also impermeable toward oxygen transport from the support. After UHV

annealing, the agglomeration of Co nanoparticles on G/ZnO and the re-dispersion of CoO on ZnO were evidenced by both XPS results and AFM images. Moreover, low defects density but p-type doping was shown in the Raman spectra of graphene after Co deposition and UHV annealing. Overall, these results prove that graphene can effectively prevent the oxidation of Co by the ZnO support and has also an effect on Co morphology.

In chapter 4, the redox properties of Co supported on bare substrates (SiO₂ and ZnO) and single layer graphene covered substrates (G/SiO₂ and G/ZnO), as well as on HOPG as a reference substrate, were investigated under low pressure (5×10^{-7} mbar) and medium pressure (7 mbar) oxidation (O₂)/reduction (H₂) conditions. After Co deposition, the surface morphologies of all five samples were studied ex-situ by AFM. It is shown that Co tends to form relatively flat layer structure on bare substrates (ZnO and SiO₂), however, nanoparticulate structure was observed on the substrates with a carbon layer on top (graphene and HOPG).

Under 5×10^{-7} mbar O₂, Co in direct contact with ZnO and SiO₂ substrates was readily oxidized even at room temperature. However, the oxidation of Co on the carbon substrates was limited even after long exposures at more elevated temperature. The reason for these differences seems to be the formation of a surface CoO layer on the Co nanoparticles (when supported by the carbon materials) which, in turn, prevents further dissociation and deeper diffusion of the oxygen into the core of the nanoparticles under the mild low pressure experimental conditions. These results were further confirmed by ARXPS measurements, where preferential oxidation of Co from the interface was observed on SiO₂ and ZnO, in contrast to the carbon substrates where surface oxidation was more pronounced.

The reduction of oxidized Co by 5×10^{-7} mbar H₂ was strongly affected by the metal support interaction. CoO on ZnO was initially partially reduced upon annealing in H₂, but higher temperature heating (always in 5×10^{-7} mbar H₂) led to its complete oxidation. This is attributed to a solid reaction between Co and ZnO, which also responsible to a flattening of Co particles morphology in the AFM topography images. Here one should note that the interaction differs among the various oxide substrates. Thus in the case of the SiO₂ substrate, CoO was fully reduced, however, at very high temperature (600 °C) while the reduction temperature was significantly lower when CoO was on the carbon surface. The reduced Co was found to agglomerate to larger particles as compared to that on the fresh deposited samples upon annealing. However, among different samples the stronger Co-substrate interaction led to the formation of relatively smaller particles.

Under 7 mbar O₂, Co was oxidized to CoO at room temperature and further to Co₃O₄ at 250 °C, independently of the substrate. In 7 mbar H₂ the XPS results revealed a two-step reduction process (Co₃O₄ → CoO → Co) for all substrates. However, the reduction temperature was still strongly affected by the graphene layer. Likewise the low pressure reduction, under 7 mbar H₂ partly reduced Co was re-oxidized by ZnO at 400 °C while Co₃O₄ was fully reduced to Co. With a single interlayer graphene, the temperature of both reduction steps for Co₃O₄ take place at lower temperature. For all substrates, cobalt agglomerated at nanometer size particles was observed in the AFM images.

The Raman results showed that a higher deposition amount of Co and a redox treatment at higher pressure introduced more defects to the graphene layer. Moreover, both Co and ZnO act catalytically for the defects formation in graphene during the medium pressure oxidation/reduction treatments. This part of the work proved that single layer graphene can be used as a buffer layer to tune the Co-support interaction; it limits the oxidation of Co at low O₂ pressure but facilitates the reduction at both low and medium pressure conditions.

In chapter 5, the graphene's effect to the interaction between a bimetallic system (Co-Pt) and the more reactive oxide support ZnO, with and without graphene was studied under 3 different environments: UHV, low and medium pressure gas atmosphere. For fresh samples, after room temperature deposition in UHV, it was observed that graphene allow better mixing of Pt and Co, in contrast to ZnO which facilitates higher cobalt surface exposure. In UHV, Co on CoPt/ZnO was oxidized upon annealing but at higher temperature compared to monometallic Co studied in Chapter 3. On the contrary on PtCo/G/ZnO cobalt oxidation is restricted at a temperature as high as 550 °C. Moreover, Co oxidation state defines the composition of PtCo overlayer. In particular, at higher temperature Co redispersed accompanied with Pt agglomerated on ZnO, while over graphene Pt seems to dominate the surface.

Upon low pressure oxidation (5×10^{-7} mbar O₂) treatments, Co was gradually oxidized in both CoPt/ZnO and CoPt/G/ZnO, however, as in the case of UHV, in the presence of graphene cobalt oxidation is restricted. The effect of graphene in limiting cobalt oxidation is twofold. Not only restricts direct oxidation by the oxide support, but also drives more Pt on the surface, protecting cobalt from gas phase oxidation. However upon higher temperature, kinetic limitations are raised and the thermodynamic tendency of cobalt to form an oxide leads to its surface segregation over Pt. As in the previous case reduction in H₂ is favored over graphene

supported sample. Addition of Pt promotes the reduction of Co on both substrates due to the hydrogen spillover effect; in this case, CoO on ZnO could also be reduced at low H₂ pressure (5×10^{-7} mbar). Under medium oxidation conditions (7 mbar O₂), Co oxidation rate was very similar on both substrates. However, we also observed Pt oxidation which was much easier on ZnO than graphene. Oxidized Pt and Co could be readily reduced to the metallic state, while a lower reduction temperature was still observed on G/ZnO.

Raman results indicated that the high annealing temperature and oxidation environment were more critical for the stability of graphene, while relatively low temperature hydrogen treatments had little influence on graphene. This part of the work proved that single layer graphene can be used to tune the metal-support interaction in a more complex system (Co-Pt). Although under all experiment conditions Pt hindered the oxidation of Co and accelerated the reduction of Co oxides, graphene was found to enhance these effects and even protected Pt from high pressure oxidation.

6.2 Perspective

In this work, single layer graphene has been used to modify the interactions between metal (Co, Co-Pt) and support (ZnO, SiO₂). Results from Raman have demonstrated that bilayer graphene islands are more stable than single layer graphene under medium pressure redox treatments. This higher stability of bilayer (and multilayer) graphene has also been proved under other conditions such as atomic hydrogen^{1,2}, argon-ion sputtering^{3,4} etc. Moreover, large scale producing and applying multilayer graphene are more practical than single layer graphene.^{5,6} Thus, it is necessary to study further the bilayer and/or fewlayer graphene's effect to the metal-support interaction. Of course there is a limit on how many graphene layers might be used since with increasing graphene layers the properties of graphene resemble those of graphite. Therefore, a comparison between graphene with different numbers of layers should be taken into account in future studies.

There are also a few interesting aspects of graphene modification. Introducing defects, functional groups and heteroatoms onto graphene can enable us to adjust and optimize the interaction between the metal nanoparticles and the graphene layer at the atomic level.⁷ As it has been reported, defects can be generated under controlled conditions by ion sputtering⁸ while nitrogen doped graphene can be produced through the CVD method,^{9,10} besides, controllable hydrogenation¹ and oxidation^{11,12} of graphene has been realized under UHV

conditions. These methods and the obtained graphene materials would be helpful for investigating the effects of modified graphene to the metal-support interactions.

This work has illustrated that the graphene layer can significantly affect the Co morphology, oxidation state and the segregation of bimetallic Co-Pt. Each of these effects plays an important role in catalytic reactions. Thus, it would be interesting to carry out probe reactions, such as CO adsorption and ethanol decomposition, on these materials and investigate the influence of graphene to these catalytic reactions.

In order to bridge the “material gap” between our model system and technical catalysts, the model substrates could be extended to graphene coated oxide supports with high surface area, which can be tested under realistic reaction conditions. For these studies, literature results can be used as a guide to produce graphene coated supports like for example SiO₂¹³ and ZnO¹⁴.

Overall, we hope that this thesis is not restricted only on the currently studied materials and can be also used to predict the behavior of other oxide supports and metals used in catalytic but also other applications (e.g. electronics). We also believe that proposes a relatively original application of graphene as an oxide support moderator/promoter. This is a new perspective as compared to previously suggested graphene use to protect metals from corrosion or as an electrode material.

6.3 References

- (1) Ryu, S.; Han, M. Y.; Maultzsch, J.; Heinz, T. F.; Kim, P.; Steigerwald, M. L.; Brus, L. E. Reversible Basal Plane Hydrogenation of Graphene. *Nano Lett.* **2008**, *8* (12), 4597–4602.
- (2) Elias, D.; Nair, R.; Mohiuddin, T. Control of Graphene's Properties by Reversible Hydrogenation: Evidence for Graphane. *Science* **2009**, *323* (5914), 610–613.
- (3) Martins Ferreira, E. H.; Moutinho, M. V. O.; Stavale, F.; Lucchese, M. M.; Capaz, R. B.; Achete, C. a.; Jorio, A. Evolution of the Raman Spectra from Single-, Few-, and Many-Layer Graphene with Increasing Disorder. *Phys. Rev. B* **2010**, *82* (12).
- (4) Krauss, B.; Lohmann, T.; Chae, D. H.; Haluska, M.; Von Klitzing, K.; Smet, J. H. Laser-Induced Disassembly of a Graphene Single Crystal into a Nanocrystalline Network. *Phys. Rev. B* **2009**, *79* (16), 1–9.
- (5) Hernandez, Y.; Nicolosi, V.; Lotya, M.; Blighe, F. M.; Sun, Z.; De, S.; McGovern, I. T.; Holland, B.; Byrne, M.; Gun'Ko, Y. K.; et al. High-Yield Production of Graphene by Liquid-Phase Exfoliation of Graphite. *Nat. Nanotechnol.* **2008**, *3* (9), 563–568.
- (6) Narita, A.; Feng, X.; Hernandez, Y.; Jensen, S. A.; Bonn, M.; Yang, H.; Verzhbitskiy, I. A.; Casiraghi, C.; Hansen, M. R.; Koch, A. H. R.; et al. Synthesis of Structurally Well-Defined and Liquid-Phase-Processable Graphene Nanoribbons. *Nat. Chem.* **2013**, *6* (2), 126–132.
- (7) Zhang, B.; Dang Sheng Su. Probing the Metal – Support Interaction in Carbon-Supported Catalysts by Using Electron Microscopy. *ChemCatChem* **2015**, *110016*, 3639–3645.
- (8) Lucchese, M. M.; Stavale, F.; Ferreira, E. H. M.; Vilani, C.; Moutinho, M. V. O.; Capaz, R. B.; Achete, C. A.; Jorio, A. Quantifying Ion-Induced Defects and Raman Relaxation Length in Graphene. *Carbon* **2010**, *48* (5), 1592–1597.
- (9) Lv, R.; Li, Q.; Botello-Méndez, A. R.; Hayashi, T.; Wang, B.; Berkdemir, A.; Hao, Q.; El ás, A. L.; Cruz-Silva, R.; Gutiérrez, H. R.; et al. Nitrogen-Doped Graphene: Beyond Single Substitution and Enhanced Molecular Sensing. *Sci. Rep.* **2012**, *2*, 586.
- (10) Zafar, Z.; Ni, Z. H.; Wu, X.; Shi, Z. X.; Nan, H. Y.; Bai, J.; Sun, L. T. Evolution of Raman Spectra in Nitrogen Doped Graphene. *Carbon* **2013**, *61*, 57–62.
- (11) Vinogradov, N. A.; Schulte, K.; Ng, M. L.; Mikkelsen, A.; Lundgren, E.; Mårtensson, N.; Preobrajenski, A. B. Impact of Atomic Oxygen on the Structure of Graphene Formed on Ir(111) and Pt(111). *J. Phys. Chem. C* **2011**, *115* (19), 9568–9577.

- (12) Starodub, E.; Bartelt, N. C.; McCarty, K. F. Oxidation of Graphene on Metals. *J. Phys. Chem. C* **2010**, *114* (11), 5134–5140.
- (13) Lim, D.; Barhoumi, A.; Wylie, R. G.; Reznor, G.; Langer, R. S.; Kohane, D. S. Enhanced Photothermal Effect of Plasmonic Nanoparticles Coated with Reduced Graphene Oxide. *Nano Lett.* **2013**, *13*, 4075–4079.
- (14) Shao, D.; Yu, M.; Sun, H.; Hu, T.; Lian, J.; Sawyer, S. High Responsivity, Fast Ultraviolet Photodetector Fabricated from ZnO Nanoparticle-Graphene Core-Shell Structures. *Nanoscale* **2013**, *5* (9), 3664–3667.

Appendix

Supporting Information

Supporting Information 1: SEM images of graphene-ZnO and graphene-SiO₂ substrates before cobalt deposition.

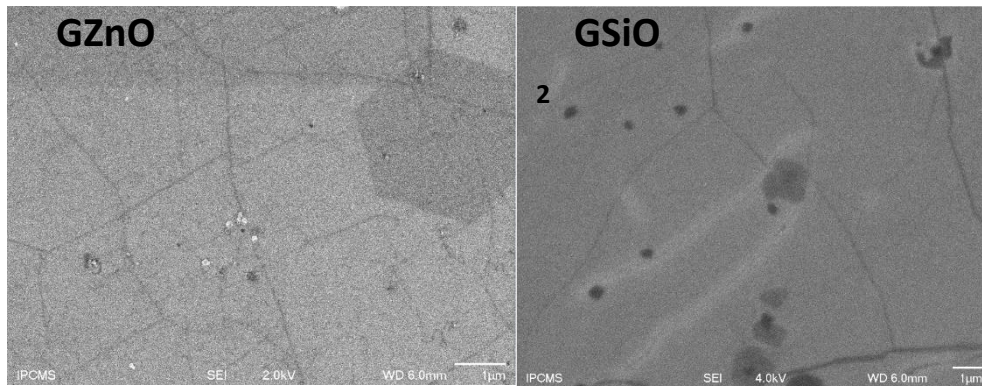


Figure S1. Scanning Electron Microscopy (SEM) images of GZnO and GSiO₂ samples before cobalt deposition.

Supporting Information 2: XPS spectra of 0.8 nm Co on SiO₂ and on G/SiO₂ fresh and after treatment in 7 mbar O₂ at two characteristic temperatures.

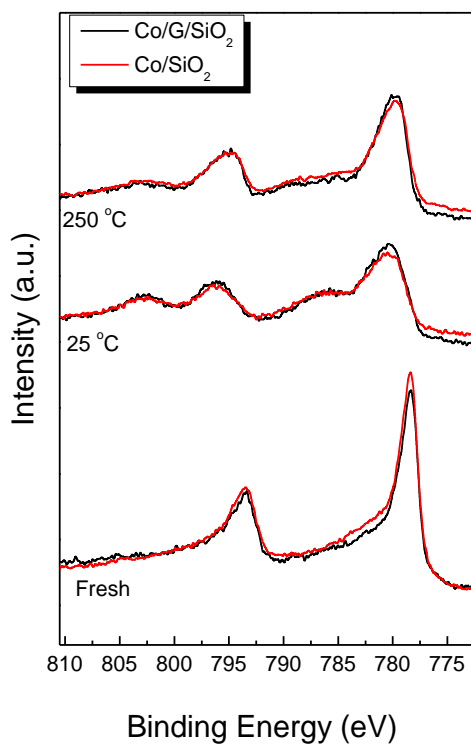


Figure S2 XPS spectra of Co/G/SiO₂ and Co/SiO₂ obtained upon oxidation in 7 mbar O₂ up to 250 °C

Supporting Information 3: Two characteristic examples of the Co 2p XPS peak fitting procedure followed for the calculation of the mean valence state of cobalt.

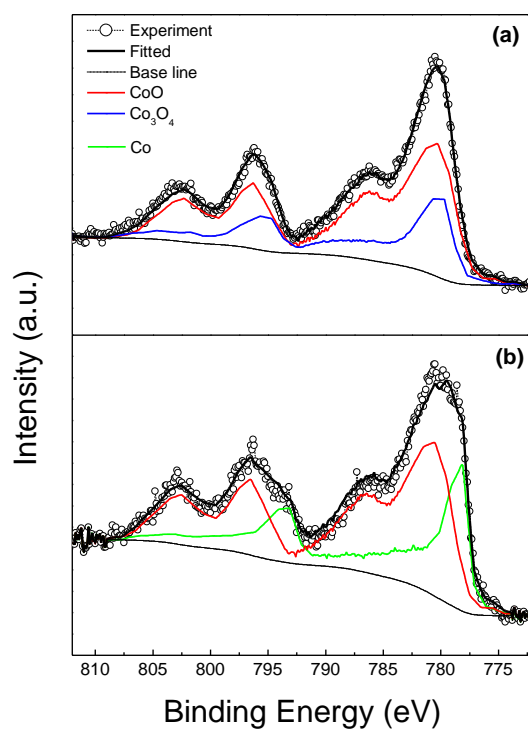


Figure S3 An example of XPS spectrum deconvolution. (a) Co/G/SiO₂ after oxidation at 150 °C and (b) Co/G/SiO₂ after reduction at 300 °C.

Supporting Information 4: Co Ledge NEXAFS spectrum of Co/ZnO(0001) annealed at 320 C in 0.3 mbar H₂

Figure S4 show the Co L_{3,2}-edge NEXAFS spectrum of Co/ZnO (0001) sample after treatment at 360 °C in 0.2 mbar H₂. The peak position and the line shape of the Co L-edge spectrum depend on the local electronic structure of the Co²⁺ ions. The low intensity the low photon energy shoulder (about 778 eV) is characteristic of tetrahedrally coordinated Co²⁺ ions probably forming a mixed Zn_{1-x}Co_xO oxide.

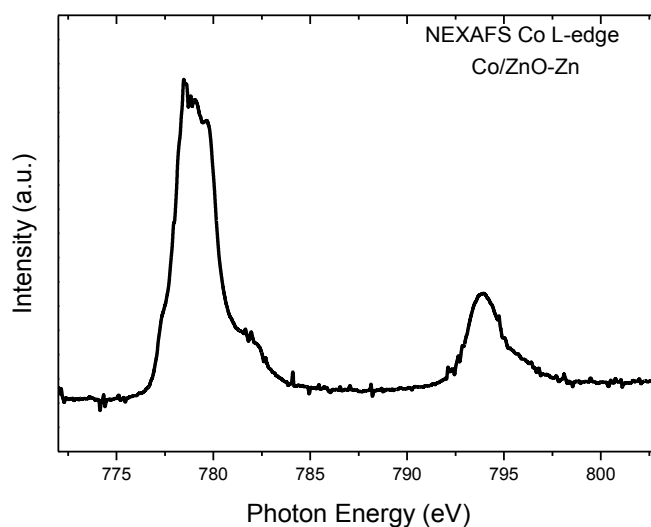


Figure S4 Co Ledge NEXAFS spectrum of Co/ZnO(0001) annealed at 320 C in 0.3 mbar H₂

Support Information 5: Histogram of diameters for Co nanoparticles on different substrates after medium redox treatments.

All AFM images were analyzed with Image Analysis software (version 3.5.0, NT-MDT). A 3rd order plane subtraction was applied to correct the scanning drift and image bow. The Co particle size distribution was obtained through “Grain Analysis” tool of Image Analysis software with parameters for densely packed nearly spherical particles. Other geometric parameters of the particles such as average size, volume, height etc. can also be obtained.

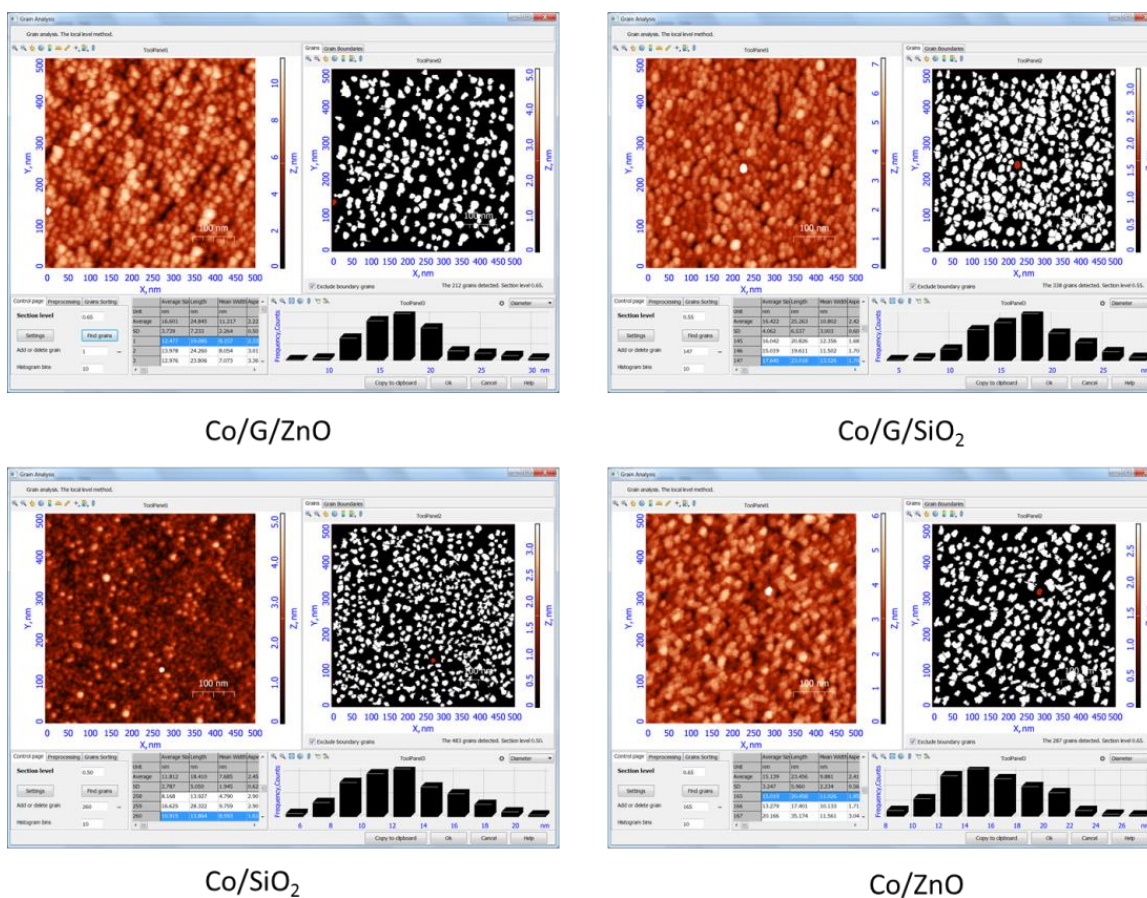


Figure S5 Histograms and processed images used for the for the estimation of the cobalt average diameter based on the AFM images after the redox treatments

Support Information 6: SESSA simulation model.

The intensity ratios of the XPS spectra were simulated by the Simulation of Electron Spectra for Surface Analysis (SESSA) software, Version 2.0 (National Institute of Standards and Technology, Gaithersburg, MD). For the SESSA simulation, the geometry between sample, X-ray gun and analyzer was set the same as the configuration of the XPS experiment. The inelastic mean free path values were calculated by the software using the TPP-2M formula. The parameters, such as photoionization cross sections, material density etc., were also used from the default database of the software. Islands morphology was chosen to simulate the particle structure of supported Co. Figure S6 shows the model of Co/G/ZnO sample. The average diameter and height values from the AFM images were used for the length and height of Co islands while the density of Co islands was calculated by (the volume of deposited Co) / (the volume of each Co island). The graphene layer thickness was set to be 0.35 nm for both Co/G/ZnO and Co/G/SiO₂ samples. Based on this model, a XPS spectrum can be simulated and the intensity ratio of Co/substrate can be calculated.

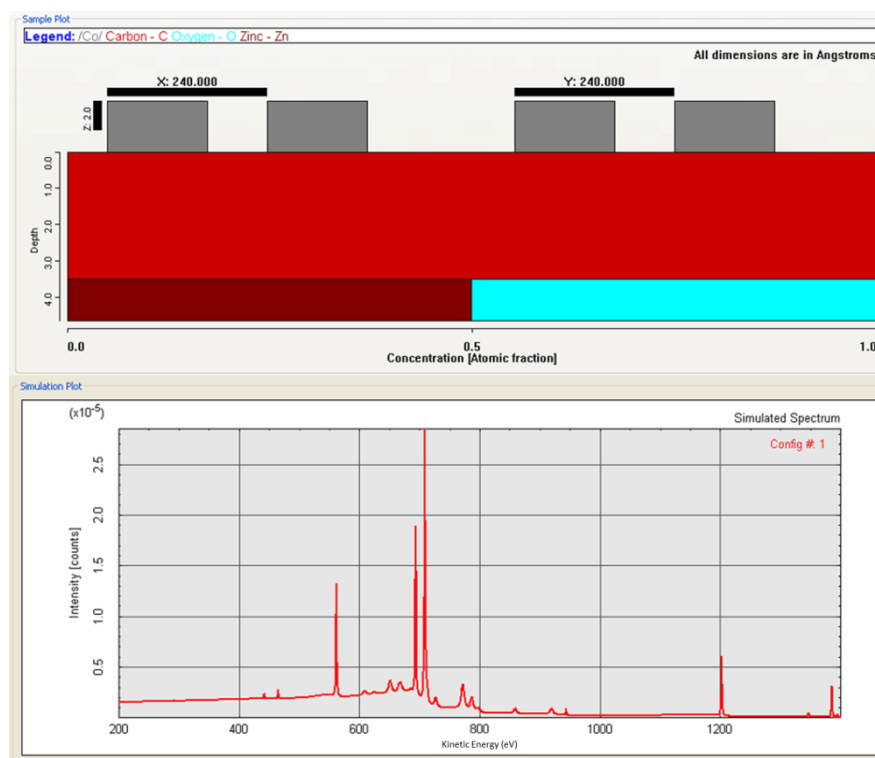


Figure S6 A model of SESSA simulation (Co/G/ZnO sample)

Symbols and Abbreviation

AFM	Atomic force microscopy
ARXPS	Angular resolved X-ray spectroscopy
CVD	Chemical vapor deposition
DFT	Density Functional Theory
FWHM	full width at half maximum
G/SiO ₂	Gaphene coated SiO ₂
G/ZnO	Gaphene coated ZnO
HOPG	Highly ordered pyrolytic graphite
HREELS	High resolution electron energy loss spectroscopy
LEIS	Low energy ion scattering
ML	monolayer
OM	Optical microscopy
Raman	Raman spectroscopy
SEM	Scanning Electron microscopy
STM	Scanning tunneling microscopy
TPD	Temperature programmed desorption
UHV	Ultra high vacuum
XPS	X-ray photoemission spectroscopy

Résumé

L'interaction métal-support (MSI) joue un rôle important dans la catalyse hétérogène. La compréhension et la modification du MSI sont des étapes essentielles pour développer catalyseurs de haute performance. Dans cette thèse, un nouveau concept, qu'il s'agit de recouvrir le support l'oxyde avec un revêtement mono-couche de graphène, a été proposé pour modifier le MSI. L'influence de la couche de graphène sur les interactions de métal (Co et Co-Pt) - oxyde (ZnO et SiO₂) et sur les propriétés d'oxydo-réduction des particules métalliques ont été évaluées via des systèmes catalytiques de modèle. Les résultats ont montré que la mono-couche de graphène peut influencer considérablement les états d'oxydation et les morphologies des Co monométallique et Co-Pt bimétallique par rapport aux ceux résultent d'un dépôt direct sur les oxydes nus. En particulier, par calcination sous vide, le graphène protège Co d'être oxydé par ZnO, ce qui conduit à la formation d'un mélange métallique Co-Pt. Co interagit avec les substrats d'oxydes pour former des particules plates qui sont facilement oxydés par O₂ en pression faible, tandis que l'insertion d'une couche intermédiaire de graphène entre la couche supérieure métallique et le supporte d'oxyde entraîne la formation des nanoparticules de Co en état très dispersés, qui sont résistants à l'oxydation. Sous la condition de réduction par H₂, le graphène favorise clairement la réduction de Co. La quantité de dépôt de Co, le substrat d'oxyde, la température de calcination et l'environnement ont été prouvés pour pouvoir influencer la stabilité de graphène. Ces résultats ouvrent des nouvelles voies possibles d'utiliser le graphène comme promoteur dans des réactions catalytiques à l'avenir.

Mots clés: Cobalt, Graphène, Platinium, ZnO, SiO₂, interaction métal-support, les propriétés redox

Résumé en anglais

The metal-support interaction (MSI) plays an important role in heterogeneous catalysis. Understanding and tuning the MSI are essential steps for developing catalysts with high performance. In this thesis, a new concept, which is coating the oxide supports with a single layer graphene, was introduced to modify the MSI. The influence of graphene layer on the metal (Co and Co-Pt) – oxide (ZnO and SiO₂) interactions and on the redox properties of metal particles were evaluated through model catalyst systems. The results showed that single layer graphene can significantly influence the oxidation states and morphologies of both mono Co and bimetallic Co-Pt as compared to the one after direct deposition on bare oxides. In particular, under vacuum annealing, graphene protects Co from being oxidized by ZnO and results in Co-Pt metallic mixture. Co interacts with oxide substrates forming flat particles which are easily oxidized by low pressure O₂, while insertion of a graphene interlayer between the metal overlayer and the oxide supports leads to the formation of highly dispersed Co nanoparticles, which are resistant to oxidation. Under H₂ reduction condition, graphene evidently facilitates the reduction of Co. The deposition amount of Co, the oxide substrate, the annealing temperature and the environment were proved to influence the stability of graphene. These results explore new directions for the possible future of using graphene as a promoter in catalytic reactions.

Key words: Cobalt, Graphene, Platinium, ZnO, SiO₂, metal-support interaction, redox properties